

**Studies of intensified liquid-liquid
extractions in small-channel contactors
and their scale-up**

Eduardo Garciadiego Ortega

Thesis submitted for the award of the degree of
Doctor of Philosophy

Department of Chemical Engineering

Faculty of Engineering Sciences

University College London

December 2019

I, Eduardo Garciadiego Ortega, confirm that the work presented in this thesis is my own. Where information has been derived from other sources, I confirm that this has been indicated in the thesis.

Eduardo Garciadiego Ortega

Abstract

This thesis presents a series of investigations focused on scaling-up intensified liquid-liquid flow processes from single-channel to commercial-scale. The process investigated consists of liquid-liquid extractions of U(VI) from nitric acid to an organic phase. These extractions are relevant to the safety and sustainability of the nuclear fuel cycle. The intensified contactor consists of a tee-junction feeding to a channel with small internal diameter (1 to 4 mm) operating under segmented flow pattern.

Segmented flow contactors intensify liquid-liquid extractions in uranium recovery processes because they provide intense mixing, short diffusion distances, and large interfacial area at low energy input. Using high-speed imaging, UV-Vis spectroscopy, pressure gradient measurements, and dimensional analysis, the operation and design trade-offs are quantitatively identified with focus on scale-up. A finite-element model is used to corroborate the experimental mass transfer results.

The scale-up is achieved via numbering-up, which increases the number of process units instead of making one larger unit. Economic parallelisation requires effective flow distribution. Multiphase flow distribution has been a persistent problem in the path towards commercialisation. This problem is addressed by modelling a double manifold with a resistance network model and a novel method to quantify maldistribution, derived from multivariate statistical analysis. The relationships between the hydraulic resistances with maldistribution, pumping power, and the number of channels are quantified.

Finally, the single-channel results and the flow distributor model are used to design, build, and test a modular multichannel segmented flow contactor prototype. The design and commissioning steps are described along with the experimental maldistribution results, including flow distribution and mass transfer results. The multichannel contactor can be operated with different number of channels at any time, thus changing a long-standing paradigm in reactor design. This promises to accelerate process development by facilitating the transition from bench to pilot and commercial scales.

Impact statement

The methodologies and results presented in this thesis can have a significant impact on academic research, but especially, commercially.

Some of the peer-reviewed publications that stemmed from the same research as this thesis have already been cited by international authors. The vision behind this thesis has made its results relevant and long-reaching. Certainly, there will come more citations to this work.

The effective parallelisation of two-inlet process equipment has been a long-standing problem in chemical engineering. The development of the resistance network model and the statistical flow maldistribution descriptors, presented in this thesis, can be used to design and build process equipment for a wide range of applications. In this thesis, the double manifolds were used to scale-out liquid-liquid extractions, however, double manifolds can also be used to scale-out single- and multiphase static-mixer processes, as well as gas-liquid, gas-liquid-solid, and liquid-liquid-solid processes under any flow pattern. This opens the door to the use of double manifolds in a wide range of process industries, including food, pharmaceuticals, petrochemicals, fine chemicals, hydrometallurgy, and new sustainable manufacturing industries.

In order to increase the impact within academic research, the methods developed and the results obtained should be applied in future research projects and publish them to show their significance and applicability. An effective strategy to maximise the impact of this research is to present the outcomes in international meeting and conferences. Academic social media platforms like ResearchGate are an important tool to connect with interested researchers and permanently showcase the results.

This thesis is focused on solving hurdles towards commercialisation of intensified liquid-liquid processes. Therefore, commercial impact is possible and should be prioritised. There are many paths towards commercial impact, the main difference among the paths is the stage at which other companies become involved. Early

involvement of a private company could accelerate the short-term impact but stifle the widespread application of the novel technologies derived from this research. Late involvement may block the realisation of the impact due to high costs, delays, and commercial inexperience. Timing the partnerships is crucial.

The benefits of realising the potential impact of this research are necessarily reflected in society. For example, an intensified PUREX process would make the nuclear fuel cycle more sustainable, safe and low cost. In general, modular intensified multiphase reactors could make manufacturing of many critical materials more sustainable, faster to develop and improve, and would reduce the costs to consumers.

Acknowledgements

I am immensely grateful to my supervisor Professor Panagiota Angeli. Her guidance, support, and patience throughout the PhD enabled me to grow as a researcher. I appreciate her generous mentorship regarding this research and my career in general. I am also thankful to my secondary supervisor, Professor Gary Lye, for his feedback and support.

I greatly appreciate the financial support provided by CONACYT and UCL during this degree. Their sponsorships were critical for me to start and complete this research.

Thank you to everyone in ThAMeS and the Chemical Engineering Department with whom I got to work. I am also grateful to Martin Blackman and everyone else in the High Precision Design & Fabrication Facility for all their help. Everyone made their unique contributions to my research and to create a rich research environment. Especially, I am thankful to Dr Dimitrios Tsaoulidis who was always helpful, thoughtful, and truly a great mentor.

Completing this degree would not have been possible without the help of my friends. Thanks to everyone I shared a laugh with, either in the UK, Europe, or back home. My friendships with Berni and Roberto are particularly appreciated. Thanks to Berni for always reminding me there is more than one way to think about everything, and thanks to Roberto for all the guanciales.

To Tania, we still have a long way to go but thanks for everything so far. I am already looking forward to what is next for us. Let's make it happen!

Last but not least, thanks to my family. I dedicate this accomplishment to all of you. Gracias mamá por todos tus sacrificios y enseñanzas. Gracias Klokli por ser mi hermana favorita y por todo tu apoyo.

List of publications and presentations

Peer-Reviewed publications

Dimitrios Tsaoulidis, Eduardo Garciadiego Ortega, Panagiota Angeli, Intensified extraction of uranium(VI) in impinging-jets contactors, Chemical Engineering Journal, Volume 342, 2018, Pages 251-259, ISSN 1385-8947, DOI: 10.1016/j.cej.2018.02.049.

Eduardo Garciadiego Ortega, Dimitrios Tsaoulidis, Panagiota Angeli, Predictive model for the scale-out of small channel two-phase flow contactors, Chemical Engineering Journal, Volume 351, 2018, Pages 589-602, ISSN 1385-8947, DOI: 10.1016/j.cej.2018.06.020.

Panagiota Angeli, Eduardo Garciadiego Ortega, Dimitrios Tsaoulidis, Martyn Earle, Intensified Liquid-Liquid Extraction Technologies in Small Channels: A Review, Johnson Matthey Technology Review, Volume 63 (4), 2019, Pages 299-310, DOI: 10.1595/205651319x15669171624235.

Eduardo Garciadiego Ortega, Dimitrios Tsaoulidis, Miguel Pineda, Eric S. Fraga, Panagiota Angeli, Hydrodynamics and mass transfer in segmented flow small channel contactors for uranium extraction, Chemical Engineering & Processing: Process Intensification, Submitted for publication on September 12th 2019.

Lectures and oral presentations

Garciadiego Ortega E., Tsaoulidis D., Angeli P. Scale-out of liquid-liquid flows in small channels. 5th Micro and Nano Flows Conference 2016 (MNF 2016). 11 – 14 September 2016, Milan, Italy.

Garciadiego Ortega E., Tsaoulidis D., Angeli P. Intensified liquid-liquid extractions. International Workshop on Process Intensification 2016 (IWPI 2016). 29 – 30 September 2016, Manchester, UK.

Garciadiego Ortega E., Tsaoulidis D., Angeli P. Liquid-liquid Extraction in Intensified Small Scale Units. 2016 AIChE Annual Meeting. 13 – 18 November 2016, San Francisco CA, US.

Garciadiego Ortega E., Tsaoulidis D., Angeli P. Intensified Liquid-liquid Processes. 2017 UCL Mexican Society Engineering Talkabout. 26 January 2017, London, UK.

Garciadiego Ortega E., Tsaoulidis D., Angeli P. Intensification of liquid-liquid processes using millichannels. Presentation within round table “Green Chemistry and Sustainability”. 6th Europe-CONACyT Symposium. 29 – 31 March 2017, European Parliament, Strasbourg, France.

Garciadiego Ortega E., Tsaoulidis D., Angeli P. Intensified Processes Using Small-scale Contactors for Energy Applications. 10th World Congress on Chemical Engineering 2017. 1 – 5 October 2017, Barcelona, Spain.

Garciadiego Ortega E., Tsaoulidis D., Angeli P. Intensified U(VI) Extractions Using Small-channel Contactors. 21st International Solvent Extraction Conference 2017. 5 – 9 November 2017, Miyazaki, Japan.

Garciadiego Ortega E., Tsaoulidis D., Angeli P. Intensification Of Liquid-liquid Processes In Small Channels And Their Scale-up. International Conference On Nanochannels, Microchannels, And Minichannels 2018. 10 – 13 June 2018, Dubrovnik, Croatia.

Tsaoulidis D., Garciadiego Ortega E., Lyu W., Angeli P. Intensified extraction of U(VI) in impinging-jets reactors. International conference on nuclear engineering (ICONE), 2018.22 – 26 July, London, UK

Garciadiego Ortega E. Process intensification and liquid-liquid reactor engineering. Invited lectures in Chemical Reactor Engineering I and II at Universidad Nacional Autonoma de Mexico. With Professor Rogelio Cuevas-Garcia and Professor Martin Hernandez-Luna. 8, 9 August 2018. Mexico City, Mexico.

Tsaoulidis D., Garciadiego Ortega E., Angeli P. Biodiesel production from cooking oil in intensified contactors. ACS National Meeting, 19 – 23 August 2018 Boston, US.

Garciadiego Ortega E., Tsaoulidis D., Angeli P. Scale-out of intensified PUREX extractions. 2018 AIChE Annual Meeting. 28 October – 2 November 2018, Pittsburgh PA, US.

Garciadiego Ortega E., Tsaoulidis D., Angeli P. Extractions of U(VI) with TBP in nitric acid media. Towards intensified contactors for nuclear fuel reprocessing. Uranium Science 2019. 21 – 22 January 2019, Bristol, UK.

Garciadiego Ortega E., Tsaoulidis D., Angeli P. Intensification and scale-up of a solvent extraction process using a modular flow distributor. 2nd International Process Intensification Conference (IPIC2). 27 – 29 May 2019, Leuven, Belgium.

Tsaoulidis D., Farooqui F., Garciadiego Ortega E., Angeli P. Scale-up studies for intensified production of biodiesel from used cooking oil. Valuable products from residual biomasses Towards a greener society (ProGreS). 23 – 24 September 2019, Sofia, Bulgaria.

Poster presentations

Li Q., Garciadiego Ortega E., Angeli P. Intensified Eu(III) extraction using ionic liquids in small channels. Sustainable Nuclear Energy Conference 2016 (SNEC 2016). 12 – 14 April 2016, Nottingham, UK.

Garciadiego Ortega E., Tsaoulidis D., Angeli P. Scale-out of liquid-liquid processes in slug flow. 2016 UCL Chemical Engineering poster competition. 13 December 2016, London, UK.

Garciadiego Ortega E., Tsaoulidis D., Angeli P. Scale-up of Liquid-Liquid Microreactors for the Energy Sector. UCL Mexico Energy Summit 2017. 22 June 2017, London, UK.

Garciadiego Ortega E., Tsaoulidis D., Angeli P. Scale-out of Liquid-Liquid Processes in Small Channels Using Double Manifolds. Industrial Advisory Board Meeting Poster Competition. 23 February 2018, London, UK.

Garciadiego Ortega E., Tsaoulidis D., Angeli P. Liquid-liquid extractions in small channels and their scale-up using modular flow distributors. Reactors, Scale-Up and Separations: Process intensification, integration and multifunctionality, Society of Chemical Industry (SCI). 12 September 2019, London, UK. Awarded with 1st Place Poster Prize.

Table of Contents

Abstract	5
Impact statement	7
Acknowledgements.....	9
List of publications and presentations	11
Table of Contents	15
List of figures	19
List of tables	27
Nomenclature	29
1 Introduction.....	31
1.1 Sustainable innovation in chemical engineering and process intensification	31
1.2 Motivation and objectives.....	34
1.3 Thesis outline.....	36
2 Literature Survey	37
2.1 Introduction	37
2.2 Applications of liquid-liquid processes.....	37
2.2.1 Key design and operation parameters in liquid-liquid extractions	39
2.2.2 Liquid-liquid extractions in small channels	43
2.3 Liquid-liquid segmented flow.....	50
2.4 Mass transfer in segmented flow.....	55
2.4.1 Mass transfer coefficient	56
2.5 Pressure drop and energy requirements of segmented flow	62
2.6 Scale-up of small-channel processes.....	65
2.6.1 Economies of scale.....	66

2.6.2 Single phase flow distribution	67
2.7 Scale-up of multiphase small-channel processes	71
2.7.1 Scale-dependence of segmented flow processes.....	71
2.7.2 Two-phase flow distribution.....	73
2.7.3 Scale comparison of intensified and conventional contactors.....	79
2.8 Overview	80
3 Research Methods.....	83
3.1 Experimental methods	83
3.1.1 Materials and flow equipment.....	83
3.1.2 Characterisation of hydrodynamic properties	85
3.1.3 High-speed imaging and post-processing	91
3.1.4 Pressure drop measurements	92
3.1.5 UV-vis spectroscopy	92
3.1.6 Liquid-liquid flow separation	93
3.2 Numerical modelling.....	94
3.2.1 Resistance network model of double manifolds.....	94
3.2.2 Correlated maldistribution characterisation	101
4 Studies of segmented flow for multiphase processing applications	109
4.1 Introduction	109
4.2 Hydrodynamic features of segmented flow.....	109
4.3 Pressure gradient in segmented flow	119
4.4 U(VI) extraction and mass transfer in segmented flow contactors	125
4.4.1 Analysis of operation and design variables on extraction efficiency.....	125
4.4.2 Mass transfer coefficient	131

4.5 Conclusions	139
5 Model for the scale-out of small channel two-phase flow contactors	141
5.1 Introduction	141
5.2 Effect of hydraulic resistances on flow maldistribution in the double manifold	142
5.3 Effect of hydraulic resistances on the pressure drop and power requirements of the double manifold	147
5.4 Effect of increasing number of channels on flow maldistribution	150
5.5 Effect of increasing number of channels on pressure drop and power requirements.	160
5.6 Design methodology for two-phase double manifolds	162
5.7 Conclusions	164
6 Double manifold prototype and experimentation	165
6.1 Introduction	165
6.2 Design parameters and trade-offs of small-channel contactors for U(VI) extraction ..	166
6.3 Application of the design methodology of double manifolds for mass transfer applications	170
6.4 Design and commissioning of a modular double manifold prototype	177
6.5 Experimental flow distribution performance of modular double manifold	183
6.6 Scaled-out reactive extraction using a modular double manifold	186
6.7 Conclusions	191
7 Conclusions and future work.....	193
7.1 Conclusions	193
7.2 Future Work.....	199
References	209

Appendix	231
1. Pressure drop model derivation.....	231
2. Derivation of holdup and specific interfacial area models	233
3. Matlab code for the calculation of the R matrix	234
4. Exponents of dependence for L_{Eff} , T_{Eff} , N , and Δp_{Eff}	235

List of figures

Figure 1-1 Sustainable development goals pertinent to this thesis.	31
Figure 1-2 Process intensification principles and domains, as defined by Gorak & Stankiewicz [3].	33
Figure 1-3 Diagram of the scope and the range of scales addressed in this thesis.	35
Figure 2-1 Single contacting stage in a liquid-liquid extraction with common terminology. Reproduced from Ruthven (2008) [9].	39
Figure 2-2 Concentration profile of solute C near an interface. The arrow represents the direction of the mass transfer. C_A , C_{Ai} , C_B , and C_{Bi} are the concentration of C in the bulk of A, in the interface on the A side, in the bulk of B and in the interface on the B side, respectively. Reproduced from Ruthven (2008) [9].	41
Figure 2-3 Schematic of liquid-liquid segmented flow pattern. L_u , L_p , and L_s are the unit, plug, and slug lengths, respectively.	51
Figure 2-4 Schematic of the circulation patterns found in segmented liquid-liquid flows in small channels. The blue phase is the continuous (wetting) phase and the yellow phase is the dispersed (non-wetting) phase.	55
Figure 2-5 Conceptual difference between processes using conventional equipment (a), and scaled-out equipment (b). Reproduced from Luis & Garcia-Verdugo [99].	65
Figure 2-6 Cost curve for microreactors and conventional reactors as a function of heat exchange duty. Reproduced from Harmsen (2013) [102].	67
Figure 2-7 Consecutive manifold. a) Shows a schematic of the flow distributor, b) shows the corresponding resistance network used to model the flow distribution.	69
Figure 2-8 Split-and-recombine flow distributor schematic. Reproduced from Wang et al. [110].	70
Figure 2-9 Schematics of a screen-header flow distributor. Reproduced from Rebrov et al. [111].	71

Figure 2-10 Matrix of the effects of maldistribution of each phase (u_c , u_d) on the mixture velocity (u_{mix}) and flow ratio (u_c/u_d). \hat{u} is the mean (or design) velocity across the channels for either phase.	74
Figure 2-11 Schematics of the two basic strategies to multiphase scale-out. In a) the split-combine approach is presented and b) shows the combine-split approach.	75
Figure 2-12 Bubble-splitting bifurcation distributor, an example of the combine-split scale-out strategy. Reproduced from Hoang [118].	76
Figure 2-13 Random mixer design proposals for 3-D multiphase monolith contactors. Reproduced from Chugh et al. [119].	76
Figure 2-14 Barrier-based two-phase flow distributor designed by Al-Rawashdeh et al. [123].	78
Figure 3-1 Density of solutions used at 293 K. In a), density of pure water and water saturated with the organic solutions. In b), density of the organic phases, pure and after saturation with water.	88
Figure 3-2 Viscosity of solutions used at 293 K. In a), viscosity of pure water and water saturated with the organic phases. In b), viscosity of the organic phases, pure and after saturation with water.	90
Figure 3-3 Interfacial tension of mutually saturated organic solutions and water at 293 K.	91
Figure 3-4 Schematic of flow setup for high-speed imaging, pressure drop measurements and flow separation.	92
Figure 3-5 Flow separator schematic showing the membrane section where the separation takes place and the pressure control section that ensures no incomplete separation nor breakthrough. Adapted from Adamo et al. [132].	94
Figure 3-6 a) Schematic of a double manifold. b) Schematic of the corresponding resistance network. A1 and A2 are the distribution sections, B1 and B2 are the barrier sections, R is the main section and C is the collection section; Q1 and Q2 refer to the flow rates of each fluid.	95

Figure 3-7 The j -th loops considered in the application of the Kirchhoff's Voltage Law.	96
Figure 3-8 Geometric interpretation of the maldistribution descriptors in flow rate maps. a) Distribution with no correlation and the maldistribution is measured with standard deviations (Eq. 3-25). b) Correlated case where the eigenvalues and the eigenvector slope are used to measure the maldistribution (Eqs. 3-26 and 3-27). c) Highly correlated distribution where the points nearly form a line segment; the length and slope of this line segment describe the maldistribution (Eqs. 3-26 and 3-27).	106
Figure 4-1 L_p/d predicted from Eq. 4-1 against experimental results with 20% bands for all cases studied.	114
Figure 4-2 $(1-L_p/L_u)$ predicted from Eq. 4-2 against experimental results with 20% bands for all cases studied.	115
Figure 4-3 Experimental and predicted (Eq. 4-3) L_u/d dependence from Ca_c . For all cases, $Q_c/Q_T=0.5$, $d=2$ mm, $u_{mix} = [1.06, 2.12, 3.18, 4.24]$ cm s ⁻¹ . Results for TBP 30% have $Re_c/Ca_c=3301$, $\mu_d/\mu_c=0.426$ (continuous line). Results for TBP 100% have $Re_c/Ca_c=792$, $\mu_d/\mu_c=0.216$ (dashed line).	116
Figure 4-4 $f_u Re_c$ predicted from Eq. 4-16 and experimental results with 20% bands for all cases studied.	121
Figure 4-5 Pressure gradient (experimental and calculated using Eq. 4-16). The base case is $d=2$ mm, $u_{mix}=1.06$ cm s ⁻¹ , TBP 30%, $Q_c/Q_T=0.500$	123
Figure 4-6 Adjusted Kreutzer model prediction (surface) and experimental results (points). The a and b parameters are adjusted with non-linear regression (using Matlab Curve Fitting); the intervals correspond to 95% confidence intervals.	124
Figure 4-7 Extraction efficiency against residence time for the base case ($d=2$ mm, $u_{mix}=1.06$ cm s ⁻¹ , TBP 30%, $Q_c/Q_T=0.5$) and for the high mixture velocity case ($d=2$ mm, $u_{mix}=4.24$ cm s ⁻¹ , TBP 30%, $Q_c/Q_T=0.5$).	126
Figure 4-8 Extraction efficiency (at $\tau=5$ s) against internal diameter ($d= 1, 2, 4$ mm) for the base case ($u_{mix}=1.06$ cm s ⁻¹ , TBP 30%, $Q_c/Q_T=0.5$) and for the high mixture velocity case ($u_{mix}=4.24$ cm s ⁻¹ , TBP 30%, $Q_c/Q_T=0.5$) cases.	127

Figure 4-9 Effect of TBP concentration in the organic phase on extraction. a) U(VI) concentration in the aqueous phase against residence time; the dashed lines correspond to the equilibrium concentrations for each organic phase. b) Extraction efficiency against residence time. Diameter = 2 mm, mixture velocity = 1.06 cm s⁻¹, and phase ratio Q_o/Q_T=0.5. 128

Figure 4-10 Effect of the organic phase fraction on the extraction of U(VI) for organic phase fractions 0.500, 0.333, 0.250. a) U(VI) concentration against residence time; the horizontal lines correspond to the equilibrium concentrations for each organic phase fraction(C_{aq}^{eq}). b) Extraction efficiency against residence time. Diameter = 2 mm, mixture velocity = 1.06 cm s⁻¹, and TBP 30%..... 130

Figure 4-11 Velocity field (a) and concentration profiles of U(VI) in the plug (b) and slug (c) from 0 to 60 s for the base case (d=2 mm, u_{mix}= 1.06 cm s⁻¹, TBP 30%, Q_o/Q_T=0.5). 135

Figure 4-12 Simulated and experimental average U(VI) concentration in the aqueous phase against time for the base case (TBP 30%) and the high TBP concentration case (TBP 100%). The dashed lines represent the equilibrium concentration values (d=2 mm, u_{mix}=1.06 cm s⁻¹, Q_o/Q_T=0.5)..... 135

Figure 4-13 Mass transfer coefficient evolution with time for the base case (TBP 30%) and the high TBP concentration case (TBP 100%). The dashed lines represent the experimental K_{aq} values at the same conditions (Table 4-4). (d=2 mm, u_{mix}=1.06 cm s⁻¹, Q_o/Q_T=0.5). 136

Figure 4-14 Initial, experimental, and final segmented flow mass transfer coefficients (K_{aq}). Initial K_{aq} is the mass transfer coefficient for the first time step of the simulation. Final K_{aq} is the value at which the segmented flow mass transfer coefficient approaches asymptotically. 137

Figure 5-1 3D Schematic of a double manifold with one inlet for each fluid, distribution sections (A1, A2, green), barrier sections (B1, B2, orange), and main channels (R, red). 141

Figure 5-2 Distribution profiles and flow rate maps for cases 3 (a to c) and 7 (d to f) from Table 5-1 ($N=5$, $Q_T=6 \times 10^{-6} \text{ m}^3 \text{ s}^{-1}$). a, b, d, e) Flowrates of each phase in the channels; the perfect distribution line is calculated as $Q_{A1,1}/N$. c, f) Flow rate maps. The circle indicates the perfect distribution case, calculated as $(Q_{A1,1}/N, Q_{A2,1}/N)$. The 95% confidence ellipses are also shown; the minor axis length, b , is zero in both cases and the ellipses collapse into line segments. 143

Figure 5-3 Contour plots of a) $\log_{10}R_{CV1}$ and b) $\log_{10}PRM$ in \log_{10} - \log_{10} planes of R_A/R_B vs. R_B/R_R . The double manifold modelled has 5 channels, $Q_{A1,1}=5 \times 10^{-6} \text{ m}^3 \text{ s}^{-1}$, $Q_{A2,1}=1 \times 10^{-6} \text{ m}^3 \text{ s}^{-1}$ ($r=5$). The arrows show the direction of greatest decrease for the maldistribution descriptors. 146

Figure 5-4 Equivalent resistances as a function of R_A/R_B and N . The dashed lines (---) show exact solutions using Eqs. 5-3 and 5-4 and the solid lines show approximations using Eq. 5-5. Calculations are for $R_B/R_R=0.1$ 149

Figure 5-5 Contour plot of $\log_{10}P_T/(Q_T^2R_R)$ in a \log_{10} - \log_{10} plane of R_A/R_B vs. R_B/R_R . The double manifold modelled is symmetrical, has 5 main channels, $Q_{A1,1}=5 \times 10^{-6} \text{ m}^3 \text{ s}^{-1}$, $Q_{A2,1}=1 \times 10^{-6} \text{ m}^3 \text{ s}^{-1}$. The pumping efficiencies are 80%. The arrows show the direction of greatest decline for the dimensionless pumping power. 150

Figure 5-6 Flow rate maps for different number of main channels. For all figures, $Q_{T,1ch}=1.2 \times 10^{-6} \text{ m}^3 \text{ s}^{-1}$, $r=5$, $R_A/R_B=10^{-3}$, $R_B/R_R=10^2$. In panel a) the axes do not start in the origin. 152

Figure 5-7 Maldistribution descriptors as functions of the number of channels for representative resistance ratios. For both panels, $Q_{T,1ch}=1.2 \times 10^{-6} \text{ m}^3 \text{ s}^{-1}$, $r=5$. Four combinations of resistance ratios are plotted; both types of lines (solid and dashed) have equal R_B/R_R values. For all points, ρ is larger than 0.95. 153

Figure 5-8 Flow rate maps of scaled-out double manifolds using the scaling laws in Eqs. 5-12 and 5-13 for $Q_{T,1ch}=1.2 \times 10^{-6} \text{ m}^3 \text{ s}^{-1}$, $r=5$. The axes do not start in the origin. The resistance ratios are $R_A/R_B=10^{-3}$ $R_B/R_R=10^2$ for $N=5$, $R_A/R_B=2.08 \times 10^{-5}$ $R_B/R_R=97.5$ for $N=50$, and $R_A/R_B=4.33 \times 10^{-7}$ $R_B/R_R=95.0$ for $N=500$ 159

Figure 5-9 Pressure drop and pumping power requirements for scaled-out double manifolds obtained using Eqs. 5-14 and 5-16, respectively. The 95% confidence intervals lines in red dashed lines are plotted using the confidence intervals in Table 5-3. The base case has $N1=5$, $r=5$, $R_A/R_B=10^{-3}$, and $R_B/R_R=100$ 162

Figure 6-1 Contactor length against extraction efficiency for four of the cases in Table 6-1. 169

Figure 6-2 Flow chart showing the sequence of inputs, calculations, and decisions needed to design a double manifold using the resistance network model and a non-linear pressure drop model in the main section..... 173

Figure 6-3 Flow distributions for double manifolds using the models in Chapter 4 and the flow chart in Fig. 6-2. Fluid 1 is the organic phase (TBP 30% v/v with kerosene) and fluid 2 is water. In all cases, the geometries are $L_R=600$ mm, $d_R=2$ mm, $L_A=50$ mm, and $L_B=120$ mm. In a), d_A and d_B are 10 and 1 mm. In b), d_A and d_B are 10 and 0.5 mm. In c), d_A and d_B are 20 and 0.5 mm. 176

Figure 6-4 Details and features of the distribution section of the double manifold prototype. The inlet and part of the inlet section are shown in a). The flange connections used to make the prototype modular and the detail of the barrier outlets are presented in b). The end-port, opposite to the inlet, used in the fill-up procedure is presented in c) 178

Figure 6-5 Distribution section and operating double manifold. One distribution section, including the entrance section, is presented in a). The double manifold in operation, with the shut-off valves open, is shown in b). Front view of the distribution sections are depicted in c). 180

Figure 6-6 Experimental flow distribution results for double manifolds with 5 channels. The point of perfect distribution is shown in all cases and is the centre of the confidence ellipses. The square, circle and star symbols represent the measurements for each test. The maldistribution descriptors (RCV_1 , RCV_2 , PRM) presented are the mean values for the three tests. The ellipse angle and axes lengths are also the mean values for the three tests..... 184

Figure 6-7 Experimental flow distribution results for double manifolds with 10 channels. The point of perfect distribution is shown in all cases and is the centre of the confidence ellipses. The square, circle and star symbols represent the measurements for each test. The maldistribution descriptors (R_{CV1} , R_{CV2} , PRM) presented are the mean values for the three tests. The ellipse angle and axes lengths are also the mean values for the three tests..... 185

Figure 6-8 Schematic of in-flow reactive extraction of acetic acid (AcOH) in the organic (continuous) phase to the alkaline aqueous (dispersed) phase and the consequent colour change of the phenolphthalein indicator (In^{2-} to H_2In)..... 187

Figure 6-9 Photographs of the double manifold prototype with 10 channels operating using the acid-base-indicator system. In a) the change of colour is noticeable along the channel length. In b) the detail of the tubing-fitting connections and drop characteristics are shown..... 188

Figure 6-10 Distance from the tee-junction where the aqueous phase becomes colourless in the acid-base-indicator reactive extraction experiments. The bars represent the means and standard deviations. a) presents the case $N=5$, $Q_{T,1ch}=1 \text{ ml min}^{-1}$. b) presents the case $N=5$, $Q_{T,1ch}=1.5 \text{ ml min}^{-1}$. c) presents the case $N=10$, $Q_{T,1ch}=1 \text{ ml min}^{-1}$. d) presents the case $N=10$, $Q_{T,1ch}=1.5 \text{ ml min}^{-1}$. Note the y-axis starts at 15 cm..... 189

Figure 7-1 Multi-level double manifold schematic with 50 main channels. This design can potentially increase the throughput with a minimal footprint. The path followed by each phase consists of one vertical feed section, an inlet section to allow a parabolic velocity profile to develop, a distribution section, a barrier section, a mixing junction, and the main channels. The a), b), and c) panels correspond to side, front, and top views, respectively. 206

Figure 7-2 Front view of a multi-level double manifold schematic with 100 main channels. Such a multi-level double manifold, depending on main channel diameter and flow velocity (Table 2-4), could process similar throughputs as conventional contactors with the advantages of segmented-flow contactors..... 207

Figure A-1 Profile of the pressure at the wall for a segmented flow pattern. Sourced from
“Experimental and numerical hydrodynamic studies of ionic liquid-aqueous plug flow in
small channels” By Li Q. & Angeli P. [8].231

List of tables

Table 2-1 Industrially important liquid-liquid reactions and extractions.	38
Table 2-2 Characteristics of different liquid-liquid contactors. Compiled from: w= Kashid et al. (2007) [14]x= Doraiswamy & Sharma (1984) [8]; y= Lo et al. (1983) [10]; z= Ruthven (2008) [9].	42
Table 2-3 Important dimensionless numbers for segmented flow mass transfer descriptions.	60
Table 2-4 Number of parallel channels of different diameters needed to process a determined throughput. Comparable conventional contactors are included for each throughput considered. The single-channel throughput in every channel is calculated for a mixture velocity of 4 cm s^{-1} . Operation years of 8000 hours are used.	80
Table 3-1 Dimensions of tubing used in flow experiments. Dimensions and uncertainties are reported by the manufacturers.	84
Table 3-2 Properties of the liquid phases and their uncertainties. These values are used to calculate dimensionless numbers.	87
Table 3-3 Examples of single-phase flow maldistribution metrics.	102
Table 3-4 Maldistribution cases and descriptors with respect to the correlation coefficient.	107
Table 4-1 Stills of segmented flow pattern observed. The aqueous phase is the dispersed phase and the organic phase is the continuous phase. Different diameter, organic phase composition, mixture velocity and phase ratio.	111
Table 4-2 Regression results and range of variables for Eqs. 4-1 and 4-2. The confidence intervals correspond to 95%. The range of Re_c is added for reference.	113
Table 4-3 Summary of constants and adjustable parameters for Eq. 4-4 according to published correlations for liquid-liquid systems. d_h is the hydraulic diameter of the square channels.	117

Table 4-4 Segmented flow mass transfer coefficient (K_{aq}), specific interfacial area (a), aqueous phase holdup (ϵ_{aq}) and their products ($K_{aq}a$, $K_{aq}a/\epsilon_{aq}$). For every case, all variables are the same as the base case, except for the stated change.....	132
Table 5-1 Maldistribution descriptors for r : 1 and 5, R_A/R_R : 0.1 and 10, R_B/R_R : 0.1 and 10. The double manifold modelled has 5 channels and a total flow rate of $6 \times 10^{-6} \text{ m}^3 \text{ s}^{-1}$. In case 5, channeling, where the fluid flows opposite to the designed direction, is observed.	142
Table 5-2 Variables and their ranges used in the regressions of the maldistribution descriptors. One regression is calculated for $r=1$ and a separate regression is made for $r>1$	155
Table 5-3 Values for the exponents in Eqs. 5-12 to 5-16. The choice of exponents depends on the inlet flow rate ratio, r . The uncertainties correspond to 95% confidence intervals.	157
Table 6-1 Lengths required to achieve extraction efficiencies of 50% and 99% and the corresponding factors of Eq. 6-1. The factor $\epsilon_{aq}/(a \times d)$ is calculated using imaging results (Chapter 4) and the film thickness calculated with Eq. 4-7. Sh_{aq} is calculated assuming $D_{U W}=10^{-9} \text{ m}^2 \text{ s}^{-1}$ and the experimental K_{aq} results in Table 4-4, except for the $d=1 \text{ mm}$ and $d=4 \text{ mm}$ cases. For every case, all variables are the same as the base case, except for the stated change.	168
Table 6-2 Exponents of dependence between mixture velocity and channel diameter with main channel length and residence time for a given %Eff, number of main channels for a given throughput, and pressure drop for a given %Eff.....	169
Table 6-3 Description of the materials and dimensions used for the three sections of the double manifold prototype. The final column is included because the L/d^4 factor is part of the hydraulic resistance calculation.....	182
Table 7-1 Summary of advantages, disadvantages, challenges, and trade-offs identified for multiphase processing technologies operating under segmented flow (Taylor flow) and scaled-up using double manifolds.	198

Nomenclature

A	Interfacial area, m^2	P	Power, W
A'	Cross sectional area, m^2	p	Pressure, Pa
a	Ellipse major axis length, $m^3 s^{-1}$ / Specific interfacial area, m^{-1}	Δp	Pressure drop, Pa
b	Ellipse minor axis length, $m^3 s^{-1}$	Pe	Peclet number
C	Concentration, $mol m^{-3}$	PRM	Phase Ratio Maldistribution
Ca	Capillary number	Q	Flow rate, $m^3 s^{-1}$
CV	Coefficient of variation	Q	Flow rates vector
D	Distribution coefficient / Diffusion coefficient, $m^2 s^{-1}$	R	Hydraulic resistance
d	Channel diameter, m	R	Hydraulic resistance matrix
%Eff	Extraction efficiency, %	R^2	Pearson Correlation Coefficient
f	Friction factor	r	Flow rate ratio
I	Cost or investment	RCV	Rotated Coefficient of Variation
I	Identity matrix	Re	Reynolds number
J	Jovanovic curvature parameter	S	Solution vector
k	Mass transfer coefficient, $m s^{-1}$	Sh	Sherwood number
K	Mass transfer coefficient, $m s^{-1}$	u	Flow velocity, $m s^{-1}$
L	Channel length, m	V	Volume, m^3
m	Slope	v	Eigenvectors of covariance matrix
N	Number of main channels / Molar flux, $mol m^{-2} s^{-1}$	We	Weber number
n	Moles, mol	X	Exponent in Eqs. 5-12 – 5-16
		Y	Exponent in Eqs. 5-12 – 5-16

Greek letters

γ	Interfacial tension, $N m^{-1}$	π	Diameter-perimeter ratio of a circumference
δ	Film thickness, m	ρ	Density, $kg m^{-3}$ / correlation coefficient
ε	Volume fraction (holdup)	Σ	Covariance matrix
θ	Correlation angle	σ	Standard deviation
λ	Eigenvalues of covariance matrix, $m^6 s^{-2}$	τ	Residence time, s
μ	Dynamic viscosity, Pa s		

Subscripts and superscripts

A1, A2	Distribution sections	k	A given channel in a section of the double manifold
aq	Aqueous phase	mix	Mixture
B1, B2	Barrier sections	N1, N2	Number of channels in scale-up
C	Collection section	out	Outlet
c	Continuous phase	p	Plug
d	Dispersed phase	R	Main section
Eff	Extraction efficiency	s	Slug
eq	Equivalent / Equilibrium	T	Total
h	Hydraulic	T,1ch	Total, for one channel
i	Either phase or fluid	u	Unit
in	Inlet	U	Uranium
j	A given channel in a section of the double manifold		

1 Introduction

1.1 Sustainable innovation in chemical engineering and process intensification

This thesis investigates the hydrodynamics and mass transfer of two-phase systems in small channels and their scale up. In particular, the process investigated is a liquid-liquid extraction relevant to the reprocessing of spent nuclear fuel (SNF). The work is presented in the wider context of major sustainability challenges faced by the process industries and chemical engineering research. As such, this dissertation responds to the call of The Sustainable Development Goals (SDGs) set by all the nation members of the United Nations in 2015 [1]. Primarily, to SDGs 7, 9, and 12: 7 Affordable and clean energy; 9 Industry, innovation, and infrastructure; 12 Responsible consumption and production (Fig. 1-1). Technical innovation is needed to achieve all the SDGs and with them a global sustainable society. In chemical engineering, innovation is needed to make more with less, in a sustainable way. Locally, this means increasing yields and selectivities. But from a wider perspective, SDGs call chemical engineers to create more societal benefit at a lower environmental cost.



Figure 1-1 Sustainable development goals pertinent to this thesis.

Liquid-liquid reaction or extraction processes are critical in manufacturing. These processes have unique characteristics compared to homogeneous or other multiphase processes. By nature of using two immiscible liquids, the mixtures are highly non-ideal and challenging to describe thermodynamically. They take place at relatively low temperatures (below bubble point), therefore have an inherently small carbon footprint

(as long as heating comes from fossil fuels). Concentrations of reagents can be higher than in gases since densities are also much larger, however, momentum transfer and mass transfer via diffusion in liquids are slower than in gases due to the higher viscosity of liquids. Besides SNF reprocessing, hydrometallurgical processes, and some pharmaceutical purifications steps, liquid-liquid processes are not utilised in process industries as commonly as gas-liquid or homogeneous processes [2]. However, due to their characteristic low carbon footprint and milder conditions, liquid-liquid processes will play a larger role in the future process industries.

Process intensification (PI) is a blueprint to achieve innovation in chemical engineering. It calls for a redesign of chemical and physical processes with precision and optimisation of the reaction and transport phenomena as the overarching guiding principles. PI follows 4 principles across 4 domains [3]. This approach is depicted in figure 1.2. The research presented here is particularly focused on the second and third PI principles. The second principle, namely, 'Give each molecule the same processing experience' is equivalent to keeping the residence time distribution (RTD) as narrow as possible. In the numbering-up approach, addressed in Chapters 5 and 6, this is achieved by having the same flow rates in each channel. The third principle, about optimising driving forces and maximising interfacial area, is considered in Chapter 4. Here, the hydrodynamics of segmented flow, including interfacial areas are studied along with the effect of changing the solvent to a higher concentration in order to maximise the mass transfer driving force. The confinement of the two-phase flow inside small channels leads, in part, to the regular segmented flow pattern so this research falls within the spatial PI domain.

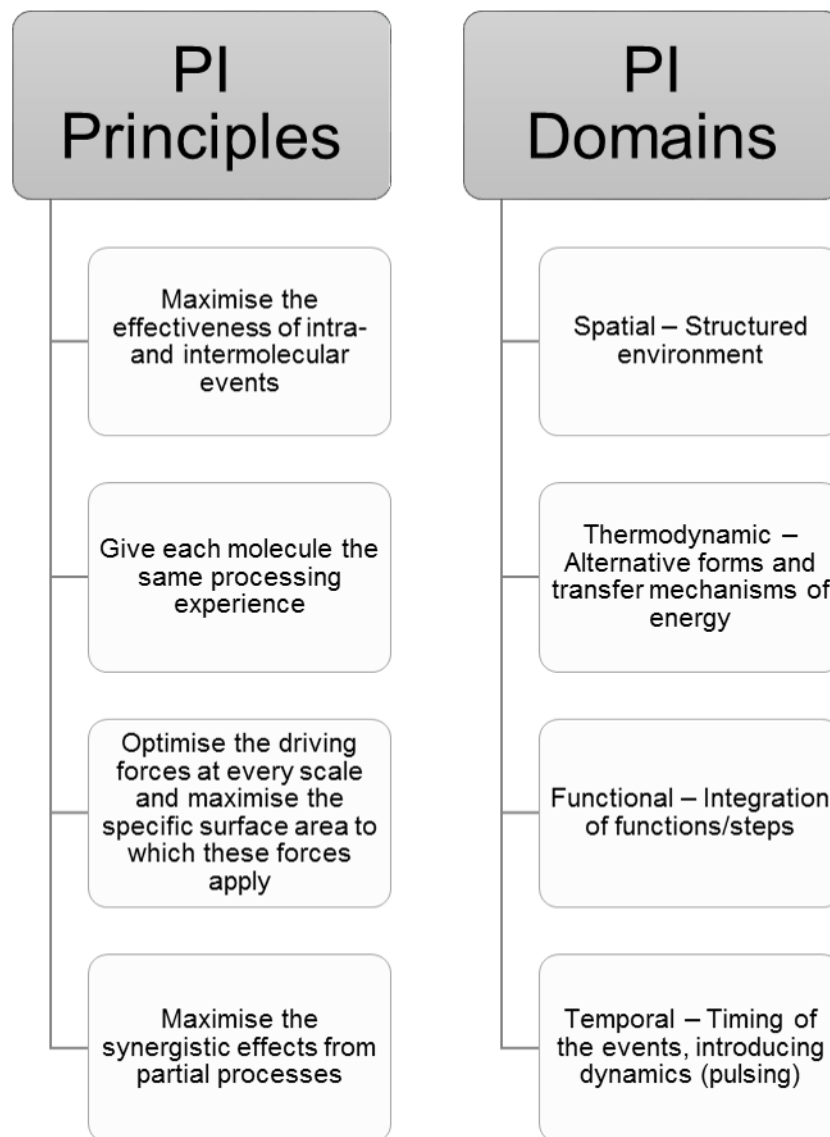


Figure 1-2 Process intensification principles and domains, as defined by Gorak & Stankiewicz [3].

PI has had a significant impact on chemical engineering research and in the development of novel processes and equipment. Notably, operating in small and micro-channels has been a prioritised area of PI research for the past decades [4]. This thesis is based on the PI principles and small scale contactor technology advancements to achieve high efficiency, large throughputs, and improve the inherent safety in liquid-liquid extractions for SNF reprocessing.

As part of the nuclear fuel cycle, the reprocessing (or recycling) of the fissile and fertile isotopes is crucial to make nuclear energy sustainable. Nuclear fuel reprocessing helps reduce the volume of intermediate- and high-level wastes (ILW, HLW), a priority of the industry [5]. Reprocessing cuts down the necessity of mining Uranium by 30% and

reduces HLW volume by 8 times [5]. The most common flowsheet for SNF reprocessing is called PUREX (plutonium uranium redox extraction) and uses TriButyl Phosphate as the extractant. The extraction steps commonly take place in mixer-settlers or pulsed columns [6]. These steps are similar to hydrometallurgical processing with the major difference of having significant radiation at the core of the process. This means the process and any proposed improvements must be safe against radiolysis. A process with radiolysis benefits from having a narrow residence time distribution (RTD), which is equivalent to the second PI principle. Several examples of nuclear fuel reprocessing in intensified small-channels are presented in Chapter 2.

The central challenge addressed in this thesis is the scale-up of intensified multiphase process technologies towards commercial scales. As mentioned above, PI partly focuses on transport precision and therefore PI is implemented at small scales, from molecular to transport-phenomena scales. There has not (yet) been widespread industrial adoption of novel PI technologies because, in most cases, the performance is correlated to the scale and increasing the dimensions results in performance loss. Since the inception of microreactor technology, scale-out by parallel operation of many contactors was seen as a solution to this problem. However, despite the important commercial potential of including small-channel contactors, there are no examples of commercially successful parallelisation of a multiphase micro contactor or reactor in the literature (a complete review is presented in Chapter 2).

1.2 Motivation and objectives

The main motivation behind this thesis is to understand the effect of scale on two-phase liquid-liquid separations in small channels and to develop a modelling framework to design scale-out manifolds. In particular, the liquid-liquid extractions relevant to SNF reprocessing are studied because they can potentially make nuclear energy safer and more sustainable by reducing the volume of the high-level waste (HLW) produced and by recycling important metals [5,6].

The objectives of this thesis are the following. (1) Review and expand the body of knowledge on small-channel liquid-liquid contactors. (2) Characterise the effect of scale on flow and mass transfer characteristics of segmented two-phase liquid-liquid flows in small channels. (3) Develop a robust design methodology to design flow distributors to scale-out two-phase flows into many parallel channels. (4) Design, build, test, and propose improvements to a multiphase flow distributor with a larger number of channels than current ones reported in the literature. (5) Discuss the potential of multi-channel multiphase processing technology; clearly identify advantages, disadvantages, challenges, and trade-offs.

The approach used to address the objectives is shown in Fig. 1.3. The results obtained at small scales inform the design and methodology for the scale-out studies. The prototype is designed using the results and methods developed after the transport phenomena and scale-out scales were investigated.

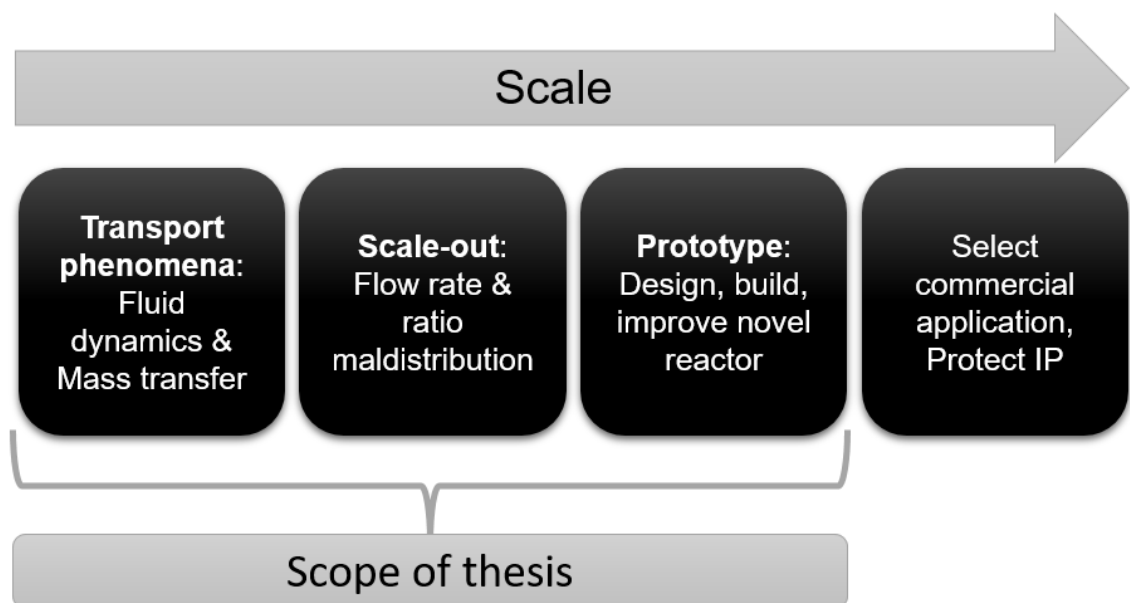


Figure 1-3 Diagram of the scope and the range of scales addressed in this thesis.

1.3 Thesis outline

This thesis is comprised of seven chapters. In **Chapter 1**, the research problem, the context around it, and the thesis scope & objectives are introduced. **Chapter 2** provides a review of the state-of-the-art in liquid-liquid extractions, particularly in small channels operating in segmented flow regime, and the challenges to scale-up small-channel contactors. In **Chapter 3**, the methods followed in this thesis, both numerical and experimental, are described. **Chapter 4** presents the hydrodynamics and mass transfer studies in the two-phase flow both experimental and numerical for a wide range of design and operation conditions. Correlations for plug and unit cell lengths, specific interfacial area, holdup and dimensionless pressure gradient are obtained. The extraction efficiency and mass transfer coefficient are measured and computational fluid dynamics results are used to corroborate the findings. The trade-offs between the various parameters are discussed. **Chapter 5** describes the methodology used to characterise the flow distribution and to design double manifolds for the scale up of two-phase flows. A novel resistance network model and statistical analysis indicators are developed to describe how the hydraulic resistances and the number of channels affect the maldistribution and the power requirements of the double manifold. In **Chapter 6**, the results from both Chapters 4 and 5 are used to design, build, test, and propose improvements to a prototype multichannel modular two-phase manifold. Insights into the potential of commercialisation are also included. **Chapter 7** presents the conclusions from the results and assess the accomplishment of the objectives. Finally, suggestions for future work are discussed. The steps to follow towards the commercial impact of this PI technology are also outlined.

2 Literature Survey

2.1 Introduction

Successful scale-up of intensified liquid-liquid processes can only be efficiently achieved with a clear picture of the state of the art. Pertinent literature is reviewed in this chapter to identify the degree of development and knowledge gaps in intensified liquid-liquid processes and their scale-up. Initially, an overview of the applications of some two-phase liquid processes is given followed by review of the hydrodynamics, mass transfer, and pressure drop in processes using segmented flow. Subsequently, the challenges to scale-up this technology are addressed and put in context with industrial requirements. The findings are analysed in the context of technological development and potential commercialisation.

2.2 Applications of liquid-liquid processes

There are numerous applications for two-phase liquid-liquid reactions and extractions of industrial importance. The reactions are most commonly found in the organic chemical industries [2,7,8] while the extractions are widely applied in organic, metals (hydrometallurgy & nuclear) and bio-based industries (e.g. food, pharma, biofuels) [2,6,9,10]. Table 2-1 presents a non-exhaustive list of liquid-liquid processes of high economic and industrial importance.

Table 2-1 Industrially important liquid-liquid reactions and extractions.

Liquid-liquid process	References
Reactions	
Hydrolysis, saponification or transesterification of esters	[7,8,11]
Nitration, alkylation or sulphonation of aromatics	[7,8]
Epoxidation of oils	[7,8]
Oligomerisation of alkenes	[7,8]
Synthesis of alkyl- and arylamines	[7,8]
Emulsion and interfacial polymerisation	[7,8,12]
Extractions	
Removal of free fatty acids from oils and fats	[7,8]
Purification step in fuel production and organic syntheses, alternative to distillation for close-boiling compounds	[7,8]
Extraction of metals in hydrometallurgical (Including urban mining) processes	[7–10]
Extraction of antibiotics (penicillin, streptomycin, novobiocin...), vitamins (A, B, C, D, E), nucleic acids, enzymes, other APIs (antihistamines, hormones...), from culture/fermentation/synthesis broths	[9,10]
Extraction of flavours, aromas, proteins in food production	[9,10]
Treatment of industrial effluents, environmental remediation	[9]
Recovery of fissile and fertile radioisotopes in nuclear fuel cycle (including PUREX process)	[5–10]

Even though some liquid-liquid processes are fundamental in several industries, they are currently underutilised. Alper identified the two main factors hampering their widespread use [7]: (1) the fundamental physical phenomena have not yet been understood sufficiently, and (2) many liquid-liquid processes are mainly carried out in a batch or semi-batch fashion. These factors impede precise design methods to be developed thus slowing down the scale-up of existing processes and the adoption of new liquid-liquid ones.

Liquid-liquid-solid reactors (e.g. where the solid holds a heterogeneous catalyst) have been even more scarcely studied and applied in industrial settings. The intensification and scale-up of liquid-liquid-solid reactors are certainly important and possible with similar methods as the ones presented in Chapters 3-6 but further discussion of liquid-liquid-solid reactors is outside the scope of this thesis.

2.2.1 Key design and operation parameters in liquid-liquid extractions

The objective of a liquid-liquid extraction process is to achieve a separation at determined compositions of both the raffinate and extract streams and solute throughput. Figure 2-1 shows a block diagram of a single contacting stage with the common terminology used for the various streams reproduced from the Encyclopedia of Separation Technology [9].

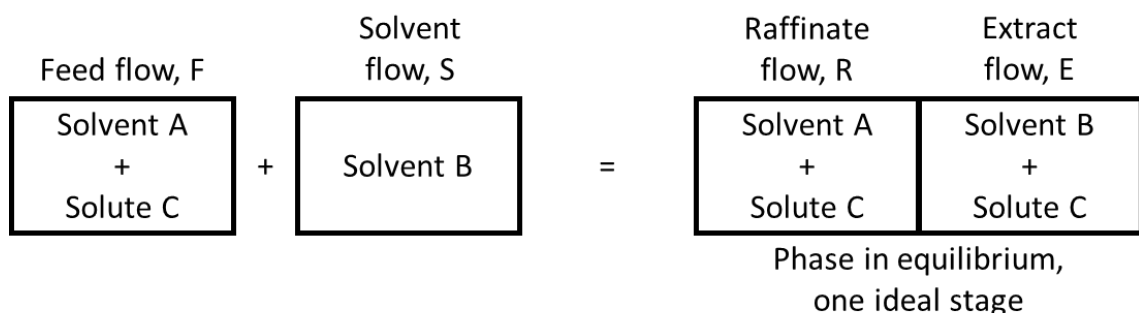


Figure 2-1 Single contacting stage in a liquid-liquid extraction with common terminology. Reproduced from Ruthven (2008) [9].

The steps to follow in order to design an efficient liquid-liquid extraction process have been detailed by Bieber & Kern [13]. In the first instance, the solvent system should be selected. Capital and utility costs are extremely sensitive to solvent selection because

high solvent selectivity to the solute results in compact equipment and smaller equipment trains. The next step is to find optimal process parameters such as temperature, pH and concentrations (including the presence of impurities). These initial steps require extensive laboratory data. Following this, the extractor equipment is selected, considering the number of stages required and the type of multistage process to use (co-current or counter-current). Finally, the control philosophy can be selected and the process flow scheme can be designed considering the solvent and product recovery stages, product purification process, auxiliaries needed, and storage requirement for feed, solvent, chemicals, and products.

There must be feedback at every design stage to ensure the design is feasible. One relevant and well-documented example of this type of feedback is found in the extraction of Uranium and Plutonium, part of the nuclear fuel cycle. In this case, tributyl phosphate (TBP) is known to extract the U(VI) and Pu(IV) almost exclusively and with high distribution coefficients ($D \equiv [M]_{\text{Extract}}/[M]_{\text{Raffinate}}$) and is thus the extractant used in this process [6,10]. TBP is a liquid with a density very similar to water (972.4 kg m^{-3} at $25 \text{ }^\circ\text{C}$) and relatively high viscosity (3.32 mPa s at $25 \text{ }^\circ\text{C}$) which make the coalescence times very long and mixing difficult [6]. Conventional equipment requires the viscosities to be below 2 mPa s and density differences of at least 100 kg m^{-3} [10]. To overcome this, the process is commercially operated with diluted TBP (usually 30% v/v) in a mixture of normal paraffins (e.g. dodecane); the 30% v/v ratio is selected because it maximises the capacity of pulse columns [6]. This example shows how equipment limitations feedback in the design process and affect the solvent selection step and highlights a key opportunity to intensify this important process.

The interfacial mass transfer taking place in solvent extraction equipment is ultimately the object of intensification efforts. The interfacial mass transfer process is described below with emphasis on the intensification opportunities, such as solvent selection, interfacial areas, mass transfer coefficients, holdup, footprint, and safety.

The interfacial flux of the solute from one phase to the other depends on the concentrations in the bulk of each phase and at the interface. Figure 2-2 shows a concentration profile of solute C in different positions close to an interface between an A-rich phase and a B-rich phase. Equation 2-1 is derived for a steady-state unidirectional transfer across an interface between two liquids [2]. N_C is the flux of C across the interface, k is the interfacial mass transfer coefficient, C is the concentration of C in the bulk and C_i is the concentration of C at the interface. The equation can be written for either side of the interface but it is conventional for k to be positive.

$$N_C = k(C - C_i) \quad (2-1)$$

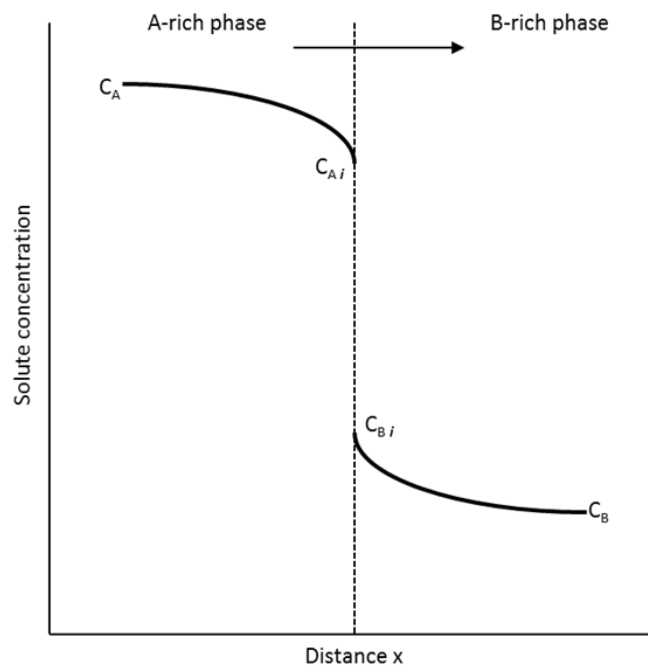


Figure 2-2 Concentration profile of solute C near an interface. The arrow represents the direction of the mass transfer. C_A , C_{Ai} , C_B , and C_{Bi} are the concentration of C in the bulk of A, in the interface on the A side, in the bulk of B and in the interface on the B side, respectively. Reproduced from Ruthven (2008) [9].

Since the concentration at the interface is not readily known, Equation 2-1 can be written in terms of deviation from equilibrium (Equation 2-2). In this case, the mass transfer coefficient is denoted with K . C_{eq} is the concentration of C in the bulk phase at equilibrium.

$$N_C = K(C - C_{eq}) \quad (2-2)$$

Liquid-liquid contactors should be designed to have high mass transfer coefficients, large interfacial areas (a , measured per unit volume of contactor), short residence times (τ), narrow residence time distributions (RTD), large holdups (ϵ , volume fraction of the dispersed phase), small plant footprint, be inherently safe, reliable, and easily maintained. Several sources were used to produce the comparison between contactors shown in Table 2-2 using some of these criteria.

Table 2-2 Characteristics of different liquid-liquid contactors. Compiled from: w= Kashid et al. (2007) [14]x= Doraiswamy & Sharma (1984) [8]; y= Lo et al. (1983) [10]; z= Ruthven (2008) [9].

Type	k_d^x / 10^5 m s^{-1}	a^x / $\text{m}^2 \text{ m}^{-3}$	τ^y	RTD ^x	ϵ^x	Power	Footprint ^y	Reliability ^y
						input ^w / kJ m^{-3}		
Mixer-settler	3 – 10	Up to 10^4	Minutes	Wide	0.05 – 0.4	150 – 250	Large	Very high
Packed column	3 – 10	100 – 1000	Minutes	Wide	0.05 – 0.1	NA	Small	High
Pulsed column	3 – 10	Up to 10^4	Minutes	Narrow	0.05 – 0.4	0.5 – 190	Small	Medium
Centrifugal contactor ^z	Highly efficient		Very short	Narrow	0.33 – 0.96 ^y	850 – 2600	Small	Low

The concept of inherent safety in process plants was developed originally by Kletz [15]. In essence, inherently safer designs avoid hazards instead of adding controls to reduce risks. Kletz uses the term intensification to mean reducing sizes of equipment, storage units, or plants. The author argues that an intensified flow process is inherently safer because inventories are smaller compared to conventional equipment and thus an accident would be less severe. Additionally, the author explains the importance of using highly concentrated (undiluted) raw materials when possible to achieve high conversions in short residence times to minimise ‘free rides’ thus minimising equipment size and unnecessary hazards [15]. This can be contrasted with the practice of diluting TBP, mentioned above.

The process intensification principles (Figure 1-2) have been sparsely applied to the field of liquid-liquid extractions and reactions. This literature relevant to the use of small channels for liquid-liquid extractions is reviewed in the next section.

2.2.2 Liquid-liquid extractions in small channels

Liquid-liquid extractions in small channels have received a lot of attention from researchers; initially regarding their potential as an analytical tool (i.e. Lab-on-a-Chip [16]) and more recently as an alternative to conventional contactors. The latter is the main subject discussed in this thesis. The following paragraphs review the most important systems that have been used as a proof-of-concept, the equipment and setups commonly used, the main advantages identified so far, and the main challenges to design, operate, scale and eventually adopt small-channel contactors commercially. Specifics on the relationships between hydrodynamics and mass transfer are discussed only for segmented flow contactors in the following sections.

The prospect of intensifying liquid-liquid extractions with small-channel contactors is mostly attractive for applications where the improvements (e.g. short residence time, narrow RTD, small footprint, inherently safer process) would be significant enough to justify changing the type of contactor currently used. This has resulted in high-value and hazardous materials to be the main focus so far for the applications of small channel contactors. High-value precious metals, such as platinum and palladium have been extracted using intensified contactors [17–19]. These metals are often found in mixtures at low concentrations (e.g. from spent automotive catalysts) and their extraction may not be economic using conventional devices. In particular, Kriel et al. demonstrated the extraction, scrub, and stripping processes using these metals and conventional extractants in flow channels with overall recovery rates over 95% [18]. Recovery of lanthanides, found in high-value electronics, has also been investigated using small-channel contactors [20,21]. Li & Angeli investigated the extraction of Eu(III) from an aqueous to an ionic liquid solution containing CMPO (Octyl(phenyl)-N,N-diisobutylcarbamoylmethylphosphine oxide) as the extractant and TBP as a modifier to

prevent a third phase from forming [20]. An example of hazardous material is the extraction of radioisotope titanium-45, highly radioactive and used in positron imaging, by Pedersen et al. [22]. These authors achieved separation >90% in residence time less than 15 s [22]. Besides achieving high extraction efficiency in a short time, these authors focused on reducing operator contact with the radioactive materials; their automated setup, which included a membrane-based separator, achieved this goal. Wang & Luo reviewed some reports of small-channel contactors used for the purification of natural products (e.g. plant alkaloid strychnine, the active ingredient in *Radix Salvia Miltiorrhiza* root, progesterone) [23]. Finally, the application which has attracted the most interest is the intensification of PUREX related extractions. Following from the large scale example and with the aim of simplifying comparisons, most authors use U(VI) dissolved in nitric acid (usually 3 M) as the aqueous solution and an organic solution consisting of 30% (v/v) TBP in dodecane or kerosene [24–29]. Hotokezaka et al. showed that undiluted TBP can be used in microchannel contactors, regardless of the high viscosity and similar density to the aqueous phase, which makes it unpractical for large-scale equipment [30]. Tsaoulidis et al. used ionic liquids instead of kerosene as the diluent, where the high viscosity of the ionic liquids was not a limitation in small-channel contactors [31–34]. Hellé et al. used Aliquat® 336, instead of TBP, as the extractant [35,36].

The equipment used to perform liquid-liquid extractions in small channels is very similar regardless of the system used. Most differences arise on the magnitude of the throughput, the methods of control or analysis, and in some cases, the materials of the equipment. In general, a liquid-liquid extraction process in a small-channel contactor requires pumps to move the liquids, a mixing inlet, the main channel where the contacting of the two phases happens, a separator, analytical techniques to measure concentrations, and a control system. Syringe pumps are common because they operate precisely and without pulsations. They are limited by the volume of the syringes and are thus limited to research applications. There are many types of inlets that can be used to bring the liquids in contact. The flow pattern that develops in the contactor depends

strongly on the type and characteristics of the inlet [23]. There has been a lot of attention to the inlet used in terms of hydrodynamics but the mass transfer that takes place in the mixing zone has been very scarcely investigated. The main channel is where the two phases flow together and where most of the mass transfer takes place. Many geometries and orientations have been explored. The most common geometries are circular and rectangular (square being a special case). The main channel can follow a straight line or change directions in 2 or 3 dimensions; the change of direction improves mixing inside the phases [37]. The channels can be oriented horizontally or vertically and depending on density differences, the effect can be important or negligible [38]. The geometry of the inlet and the geometry of the main channel can be modified independently and this opens a possibility to find optimal geometries to maximise the performance of the contactor, however, it also opens a large variable space that has not been studied systematically.

Besides simply changing the channel geometry, one option, still within the spatial PI domain, is to use highly structured flow paths, including static mixers. This is most commonly done with single-phase flows to improve mixing and it is already commercially applied, as reviewed by Jensen and Woitalka et al. [4,39]. One particular case of structured flow paths is the use of periodic open cellular structures (POCS). POCS consist of consecutive unit cells of a particular shape that can improve the mixing and heat transfer of a single- or two-phase process. They have been studied with a few gas-liquid [40] and liquid-liquid [41,42] processes but these results fall outside the scope of this literature review.

Another notable technology in liquid-liquid process intensification, outside the spatial PI domain and in the thermodynamic PI domain, is the use of ultrasound to assist in liquid-liquid extraction in microchannels. By adding an ultrasound field to the process, emulsification can occur and the interfacial area and mixing are potentially improved. Even though promising results have been reported by John et al. [43,44], more research is needed into this type of processes to fully understand the advantages and trade-offs.

Phase separation is another important process to consider. After sufficient residence time, the liquids flowing together have to be separated for further processing. Two separation mechanisms can be used, surface-based and gravity-based separations. Since interfacial phenomena are important in small channels, surface-based separators have been studied, which use side channels or membranes that are preferentially wetted by the organic or the aqueous phases. Currently, however, there are few commercially available options (e.g. Zaiput Flow Technologies). Gravity-based separators (operating like settler tanks) can be used for systems with high throughput and sufficient density difference ($>100 \text{ kg m}^{-3}$ [10]). In gravity settlers, however, the mass transfer continues and reduces the benefits of narrow RTDs in the small channel. In some cases, back-pressure regulators are used after the main channel or separator; usually to prevent evaporation of the solvents used. The process performance (i.e. extraction efficiency) can be measured online, using optical methods (e.g. colour changes or spectroscopic techniques), or after collection of the extract or raffinate streams. Performance proxies, important for process control, can also be measured, such as drop sizes and their distribution. Jensen recently identified the need for innovation in on-line monitoring for flow systems which would accelerate development and maximise process quality [4].

The advantages that small-channel contactors have over conventional equipment can be categorised as incremental or radical. Incremental advantages are those for which the use of small channels improve on an aspect of the extraction process compared to conventional equipment. In contrast, radical advantages refer to ways in which the use of intensified contactors change the extraction process in a way that is not comparable to conventional contactors. Examples for both types of advantages are given below.

The incremental advantages of small-channel contactors over conventional contactors include higher mass transfer coefficients, larger specific interfacial areas, a narrower RTD for both phases, higher holdup of the dispersed phase, and lower energy

use. For example, Kashid et al. report mass transfer coefficients up to $6.3 \times 10^{-4} \text{ m s}^{-1}$, specific interfacial area up to 4800 m^{-1} (for $d=0.5 \text{ mm}$) and power inputs per unit volume about three orders of magnitude below conventional contactors such as extraction columns and mixer-settlers [14]. Arsenjuk et al. studied the residence time distribution in small-channel contactors using fluorescein solutions and kerosene [45]. These authors found the RTD in the dispersed phase is very narrow but in the continuous phase, back-mixing can be observed. Even though the authors make no comparison with conventional contactors, the RTD measured in the flow contactor appears to be minor compared to conventional contactors. It is clear the incremental advantages are necessary to make intensified contactors competitive and it is important to maximise them, however, the radical advantages may be the factor that drives small channel contactors to commercial applications.

The radical advantages of small-channel contactors include the ability to do faster and streamlined testing of prototypes or process conditions as well as regularity- and symmetry-based modelling which can lead to optimisation and modularity that enables simple scale-up and production flexibility. These advantages are discussed in the paragraphs below.

Small-channel contactors can accelerate process innovations, such as the implementation of novel extractants or solvents because they use small volumes and short residence times. The works by Tsaoulidis et al. and Hellé et al. serve as examples of simple experimental setups to determine the effects that different solvents (ionic liquids [31–34]) or a different extractant (Aliquat® 336 [35,36]) can have on the U(VI) extraction process. The key feature is that these authors tested the novel solvent or extractant in the same conditions proposed to be used at large scales, this proposition is economically and technically impossible for conventional contactors. In conventional contactors, the implementation of new solvent-extractant systems requires extensive and expensive testing at several stages [10,46]. Wang & Luo found that intensified contactors are less labour intensive and provide higher yields compared to conventional

extraction methods; this could lead to making new products commercially viable that were not with conventional processes [23].

In terms of modelling, small-channel contactors operating under segmented flow regime (reviewed in section 2.3), have well characterised hydrodynamics and mass transfer which can potentially lead to an unprecedented level of detail in their modelling and thus optimisation and control [33,47]. Extractions carried out in conventional contactors, like mixer-settlers or pulsed columns, suffer from inhomogeneous flow fields that cannot be well characterised. Their modelling and control routines use broad correlations with large uncertainties which leads to overdesign and inefficient use of solvents. The improved efficiency offered by the detailed models of intensified contactors can lead to using more expensive, yet more effective, solvents (such as ionic liquids), as proposed by Tsaoulidis et al. [31–34].

Modularity, in this context, is the capability to add or enable (or remove or disable) an equipment or part of it to either change the process or increase (or reduce) the capacity. Modularity can take many forms in process intensification, for example, Chambers et al. designed a multichannel gas-liquid flow reactor which is modular because the component pieces can be easily replaced in case of corrosion [48]. Al-Rawashdeh et al. designed a similar multichannel gas-liquid contactor which is modular in terms of channel geometry because it can use circular or square reaction channels interchangeably [49]. In flow chemistry, plug-and-play modules are used to do different processes with similar equipment, as recently demonstrated by Cole et al. [50]. One important type of modularity is the one where capacity is added (or removed) in response to economic or other drivers. This type of modularity offers a complete departure from conventional equipment design. Usually, a contactor or reactor is designed and built for a nominal throughput and in practice, it can be used within a small range of that throughput; the production rate cannot thus respond to economic or other drivers which can lead to lost profit. With modular contactors, each module is designed for a nominal throughput but the capability to add and remove modules means the practical throughput

is very flexible and the same equipment can be used for wide range of production rates which maximises profitability of a process.

Harmsen identified four hurdles most intensified processes must address before being implemented industrially [51]. These are: (1) risk of failure by combining novel aspects, (2) scale-up knowledge uncertainty, (3) equipment unreliability, and (4) higher safety, health and environmental risks. For the specific case of small-channel contactors, safety is not a concern, rather, it is a driver because they are inherently safer than conventional equipment. The first and third hurdles are discussed together followed by a discussion of the second one.

Harmsen contextualises the hurdles for the case of in-flow operations [51]. The risks of novelty and reliability for small-channel contactors do not stem from inherent issues in the technology but rather from the cost and lack of motivation to change processes from conventional to intensified ones. In order to address this issue, the role of academic research is invaluable in the 'de-risking' and maturing of intensified process technologies. In this way, small-channel contactors (for both gas-liquid and liquid-liquid processes) are strong candidates for further exploitation since a lot can be gained, in terms of commercial potential, in comparison with conventional equipment.

The scaling risks, specifically for small-channel contactors, are two-fold. On one hand, most extraction processes take place either in counter-current flow or in multiple stages. Small-channel contactors do not operate in counter-current flow and must be operated in multiple stages. There have been a few demonstrations of multistage small-channel contactors [47,52–55] therefore, this hurdle is not of significant concern. On the other hand, the attainable throughput of small-channel contactors is very small compared to conventional equipment and there are no examples in the literature of large-scale applications of small-channel contactors. While these intensified contactors are highly efficient, the scale-up of the throughput without losing the small-scale advantages remains the main challenge. Scale-up of the throughput can be achieved by increasing the number of channels operating in parallel (called scale-out or number-up). It is not

trivial, however, to reproduce accurately the flow conditions of a single channel in many parallel ones. The challenge is to design a flow distributor within the process-specific maldistribution tolerance of the total flow rate and the ratio of the two phases. This key issue is reviewed in detail in sections 2.6 and 2.7.

2.3 Liquid-liquid segmented flow

There are numerous flow patterns which two-phase flows adopt when they take place in small channels. The morphology of the interfaces depends on the various forces acting on the fluids and their relative predominance. There are several reviews on flow patterns in microchannels and small channels available [56–58]. The flow pattern that attracts the most interest for mass transfer application is the segmented flow pattern as it strikes a balance between fast mass transfer and fast coalescence at the end of the process, among other advantages (e.g. narrow RTD, simplified modelling) [38,59,60]. The description of other flow patterns and their potential applications are outside the scope of this review. This section reviews the general characteristics of the segmented flow pattern, in which conditions it is generally found, and its most important characteristics are reviewed, such as, plug length, specific interfacial area, film thickness, plug velocity, and recirculation inside the phases.

Segmented flow is a flow pattern commonly found in gas-liquid and liquid-liquid systems flowing in small channels at low velocities. This flow pattern is also referred to as Taylor flow (particularly for gas-liquid systems), plug flow, or slug flow. This flow pattern consists of plugs (dispersed phase) and slugs (continuous phase), and a continuous-phase film between the plugs and the channel wall (Fig. 2-3). The recirculation inside the fluids enhances the high mass transfer rates commonly observed in this flow pattern. The interactions between the liquids and the tubing material determine which liquid is the continuous or dispersed phase. Other effects, such as viscosity ratio and pumping order can be determinant when the liquid-solid surface interactions are similar to both liquids [59]. Non-polar liquids preferably wet commonly used fluoropolymers (e.g. polytetrafluoroethylene (PTFE), perfluoroalkoxy polymer resin

(PFA), fluorinated ethylene propylene (FEP)) over aqueous, polar liquids. The plugs have equivalent diameter larger than the channel diameter, and acquire an elongated shape. A pair of a consecutive plug and a slug is a unit. One of the most important characteristics of this flow pattern is its regularity, across units. This section briefly reviews the available literature on the flow conditions at which liquid-liquid segmented flow is found, as well as important characteristics of this flow pattern, including plug, slug and unit lengths, film thickness, interfacial area, plug velocity, and recirculation inside each phase.

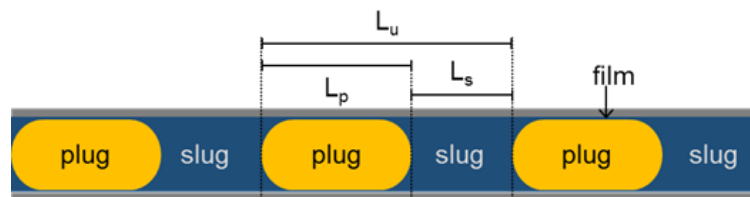


Figure 2-3 Schematic of liquid-liquid segmented flow pattern. L_u , L_p , and L_s are the unit, plug, and slug lengths, respectively.

There are no universally well-defined limits to where segmented flow pattern is found. Establishing the limits of the flow pattern is a persisting challenge. Any rule or correlation that connects a flow condition (flow rates, inlet and channel geometry, and flow rate ratio) with a flow pattern boundary should define how the flow patterns are distinguished. Jovanovic et al. proposed that segmented flow is stable when the coefficients of variation (CV, standard deviation divided by mean) of plug and slug lengths are below 50% [61].

There are several works on flow pattern maps for liquid-liquid flow or on the flow pattern boundaries of segmented flow. Kashid & Agar studied the limits of segmented flow in a cyclohexane-water system for 0.25 to 1 mm channels [60]. They found segmented flow to be stable around flow rate ratios of one and, in terms of flow rates, the segmented flow region expanded as the channel diameter increased. Zhao et al. studied water-kerosene systems and found segmented flow for Weber number ($We_i = du_i^2 \rho_i / \gamma$, where u_i is the superficial velocity of phase i) for both phases below one [62]. Biswas et al. studied segmented flow in vertical and horizontal channels with diameters up to 6 mm using a water-toluene system [38]. These authors found

segmented flows in all channel diameters; this is the largest diameter where uniform segmented flow is reported. Jovanovic et al. also studied a water-toluene system and reported that segmented was bounded by $We_i < 0.1$ [63]. Recently, Cao et al. proposed the following correlation to describe the transition to plug flow [64]:

$$c_0 Re_c^{c_1} We_c^{c_2} = Re_d^{c_3} We_d^{c_4} \quad (2-3)$$

where different coefficients (c_i) are used for the annular-segmented and dispersed-segmented flow transitions.

The important hydrodynamic characteristics in segmented flow, depicted in Figs. 2-3 and 2-4, are the plug and slug lengths, the film thickness, the plug interfacial area (which is related to the specific interfacial area), the plug velocity (or its residence time), and the recirculation patterns inside both phases. Each one of these characteristics is reviewed below.

The lengths of the plug, slug, and unit (Fig. 2-3) depend on the conditions at the inlet (geometry, velocities, and liquids properties), where the liquid phases meet, and affect several aspects of processing using segmented flow. Garstecki et al. studied the drop break-up mechanism in T-junctions and identified a scaling rule for dimensionless plug lengths (L_p/d) with respect to flow rate ratio (Q_d/Q_c) [65]. Several authors have proposed correlations similar to the one by Garstecki et al. with the inclusion of terms to account for viscous or inertial effects (e.g. using Ca , Re , We) [34,64,66–68]. These models are summarised in Eq. 2-4, where c_i are coefficients independent of Q_d/Q_c and Ca_c .

$$\frac{L_p}{d} = c_1 + c_2 \left(\frac{Q_d}{Q_c} \right)^{c_3} Ca_c^{c_4} \quad (2-4)$$

The thickness of the continuous-phase film (δ) around the plugs plays a critical role in the plug velocity and interfacial area. The film has been studied extensively in gas-liquid systems but fewer studies are available for liquid-liquid systems. Usually the film is measured optically; Mac Giolla Eain et al. developed a curvature-correction

technique based on refractive index differences to account for optical effects close to the curved channel wall [69]. These authors were able to measure the film thickness with an error between 2 and 11%. The film is not uniform in all conditions, Li & Angeli found the film thickness is uniform across the length of the plug when the L_p/d values are above 1.82 [68]; similarly, Mac Giolla Eain et al. found uniform film thickness for L_p/d above 1.86 [69]. Below these L_p/d conditions, the plugs are curved along the whole length and no uniform film thickness can be measured, but an average can be estimated. The dimensionless film thickness (δ/d) depends on the capillary number and another number that includes inertial effects (Reynolds or Weber numbers). Li & Angeli, Dore et al., and Tsaoulidis & Angeli measured the film thickness for segmented flows using high-viscosity ionic liquids (high Ca) as continuous phase and found large ranges for δ/d (0.02 to 0.15) [34,68,70]. Mac Giolla Eain et al. tested a wide range of liquids as continuous phase; the range of δ/d for water-dodecane, a relevant system to this thesis, is 0.015 to 0.023, between Ca of 0.002 and 0.003. These authors proposed a correlation, presented in Eq. 2-5, where $Ca=\mu_c u_p/\gamma$ and $We=\rho_c u_p^2 d/\gamma$.

$$\frac{2\delta}{d} = 0.35Ca^{0.354}We^{0.097} \quad (2-5)$$

The rate of mass transfer depends directly on the extent of interfacial area available for the solute transport to occur. The interfacial area is measured per unit volume of the contactor and called specific interfacial area (a , $m^2 m^{-3}$). By modelling the plugs as consisting of straight cylinders with hemispherical caps, the specific interfacial area can be calculated with Eq. 2-6 [20,71–73].

$$a = \frac{4 L_p}{d L_u} \quad (2-6)$$

This model neglects the film thickness and therefore it is best applicable to low capillary numbers, where the film thickness is negligible. In general, the specific interfacial area depends on the channel diameter, the flow rate ratio, the total mixture velocity, the properties of the liquids and the inlet geometry. Interfacial areas ranging from 2760 to 4800 m^{-1} in 0.5, 0.75, 1 mm I.D. channels have been reported by Kashid et al. [14]. Li &

Angeli measured specific interfacial areas up to 8500 m⁻¹ for channels of 0.2 mm I.D. [20]. Reference values for the specific interfacial area in conventional contactors are shown above in Table 2-2.

The plug velocity (u_p) is higher than the average velocity because of the presence of the thin film of the continuous phase surrounding it. This reduces the residence time of the plug in the contactor and must be accounted for when segmented flow processes are considered. Li & Angeli [68] compared the models to experimental data and determined the models by Kashid et al. (Eq. 2-7) [74] and Gupta et al. (Eq. 2-8) [75] closely predict the experimental results.

$$\frac{u_p}{u_{mix}} = \frac{2}{1 + \left(\frac{R_p}{R}\right)^2} \quad (2-7)$$

$$\frac{u_p}{u_{mix}} = \frac{2 + \left(\frac{R_p}{R}\right)^2 \frac{\mu_c - 2}{\mu_d}}{1 + \left(\frac{R_p}{R}\right)^4 \frac{\mu_c - 1}{\mu_d}} \quad (2-8)$$

In both models, R_p is the radius of the plug and R is the channel radius ($d/2$). As can be seen, a good estimate of the film thickness is crucial for estimating the plug velocity, and thus the dispersed phase residence time. Abiev et al. also proposed a model which only depends on the capillary number and successfully predicts experimental u_p values [71].

The recirculation inside each phase plays an important role in achieving the large mass transfer rates observed in liquid-liquid segmented flows; Fig. 2-4 shows these patterns schematically. However, there are few systematic studies available on the recirculation patterns inside the phases in slug flow. The *circulation time* is used to quantify the mixing inside each phase and is defined as the time for the fluid to move from one end to the other of the plug or slug [76]; shorter circulation times imply better mixing. Thulasidas et al., for Taylor bubble flow, found that the circulation time in the slug is constant at low capillary numbers and above $Ca=10^{-2}$; increasing Ca increases the circulation time (slower mixing) [76]. Abadie et al., also in gas-liquid Taylor flow, studied the recirculation in the continuous phase and found that the circulation time increases

exponentially with L_s/u_p ; longer slugs or slower plugs increase the mixing time [77]. The recirculation inside the plugs has been considerably less studied. Dore et al. used particle image velocimetry (PIV) to study the recirculation in aqueous plugs with an ionic liquid continuous phase [70], and found an inverse correlation of circulation time with capillary number in long plugs (better mixing at higher velocities), but in short plugs the correlation was more complex.

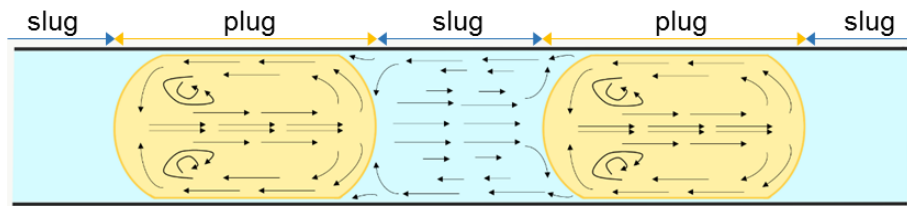


Figure 2-4 Schematic of the circulation patterns found in segmented liquid-liquid flows in small channels. The blue phase is the continuous (wetting) phase and the yellow phase is the dispersed (non-wetting) phase.

2.4 Mass transfer in segmented flow

The mass transfer of one or more components across the liquid-liquid interface is the main step in extraction processes. In small-channel contactors, operating under segmented flow, mass transfer is closely related to the hydrodynamics because the mass transfer rate intimately depends on the available interfacial area and the intensity of mixing inside each phase. Characterising mass transfer and its relationships with the hydrodynamic features and input variables of segmented flow is critical to their development and widespread industrial adoption.

Biswas et al. and Jovanovic et al. have performed comparisons between the mass transfer performance in intensified contactors operating under different flow patterns [38,63]. Jovanovic et al determined segmented flow to have the best performance in comparison with dispersed, parallel, and annular flow, given the large available interfacial area and the ability to control it within some range. Biswas et al. in turn, determined segmented flow to have the best performance among dispersed, annular, and inverted-dispersed flows when considering the mass transfer coefficients

and the rate of solute transferred per unit pressure gradient. These authors determined that in plug flow, three to seven times more solute can be transferred between phases for a given pressure gradient, which is a measure of the pumping costs.

Numerous experimental and numerical studies are available on mass transfer in liquid-liquid segmented flow systems. This section reviews some important publications on this topic and analyses the effects that different design and operation variables have on the mass transfer efficiency.

2.4.1 Mass transfer coefficient

The mass transfer coefficient (Eqs. 2-1,-2) and the volumetric mass transfer coefficient (product of mass transfer coefficient and specific interfacial area) characterise the mass transfer performance in a contactor because they do not depend on the driving force (concentration difference) and can thus be compared among different concentrations.

In order to compare the mass transfer coefficients among contactors, some conditions should be met. (1) The mass transfer coefficient should be calculated in the same way, (2) the systems should have similar properties, and (3) no reaction or the same reaction should take place in the contactors. The first condition is necessary because some authors report overall mass transfer coefficients (including the mixing inlet, main channel, and separator) whilst others report segmented flow mass transfer coefficients measured in the main section only, where segmented flow is observed. Comparisons between overall mass transfer coefficients and segmented flow mass transfer coefficients are not possible without knowledge of the mass transfer coefficients in the mixing and separator sections, which have not yet been studied systematically. The second condition requires diffusion coefficients, viscosities, densities, and presence of surfactants to be similar since mass transfer rates depend strongly on these properties. For example, it is not possible to compare two contactors using mass transfer coefficients obtained for gas-liquid and liquid-liquid systems. Finally, the third condition acknowledges that if a reaction is taking place in either phase, the mass transfer rate

and mass transfer coefficient is increased. In order to compare the contactors, the reaction kinetics would be known.

Kashid et al. and Tsaoulidis have presented extensive tables of mass transfer coefficients [14,78]. This section, instead of reviewing values, focuses on analysing the dependencies various authors have found between mass transfer coefficients and design and operation variables in liquid-liquid non-reactive segmented flow contactors. Kashid et al. studied three liquid-liquid extraction systems experimentally [14]. They determined the effect of velocity, diameter, and flow rate ratio on the overall volumetric mass transfer coefficient. Their results show that, for the same residence time, the volumetric mass transfer coefficient (k_{La}) increases with velocity, up to a certain value, above which the k_{La} remains relatively constant. They also found that the overall volumetric mass transfer coefficient is larger for smaller diameters and the difference is amplified at higher velocities. These authors found that changing the flow rate ratio between the two liquids can affect the volumetric mass transfer coefficient, mainly by increasing the interfacial area.

Yin et al. experimentally studied the extraction of La(III) in segmented flow contactors [21], and in particular the effects of the flow rate, channel diameter, and channel length on the overall volumetric mass transfer coefficient. Their results showed that the mass transfer coefficient increases with the flow rate, decreases with the diameter, and decreases with the channel length. Analysis of their data shows that the mass transfer coefficient depends approximately linearly with the flow velocity for a given channel geometry and residence time.

Di Miceli Raimondi et al. studied both numerically and experimentally the mass transfer coefficient during segmented flow liquid-liquid extraction in square channels and found good agreement between a model (Eq. 2-9) and experimental results (within 30%) [79,80]:

$$k_d d_d = \alpha \left(\frac{V_d}{V_u} \right)^{0.17} (u_d w)^{0.69} \left(\frac{u_d}{\gamma} \right)^{-0.07} \left(\frac{w}{d_d} \right)^{0.75} \quad (2-9)$$

where α is a constant that depends on the properties of the fluids, d_d is the diameter of a sphere with the same volume as the drop, $V_{d,u}$ is the volume of the plug and the unit, u_d is the velocity of the plug, w is the width of the channel, and γ is the interfacial tension. This correlation shows that k_d depends on the velocity with an exponent of 0.62 and on the channel width with an exponent of 1.44. Tsaoulidis et al. studied the extraction of U(VI) into ionic liquid solutions with TBP in segmented flow contactors [31–33]. They found the overall volumetric mass transfer coefficient increases with the velocity, decreases with the channel size, decreases with the residence time (channel length), and increases as the organic-to-aqueous flow rate ratio increases up to one. Additionally, these authors studied the effect of nitric acid concentration on the mass transfer coefficient; they found, for a given residence time, k_{LA} decreases for higher concentrations of nitric acid. Since the mass transfer coefficient takes into account the driving force, the relationship between nitric acid concentration and mass transfer coefficient indicates that the acid concentration affects the mixing or the area available.

Li & Angeli studied Eu(III) extraction in segmented flow contactors using an ionic liquid solution as the continuous phase [20]. They found the overall volumetric mass transfer coefficient decreases with the residence time, increases with the mixture velocity, and decreases with the channel dimensions. Interestingly, they studied the recirculation times and volumetric mass transfer simultaneously and found that short recirculation times, thus short plugs, exhibit high mass transfer coefficients.

Zhang et al. studied experimentally the effects of fluids properties, channel size and temperature on the mass transfer performance in segmented flow contactors [81]. They found that increasing the flow rate of either phase increases the volumetric mass transfer coefficient, where increasing the continuous-phase flow rate increases the mass transfer predominantly, while increasing the dispersed-phase flow rate increases the available interfacial area. Their results show both k_L and k_{LA} increase as the diameter decreases. The mass transfer coefficient decreases approximately linearly with respect to the channel diameter. With respect to temperature, they found that higher temperature

leads to faster mass transfer rates due to increased diffusivity coefficients, however, the authors argue that the decrease of μ_c with higher temperatures affects negatively the mass transfer. These authors modified a gas-liquid model by Yue et al. [82] to adjust to their data, shown in Eq. 2-10.

$$k_d(a \times d) = 1.23 \left(\frac{D_{A|d} u_d}{d} \right)^{0.5} \left(\frac{L_p}{d} \right)^{0.806} \left(\frac{L_u}{d} \right)^{-1.05} \quad (2-10)$$

where $D_{A|d}$ is the diffusion coefficient of component A in the dispersed phase. According to these results, long plugs are favourable and long units are unfavourable; this is probably an effect on the interfacial area, rather than the mixing.

The next step in assessing the effect of different variables on the mass transfer performance is to use dimensionless numbers obtained by dimensional analysis. However, the lack of data for a wide range of conditions in geometrically similar setups has hindered its widespread use in liquid-liquid segmented flow contactors. The key dimensionless numbers to describe mass transfer, their definitions, and their interpretation are presented in Table 2-3, where $D_{A|i}$ is the diffusivity of component A in the i -th phase, u and l are any appropriate characteristic velocity and length, respectively, used to define the number. As a relevant example of dimensional analysis, according to Treybal, the mass transfer coefficient for the continuous phase in liquid-liquid stirred vessels can be approximated by $Sh_c(K_c d_d / D_{A|c}) = 6.6$, where d_d is the mean diameter of the drops in the vessel [83,84].

Table 2-3 Important dimensionless numbers for segmented flow mass transfer descriptions.

Dimensionless number	Definition	Interpretation
Sherwood (Sh_i)	$Sh_i = \frac{K_i \ell}{D_{Aji}}$	Total mass transfer with respect to diffusional mass transfer
Schmidt (Sc_i)	$Sc_i = \frac{\mu_i}{\rho_i D_{Aji}}$	Diffusivity of momentum with respect to mass diffusivity
Peclet (Pe_i)	$Pe_i = Re_i Sc_i = \frac{u \ell}{D_{Aji}}$	Flow velocity with respect to the velocity of mass diffusion
Damköhler (Da_i)	$Da_i = K_i a \tau$	Dimensionless degree of advance of the extraction

Ramji et al. studied segmented flow mass transfer numerically and are thus able to remove any hydrodynamic effects such as the effect of velocity on plug length [85]. They studied the effects of the Peclet ($=u_d L_u / D_{A(d)}$) and Reynolds ($=\rho_d u_d L_u / \mu_d$) numbers as well as the viscosity ratio on the mass transfer coefficient. They found the mass transfer coefficient increases with Pe , has a very weakly dependence on Re_d and increases when the continuous phase viscosity increases. The authors do not provide a correlation between the mass transfer coefficient and the factors they analyse, however, with regression analysis of the data presented, a correlation can be obtained. The correlation uses the 12 data points presented by the authors and the results, including goodness of fit, are presented below.

$$k_c = \exp(3.57) Pe^{0.122} \quad (2-11)$$

Re_d is not part of the correlation as the p-value, a measure of how an effect compares to random chance, is above 0.05 (p-value=0.846). The R^2 of the correlation is 0.866 and the 95% confidence intervals for the first and second exponents are 7.6% and 30%, respectively. Li et al. proposed correlations for the plug and slug mass transfer

coefficients using a sulphuric acid/cyclohexanone oxime/n-hexane system [86]. They found the mass transfer coefficient increases with flow rate and proposed correlations for $Sh_i(=K_iL_p/D_{A|i})$ as function of $Re(=\rho_cud/\mu_c)$ and Q_d/Q_T , as shown in Eq. 2-12.

$$Sh_i = a_1 Re^{a_2} \left(\frac{Q_d}{Q_T} \right)^{a_3} \quad (2-12)$$

The values of a_1 , a_2 , and a_3 are 99.73, 2.44, 1.05 and 38.35, 2.47, 0.47 for the continuous and dispersed phases, respectively. These results indicate the mass transfer coefficients increase sharply with the velocity with exponents close to 2.5. The correlation in Eq. 2-12 is obtained for a single channel diameter ($d=1$ mm) and a single pair of immiscible liquids; it may be best not to extrapolate this correlation to other channel sizes and fluid properties without further results. Matsuoka et al. studied the water/phenol/dodecane system in segmented flow for a range of diameters (0.6 to 2 mm) at a flow rate ratio of one [73]. These authors found a linear correlation (in log-log axes) for the $Sh_d(=K_Ld/D_{A|d})$ and the $Re_d(=\rho_d u_{mix}d/\mu_d)$ numbers at $Sc_d(=\mu_d/(\rho_d D_{A|d}))$ equal to 1994 and 248 (using data by Di Miceli Raimondi et al. [79]); the Sherwood number ranges from 20 to 100. Although the exponent is not presented by the authors, the linear relationship plot can be analysed to estimate the exponent (slope in the log-log plot) for Re_d to be 0.6. This study covers the widest diameter range in the literature.

While there is no analytical solution for the diffusive and convective mass transfer in segmented flow contactors, Levich developed a model to quantify the convective flux across the interface of a moving drop [87]. The model is developed for low continuous-phase Reynolds numbers (<1) and large dispersed-phase Peclet numbers and is given in Eq. 2-13. Bird et al. have pointed out that, in order to include molecular diffusion contributions, two units should be added to the Sherwood number [88].

$$Sh_d = \frac{2}{\sqrt{6\pi}} Pe_d^{1/2} \left(1 + \frac{\mu_d}{\mu_c} \right)^{-1/2} \quad (2-13)$$

Levich argues that these results would approximately hold for higher continuous-phase Reynolds numbers, as long as the continuous phase flow remains laminar. The

dependencies described by Levich correspond, in sign and approximately in magnitude to the experimental and numerical findings for segmented flow reviewed above and therefore this analytical solution could be used to interpret and extrapolate experimental and numerical results.

The results reviewed here show there is some consensus on the overall effects of the design and operation variables on the mass transfer coefficients. In general, the mass transfer coefficients in segmented flow contactors are larger for smaller channels, are larger at higher velocities, are larger for higher μ_c , and become smaller at larger residence times. In terms of plug lengths and flow rate ratios, these factors mainly contribute to change the interfacial area available and only partly to change the recirculation times and quality of mixing. The use of dimensionless numbers to describe mass transfer results enables comparisons between different cases and use for design purposes.

2.5 Pressure drop and energy requirements of segmented flow

The pressure drop observed in channels operating in the segmented flow regime has been extensively studied for gas-liquid systems and significantly less for liquid-liquid ones. There are two main motivations to study the magnitude of the pressure gradient its dependence on design and operation variables. The first motivation is practical, since the pressure drop in segmented flows is required to determine the capacity and power of the pumps utilised, which have a significant impact on the capital and operation expenditures. The second motivation is related to understanding the hydrodynamic characteristics of the segmented flow pattern, and ultimately to optimise processes using it. Pressure drop measurements are simpler to perform and often more precise than other measurements. In these cases, knowledge of the relationships between pressure drop and process performance results important. For example, Kreutzer et al. suggested using the pressure drop measurements to calculate the plug length [89].

There are two essentially different ways to analyse the pressure drop in liquid-liquid segmented flows. One option is to use methodologies originally developed for two-phase flows in large-diameter pipes. These methodologies were first developed by Lockhart & Martinelli and do not consider the particular flow pattern, instead, they assume a homogeneous mixture [90,91]. Lockhart-Martinelli types of correlations have been scarcely used in small-channel gas-liquid systems [92,93]. Zhang et al. applied several Lockhart-Martinelli correlations to experimental gas-liquid data in small channels with diameters ranging from 7 μm to 6.25 mm and found that no single correlation, including the one proposed by the authors, could predict the results accurately with a mean standard deviation of 38% [93]. These results suggest that the homogenous mixture model may not be appropriate for the highly structured flow patterns found in small-channels, which are a consequence of the strong capillary forces.

The other option is to take into consideration the morphology of the flow patterns. The first studies in this direction were performed by Bretherton [94], who calculated the pressure difference across a bubble in a small-channel and found it is proportional to $\text{Ca}^{2/3}$. This result was subsequently used by Kreutzer et al. to propose a model that could predict the pressure drop along a channel in gas-liquid Taylor flow [89].

$$f\text{Re} = 16 \left(1 + a \frac{d}{L_s} \left(\frac{\text{Re}}{\text{Ca}} \right)^b \right) \quad (2-14)$$

where $f(=\Delta p d / (2L \rho u^2))$ is the friction factor, L_s/d is the dimensionless slug length, and the adjustable parameters a and b are found through regression analysis of experimental data or numerical simulations. This model separates the contributions of the continuous phase and of the bubbles to the overall pressure drop. Walsh et al. expanded the number of gas-liquid systems and found that the Kreutzer model closely predicted the results, with a slightly different value for a [95]. Warnier et al. used the model by Kreutzer in a wider range of conditions in a nitrogen-water system [96]. They determined that the model above had significant variability and proposed a function of A'/A_p (cross-sectional

area of the channel with respect to the cross-sectional area of the plug), Ca , and Re/Ca to substitute the parameter a .

Jovanovic et al. developed a model to calculate the pressure drop considering three contributions to the overall pressure drop using liquid-liquid systems; the contributions include the continuous phase, the dispersed phase, and the interface [97]. This model depends on several variables, namely, u_p , u_{mix} , d , δ , γ , μ_c , μ_d , L_p , and L_u ; The large number of variables and the difficulty to measure δ and u_p with high accuracy hinders the use of this model. They showed the model closely matches with the experimental results for water-toluene and ethylene glycol-toluene systems in 248 and 498 μm I.D. capillaries. Furthermore, Tsaoulidis et al. found this model closely predicted the values in water-ionic liquid systems [59].

Mac Giolla Eain et al. reviewed the pressure drop models, compared them to experimental gas-liquid and liquid-liquid pressure drop measurements and proposed a new model for segmented flow [98]. These authors found that the practice of separating the contributions from different sources (e.g. continuous phase, dispersed phase, film, and Laplace pressure) has been adopted in several models. By comparing experimental data with predictions from several models, these authors showed none of the published models considered can accurately predict the pressure drop in liquid-liquid systems. The model by Kreuzer et al. was found to have large errors for liquid-liquid systems and the model by Jovanovic et al. systemically underestimated the experimental results. The authors modified a model by Warnier et al. [96] to adjust to the experimental data and found that the friction factor depends on Q_d/Q_T , Ca , L_s/d , and A'/A_p' ; the experimental results fall within 20% error from the predicted values.

The models reviewed above only predict pressure drops above Hagen-Poiseuille's prediction and, even though they are presented in dimensionless form, the experiments used to corroborate the results used few channel diameters and below the practical range for commercial applications. Steps forward in modelling pressure drop in segmented flows should include: formalise the various contributions to the overall

pressure drop, capture the dependence on channel diameter (especially for larger diameters), and determine what variables are important, and to what degree, in the calculation of the overall pressure gradient. Chapter 4 presents progress towards these goals for liquid-liquid segmented flows.

2.6 Scale-up of small-channel processes

Early studies on microreactor technology envisioned the throughput could be scaled to production levels simply by scaling-out, this is, via arranging enough parallel microreactors to achieve the desired throughput. The key idea of scaling-out is to retain the reaction conditions of the single-channel reactor for the whole parallel arrangement. Fig. 2-5, reproduced from Luis & Garcia-Verdugo [99], shows, conceptually, how scaled-out equipment would replace a conventional one.

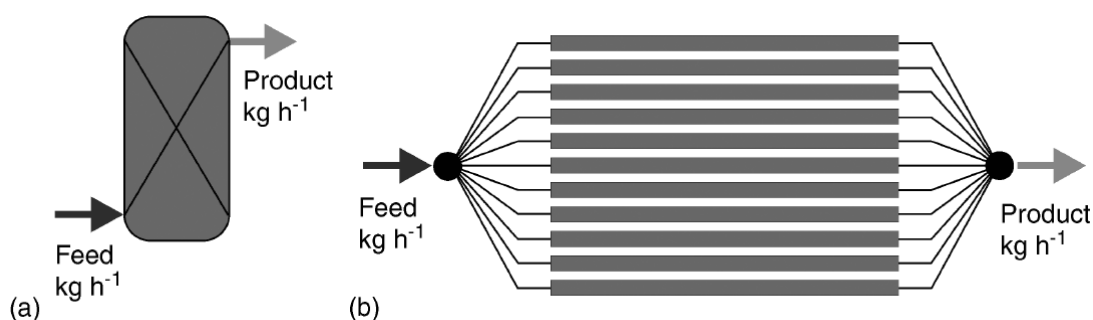


Figure 2-5 Conceptual difference between processes using conventional equipment (a), and scaled-out equipment (b). Reproduced from Luis & Garcia-Verdugo [99].

The scale-out approach has proved challenging for both single- and multi-phase processes. Recent reviews by Jensen and Zhang et al. have highlighted that the slow development in this area is due to the complex problem of flow distribution and the lack of effective flow distributor designs [4,100]. It is now recognised that, in order to scale-up the throughput of a microreactor, a combined approach of scaling-up the size of the channels followed by scaling-out is the most effective path [4,100]. The scaling of the reactor dimensions has to preserve the mass (and heat) transfer advantages that are observed in the microscale systems. This is particularly difficult for multiphase processes where the flow patterns (and interfacial areas) also depend on the reactor scales.

The rest of this section presents the economic implications of scaling-out and critically reviews relevant developments on flow distribution for single-phase processes.

2.6.1 Economies of scale

The capital investment of a plant or equipment is a function of the capacity, or nominal throughput [101]. Eq. 2-15 shows this relationship, where I is the capital investment, k is a parameter independent of the scale, Q is the capacity or throughput, and b is the scaling exponent.

$$I = kQ^b \quad (2-15)$$

Values of b are published for some equipment in engineering and economics literature [101]. Economies of scale are true when the exponent b is less than 1.

Harmsen quotes values of b for conventional reactors and contactors around 0.6 and 0.65 [51,102]. It has been argued that the exponent for a process scaled-up via parallelisation (scale-out) has a value equal to 1 and would be competitive only at low throughputs [51,102,103]. This is strictly true for the parallel channels but not for the whole scaled-out contactor because the number of pumps does not scale linearly with the number of channels. Kaske et al. identified that the pumps are the most expensive item in a micro-reactor/contactator setup and thus, their number has to be minimised [104]. Figure 2-6, reproduced from Harmsen [102], shows an example of how the capital cost of microreactors scales linearly while conventional reactors have exponents less than 1. This figure has limitations, such as using heat exchange duty as a proxy for capacity and only having one data point for the intensified case.

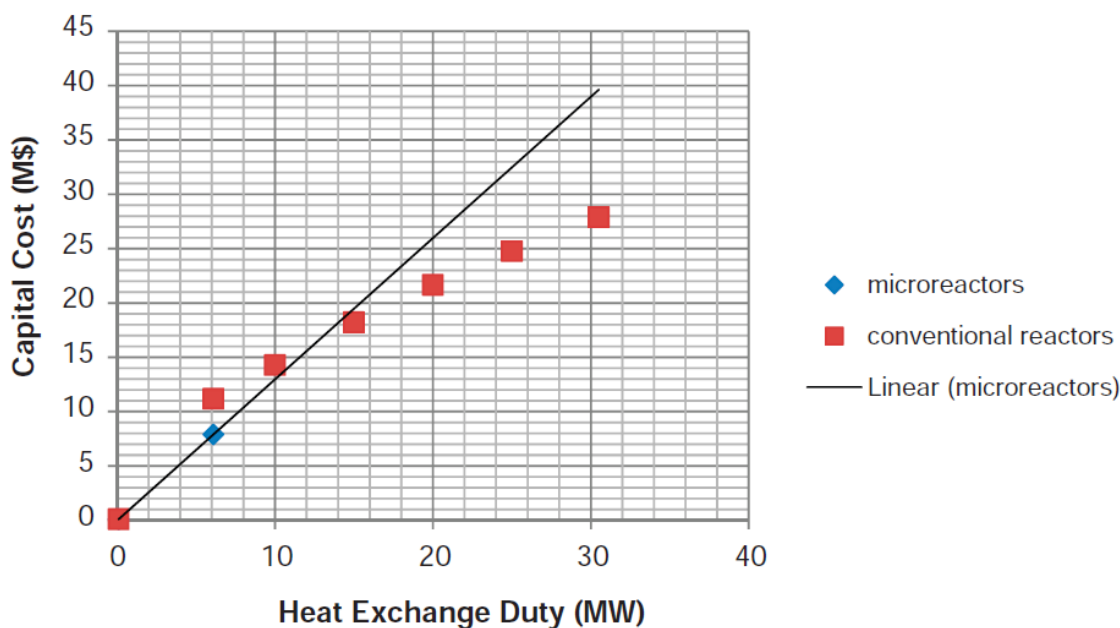


Figure 2-6 Cost curve for microreactors and conventional reactors as a function of heat exchange duty. Reproduced from Harmsen (2013) [102].

Figure 2-6 illustrates the importance of economies of scale that must be achieved by intensified technology. Even though their efficiency is very high, any intensified contactor should scale favourably in economic terms to be competitive at large, industrially-relevant scales.

Two complementary goals can be identified from the study of economies of scale for intensified contactors. The first one is to minimize the parameter k (the slope in Fig. 2-6) by minimising scale-independent costs (i.e. maximise the efficiency of the single-channel process). The second goal is to reduce the scaling exponent (b) by designing flow distributors which reduce the need to use parallel pumps for parallel main channels. Both of these goals are addressed in this thesis.

2.6.2 Single phase flow distribution

This section provides a critical review of different flow distributor designs that have been applied to single-phase processes and their applicability to multiphase processes. Four main types of distributor designs are identified, namely, bifurcation distributors, consecutive manifolds, split-and-recombine distributors, and screen-header distributors. They are analysed in terms of effectiveness, efficiency of energy and space use, ease of manufacturing, and potential to be used in multiphase processes.

Bifurcation distributors use the simplest way to distribute a flow. In the simplest arrangement, this distributor divides a single stream into two parallel ones using tee-junctions. It can do so radially or using other types of junctions but the core concept is the same. Amador et al. showed this type of distributor can produce approximately equipartitioned flows as long as the fabrication tolerances are sufficiently tight [105]. This flow distributor is limited to distribute a flow into a power-of-two number of channels (2, 4, 8, 16 ...) which may be restrictive for large number of channels; also, this flow distributor has a relatively large footprint. This type of distributor may be suitable for multiphase processes, as long as the number of channels is not very large.

Consecutive manifolds, shown in Fig. 2-7 a, consist of a distribution section, which feeds to the main channels and then an optional collection section. The flow distribution is not simple to calculate but is well understood since the initial works by Commenge et al. and Amador et al., who used CFD and a resistance network model as shown in Fig. 2-7 b [105,106]. Wang extended this model for high Reynolds numbers and found the resistance network model is suitable for their modelling [107]. The hydraulic resistance these models use is simply the pressure drop divided by the volumetric flow rate, a physically-sound analogy to Ohm's Law, according to Oh et al. [108]. Unlike bifurcation distributors, consecutive manifolds are not limited to any number of channels and their footprint is small. There are no publications on their energy efficiency. Amador et al. compared the modelling results to experimental data and determined the fabrication tolerances have a slight effect on the flow distribution [105]. This type of flow distributor is suitable for multiphase processes but the effect of the design variables on the effectiveness of the flow distribution has to be studied systematically; this is addressed in Chapter 5 of this thesis.

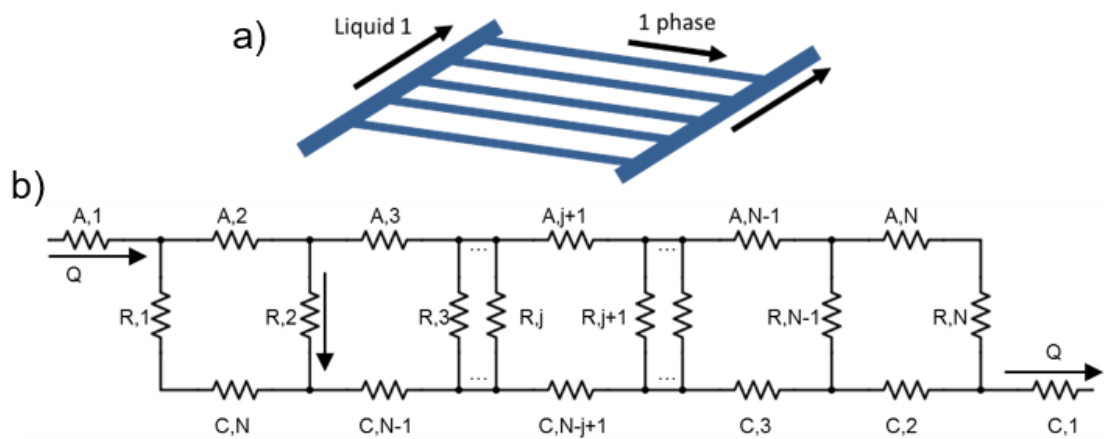


Figure 2-7 Consecutive manifold. a) Shows a schematic of the flow distributor, b) shows the corresponding resistance network used to model the flow distribution.

Split-and-recombine distributors (Fig. 2-8) were first proposed for microreactor scale-out by Tonomura et al. [109]. They have a similar structure to bifurcation distributors with the key difference that the channels are connected again after every bifurcation. In comparison to bifurcation distributors, split-and-recombine ones perform well if the inlet flow or composition changes and if there is a blockage downstream in the main channels [109,110]. This type of distributor, unlike bifurcation ones, is not limited to any number of channels but requires several additional connections for every additional main channel, which would occupy a large footprint, even for a small number of main channels. This flow distributing structure may prove useful for specific applications where blockages are of particular concern.

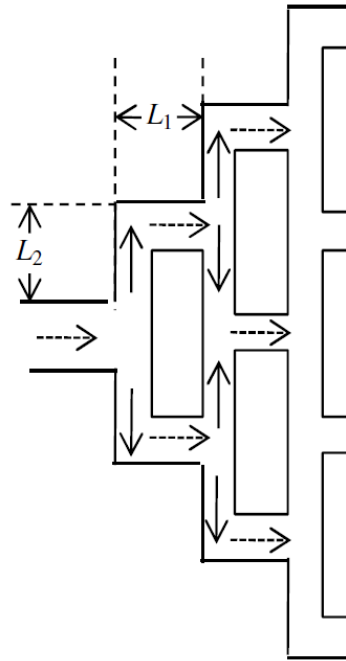


Figure 2-8 Split-and-recombine flow distributor schematic. Reproduced from Wang et al. [110].

Screen-header flow distributors, shown in Fig. 2-9, have been used to scale-out microreactors into 3-D monoliths, unlike the 2-D flow distributors reviewed above. They consist of two perpendicular screens, which distribute the flow into vertical slots and then into horizontal ones, before they feed into the 3-D arranged main channels. Rebrov et al. developed equations for optimal design of this type of flow distributor [111]. 3-D flow distributors are space-efficient but their design cannot easily be transferred into multiphase flows.

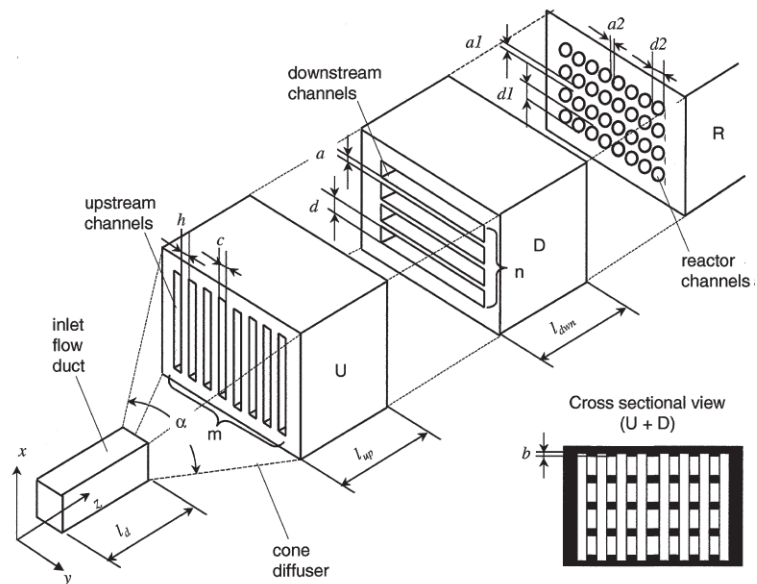


Figure 2-9 Schematics of a screen-header flow distributor. Reproduced from Rebrov et al. [111].

2.7 Scale-up of multiphase small-channel processes

To increase the throughput of small-channel contactors, the channel dimensions are scaled first followed by scaling-out into many parallel channels. This section reviews both the scale-up and the scale-out literature available for multiphase small-channel processes.

2.7.1 Scale-dependence of segmented flow processes

There is a limited number of studies where the effects of the dimensions on the process performance are analysed systematically for multiphase small channel contactors. The results reviewed here focus on liquid-liquid contactors under segmented flow regime. The literature reviewed is ordered according to the largest channel size studied. A short analysis of the gaps and inconsistencies found in the literature is presented at the end of this section.

Garstecki et al. were among the first to report drop lengths (in segmented flow) using the channel dimensions as a reference to have dimensionless quantities [65]. They found that, for channel widths of either 50 or 100 μm , the same relationship (function of Q_d/Q_c) could describe the dimensionless plug length. Jovanovic et al. studied the effect of size in channels with hydraulic diameters of 248 and 498 μm [97]. These authors used

dimensionless numbers, such as Reynolds (Re), capillary (Ca), Weber (We), and Bond (Bo) to describe the hydrodynamics of segmented flow. Even though they did not obtain correlations that could relate segmented flow hydrodynamic properties (e.g. dimensionless plug/slug lengths) with the dimensionless numbers, they found that, for the same fluids, larger channels produce longer slugs. Li & Angeli studied several hydrodynamic characteristics of segmented flows using channels with diameters of 200 and 500 μm . They found the dimensionless film thickness has a very limited dependence on the channel size (exponent ≈ 0.1). The dimensionless plug velocity and length were found to be independent of the diameter. The pressure gradient depended strongly on the diameter but the relationship was not shown explicitly. Cao et al. studied the dimensionless plug length (L_p/d) and the plug velocity relative to the mixture velocity using channels with hydraulic diameters of 200, 400, and 600 μm [64]. They proposed a power-law correlation of the dimensionless plug length (L_p/w) with Q_d/Q_c , Re_d , and We_d . From their correlation, it can be calculated that the effect of channel size on L_p/w has an exponent of -0.05, which is very small and can be considered to be independent. Their findings on plug velocity do not show a trend with respect to channel size. Shimanouchi et al. reported a reactive extraction process under segmented flow regime using channels with diameters of 500 and 800 μm [112]. Under similar hydrodynamic conditions (i.e. same fluids, flow rate ratio, and mixture velocity), the performance was practically the same, with some small improvements in the small channel. Zhang et al. studied the channel size effects on interfacial area, plug velocity, and mass transfer coefficient using channels with diameters of 0.8, 1.2, and 1.8 mm [81]. These authors found that the relative velocity of the plugs with respect to the total superficial velocity becomes larger for larger diameters. According to their results, the dimensionless interfacial area depends only on Q_d/Q_T and is independent of the channel size. Finally, they found that the mass transfer coefficient (k_L) decreases approximately linearly with respect to the channel diameter. Tsaoulidis & Angeli studied the effect of channel size on segmented flow hydrodynamics and mass transfer for channel sizes of 0.5, 1, and 2 mm [33,34]. They found the dimensionless plug length to be a function of the diameter

with an exponent close to 0.5. The dimensionless film thickness has a smaller exponent, of 0.1. The relative plug velocity also increases with the diameter. The recirculation time was found to increase (slower mixing) with increasing channel size, this is mainly attributed to the increase in plug length. Larger channels have smaller pressure drops. The extraction efficiency and the volumetric mass transfer coefficient, at the same mixture velocity and residence time, are higher in the smaller channels, mainly because of the larger specific interfacial areas available in the smaller channels.

There is considerable variation in the findings of scale-dependency of the hydrodynamic features and mass transfer performance of segmented flow contactors. This review shows that most studies have used microchannels with $d < 1$ mm. The results coincide, broadly, in two critical aspects, in larger channel sizes, the mass transfer rate is slower (smaller specific interfacial areas, slower mixing, lower mass transfer coefficient) but the pressure drop is reduced. This opens up a trade-off analysis that needs to be considered in the design of segmented flow contactors.

2.7.2 Two-phase flow distribution

The distribution of two-phase flows has not yet been accomplished on a commercial scale but research literature is available on the topic. Luis & Garcia-Verdugo identified six important issues regarding the scale-out of two-phase systems [99]. These are (1) blockage by solid particulates in the small channels, (2) inhomogeneous distribution of flow between the channels, (3) cost of manufacturing the scale-out contactors, (4) precision of flow control, pulse-free flow, (5) pressure drop in the multichannel contactor, and (6) control of large parallel reaction systems. While all these issues are important, the first two need to be tackled first in order to consider the rest. The same authors identified that the solids-handling issue can be solved by using operating under segmented flow regime and relatively large channels. The challenge is then to design an economically viable and effective flow distributor to operate under segmented flow.

The effects of maldistribution on the performance of single-phase multichannel processes are well documented [113–115]. The various channels have different flow rates thus different residence times, which affect the conversion and selectivity of a reaction. For multiphase processes, this has been studied much less. Fig. 2-10 shows that, since each phase can be maldistributed independently, the maldistribution affects the mixture velocity (with similar effects on the residence time as in the single-phase case) and the ratio of the phases inside each channel. Multiphase processes are generally very sensitive to the phase flow rate ratio so the effects of maldistribution on multiphase processes can be very different from the single-phase cases.

	$u_{ci} < \hat{u}_c$	$u_{ci} > \hat{u}_c$
$u_{di} < \hat{u}_d$	↓ u_{mix}	↑ $\frac{u_c}{u_d}$
$u_{di} > \hat{u}_d$	↓ $\frac{u_c}{u_d}$	↑ u_{mix}

Figure 2-10 Matrix of the effects of maldistribution of each phase (u_c , u_d) on the mixture velocity (u_{mix}) and flow ratio (u_c/u_d). \hat{u} is the mean (or design) velocity across the channels for either phase.

Schubert et al. studied a gas-liquid monolith reactor for the hydrogenation of glucose that was supposed to operate under segmented flow [116]. They did not use an effective two-phase flow distributor and found that many channels did not have a segmented flow pattern. The maldistribution of each phase, up to the point where the flow patterns were disrupted severely reduced the selectivity and conversion of the reaction processes. These negative results highlight the importance of multiphase flow distribution in the path to large-scale intensified reactors and contactors.

The flow distribution of two fluid phases can be done in two essentially different ways. Either the two fluid phases are divided into the required number of channels and then the fluids are put in contact (split-combine), or, the fluids are combined first and then

the two-phase flow is divided into the required number of channels (combine-split). Fig. 2-11 shows both approaches schematically.

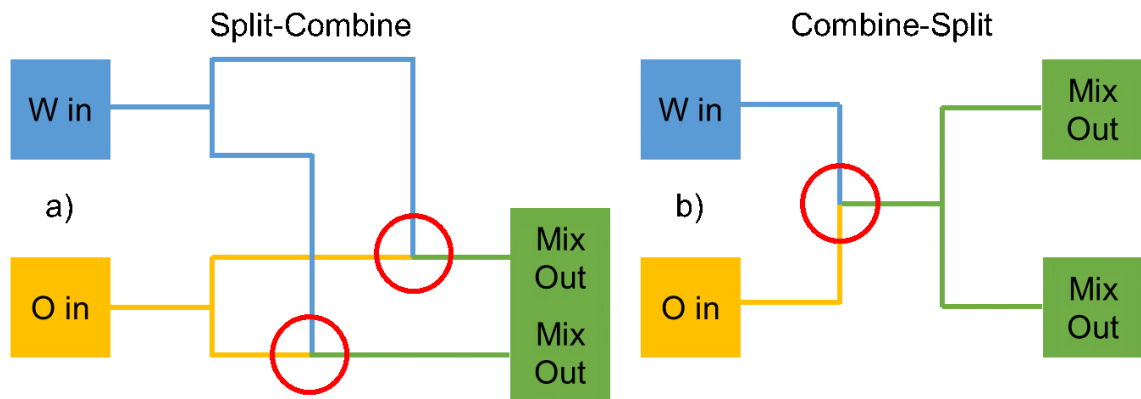


Figure 2-11 Schematics of the two basic strategies to multiphase scale-out. In a) the split-combine approach is presented and b) shows the combine-split approach.

The combine-split approach requires fewer mixing points but splitting (equally) multiphase flows is challenging. Hoang et al. developed a bubble-splitting distributor, shown in Fig. 2-12 [117,118]. With a bifurcation structure, a gas-liquid segmented flow is divided into up to 8 channels. The splitting is restricted in terms of flow rates, as only slow flow rates with very large liquid-to-gas ratios were effectively split. While it is an important proof-of-concept, it would not be able to serve as a commercial-scale multiphase distributor. Chugh et al. proposed the use of random mixers to mix the two fluids before they enter a 3-D monolith, as shown in Fig. 2-13 [119]. The random mixers designs are a chamber (figure 2-13 a), a radial manifold for the liquid phase (figure 2-13 b), and a cylinder packed with PVC spheres (figure 2-13 c). In contrast to intensified technologies, these proposed mixers cannot be accurately modelled or operated. This method may be suitable for systems that do not require precise flow distribution and may afford to have poor performance in exchange for a low-cost, simple flow distributor.

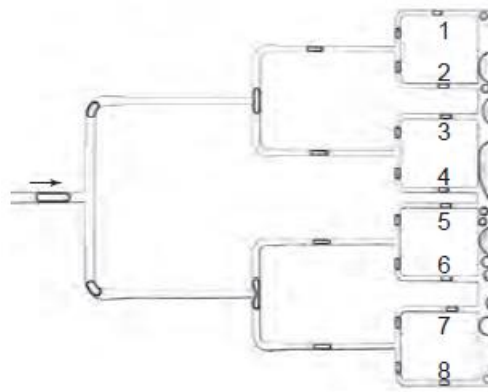


Figure 2-12 Bubble-splitting bifurcation distributor, an example of the combine-split scale-out strategy. Reproduced from Hoang [118].

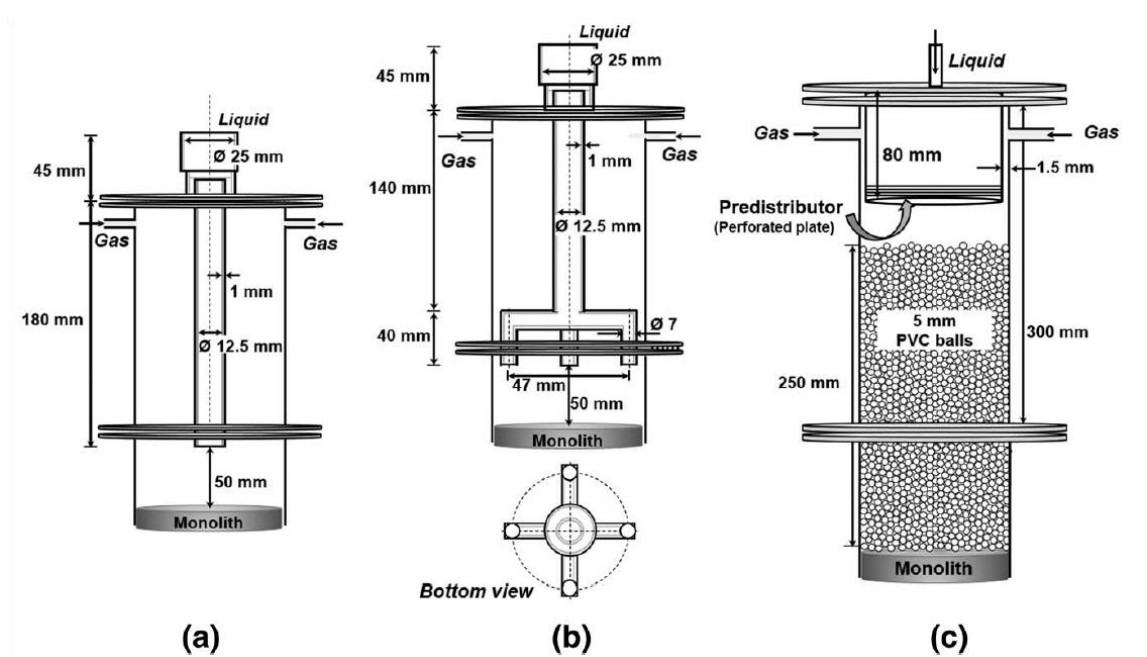


Figure 2-13 Random mixer design proposals for 3-D multiphase monolith contactors. Reproduced from Chugh et al. [119].

The split-combine approach to multiphase scale-out requires splitting single-phase flows, which has received more attention (section 2.6.1) and is inherently simpler. The single-phase splitting can take place using bifurcation distributors, consecutive manifolds, or split-and-recombine distributors. Chambers et al. designed, without an explicit methodology, a scaled-out gas/liquid microreactor for fluorination reactions [48]. They achieved high conversion and yield thus serving as proof of concept for scaled-out multiphase microreactors. Their prototype, built by combining chemical etching and standard drilling, can operate with up to 3, 9 or 30 channels at a time and is made of

stainless steel lined with PTFE. The authors did not show details of the flow distribution in the channels or results with the different configurations, only conversion and yield. Su et al. scaled-out a gas-liquid photoredox reaction into 2, 4, and 8 channels using T-junctions in a bifurcation approach [120]. They found standard deviations on the liquid phase flow rate to be, mostly, below 10% and decrease with total velocity (calculated as the sum of inlet superficial velocities). Kashid et al. presented the earliest works on liquid-liquid scale-out [121]. These authors used six-channel commercial radial distributors for each phase and then contacted them using Y-junctions. They achieved segmented flow in all the channels and reported standard deviation of the phase flow rate ratio below 5%. The radial distributor is not a viable alternative for large-scale numbering-up. Al-Rawashdeh et al. studied the flow distribution for gas-liquid systems using consecutive manifolds for both phases (Fig. 2-14) [49,122,123]. They used resistance network models and experimental setups (up to 8 channels) to study the maldistribution and their relationship with the design of the manifolds. In particular, they analysed the effect of fabrication tolerances on flow maldistribution, which had not been considered before. Darekar et al. studied a flow distributor with the same design as Fig. 2-14 using computational fluid dynamics (CFD) and experimentally [124]. They studied the effect of flow rate, inlet channel diameter, outlet channel diameter, and distance between outlets for up to six channels. After several design iterations these authors achieved non-uniformity around 5%. These studies form the basis for the further development of scaled-out intensified multiphase processes.

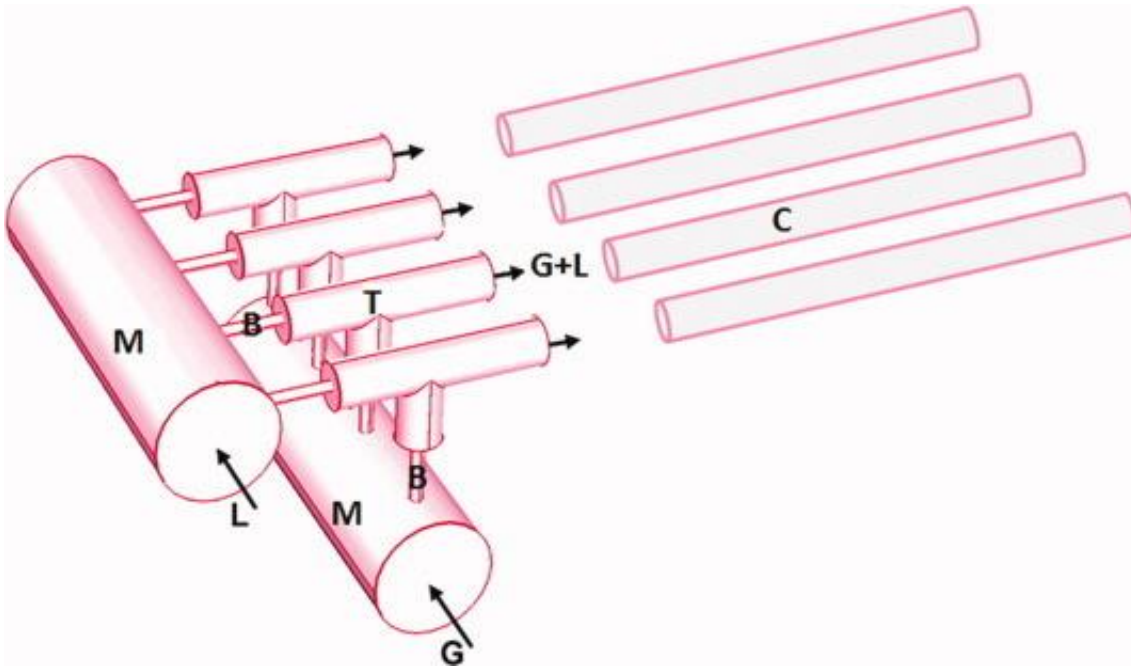


Figure 2-14 Barrier-based two-phase flow distributor designed by Al-Rawashdeh et al. [123].

This section reviewed the challenges, necessary considerations, approaches, and recent advances to scale-out of multiphase systems. Regarding the split-combine and combine-split approaches, it is clear that the former is more adequate for the purpose of large-scale intensified contactors. However, since the largest number of channels reported for a scale-out contactor is eight, there are clearly opportunities to develop this area further. Three areas to address are, (1) a more robust quantification of the maldistribution; previous works report statistically incomplete results (e.g. standard deviations of the flow rate of one phase only) ignoring the multivariate nature of multiphase distribution. (2) Understand how maldistribution changes with the number of channels (i.e. incorporate the number of channels as a variable); this is particularly important considering commercial applications will require large numbers of channels. Finally, (3) understand the economic trade-offs of scaling-out; these include the capital cost of building the flow distributors and the pumping power costs. This review has shown there is a need for a robust methodology for the design of two-phase flow distributors that addresses the current gaps in this area and the needs of commercial applications.

2.7.3 Scale comparison of intensified and conventional contactors

The previous two sections have reviewed the available literature on scale-out multiphase processes operating under segmented flow. In this section, the results are compared with conventional contactors.

The total throughputs, in terms of total volume per unit time, that Su et al. (d=0.75 mm, 8 channels) [120], Kashid et al. (d=0.5 mm, 6 channels) [121], Al-Rawashdeh et al. (d=0.9 mm, 4 channels) [122], and Darekar et al. (d=2 mm, 6 channels) [124] reported are, approximately, 1.4×10^{-3} , 4.8×10^{-4} , 2×10^{-4} , and $4.8 \times 10^{-3} \text{ m}^3 \text{ h}^{-1}$. These throughputs are several orders of magnitude away from being commercially competitive, both because they use small channel diameters and number of channels. Table 2-4 presents examples of conventional contactors and related throughputs, and the numbers of channels that would be required to achieve the same throughputs, for different channel sizes. The number of channels needed scales linearly with the throughput and is inversely-squared proportional to the diameter. The strong dependence of throughput on channel diameter is the driving force to investigate segmented flow processes at diameters as large as 4 mm.

Table 2-4 Number of parallel channels of different diameters needed to process a determined throughput. Comparable conventional contactors are included for each throughput considered. The single-channel throughput in every channel is calculated for a mixture velocity of 4 cm s⁻¹. Operation years of 8000 hours are used.

Total				
throughput	Comparable conventional	N	N	N
/ m³ h⁻¹	contactor	(d=1 mm)	(d=2 mm)	(d=4 mm)
(m³ yr⁻¹)				
5×10 ⁻³	Lab-scale centrifugal extractor [125]	45	12	3
(40)	Impinging jet contactor [29]			
5×10 ⁻²	Bench-scale rotating disc contactor	443	111	28
(400)	[126]			
5×10 ⁻¹	Pilot plant centrifugal extractor [127]	4421	1106	277
(4000)	Graesser raining bucket extractor [2]			

2.8 Overview

This literature review provides a broad overlook of the use of small-channel contactors for liquid-liquid extraction applications. Conventional processes and equipment are described and the opportunities for intensification are highlighted. These opportunities go beyond increasing the mass transfer rates and include safe operations with reduced solvent usage. Several examples of applications of small-channel contactors are presented. Liquid-liquid segmented flow is reviewed in terms of hydrodynamics, pressure drop models, and mass transfer performance. Emphasis is given on the effect of channel size and scale-up of contactors operating under segmented flow. The numbering-up strategy is analysed, first from an economic point of view, followed by a technical one.

Several conclusions can be made from the literature reviewed. Clearly, many liquid-liquid processes are important economically and through process intensification can they be largely improved. Liquid-liquid segmented flow has been extensively studied

in the past few years but given the wide range of parameters that affect its hydrodynamic and mass transfer characteristics, the effects of design and operation parameters are not fully characterised yet. The throughput achievable using a single channel is not sufficient, not even for a niche application. To increase throughputs both scale-up of the diameter and parallelisation (numbering-up, scale-out) are necessary (see Table 2-4). This challenge remains largely unexplored and the few publications on the topic have been reviewed. A rigorous analysis of multiphase scale-out is critically needed to further intensify liquid-liquid processes.

3 Research Methods

3.1 Experimental methods

3.1.1 Materials and flow equipment

The substances and solutions used in the experiments described in sections 4.1 - 4.4 were the following: The aqueous phase was deionised water saturated with the respective organic phase. The organic phases were pure tributyl phosphate (TBP) (97% Aldrich), referred onwards as TBP 100%, and a solution of TBP 30% v/v in kerosene (low odour, Alfa Aesar). The organic solutions were equilibrated with water.

In section 4.6, the aqueous phase was substituted with a 3 M nitric acid (HNO_3) (Sigma-Aldrich) solution. For the uranium extraction experiments, uranyl nitrate hexahydrate ($\text{UO}_2(\text{NO}_3)_2 \cdot 6\text{H}_2\text{O}$) was used. This salt contains uranium in its sixth oxidation state and it is referred onwards as U(VI). It was initially dissolved in the organic-saturated nitric acid 3M phase. Different concentrations of U(VI) were used depending on the experiment.

In Chapter 6, the following substances and solutions were used: The aqueous phase was a 10^{-2} M KOH (Sigma-Aldrich) solution in deionised water; 1 mL of phenolphthalein solution (0.5%, Reagecon) was added for every 250 mL of the aqueous solution. The organic phase consisted of acetic acid (glacial Sigma-Aldrich) 10^{-2} M dissolved in kerosene.

The set up consisted of the following: tubing, mixing junctions, pressure-probe tees, visualisation boxes, and syringe pumps. Three channel sizes with different diameters were used; their dimensions are presented in table 3-3. The material for the 1 and 4 mm tubing is a perfluoroalkoxy alkane polymer (PFA). The 2 mm tubing is made of fluorinated ethylene propylene (FEP). Both PFA and FEP are fluoropolymers very similar to each other and to Teflon (PTFE). These materials are hydrophobic and are preferably wetted by the organic phases over the aqueous phases. The mixing junctions were in all cases tees with internal diameter (ID) that matched the ID of the tubing. The

mixing tees were used such that the organic phase (wetting phase) was fed on the same axis as the tee exit while the aqueous phase (non-wetting) was fed perpendicularly to the tee exit. The 1 mm and 2 mm mixing tees were made in-house by drilling PTFE tees (IDEX) in the High Precision Design & Fabrication Facility within the Faculty of Engineering at UCL. The 4 mm tees are made of PTFE and are available commercially (BOLA). The tees used along the two-phase flow channel in the pressure drop measurements were drilled only in the direction of the flow to have the same diameter as the flow channel. These pressure-port tees are made of PTFE (IDEX and BOLA in the 4 mm case), which has the same wettability as PFA; no disruption to the flow was observed in any case. The visualisation boxes used to obtain the imaging results (section 4.3) were prepared with a transparent polystyrene box (with flat faces) filled with a glycerol-in-water mixture 10% m/m to match the refractive index of the fluoropolymer tubing.

Table 3-1 Dimensions of tubing used in flow experiments. Dimensions and uncertainties are reported by the manufacturers.

Nominal diameter (d) / mm	Internal diameter (ID) / mm	ID uncertainty / mm	Outer diameter (OD) / mm	Manufacturer (part number)
1	1.000	0.025	1.587	IDEX (1507)
2	2.000	0.075	3.000	IDEX (1677)
4	4.00	0.10	6.00	BOLA (S 1815-20)

Syringe pumps (Legato210 kdScientific) were used for the flow experiments presented in Chapter 4. The manufacturer reports a flow rate accuracy of 0.35%, however, in-house testing showed the flow rate uncertainty to be <1.5% for the range of

flow rates investigated. In Chapter 6, HPLC pumps were used (ECP2300 ECOM). The accuracy reported by the manufacturer matched the flow rate uncertainty measured of 2%.

In Chapter 4, for the hydrodynamic studies (sections 4.2 and 4.3) four mixture velocities (u_{mix}) (1.06, 2.12, 3.18, 4.24 cm s⁻¹) and four organic phase flow rate fractions (0.500, 0.333, 0.250, 0.200) were used in the three channel sizes. All of these flow conditions exhibit segmented flow and allow for a factorial design of experiment. For the mass transfer experiments (section 4.4), two mixture velocities (1.06, 4.24 cm s⁻¹) and three organic phase flow rate fractions (0.500, 0.333, 0.250) were tested. The initial concentration of $\text{UO}_2(\text{NO}_3)_2 \cdot 6\text{H}_2\text{O}$ was 0.05 mol L⁻¹ in the nitric acid solution for all cases studied. The following conditions were selected as base case: TBP 30%, $d=2$ mm, $u_{\text{mix}}=1.06$ cm s⁻¹, 0.500 organic phase flow rate fraction. Three residence times were considered, equal to 5, 10, and 20 s, which were obtained by changing the channel length.

3.1.2 Characterisation of hydrodynamic properties

The properties of the liquids used in sections 4.1-4.4, and 4.6 were characterised. Specifically, the density, viscosity, and interfacial tension were measured at room temperature (20 ± 1 °C). Whenever possible, comparisons with values found in the literature are drawn.

The liquids tested were deionised water, TBP, TBP 30% v/v in kerosene, and kerosene. Kerosene properties are included to highlight its role in the properties of the TBP 30% solution. In all the experiments, the aqueous and organic solutions were mutually saturated. The properties of saturated and unsaturated liquids were measured and compared in order to emphasise the effect of the mutual saturation on the hydrodynamic properties.

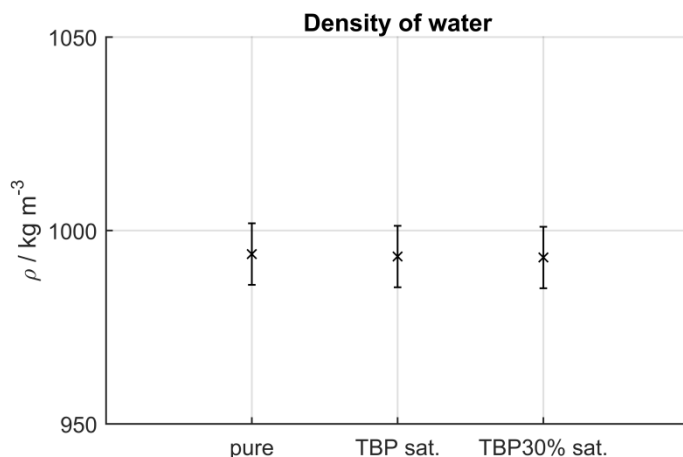
The density was determined gravimetrically using an analytical balance (Sartorius BP121S) and a class A volumetric flask (5 ml, Fisherbrand). The results are

presented in Figure 3-1. The density of water is not affected by the saturation with the organic phases. The solubilities (at 25 °C) of TBP and kerosene (dodecane) in water are 0.39 g/litre [6] and 3.7×10^{-3} mg/litre [128], respectively. The densities of the organic solutions are also unaffected by the saturation with water. The solubilities (at 25 °C) of water in TBP and in kerosene are 64 g/litre [6] and 65 g/litre [129], respectively. The similar bulk density of water and TBP and the low mutual solubility of water and kerosene explain the values obtained for the densities. Tian & Lui reported experimental densities of TBP and binary solutions with dodecane at 25 °C [130]. Estimated using linear interpolation, the TBP 30% solution v/v in dodecane has a density of 808 kg m^{-3} at 25 °C. The difference of 36 kg m^{-3} with respect to the experimental (unsaturated) value in Figure 3-1 can be explained in part by the five degrees temperature difference and by the difference in the solvent; the dodecane used in their work has a lower density (745.79 kg m^{-3} at 25 °C) compared to the kerosene used in this work (795.8 kg m^{-3} at 20°C). The density values used for the calculation of dimensionless numbers for hydrodynamic characterisation are presented in Table 3-2.

Table 3-2 Properties of the liquid phases and their uncertainties. These values are used to calculate dimensionless numbers.

Liquid phase	Density	Density	Viscosity	Viscosity	Interfacial tension	Interfacial tension
	(ρ)	uncertainty (1σ)	(μ)	uncertainty (1σ)	(γ)	uncertainty (1σ)
	/ kg m ⁻³	/ kg m ⁻³	/ mPa s	/ mPa s	/ mN m ⁻¹	/ mN m ⁻¹
Water sat. with TBP	993.3	7.9	0.9405	0.0073	-	-
Water sat. with TBP 30%	993.0	7.9	0.9620	0.0064	-	-
TBP sat. with water	973.3	7.8	4.355	0.077	7.714	0.047
TBP 30% sat. with water	844.3	6.8	2.256	0.026	9.950	0.063

a)



b)

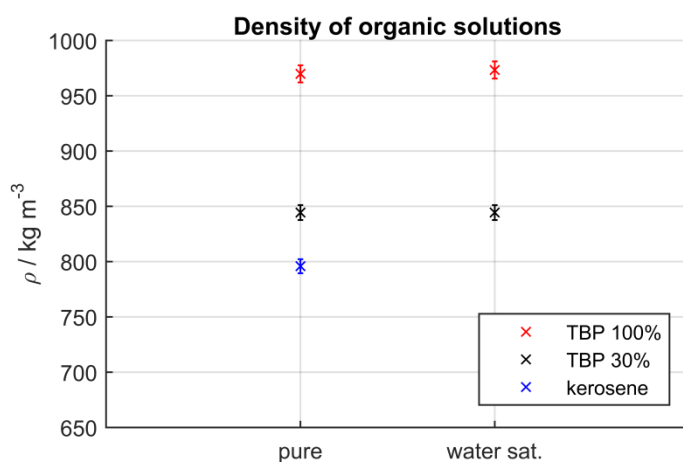


Figure 3-1 Density of solutions used at 293 K. In a), density of pure water and water saturated with the organic solutions. In b), density of the organic phases, pure and after saturation with water.

The viscosity of the solutions was measured with a cone-plate rheometer (MCR302 Anton Paar). The results are presented in Figure 3-2. The viscosity of water increases 3.2% and 5.6% when it is saturated with TBP and TBP 30%, respectively. The viscosity is more sensitive to the composition than the density; in this case, the presence of large molecules (TBP and long hydrocarbon chains) in the solution increase the viscosity compared to the pure case. The viscosity of the organic solutions also increases after saturation with water. This is more noticeable for the TBP solution where the viscosity increases by 15%, compared to the TBP 30% solution with a 2.1% increase. These results are explained considering the intermolecular forces in the solutions, the water and the double-bonded oxygen in TBP can form polar-polar bonds

which increase the viscosity of the solutions. In the TBP 30% solution, where there is a large fraction of kerosene, the effect is less noticeable. Tian & Lui also reported experimental viscosities of TBP and binary solutions with dodecane at 25 °C [130]. They report a TBP viscosity at 25 °C of 3.399 mPa s, 11% lower than the one reported here, the difference can be attributed to the small temperature difference. The viscosity of the TBP 30% v/v dodecane solution, estimated with linear interpolation, is 1.58 mPa s (at 25 °C), which is 0.63 mPa s lower than the one reported here (at 20 °C). However, the difference can be explained by the temperature difference and the viscosity difference of the solvents (1.991 mPa s for kerosene at 20 °C and 1.336 mPa s for dodecane at 25 °C). The viscosity values used for the calculation of dimensionless numbers for hydrodynamic characterisation are presented in Table 3-2.

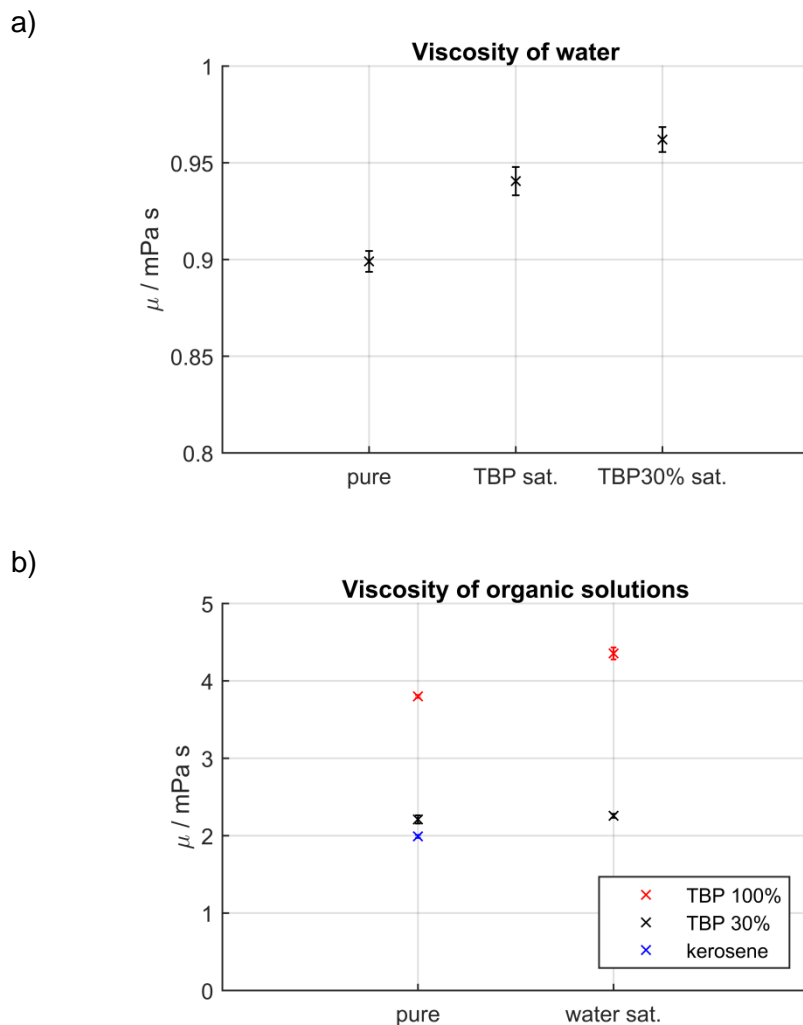


Figure 3-2 Viscosity of solutions used at 293 K. In a), viscosity of pure water and water saturated with the organic phases. In b), viscosity of the organic phases, pure and after saturation with water.

Interfacial tensions were measured with a ring-probe tensiometer (K100 Krüss), and the results for the water-organic solutions are shown in Figure 3-3. Kerosene has the highest interfacial tension value followed by the TBP 30% solution and then the TBP. The water-TBP 30% interfacial tension value is much closer to the water-TBP value than the water-kerosene value because the slightly-polar structure of TBP allows it to concentrate on the interface. Nave et al. studied the surface properties of TBP in dodecane/water mixtures and reported the critical micellar concentration (cmc) to be at 0.28 mol/litre of TBP in dodecane at 25°C [131], where a 30% v/v solution of TBP in dodecane is 1.094 mol/litre (at 25 °C). Therefore, the TBP 30% solution used in this work has a TBP concentration, most likely, above the cmc thus explaining why the interfacial

tension between the water-TBP 30% and water-TBP mixtures are so similar. The interfacial tension values used for the calculation of dimensionless numbers for hydrodynamic characterisation are presented in Table 3-2.

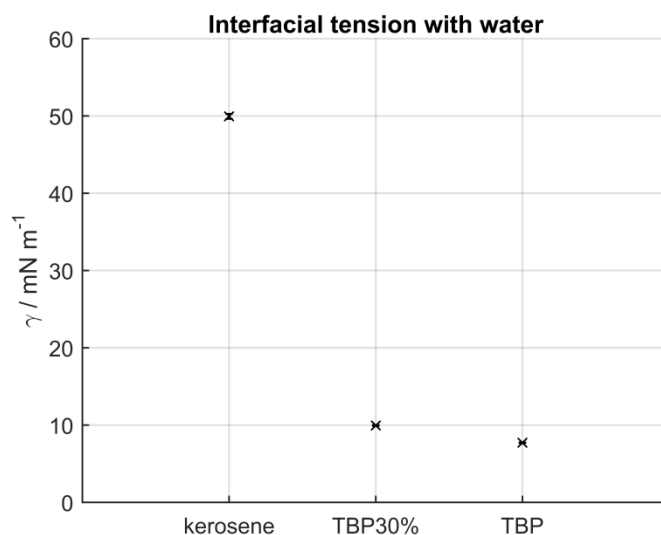


Figure 3-3 Interfacial tension of mutually saturated organic solutions and water at 293 K.

3.1.3 High-speed imaging and post-processing

High-speed imaging was used to measure the characteristics of the segmented flow at various conditions (Chapter 4). A high-speed camera (v1212 Phantom) was used for this purpose, as shown on the flow setup schematic in Figure 3-4. Visualisation boxes made with transparent polystyrene with flat faces were used to match the refractive index of the fluoropolymer tubing. The visualisation boxes were filled with a glycerol-in-water 10% m/m mixture. The resolution in the images depends on the channel internal diameter since the camera was readjusted for each channel. The resolutions of the images are 101 px mm^{-1} , 51.5 px mm^{-1} , and 12.8 px mm^{-1} for the 1, 2, and 4 mm channels, respectively. The lengths reported are the average and standard deviation of 5 plugs or slugs measured consecutively after the flow is fully developed.

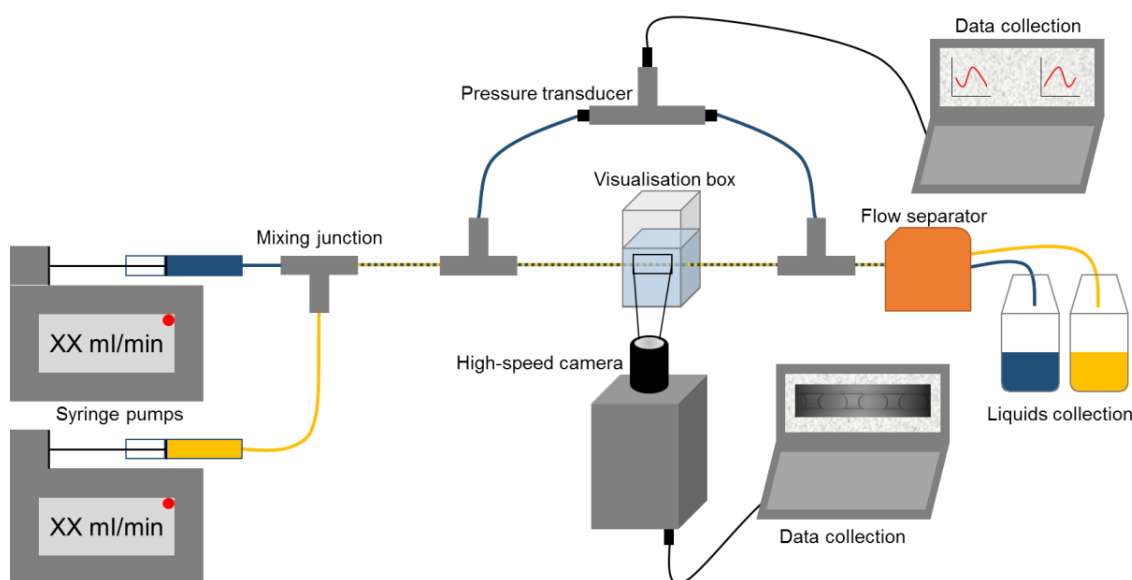


Figure 3-4 Schematic of flow setup for high-speed imaging, pressure drop measurements and flow separation.

3.1.4 Pressure drop measurements

The pressure drop of the two-phase flows (Chapter 4) was measured using a differential pressure transducer (UNIK 5000 GE) and an in-house LabVIEW-based application. Pressure ports were placed at two points downstream from the mixing junction. The pressure ports had the same internal diameter as the tubing and no disruption to the flow was noticeable. The tubing to the pressure transducer was filled with the continuous phase in the main channel. The first port was placed at least 40 \times d units away from the mixing tee in order to ensure segmented flow was fully developed. Since the signal-to-noise ratio (SNR) depends on the distance between the pressure ports, this position of the second pressure port was selected for each internal diameter to ensure a high SNR. The distances were 62.6, 78.2, 133.0 cm for the 1, 2, 4 mm channels, respectively. These experiments did not use the flow separator, and the phases were collected in a container. Measurements were recorded over 20 s with a 5 kHz frequency and were repeated. The uncertainties of these measurements are the standard deviation of \approx 20,000 data points.

3.1.5 UV-vis spectroscopy

The concentration of U(VI) species (Chapter 4) at the outlet of the aqueous phase was measured with a UV-vis spectrometer (USB2000+ Ocean Optics). The

concentrations were measured against a calibration prepared in-situ at wavelengths between 415 and 420 nm, where the peak of absorbance was observed. The cuvettes used in the spectrometer hold approximately 1.3 ml. Each measurement was repeated three times.

Batch equilibrium experiments were done for TBP 100% and TBP 30% at 1:1 volume ratios under agitation for over 3 hours at room temperature. The distribution coefficients (D) measured are 28.7 ± 1.8 for TBP 100% and 8.10 ± 0.36 for TBP 30% (standard deviations correspond to three repetitions). Darekar et al. reported a distribution coefficient for TBP 30% v/v in dodecane with a 3 M nitric acid solution at room temperature of 7.0 [25]. Since undiluted TBP is rarely used, no comparable distribution ratios are reported in the literature, however, it can be calculated from the work by Hotokezaka et al. [30]. The distribution coefficient for TBP 100% v/v in dodecane with 3 M nitric acid solution at room temperature was found to be between 9 and 33. The distribution coefficient for concentrated TBP is expected to be higher than in diluted solutions on the basis of Le Chatelier's principle.

3.1.6 Liquid-liquid flow separation

The two-phase flow was separated in-line using a membrane-based flow separator (SEP-10 Zaiput Flow Technologies). The SEP-10 flow separator has a dead volume of approximately 400 μL . Figure 3-5 shows the flow separator parts and how it operates. The membrane used is made of PTFE (part number OB-900-S10) and is hydrophobic, thus allowing the organic phase to permeate while it retains the aqueous phase. The maximum flow rate that the separator can effectively separate with no retention or breakthrough depends on the membrane, the viscosity and the interfacial tension of the fluids. In the case of the PTFE membrane and the aqueous-TBP or aqueous-TBP 30% flows, the maximum flow rate was about 10 ml min^{-1} for all the flow rate ratios tested.

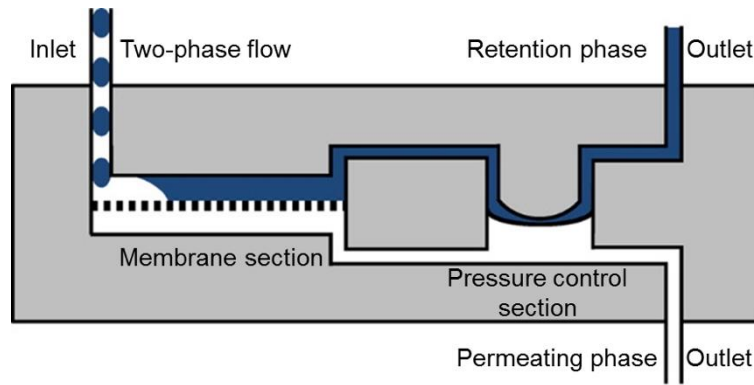


Figure 3-5 Flow separator schematic showing the membrane section where the separation takes place and the pressure control section that ensures no incomplete separation nor breakthrough. Adapted from Adamo et al. [132].

3.2 Numerical modelling

3.2.1 Resistance network model of double manifolds

Flow distributors, such as double manifolds, can be modelled using resistance network models, as reviewed by Oh et al. [108]. This type of modelling is preferred over computational fluid dynamics due to the simplicity and speed to set-up and run parametric studies [105]. The resistance network model considers the analogy between fluid flow in hydraulic circuits and electrons flow in electric circuits. This modelling approach has been used extensively to design and optimise single-phase flow distributors [105,106,133]. The overall pressure drop and fabrication tolerances of the designed manifold were also considered by Amador [134].

The analogy is extended here to account for two-phase incompressible flows. The model considers that volumes are additive which means that it cannot be used when there are large volume changes due to compressibility or mass transfer.

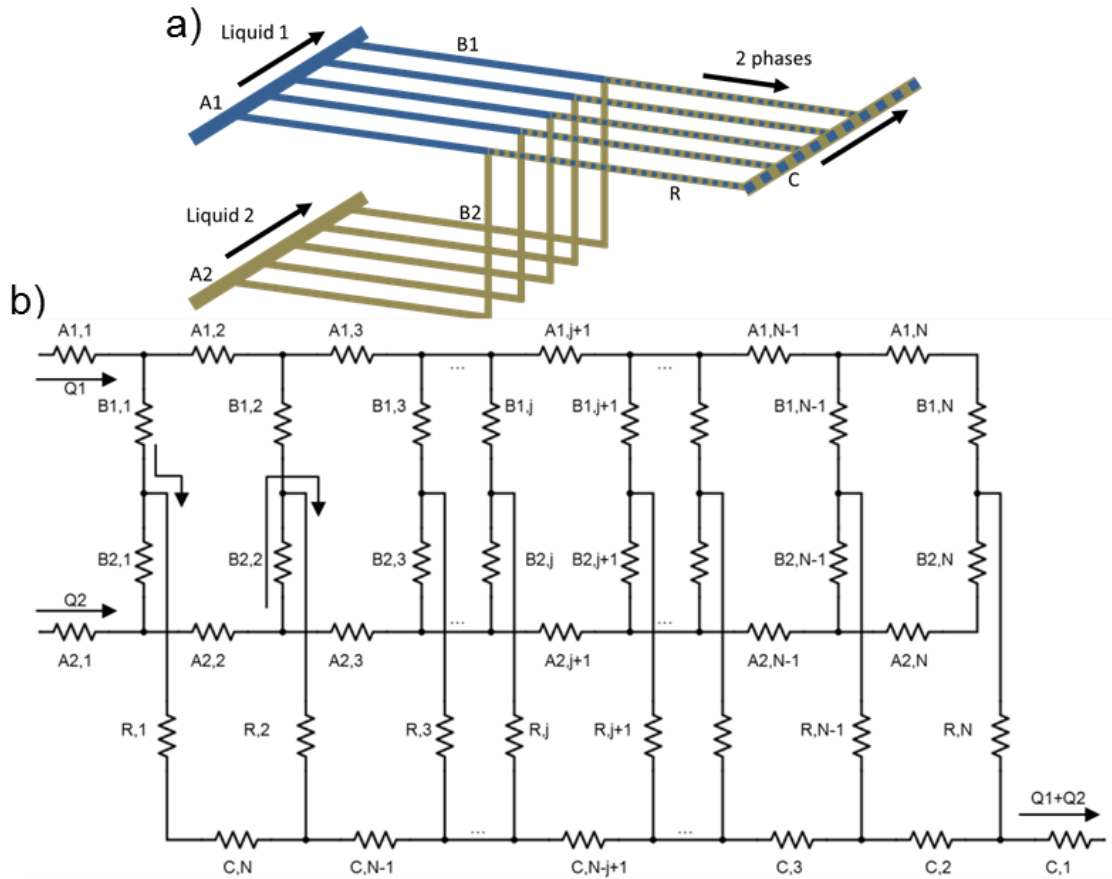


Figure 3-6 a) Schematic of a double manifold. b) Schematic of the corresponding resistance network. A1 and A2 are the distribution sections, B1 and B2 are the barrier sections, R is the main section and C is the collection section; Q1 and Q2 refer to the flow rates of each fluid.

A manifold for incompressible two-phase flows and its electrical-circuit analogue are shown in Fig. 3-6 a and b respectively. Kirchhoff's current law (KCL) and Kirchhoff's voltage law (KVL) are used to solve the circuit in Fig. 3-6 b. KCL is analogous to mass conservation, while KVL is analogous to energy conservation. Eqs. 3-1 and 3-2 are the algebraic representations of KCL and KVL respectively for flow systems.

$$\sum_{k=1}^n Q_k = 0 \quad (3-1)$$

$$\sum_{i=1}^j \Delta p_i = \sum_{i=1}^j R_i Q_i = 0 \quad (3-2)$$

where, Q is the volumetric flow rate, Δp is the pressure drop, and R is the hydraulic resistance defined as the ratio of pressure drop over the volumetric flow rate. The sum in Eq. 3-1 applies at every node of the circuit. The sum in Eq. 3-2 adds the pressure drops in a closed loop in the circuit. In a double manifold with N main channels, $2(N-1)$

loops can be independently defined. Between the j -th and $(j+1)$ -th main channels, two loops are defined. These loops are highlighted in Fig. 3-7. Fig. 3-7 A, shows a loop including channels labelled $A_{1,j+1}$; $B_{1,j+1}$; R_{j+1} ; C_{N-j+1} ; R_j ; and $B_{1,j}$, while Fig. 3-7 B shows the other independent loop containing channels labelled $A_{2,j+1}$; $B_{2,j+1}$; R_{j+1} ; C_{N-j+1} ; R_j ; and $B_{2,j}$.

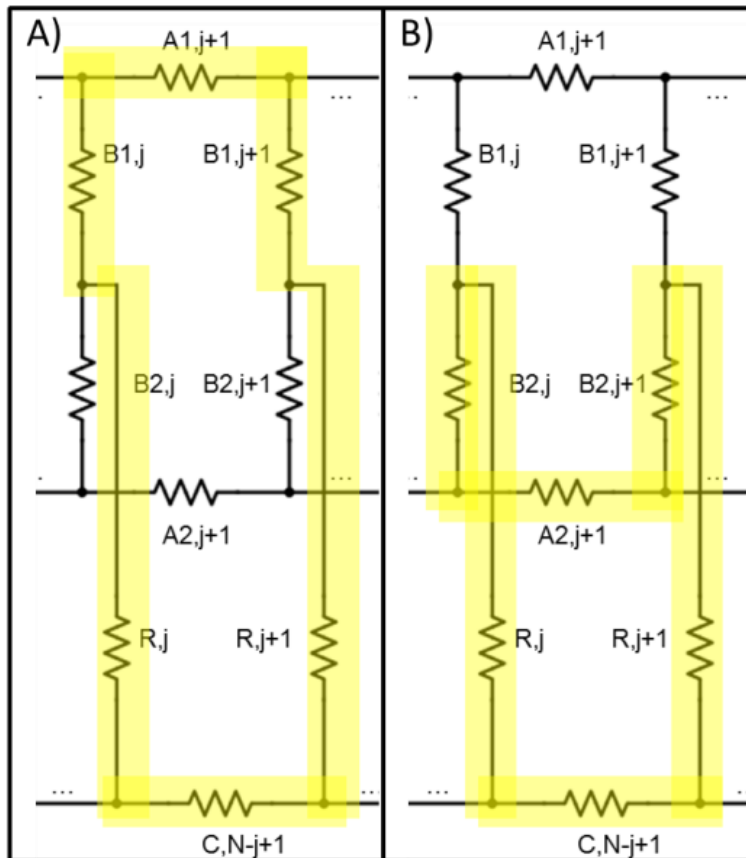


Figure 3-7 The j -th loops considered in the application of the Kirchoff's Voltage Law.

For these two loops, Eqs. 3-3 and 3-4 are obtained by applying the KVL. In total there are $N-1$ equations for each type of loop.

$$(QR)_{A_{1,(j+1)}} + (QR)_{B_{1,(j+1)}} + (QR)_{R_{(j+1)}} - (QR)_{B_{1,j}} - (QR)_{R_j} - (QR)_{C_{(N-j+1)}} = 0$$

$$(j=1 \dots N-1) \quad (3-3)$$

$$(QR)_{A_{2,(j+1)}} + (QR)_{B_{2,(j+1)}} + (QR)_{R_{(j+1)}} - (QR)_{B_{2,j}} - (QR)_{R_j} - (QR)_{C_{(N-j+1)}} = 0$$

$$(j=1 \dots N-1) \quad (3-4)$$

Applying KCL along the distribution channels (sections A1 and A2) at each junction, Eqs. 3-5 and 3-6 are obtained.

$$Q_{A1,(j+1)} = \sum_{k=1}^{k=N} Q_{B1,k} - \sum_{k=1}^{k=j} Q_{B1,k} = \sum_{k=j+1}^{k=N} Q_{B1,k} \quad (j=1 \dots N-1) \quad (3-5)$$

$$Q_{A2,(j+1)} = \sum_{k=1}^{k=N} Q_{B2,k} - \sum_{k=1}^{k=j} Q_{B2,k} = \sum_{k=j+1}^{k=N} Q_{B2,k} \quad (j=1 \dots N-1) \quad (3-6)$$

The same procedure along the collection channels (section C) yields Eq. 3-7.

$$Q_{C,(N-j+1)} = \sum_{k=1}^{k=j} Q_{R,k} \quad (j=1 \dots N-1) \quad (3-7)$$

Additionally, Eq. 3-8 is the result of applying KCL for the junctions where both manifolds meet before entering the main channels (sections B1, B2, R). There are N equations like this, one per main channel.

$$Q_{B1,j} + Q_{B2,j} - Q_{R,j} = 0 \quad (j=1 \dots N) \quad (3-8)$$

Finally, Eqs. 3-9 and 3-10 express the mass balance at the respective manifold of each phase:

$$\sum_{k=1}^N Q_{B1,k} = Q_{A1,1} \quad (3-9)$$

$$\sum_{k=1}^N Q_{B2,k} = Q_{A2,1} \quad (3-10)$$

Eqs. 3-5 to 3-7 are substituted in Eqs. 3-3 and 3-4. The resulting equations are divided by $R_{R,j}$ to yield Eqs. 3-11 and 3-12. As in the case for Eqs. 3-3 and 3-4, there are N-1 equations for each type of loop.

$$\sum_{k=j+1}^{k=N} Q_{B1,k} \frac{R_{A1,(j+1)}}{R_{R,j}} + Q_{B1,(j+1)} \frac{R_{B1,(j+1)}}{R_{R,j}} + Q_{R,(j+1)} \frac{R_{R,(j+1)}}{R_{R,j}} - Q_{B1,j} \frac{R_{B1,j}}{R_{R,j}} - Q_{R,j} - \sum_{k=1}^{k=j} Q_{R,k} \frac{R_{C,(N-j+1)}}{R_{R,j}} = 0 \quad (j=1 \dots N-1) \quad (3-11)$$

$$\sum_{k=j+1}^{k=N} Q_{B2,k} \frac{R_{A2,(j+1)}}{R_{R,j}} + Q_{B2,(j+1)} \frac{R_{B2,(j+1)}}{R_{R,j}} + Q_{R,(j+1)} \frac{R_{R,(j+1)}}{R_{R,j}} - Q_{B2,j} \frac{R_{B2,j}}{R_{R,j}} - Q_{R,j} - \sum_{k=1}^{k=j} Q_{R,k} \frac{R_{C,(N-j+1)}}{R_{R,j}} = 0 \quad (j=1 \dots N-1) \quad (3-12)$$

Eqs. 3-8 to 3-12 form a system of $3N$ linear equations for N main channels. $2N-2$ equations are obtained with the KVL analogy (Eqs. 3-11 and 3-12), there are N equations describing the mixing of the manifolds (Eq. 3-8) and 2 equations for the overall mass balance (Eqs. 3-9 and 3-10). The system can then be solved for $3N$ variables. These variables are the flow rates in the barrier channels for both phases ($2N$) and the main channels (N). Furthermore, with these results, and using Eqs. 3-5 to 3-7, the flow rates in the rest of the channels (distributing and collecting sections) can be calculated. Eq. 3-13 is the system to be solved. Appendix 3 includes a code to implement \mathbf{R} in Matlab.

$$\mathbf{R} \cdot \mathbf{Q} = \mathbf{S} \quad (3-13)$$

where \mathbf{R} is the resistances matrix, \mathbf{Q} is the flow rates vector and \mathbf{S} , the solution vector, is the right-hand-side of Eqs. 3-8 to 3-12. The value of \mathbf{Q} depends only on the values of resistance ratios in matrix \mathbf{R} , which is dimensionless, and the inlet flow rates of both liquids, $Q_{A1,1}$ and $Q_{A2,1}$ in vector \mathbf{S} .

Eq. 3-13 can be solved for \mathbf{Q} in a single step when all the hydraulic resistances are independent of the flow rate. When the resistance terms are not independent of the flow rates, Eq. 3-13 needs to be solved iteratively. In this case, the solution for the independent resistances can be used as initial guess. The model developed is applicable if volume conservation holds approximately (i.e. the density of both phases change less than 5%).

In the single phase flow sections (distribution and barrier), the hydraulic resistances are independent of the flow rates if the flow is laminar and incompressible. In these conditions, the Hagen-Poiseuille equation (Eq. 3-14) can be applied and the hydraulic resistance depends on the channel geometry.

$$\Delta p = \frac{128\mu L}{\pi d^4} Q \quad (3-14)$$

The pressure drop in fittings such as reducers, expansions, elbows, and tees is not significant at low Reynolds numbers; however, these effects can also be included in the pressure drop correlation if necessary. For the pressure drop in the main channels with both phases present, two options can be considered: Either the multiphase flows have hydraulic resistances independent of the flow rate, e.g. homogeneous model [92,135]; or the resistances depend on the flow rates. In the latter case Eq. 3-13 is solved iteratively using a non-linear pressure drop model for the two-phase flows. Al-Rawashdeh et al. showed this procedure [123]. In this work, the homogeneous model was selected for the two-phase flow channels for two main reasons. With this model, Eq. 3-13 can be solved in a single step and a wide range of parameters can be studied with minimal computational costs. In addition, the effects of the design variables (the hydraulic resistance of each section) on the maldistribution and pumping requirements can be isolated from complex pressure drop correlations.

In vector \mathbf{S} , the two inlet flow rate variables ($Q_{A1,1}$, $Q_{A2,1}$) can be written in terms of the total flowrates in the main channels and the inlet flow rate ratio of the two phases, as follows:

$$Q_T = Q_{T,1ch}N = Q_{A1,1} + Q_{A2,1} \quad (3-15)$$

$$r = \frac{Q_{A1,1}}{Q_{A2,1}} \quad (3-16)$$

Where Q_T , $Q_{T,1ch}$, and r , are the total inlet flow rate, the total flow rate in one main channel (assuming perfect distribution) and the ratio of the inlet flowrates, respectively. Both $Q_{T,1ch}$ and r are independent of N which makes them more suitable for the scale-out studies of double manifolds than $Q_{A1,1}$ and $Q_{A2,1}$. From the above:

$$Q_{A1,1} = Q_T \frac{r}{r+1} = Q_{T,1ch}N \frac{r}{r+1} \quad (3-17)$$

$$Q_{A2,1} = Q_T \frac{1}{r+1} = Q_{T,1ch}N \frac{1}{r+1} \quad (3-18)$$

Both inlet flow rates, the only non-zero elements in \mathbf{S} , have Q_T (or $Q_{T,1ch}N$) as a factor, therefore Eq. 3-13 can be nondimensionalised dividing by Q_T (or $Q_{T,1ch}N$).

Matrix \mathbf{R} has as many variables as there are channels in the manifold. In what follows, in each of the different manifold sections (distribution of the single phases, barrier, main, collection) the channels are assumed to have the same resistance. In this case, the number of variables is reduced from $6N+3$ (one for the number of main channels, two for the inlet flow rate of each phase and $6N$ for each resistor) to 7 variables ($N, Q_T, r, R_A, R_B, R_R, R_C$). Furthermore, if the collection section is not included ($R_C=0$), as is the case when the output of each main channel is collected separately, one less variable is needed. Additionally, it follows from Eqs. 3-11 and 3-12 that only the ratios of resistances are necessary, which eliminates one more variable. Thus, 5 input variables are necessary to use the model under these assumptions, namely N, Q_T (or $Q_{T,1ch}$), $r, R_B/R_R$, and R_A/R_R (or any other combination of the resistance ratios). Of these input variables, R_A and R_B are the design variables of the double manifold; the rest of the variables depend on the throughput required and the requirements of the process in the single channel. The resistance network model and the flow maldistribution characterisation are studied with an in-house built Matlab code.

3.2.1.1 Solution to non-linear pressure drop in the double manifold

In order to solve for \mathbf{Q} in Eq. 3-13, \mathbf{R} and \mathbf{S} must be independent of all the elements in \mathbf{Q} . As described above, solving for this case helps to elucidate the relationships between \mathbf{R}, \mathbf{S} , and \mathbf{Q} ; and this is investigated thoroughly in Chapter 5. However, in general, some elements in \mathbf{R} may depend on some elements in \mathbf{Q} . This section presents the iterative method applied to solve this general, nonlinear case.

The hydraulic resistances of the A and B sections, where there are only single-phase flows, may depend on the flow rate due to changes in height (hydrostatic pressure) or, at high Reynolds numbers, due to bends, contractions and expansions. The hydraulic resistance of the R section with a two-phase flow is expected to depend on the flow rate and the flow rate ratio of the phases in each channel. Furthermore, the mixing section leading to the R section will also have a pressure drop associated to it due to the acceleration of the flow and a Young-Laplace effect because the interface is formed and

deformed in this point of the contactor. The hydraulic resistance of the mixing section can be attributed to the R section. Since resistances in series are additive, the hydraulic resistance for each section (A1, A2, B1, B2, and R) are the sum of the linear and nonlinear effects.

In order to solve for \mathbf{Q} using an iterative method, an initial estimate is needed. One alternative is to use the ideal distribution as the initial estimate (\mathbf{Q}_{ideal}). In nonlinear systems with large maldistribution, this may not give accurate results. The second alternative is to use \mathbf{Q}_{ideal} to calculate \mathbf{R} and subsequently use this matrix to solve Eq. 3-13 and obtain the initial estimate. This method to calculate an initial estimate is more robust and more likely to lead to accurate results. This method is used in Chapter 6 where the empirical, nonlinear pressure drop model for segmented flow is used to design a double manifold prototype.

3.2.2 Correlated maldistribution characterisation

The most common metrics of flow distribution used in single-phase flow distributors are shown in Table 3-3, where Q_j is the flow rate in the j-th channel, \bar{Q} is the mean flow rate, and N is the number of parallel channels. The coefficient of variation (CV), defined as the standard deviation of the flowrates relative to the mean, is the most common maldistribution metric. The mean value of the flow rate (\bar{Q}) (also termed nominal or design flow rate) plays an important role because it is the flow rate all channels should have if the flow is perfectly distributed.

Table 3-3 Examples of single-phase flow maldistribution metrics.

Maldistribution equation	Measure of dispersion	References
$\frac{\sum Q_j - \bar{Q} }{N\bar{Q}}$	Mean absolute deviation	[136]
$\frac{\max(Q_j) - \min(Q_j)}{\max(Q_j)}$	Range relative to maximum	[113]
$\frac{\max(Q_j) - \min(Q_j)}{\bar{Q}}$	Range relative to mean	[106,137]
$\frac{\sqrt{\frac{1}{N} \sum (Q_j - \bar{Q})^2}}{\bar{Q}}$	Coefficient of variation (CV)	[105,111,113,138–143]

Single-phase maldistribution metrics must be modified before they can be applied to two-phase cases. In addition to the overall flowrate, the ratio of the flow rates of the two phases is also important. Previous works have only reported the CV of one of the phase flow rates, of the total flow rate, of the bubble velocity in plug flows [49,120] or of both phase flow rates [122,144–146]. These metrics are not sufficient in the multiphase cases because they do not consider the maldistribution of the ratio of the phases.

The maldistribution in the flow of two immiscible and incompressible phases is studied here with a method derived from principal component analysis (PCA), a common statistical approach for multivariate data [147]. Following this analysis, all factors affecting maldistribution can be studied with the least number of variables. To completely characterise the dispersion of a two-variable system, in this case, the maldistribution of two fluids in parallel channels, a 2x2 covariance matrix is required. The covariance matrix (Σ) for a bivariate distribution, shown in Eq. 3-19, is a symmetric matrix with both variances (σ_1^2, σ_2^2) and the covariance terms ($\text{cov}(1,2), \text{cov}(2,1)$) in the two diagonals.

$$\Sigma = \begin{bmatrix} \sigma_1^2 & \text{cov}(2,1) \\ \text{cov}(1,2) & \sigma_2^2 \end{bmatrix} \quad (3-19)$$

$$\sigma_i^2 = \frac{1}{N} \sum_{j=1}^N (Q_{j,i} - \bar{Q}_i)^2 \quad (i=1, 2) \quad (3-20)$$

$$\text{cov}(1,2) = \text{cov}(2,1) = \frac{1}{N} \sum_{j=1}^N (Q_{j,1} - \bar{Q}_1)(Q_{j,2} - \bar{Q}_2) \quad (3-21)$$

$$\rho = \frac{\text{cov}(1,2)}{\sigma_1 \sigma_2} = \frac{\text{cov}(2,1)}{\sigma_1 \sigma_2} \quad (3-22)$$

where N is the number of the parallel channels of the manifold, $Q_{j,i}$ is the flow rate of the i-th phase in the j-th channel, and \bar{Q}_i is the average or nominal flow rate of the i-th phase in the channels. Σ can be calculated given the flow rate of each phase in every channel of the manifold (the $Q_{j,i}$ data). The correlation coefficient (ρ), defined in Eq. 3-22, is a dimensionless number calculated as the ratio of the covariance term and the product of the standard deviations of the two variables, σ_1 and σ_2 . It follows from the symmetry of Σ that three scalar variables are necessary to characterise the maldistribution completely.

According to PCA the eigenvalues and eigenvectors of Σ are first calculated and then used to define new variables that best describe the dispersity of the data; these new variables are linked to the physical properties of the system. Eigenvalues satisfy the characteristic equation, $\det(\Sigma - \lambda \mathbf{I}) = 0$; and eigenvectors satisfy the eigenvalue equation $(\Sigma - \lambda \mathbf{I})\mathbf{v} = \mathbf{0}$, where \mathbf{I} is the identity matrix. The eigenvalues, the eigenvector slope (m), and the angle of correlation of the variables (θ) are calculated as follows:

$$\lambda_{1,2} = \frac{\sigma_1^2 + \sigma_2^2 \pm \sqrt{(\sigma_1^2 - \sigma_2^2)^2 + 4\rho^2 \sigma_1^2 \sigma_2^2}}{2} \quad (3-23)$$

$$m = \tan \theta = \frac{\lambda_1 - \sigma_1^2}{\rho \sigma_1 \sigma_2} \quad (3-24)$$

If $|\rho|$ is small (i.e. < 0.05), Σ is approximated by a diagonal matrix (elements outside the main diagonal are insignificant) and the flow rates of each phase are uncorrelated. It follows from Eq. 3-23 that the eigenvalues are equal to the variances and in this case, two CVs, as defined by Eq. 3-25, can completely characterise the maldistribution in the flow distributor.

$$CV_i = \frac{\sigma_i}{Q_i} \quad (i=1, 2) \quad (3-25)$$

However, if $|\rho|$ is not small, the flow rates of the two phases are correlated. In this case, λ_1 , λ_2 , and m , characterise maldistribution. In order to have a dimensionless measure of the maldistribution, the rotated coefficient of variation (RCV) is defined (Eq. 3-26), which is analogue to CV in Eq. 3-25.

$$RCV_i = \frac{\sqrt{|\lambda_i|}}{Q_i} \quad (i=1, 2) \quad (3-26)$$

The eigenvector slope defined in Eq. 3-24 is related to the ratio of flow rates of both phases. The closer the value of m is to the value of the ratio, the better the fluids are distributed with respect to the flow rate ratio. Eq. 3-27 defines the phase ratio maldistribution descriptor (PRM).

$$PRM = 1 - \frac{m}{\frac{Q_2}{Q_1}} \quad (3-27)$$

PRM measures how different the eigenvector slope and the design phase ratio are. It tends to zero as the two values approach each other.

There is an extreme case for correlated flow rates. When $|\rho|$ is close to unity (i.e. >0.95), the flow rate distribution of the two phases is highly correlated. In this situation, λ_2 and RCV_2 are very small, and only RCV_1 , and PRM are necessary to describe the maldistribution. For the highly correlated case, the two descriptors can be interpreted as follows:

- RCV_1 indicates the maldistribution of the total flow rate in each of the parallel channels, independently of the ratio of the phases.
- PRM indicates the differences in the phase ratio in the parallel channels from the required ratio. PRM is independent of the total flow rate in each channel and its maldistribution.

Three possibilities of correlation are illustrated in Fig. 3-9 in a map of flow rates, with Q_1 and Q_2 as coordinates. Fig. 3-9a shows an uncorrelated case where maldistribution is quantified with the standard deviations, nondimensionalised as shown

in Eq. 3-25. Fig. 3-9b shows a correlated case with both eigenvectors shown. Both eigenvalues and the eigenvector slope, nondimensionalised with Eqs. 3-26 and 3-27, are used to measure maldistribution in this case. In Fig. 3-9c, a highly correlated case is presented and the points nearly form a line segment. Only one eigenvalue and the eigenvector slope are needed to quantify maldistribution in this case.

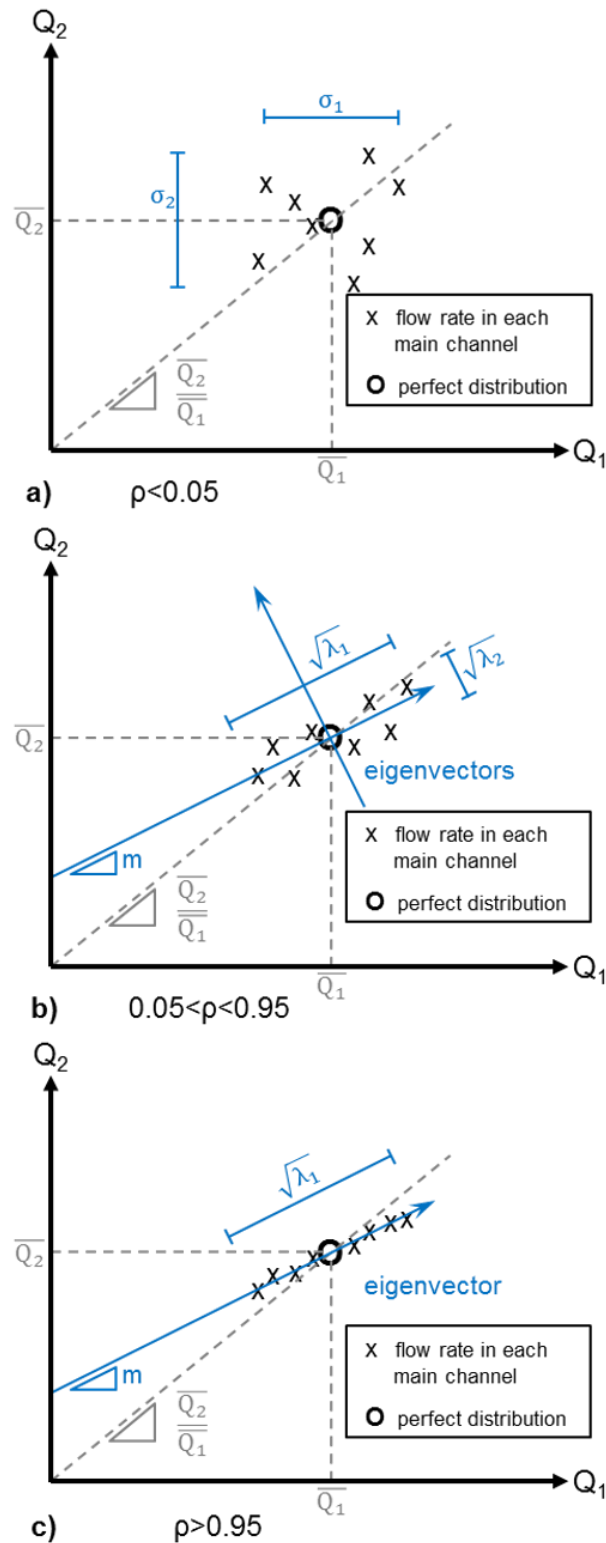


Figure 3-8 Geometric interpretation of the maldistribution descriptors in flow rate maps. a) Distribution with no correlation and the maldistribution is measured with standard deviations (Eq. 3-25). b) Correlated case where the eigenvalues and the eigenvector slope are used to measure the maldistribution (Eqs. 3-26 and 3-27). c) Highly correlated distribution where the points nearly form a line segment; the length and slope of this line segment describe the maldistribution (Eqs. 3-26 and 3-27).

The analysis above describes a novel and rigorous way to measure maldistribution of two fluids in parallel channels. The three cases, dependant on the correlation coefficient, are summarised in Table 3-4.

Table 3-4 Maldistribution cases and descriptors with respect to the correlation coefficient.

Maldistribution Case	Correlation Criteria	Maldistribution Descriptors
Uncorrelated	$ \rho < 0.05$	CV_1, CV_2
Correlated	$0.05 < \rho < 0.95$	RCV_1, RCV_2, PRM
Highly correlated	$ \rho > 0.95$	RCV_1, PRM

In addition to the methodology above, $\bar{Q}_1, \bar{Q}_2, \lambda_1, \lambda_2,$ and θ can be used to calculate confidence ellipses in flow rate maps. This 2-dimensional confidence interval is centred in (\bar{Q}_1, \bar{Q}_2) and is tilted at an angle θ . The major and minor axes lengths, a and b respectively, depend on the eigenvalues and the degree of confidence selected. The axes lengths are proportional to the square root of the chi-squared critical value.

$$a = 2\sqrt{5.991 \lambda_1} \quad (3-28)$$

$$b = 2\sqrt{5.991 \lambda_2} \quad (3-29)$$

For a confidence of 95%, the chi-squared critical value for 2 degrees of freedom is 5.991 [148]. The confidence ellipse together with the flow rate map of the particular system can be used to define the maximum tolerable maldistribution of the system.

If the flowrates Q_{ji} can be measured before the fluids are mixed together then the statistical analysis above can also be applied to miscible fluids. In some cases, it may be more useful to use mass flow rates rather than volumetric flow rates.

4 Studies of segmented flow for multiphase processing applications

4.1 Introduction

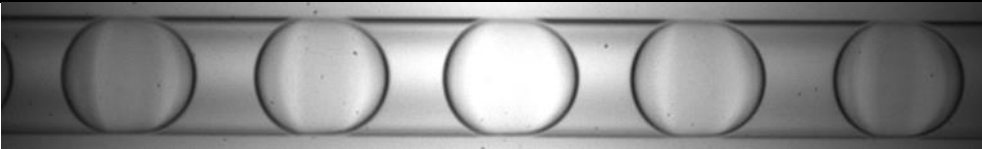
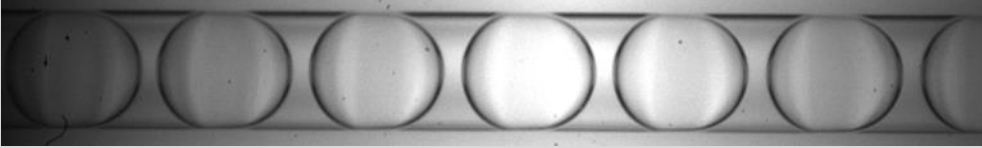
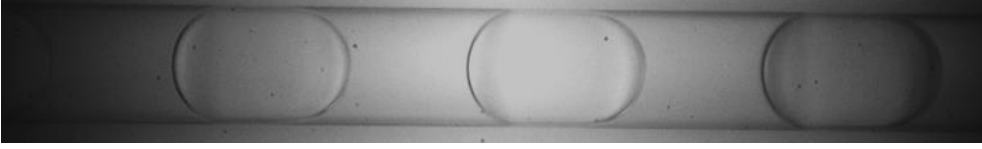
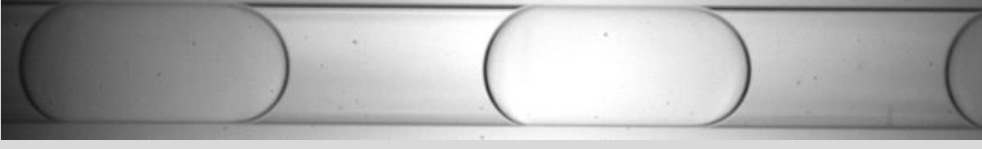


In this chapter, the hydrodynamics and mass transfer during the extraction of uranyl nitrate in tributyl phosphate (TBP) solutions, relevant to spent nuclear fuel reprocessing, are investigated in small circular channels with diameters varying over a large range from 1 to 4 mm. For all the conditions investigated, segmented flow establishes in the channels. The effects of design and operational parameters such as TBP concentration, flow rate ratio, channel diameter and mixture velocity on the hydrodynamic characteristics and on the extraction performance are investigated. Images of various flow conditions are presented. Then, correlations based on dimensionless numbers are proposed for the main hydrodynamic parameters, including plug/slug/unit lengths, holdup, interfacial area and pressure gradient. The extraction efficiency and mass transfer coefficients are measured and further compared against those from conventional contactors. A simplified numerical model was able to predict the mass transfer in segmented flow reasonably well. The findings show that segmented flow contactors have high mass transfer rates, while, importantly, they can accommodate fluids with different properties; in the case of uranyl nitrate extraction, pure TBP can be used as extractant instead of the conventional TBP solution in an organic phase, which improves significantly the mass transfer.



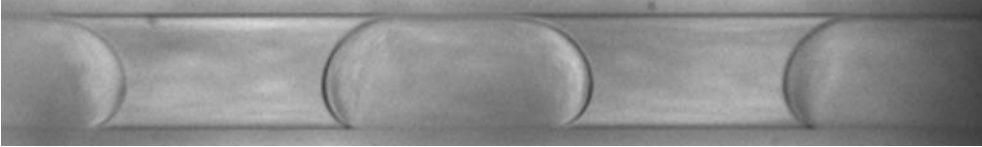

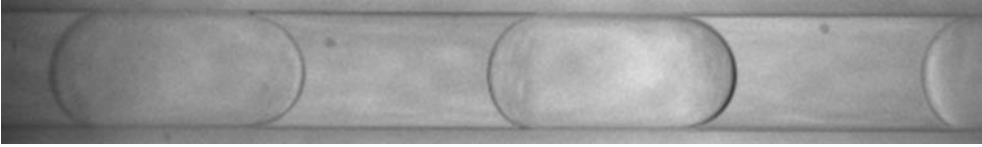
4.2 Hydrodynamic features of segmented flow

The experimental results of plug and slug lengths under various conditions are presented here. This section includes the photographs of the segmented flow pattern under a range of conditions. Furthermore, the plug and slug lengths are measured in the full-factorial design described in section 3.1 and the data are analysed based on the Buckingham theorem below.

The photographs of segmented flow under several flow conditions are presented in Table 4-1. The photographs are scaled to be of the same size, so channels of different sizes appear to have the same diameter. Several effects are noticeable. The effect of u_{mix} can be seen by comparing lines #4 and #5. The increase in velocity, with all other parameters constant, makes both the plugs and slugs shorter while the plugs acquire a bullet-like shape. The effect of high TBP concentration, thus high continuous phase viscosity and density, and decreased interfacial tension can be noted by comparing pairs #1-#3, #4-#8, and #9-#11. The effects on plug length or unit length are neither strong nor homogeneous, this indicates the effect of using TBP 100%, which introduces changes to several properties simultaneously, is more easily discerned with dimensional analysis. The effect of flow rate ratio, expressed here as the continuous organic phase flow rate fraction, can be noted by comparing groups #1-#2, #4-#6-#7, and #9-#10. In the 2 mm and 4 mm channel cases (#4-#6-#7 and #9-#10, respectively), the effect of reducing the organic phase flow rate fraction is to elongate the dispersed phase plugs while the slugs shorten. In the 1 mm case (#1-#2) it appears as the plugs have roughly the same size while the slugs are shorter when the organic phase flow rate fraction is lower. Finally, the diameter effect can be noted across several experiments, for example by comparing the results in groups #1-#4-#9. Relative to the diameter, the plugs and slugs are longer for the 2 and 4 mm cases than the 1 mm case. The 2 mm and 4 mm cases give similar plug and slug lengths, relative to the diameter, according to the images. The next step is to analyse the measured lengths and suggest relationships that encompass these effects.

Table 4-1 Stills of segmented flow pattern observed. The aqueous phase is the dispersed phase and the organic phase is the continuous phase. Different diameter, organic phase composition, mixture velocity and phase ratio.

#	d / mm	Organic phase	u_{mix} / cm s ⁻¹	Q_c/Q_T	Image
1	1	TBP 30%	1.06	0.500	
2	1	TBP 30%	1.06	0.333	
3	1	TBP 100%	1.06	0.500	
4	2	TBP 30%	1.06	0.500	
5	2	TBP 30%	4.24	0.500	
6	2	TBP 30%	1.06	0.333	

7	2	TBP 30%	1.06	0.250	
8	2	TBP 100%	1.06	0.500	
9	4	TBP 30%	1.06	0.500	
10	4	TBP 30%	1.06	0.333	
11	4	TBP 100%	1.06	0.500	

From the experimental data, the dimensionless plug length (L_p/d) and the slug length fraction ($1-L_p/L_u$) were found to best correlate with the following dimensionless numbers: the continuous (organic) phase flow rate fraction (Q_c/Q_T), the dispersed to continuous phase viscosity ratio (μ_d/μ_c), the capillary number based on the continuous phase ($Ca_c=\mu_c u_{mix}/\gamma$), and the ratio of the Reynolds ($Re_c=\rho_c u_{mix}d/\mu_c$) and capillary numbers of the continuous phase ($Re_c/Ca_c=\rho_c \gamma d/\mu_c^2$). Eqs. 4-1 and 4-2 present the correlations and Table 4-2 lists the coefficients with 95% confidence intervals, the R^2 of the regressions and the range of the input variables. The measured ranges of L_p/d and $1-L_p/L_u$ are [1.36 – 5.60] and [0.576 – 0.879], respectively.

$$\ln\left(\frac{L_p}{d}\right) = a_1 + a_2 \ln\left(\frac{Q_c}{Q_T}\right) + a_3 \ln\left(\frac{\mu_d}{\mu_c}\right) + a_4 \ln(Ca_c) + a_5 \ln\left(\frac{Re_c}{Ca_c}\right) \quad (4-1)$$

$$\ln\left(1 - \frac{L_p}{L_u}\right) = b_1 + b_2 \ln\left(\frac{Q_c}{Q_T}\right) + b_3 \ln\left(\frac{\mu_d}{\mu_c}\right) + b_4 \ln(Ca_c) \quad (4-2)$$

Table 4-2 Regression results and range of variables for Eqs. 4-1 and 4-2. The confidence intervals correspond to 95%. The range of Re_c is added for reference.

Coefficient	a	b	Variable range
1	-2.56±0.65	-0.82±0.39	-
2 (Q_c/Q_T)	-0.872±0.063	1.181±0.038	0.200 – 0.500
3 (μ_d/μ_c)	-0.36±0.15	-0.099±0.089	0.2160 – 0.4264
4 (Ca_c)	-0.280±0.069	-0.130±0.042	2.406×10^{-3} – 2.396×10^{-2}
5 (Re_c/Ca_c)	0.099±0.061	-	395.9 – 6602
Re_c	-	-	2.371 – 63.53
R^2	0.944	0.983	

The variables with the lowest relative confidence intervals in both Eqs. 4-1 and 4-2 are Q_c/Q_T and Ca_c . As less dispersed phase is added (higher Q_c/Q_T), the plugs become shorter (lower L_p/d). The effect of the capillary number is explained by the forces at the inlet; higher Ca_c implies higher velocity at the T-junction that tends to break the forming plugs with higher frequency. The viscosity ratio is important for L_p/d but not as

important for L_p/L_u , while the effect of Re_d/Ca_c , for the ranges investigated, is small but not negligible. The goodness-of-fit for both regressions is shown in Figs. 4-1 and 4-2. Most experimental results are contained within 20% of the predicted values. These results were obtained using two fluids pairs, namely, water-TBP 30% and water-TBP 100%, and the regression coefficients should be applied cautiously to other fluid systems. However, the overall dependencies of the lengths from the input variables will likely hold for geometrically similar systems (T-junctions and circular channels). Empirical correlations are most useful from a design perspective but also serve as an important benchmark to first-principles models which should aim to predict the hydrodynamic characteristics of liquid-liquid segmented flows at least with the same accuracy as empirical models.

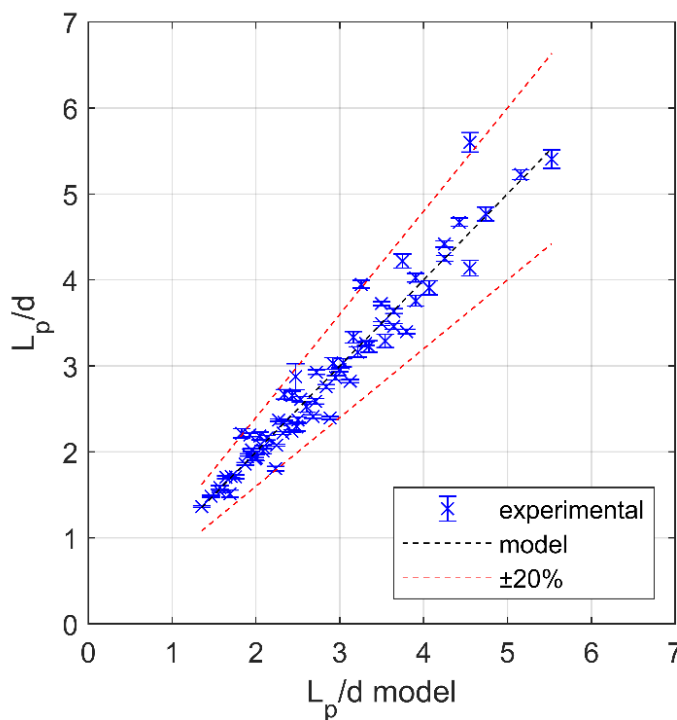


Figure 4-1 L_p/d predicted from Eq. 4-1 against experimental results with 20% bands for all cases studied.

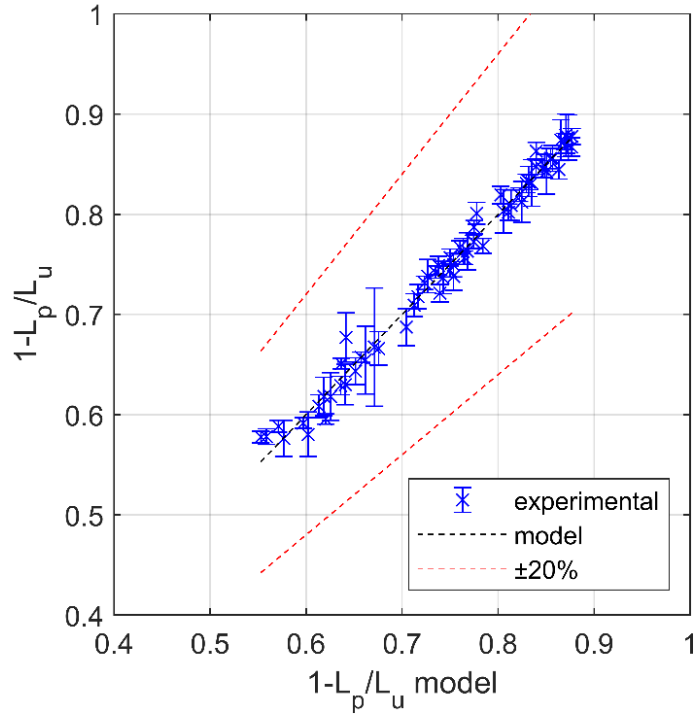


Figure 4-2 (1-L_p/L_u) predicted from Eq. 4-2 against experimental results with 20% bands for all cases studied.

In segmented flow, the unit length (L_u), defined as the length of a plug and a slug, is an important variable. In Eq. 4-3, derived from Eqs. 4-1 and 4-2, L_u/d is given as a function of Q_c/Q_T , μ_d/μ_c , Ca_c and Re_c/Ca_c . Fig. 4-3 shows the dependence of L_u/d on Ca_c , and therefore u_{mix} for similar flowrates but different organic phases, and therefore different μ_d/μ_c and Re_c/Ca_c . L_u/d decreases as Ca_c (and u_{mix}) increases for both organic phases. For a given Ca_c , L_u/d is lower for the less viscous continuous phase (TBP 30% in this case). Similarly to the L_p/d case explained above, a higher velocity at the T-junction breaks the forming plugs with higher frequency resulting in shorter units (lower L_u/d). Since L_u/d is estimated by combining two correlations, the errors can be compounded and a loss of accuracy is expected.

$$\frac{L_u}{d} = \left(\frac{Re_c}{Ca_c}\right)^{0.099} \frac{0.077}{\left(\frac{Q_c}{Q_T}\right)^{0.872} \left(\frac{\mu_d}{\mu_c}\right)^{0.36} Ca_c^{0.28-0.44} \left(\frac{Q_c}{Q_T}\right)^{2.05} \left(\frac{\mu_d}{\mu_c}\right)^{0.26} Ca_c^{0.15}} \quad (4-3)$$

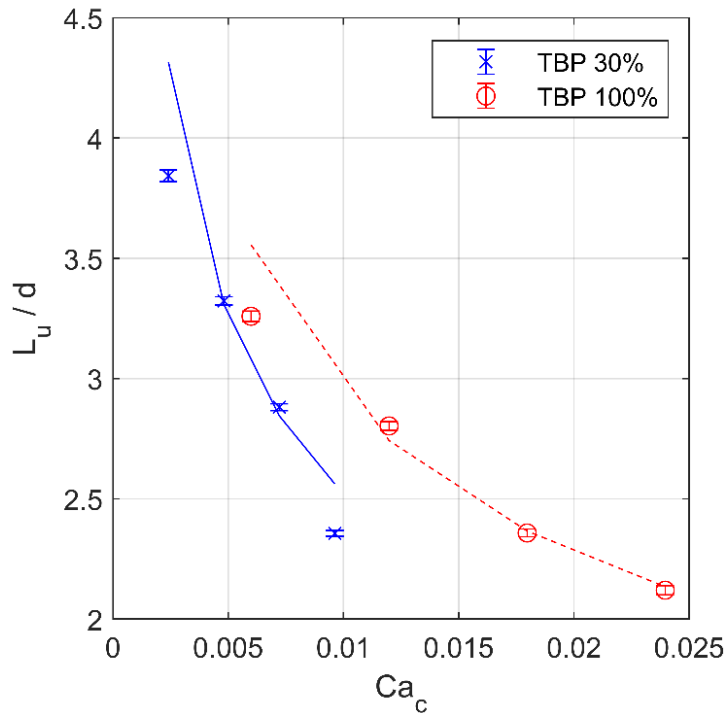


Figure 4-3 Experimental and predicted (Eq. 4-3) L_u/d dependence from Ca_c . For all cases, $Q_d/Q_T=0.5$, $d=2$ mm, $u_{mix} = [1.06, 2.12, 3.18, 4.24]$ cm s⁻¹. Results for TBP 30% have $Re_d/Ca_c=3301$, $\mu_d/\mu_c=0.426$ (continuous line). Results for TBP 100% have $Re_d/Ca_c=792$, $\mu_d/\mu_c=0.216$ (dashed line).

A number of correlations have previously been given in the literature for L_p/d in liquid-liquid segmented flows which have the form of Eq. 4-4 (section 2.3). These are summarised in Table 4-3. The correlations by Gartstecki et al. and Prilezski et al. have an additive constant (c_1) in Eq. 4-4. The power-law term includes the effect of the flow rate ratio ($(Q_d/Q_c)^{c_3}$), the capillary number ($Ca_c^{c_4}$) (which includes the effect of velocity), and another factor which may account for the effects of viscosities and the of the channel diameter (c_2). For gas-liquid systems, Haase reviewed several L_p/d correlations [72].

$$\frac{L_p}{d} = c_1 + c_2 \left(\frac{Q_d}{Q_c} \right)^{c_3} Ca_c^{c_4} \quad (4-4)$$

Table 4-3 Summary of constants and adjustable parameters for Eq. 4-4 according to published correlations for liquid-liquid systems. d_h is the hydraulic diameter of the square channels.

Reference	Notes	c_1	c_2	c_3	c_4
Garstecki et al. [65]	T-junction Rectangular section $d_h=40-88 \mu\text{m}$	1	Parameter ≈ 1	1	0
Fu et al. [66]	Flow focusing inlet Rectangular section $d_h=400-600 \mu\text{m}$	0	Parameter 0.72 for $L_p/d < 2.35$; 0.30 for $L_p/d > 2.35$	Parameter 0.14 for $L_p/d < 2.35$; 0.23 for $L_p/d > 2.35$	Parameter -0.19 for $L_p/d < 2.35$; -0.42 for $L_p/d > 2.35$
Prilezski et al. [67]	T-junction Rectangular channels $d_h=33 \mu\text{m}$	Parameter 1.44	$f(\mu_d)$ $1.72/\mu_d$	1	0
Li & Angeli [68]	T-junction Circular section $d=200-500 \mu\text{m}$	0	Parameter 0.757	Parameter 0.512	Parameter -0.273
Tsaoulidis & Angeli [34]	T-junction Circular section $d=0.5-2 \text{ mm}$	0	$f(\text{Re}_c/\text{Ca}_c)$ $2.2882 \times (\text{Re}_c/\text{Ca}_c)^{-0.5017}$	u_c/u_{mix} instead of Q_d/Q_c $(u_c/u_{\text{mix}})^{-0.9634}$	Parameter -0.2289
Cao et al. [64]	Cross-junction Rectangular section $d_h=200-600 \mu\text{m}$	0	$f(\text{Re}_d/\text{Ca}_d)$ $0.55 \times (\text{Re}_d/\text{Ca}_d)^{-0.05}$	Parameter 0.66	Ca_d instead of Ca_c -0.33
This work	T-junction Circular section $d=1-4 \text{ mm}$	0	$f(\text{Re}_c/\text{Ca}_c, \mu_d/\mu_c)$ $0.0773 \times (\text{Re}_c/\text{Ca}_c)^{0.099} \times (\mu_d/\mu_c)^{-0.36}$	Q_c/Q_T instead of Q_d/Q_c $(Q_c/Q_T)^{-0.872}$	Parameter -0.28

The values of the adjusted parameters summarised in Table 4-3 differ because they are obtained for different fluids, geometries and flowrates. However, certain trends can be identified. The effect of increasing Ca_c , and thus u_{mix} , is to shorten the plugs because the parameter c_4 is between -0.42 and 0 (Cao et al. use the dispersed phase superficial velocity to define Ca_d but, at fixed Q_d/Q_c , changes in u_{mix} are reflected in the variations of Ca_d [64]). In addition, increasing the flow rate of the dispersed phase elongates the plugs (positive exponent in Q_d/Q_c or negative exponent in u_c/u_{mix} or Q_c/Q_T). Finally, the dependence of L_p/d on the channel diameter is found to have an exponent less than 0.1 for most cases except in the results by Tsaoulidis & Angeli [34] where L_p/d

$\propto d^{0.5}$. To the best of the author's knowledge, there are no available correlations for L_s or L_u for liquid-liquid segmented flow contactors.

The above results will be used to derive correlations for the dispersed phase in-situ volume fraction (hold up, ε_d), important for calculating the equilibrium concentrations and the mass transfer coefficient. It was found that the plug and slug lengths did not vary significantly along the test channels. This is usually the case in liquid-liquid flows even when there is mass transfer since the fluids are incompressible and the volumes of the plugs and slugs do not vary significantly along the channel. To estimate the dispersed phase volume fraction, the shape of the plugs is approximated by a cylinder with hemispherical caps at the end; the film thickness is thus considered constant. The holdup can be estimated from Eqs. 4-5 and 4-6 where ε_d^{\max} is an upper limit for the holdup when the film thickness is infinitesimally small. Further details regarding the derivation of the holdup is presented in Appendix 2. ε_d^{\max} is, thus, only a function of plug and unit lengths, while ε_d (Eq. 4-6) depends on the film thickness as well.

$$\varepsilon_d^{\max} = \frac{L_p}{L_u} - \frac{d}{3L_u} \quad (4-5)$$

$$\varepsilon_d = \left(1 - 2\frac{\delta}{d}\right)^2 \varepsilon_d^{\max} \quad (4-6)$$

In Eq. 4-6, δ is the film thickness, which can be calculated from correlations or measured; it was not obtained in this study as it would require images with higher resolution to the ones used. For the range of conditions and the properties of the liquids used, the correlation by Mac Giolla Eain et al. can be applied (Eq. 4-7) [69]. The correlation is given by the authors in terms of $Ca_c (= \mu_c u_{\text{mix}} / \gamma)$ and $We_c (= Re_c Ca_c = \rho_c u_{\text{mix}}^2 d / \gamma)$ and is also written in Eq. 4-7 in terms of Ca_c and $Re_c / Ca_c (= \rho_c \gamma d / \mu_c^2)$ to show explicitly the effect of velocity. The factor $(1 - 2\delta/d)^2$ that appears in Eq. 4-6 varies between 0.83 and 0.95 for all the experimental conditions tested.

$$\frac{2\delta}{d} = 0.35 Ca_c^{0.354} We_c^{0.097} = 0.35 Ca_c^{0.548} \left(\frac{Re_c}{Ca_c}\right)^{0.097} \quad (4-7)$$

The specific interfacial area (a), defined as the interfacial area per unit volume of the contactor, is also used in the calculation of the mass transfer coefficient and is not easily measured. Considering the plug shape discussed above, the specific interfacial area can be calculated from Eqs. 4-8 and 4-9, with extended derivation details available in Appendix 2. As with the holdup, $a^{\max} \times d$ is derived considering infinitesimally small film thickness and depends only on the plug and slug lengths while a (Eq. 4-9) requires the film thickness as well. For the conditions studied the factor $(1-2\delta/d)$ varies between 0.91 and 0.97.

$$a^{\max} \times d = 4 \frac{L_p}{L_u} \quad (4-8)$$

$$a = \left(1 - 2 \frac{\delta}{d}\right) a^{\max} \quad (4-9)$$

Eqs. 4-1 and 4-2 can be substituted in Eqs. 4-5 and 4-8 to provide estimations for ε_d^{\max} and a^{\max} (Eqs. 4-10 and 4-11). These equations have multiple terms but the overall effect of each dimensionless number can still be analysed. In the case of the maximum holdup, Q_c/Q_T , μ_d/μ_c , and Ca_c correlate negatively, while Re_c/Ca_c correlates positively. On the other hand, $a^{\max} \times d$ increases with Ca_c and μ_d/μ_c but decreases as Q_c/Q_T increases. The only term in both equations that depends on the channel size is Re_c/Ca_c ; ε_d^{\max} has a small and positive dependence on d while $a^{\max} \times d$ is independent of the channel size.

$$\begin{aligned} \varepsilon_d^{\max} = 1 - 4.3 \left(\frac{Q_c}{Q_T}\right)^{0.872} \left(\frac{\mu_d}{\mu_c}\right)^{0.36} \left(\frac{Re_c}{Ca_c}\right)^{-0.099} Ca_c^{-0.280} - 0.44 \left(\frac{Q_c}{Q_T}\right)^{1.18} \left(\frac{\mu_d}{\mu_c}\right)^{-0.099} Ca_c^{-0.130} + \\ 1.89 \left(\frac{Q_c}{Q_T}\right)^{1.03} \left(\frac{\mu_d}{\mu_c}\right)^{0.26} \left(\frac{Re_c}{Ca_c}\right)^{-0.099} Ca_c^{-0.41} \end{aligned} \quad (4-10)$$

$$a^{\max} \times d = 4 - 1.8 \left(\frac{Q_c}{Q_T}\right)^{1.18} \left(\frac{\mu_d}{\mu_c}\right)^{-0.099} Ca_c^{-0.130} \quad (4-11)$$

4.3 Pressure gradient in segmented flow

Pressure drop is an important parameter for the design of segmented flow contactors that can be used to calculate pumping requirements, to design flow distributors for scale-out (Chapter 5) and even to estimate plug or slug lengths, as

proposed by Kreutzer et al. [89], which is particularly useful in the case of non-transparent channels.

Several models to predict the pressure gradient for segmented flow pattern flows are reviewed in section 2.5. Among the limitations of the previous models, the range of input variables is mainly addressed here. Kreutzer et al. [89] and Mac Giolla Eain et al. [98] obtained their results using a single channel size each (2.3 and 1.59 mm respectively) while Jovanovic used two small channel sizes in a relatively narrow range (0.248 and 0.498 mm) [97]; this indicates that there is a need for a pressure drop model to be validated for large diameters and in a relatively wide range. Furthermore, there is a need to model the pressure gradient using readily available measurements, unlike the film thickness.

Previous numerical simulations have shown that in plug flow in circular channels the pressure profile followed the Hagen-Poiseuille equation, interrupted by periodic increases when plugs were present [68]. The periodicity of the pressure variation is used here to develop a new pressure gradient model for segmented flow contactors. In the model, the average pressure gradient in a tube with length L ($(\Delta p/L)_{\text{average}}$) with a fully developed segmented flow, is modelled as a periodic function with a period of L_u (Eq. 4-12) [149].

$$\left(\frac{\Delta p}{L}\right)_{\text{average}} = \frac{\int_0^L \left(\frac{\Delta p}{L}\right) dx}{\int_0^L dx} = \frac{1}{L_u} \int_0^{L_u} \left(\frac{\Delta p}{L}\right) dx \quad (4-12)$$

The full derivation of the two-phase pressure gradient model is presented in Appendix 1. The pressure gradient in a unit cell is composed of contributions from the plug and the slug sections (Eq. 4-13). The pressure gradient in the slug is calculated from the Hagen-Poiseuille equation. The contribution from the plug section $((\Delta p/L)_d)$ is unknown and captures the complex pressure losses in this region (including frictional and Laplace effects).

$$\left(\frac{\Delta p}{L}\right)_{\text{average}} = \frac{32\mu_c u_{\text{mix}}}{d^2} \left(1 - \frac{L_p}{L_u}\right) + \left(\frac{\Delta p}{L}\right)_d \frac{L_p}{L_u} \quad (4-13)$$

Eq. 4-13 can be written in dimensionless form (Eq. 4-14) with the definition of an overall friction factor ($f_u = (\Delta p/L)_{\text{average}} d / (\rho_c u_{\text{mix}}^2)$), a dispersed phase friction factor ($f_d = (\Delta p/L)_d d / (\rho_d u_{\text{mix}}^2)$), and a dispersed phase Reynolds number ($Re_d = \rho_d u_{\text{mix}} d / \mu_d$).

$$f_u Re_c = 32 \left(1 - \frac{L_p}{L_u}\right) + f_d Re_d \frac{L_p \mu_d}{L_u \mu_c} \quad (4-14)$$

Eqs. 4-13 and 4-14 have one degree of freedom and an additional equation is needed. From the experimental data the following empirical correlation was obtained for f_d :

$$f_d = 0.888 f_u^{1.046} \quad (4-15)$$

This correlation has an R^2 of 0.995 for the conditions presented in section 4-2. The coefficient and exponent have 95% confidence intervals of 2.3% and 1.6%, respectively.

By substituting Eq. 4-15 in Eq. 4-14, the following equation is obtained:

$$f_u Re_c = 32 \left(1 - \frac{L_p}{L_u}\right) + 0.888 f_u^{1.046} Re_d \frac{L_p \mu_d}{L_u \mu_c} \quad (4-16)$$

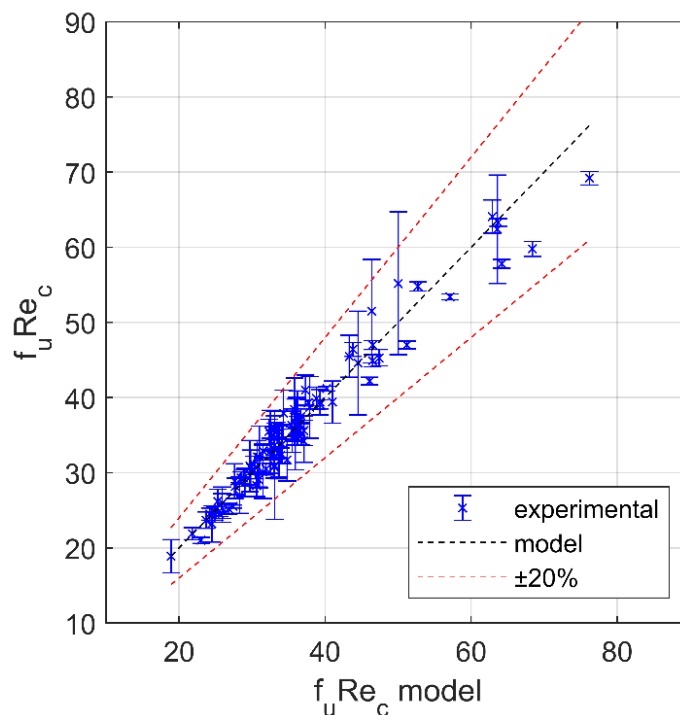


Figure 4-4 $f_u Re_c$ predicted from Eq. 4-16 and experimental results with 20% bands for all cases studied.

The experimental results are compared to the model in Fig. 4-4. The model described by Eq. 4-16 is implicit with respect to f_u and must be solved numerically given the Reynolds numbers for both phases, the length fraction of the plug and the viscosity ratio. This pressure drop model does not include the plug velocity or film thickness. Most of the other models show the capillary number explicitly. The model in Eq. 4-16 includes the dependence on the capillary number implicitly in the length fraction of the plug (Eq. 4-2). Eq. 4-16 accurately predicts the pressure drop for the ranges of Q_o/Q_T , μ_o/μ_d , Ca_c , and Re_c in Table 4-2. Different values of the coefficient and exponent in the calculation of the overall friction factor in Eq. 4-15 would be needed for conditions outside these values or for different inlet or channel geometries.

The effects of the test section diameter and of the operational variables on the pressure gradient are shown in Fig. 4-5. The average pressure gradient is proportional to d^{-2} , u_{mix}^1 , and μ_c^1 . In Eq. 4-16, the effect of the flow rate ratio is only captured in the plug length fraction, which strongly depends on Q_o/Q_T . Since the organic (continuous) phases are more viscous than the aqueous (dispersed) phase, reducing Q_o/Q_T results in lower pressure gradient, as shown in Fig. 4-5 c.

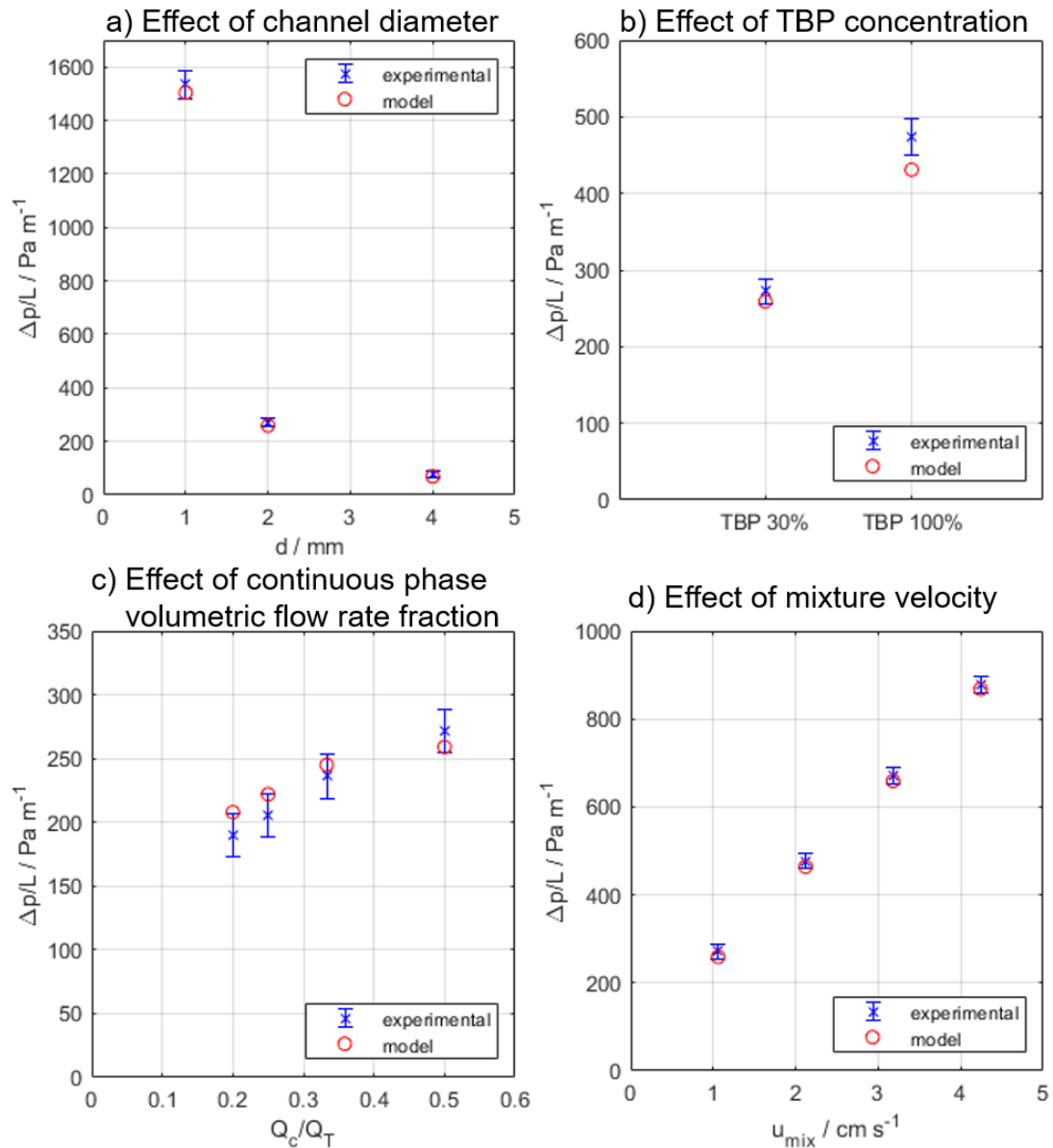


Figure 4-5 Pressure gradient (experimental and calculated using Eq. 4-16). The base case is $d=2$ mm, $u_{\text{mix}}=1.06$ cm s^{-1} , TBP 30%, $Q_c/Q_T=0.500$.

The experimental results are also compared to the predictions of the models by Kreutzer et al. [89] and Jovanovic et al. [97]. The model by Kreutzer et al. is fitted with regression analysis and the results are presented in Fig. 4-6. The adjustable parameters for this model give $a=0.034\pm 333\%$ and $b=0.22\pm 202\%$, where the percentages correspond to 95% confidence intervals. Kreutzer et al. had reported values of 0.17 and 0.07 for a and 0.33 for b [89].

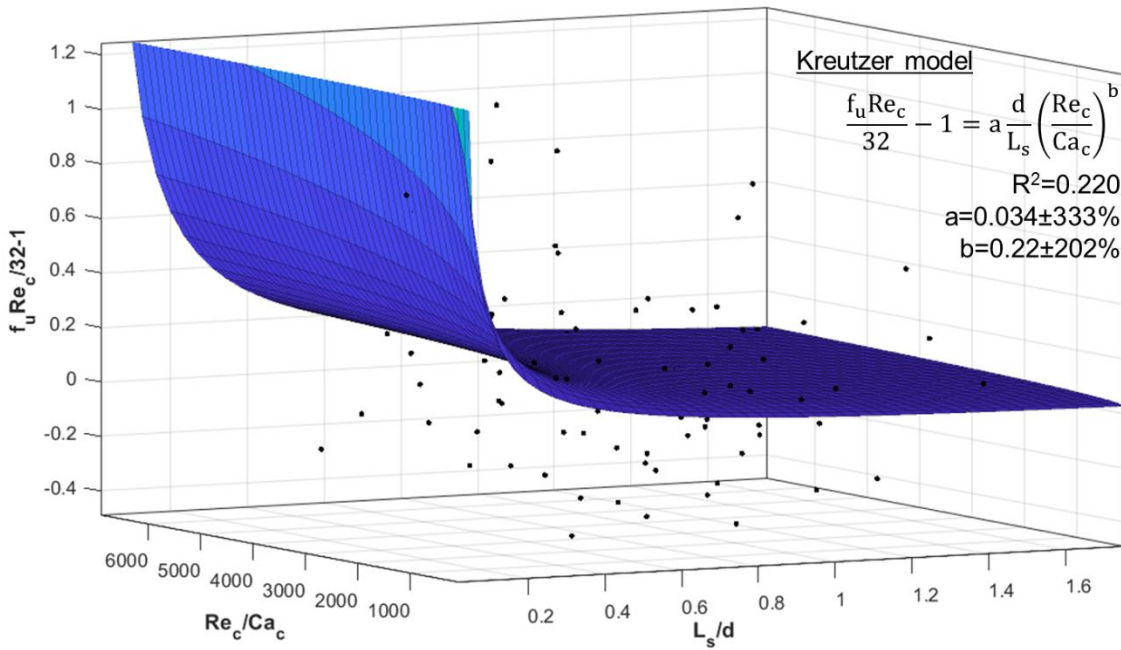


Figure 4-6 Adjusted Kreutzer model prediction (surface) and experimental results (points). The a and b parameters are adjusted with non-linear regression (using Matlab Curve Fitting); the intervals correspond to 95% confidence intervals.

The models by Jovanovic et al. are adjusted by fitting the curvature parameter (J); the best fit for J is $5.1 \pm 60\%$ and $5.9 \pm 51\%$ for the stagnant film and the moving film models, respectively (7.16 by Jovanovic et al. [97]); the percentages correspond to 95% confidence intervals. In order to use the model by Jovanovic et al., the film thickness is estimated from the model proposed by Mac Giolla Eain et al. [69] (Eq. 4-7) while u_p/u_{mix} is estimated from the correlation by Abiev et al. [71]. These additional estimations of δ and u_p have large uncertainties associated. In conclusion, the models by Kreutzer et al. and Jovanovic et al. are found to poorly predict the experimental pressure gradient results, especially when contrasted to the accuracy of the model presented in Eq. 4-16.

The plug length fraction can be directly calculated from Eq. 4-16 given the pressure gradient, the properties of the fluids, the channel diameter, the flow rate ratio of the two phases, and the mixture velocity. Therefore, the pressure gradient could be used to estimate $a^{max} \times d$ using Eq. 4-8. However the pressure gradient measurement alone is not sufficient to describe fully the segmented flow geometry, and an additional measurement is necessary to calculate L_p/d or L_u/d . A second measurement could be

the plug formation frequency obtained by analysing the pressure drop signal, as proposed by Miyabayashi et al. [150].

4.4 U(VI) extraction and mass transfer in segmented flow

contactors

4.4.1 Analysis of operation and design variables on extraction efficiency

The extraction results are presented here for the cases described in section 3.1. A base case is studied first ($d=2$ mm, $u_{\text{mix}}=1.06$ cm s⁻¹, TBP 30%, $Q_o/Q_T=0.5$) and then the effects of changes in certain parameters are investigated, including mixture velocity ($u_{\text{mix}}=4.24$ cm s⁻¹), channel size (1, 4 mm), TBP concentration (100%) and phase fraction ($Q_o/Q_T=0.333, 0.250$). The mixture velocity and internal channel diameter are considered because they impact the throughput of the process, the phase fraction determines the organic phase usage and the TBP concentration affects the equilibrium constants and the efficiency of the process.

The concentration in the aqueous phase at the exit ($C_{\text{aq}}^{\text{out}}$) is measured with UV-vis spectroscopy and the extraction efficiency (%Eff) is calculated according to Eq. 4-17. The extraction efficiency provides a measure of mass transferred relative to the maximum possible, in a given residence time.

$$\% \text{Eff} = \frac{C_{\text{aq}}^{\text{out}} - C_{\text{aq}}^{\text{in}}}{C_{\text{aq}}^{\text{eq}} - C_{\text{aq}}^{\text{in}}} \times 100\% \quad (4-17)$$

In the equation above, $C_{\text{aq}}^{\text{eq}}$ is the equilibrium concentration of U(VI) at the conditions of the experiment. $C_{\text{aq}}^{\text{eq}}$ is calculated using the inlet phase flowrate ratio rather than the in situ holdup because the flowrate ratio is the average volume ratio in the contactor. $C_{\text{aq}}^{\text{in}}$ and $C_{\text{aq}}^{\text{out}}$ are the concentrations of U(VI) at the inlet and at the outlet in the aqueous phase, respectively.

The effect on %Eff of increasing mixture velocity with respect to the base case, while keeping the other conditions constant, is presented in Fig. 4-7. For both mixture velocities, after 5 s residence time the extraction is above 40% efficiency. However, the

base case, at low u_{mix} , has a slow increase in %Eff, compared to the high u_{mix} case. With the higher mixture velocity, the extraction efficiency is >90% after 20 s of residence time, while in the base case the efficiency is below 80% for the same residence time. The increase in the extraction efficiency with mixture velocity is attributed to two phenomena, the increase in interfacial area and in circulation intensity in both the plugs and the slugs. The specific interfacial areas (estimated from Eq. 4-9 and the imaging results for water-TBP 30% at the same flow conditions) for the low and high u_{mix} cases are 1123 and 1224 m^{-1} , respectively. In addition, as the mixture velocity increases the circulation time in the plugs decreases leading to better mixing [70].

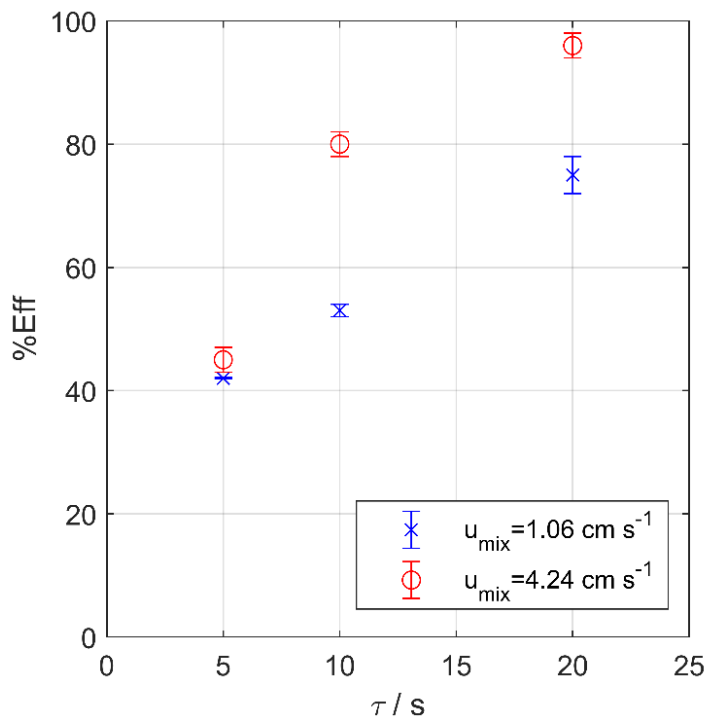


Figure 4-7 Extraction efficiency against residence time for the base case ($d=2 \text{ mm}$, $u_{\text{mix}}=1.06 \text{ cm s}^{-1}$, TBP 30%, $Q_c/Q_T=0.5$) and for the high mixture velocity case ($d=2 \text{ mm}$, $u_{\text{mix}}=4.24 \text{ cm s}^{-1}$, TBP 30%, $Q_c/Q_T=0.5$).

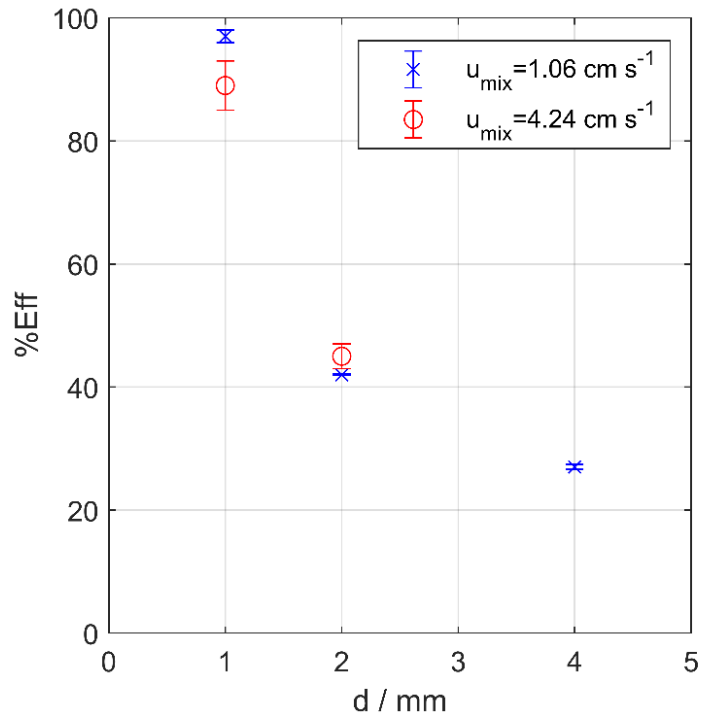


Figure 4-8 Extraction efficiency (at $\tau=5$ s) against internal diameter ($d= 1, 2, 4$ mm) for the base case ($u_{mix}=1.06 \text{ cm s}^{-1}$, TBP 30%, $Q_c/Q_T=0.5$) and for the high mixture velocity case ($u_{mix}=4.24 \text{ cm s}^{-1}$, TBP 30%, $Q_c/Q_T=0.5$) cases.

The effect of the channel internal diameter on the extraction efficiency is presented in Fig. 4-8 at a residence time of 5 s for all cases. The separator could not operate effectively at the large mixture velocity in the 4 mm channel and this case is not included here. As can be seen, there is an inverse relationship between the extraction efficiency and the internal diameter. For the 1 mm case, extraction efficiency >85% is achieved for both velocities. The %Eff in the 2 mm channel is about half of that in the 1 mm channel and about double of the one in the 4 mm channel. The specific interfacial area follows the same relationship as %Eff; for $u_{mix}=1.06 \text{ cm s}^{-1}$, it is equal to 2726, 1123, and 561 m^{-1} , and for $u_{mix}=4.24 \text{ cm s}^{-1}$, 2163, and 1224 m^{-1} , for the 1, 2, and 4 mm channels respectively.

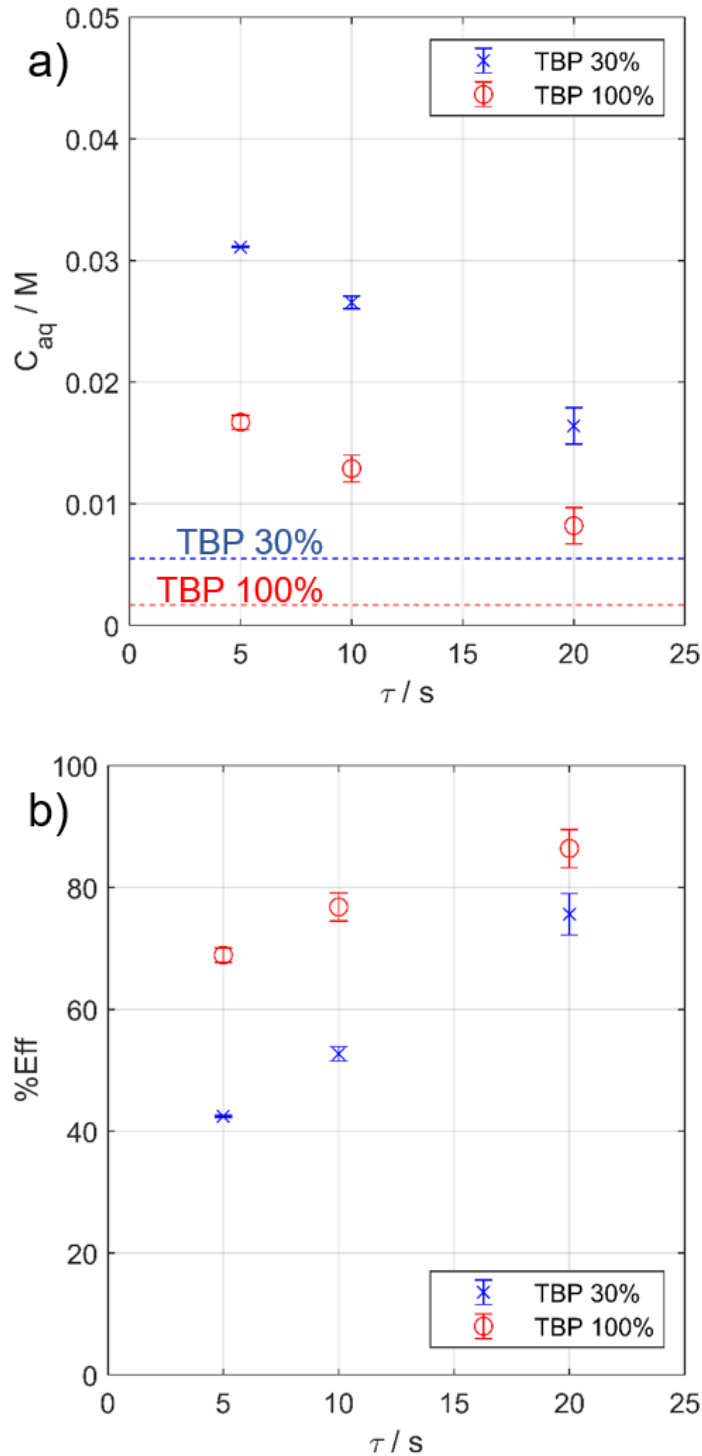


Figure 4-9 Effect of TBP concentration in the organic phase on extraction. a) U(VI) concentration in the aqueous phase against residence time; the dashed lines correspond to the equilibrium concentrations for each organic phase. b) Extraction efficiency against residence time. Diameter = 2 mm, mixture velocity = 1.06 cm s^{-1} , and phase ratio $Q_c/Q_T=0.5$.

When 100% TBP is used as the organic phase, the amount of U(VI) extracted is increased as can be seen in Fig. 4-9. Since C_{aq}^{eq} is different for both cases, the results are presented in terms of U(VI) concentrations and extraction efficiency. The mass transfer in the first 5 s of residence time is much larger for the TBP 100% case, compared to the 30% TBP, because the driving force for the mass transfer at the inlet ($C_{aq}^{in}-C_{aq}^{eq}$) is larger for the pure TBP case. The improved extraction efficiency is attributed primarily to the difference in the driving force while the interfacial area plays practically no role in this case. The specific interfacial area in the case of 100% TBP is only 0.5% larger than in the case of 30% TBP, estimated from the water-TBP 100% and water-TBP 30% hydrodynamic data. However, it is possible that the mass transfer coefficient is different for the two organic phases; this is considered in the next section.

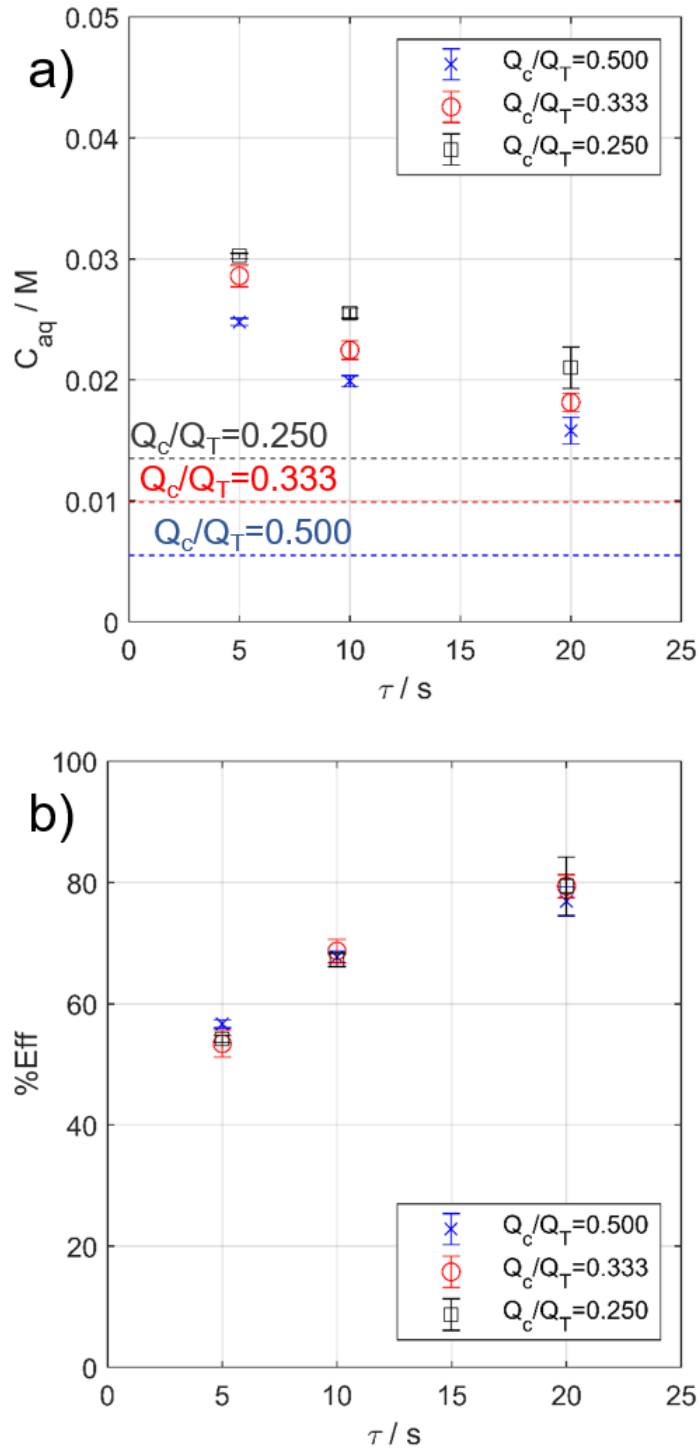


Figure 4-10 Effect of the organic phase fraction on the extraction of U(VI) for organic phase fractions 0.500, 0.333, 0.250. a) U(VI) concentration against residence time; the horizontal lines correspond to the equilibrium concentrations for each organic phase fraction (C_{aq}^{eq}). b) Extraction efficiency against residence time. Diameter = 2 mm, mixture velocity = 1.06 cm s^{-1} , and TBP 30%.

The effect of organic phase fraction on mass transfer is presented in Fig. 4-10 in terms of both U(VI) concentration and %Eff. The dashed lines in Fig 4-10 a represent the different C_{aq} for each case; higher Q_D/Q_T correspond to lower C_{aq}^{eq} . For all residence times, the relative order of the concentrations is the same as that of the equilibrium concentrations. For lower Q_D/Q_T , the equilibrium concentration in the aqueous phase is higher and therefore the driving force for mass transfer is reduced. In terms of extraction efficiency (Fig. 4-10 b), the three Q_D/Q_T cases are almost the same. As Q_D/Q_T decreases, the interfacial area increases (specific interfacial areas are, 1123, 1422, 1592 m^{-1} , for $Q_D/Q_T = 0.500, 0.333, 0.250$, respectively) while the driving force decreases; these changes have opposite effects on the rate of mass transfer and result in similar extraction efficiencies for the three cases.

4.4.2 Mass transfer coefficient

The mass transfer coefficient for the aqueous phase (K_{aq}) is calculated as follows:

$$N_U = \frac{dn_U^{aq}}{d\tau} \frac{1}{A_p} = -K_{aq}(C_{aq}(\tau) - C_{aq}^{eq}) \quad (4-18)$$

where N_U is the flux of U(VI) across the interphase, n_U^{aq} is the number of U(VI) moles in the aqueous phase, A_p is the interfacial area and the term $C_{aq}(\tau) - C_{aq}^{eq}$ is the driving force for the mass transfer. Multiplying Eq. 4-18 by the contactor volume to get the specific interfacial area (a) and dividing by the volume of the aqueous phase to substitute n_U^{aq} with C_{aq} , Eq. 4-19 is obtained:

$$\frac{dC_{aq}}{d\tau} = -\frac{K_{aq}a}{\varepsilon_{aq}}(C_{aq}(\tau) - C_{aq}^{eq}) \quad (4-19)$$

where ε_{aq} is the holdup of the aqueous (dispersed) phase. By integrating between periods τ_1 and τ_2 , Eq. 4-20 is obtained, where $K_{aq}a/\varepsilon_{aq}$ is constant with respect to residence time:

$$K_{aq} = \frac{\varepsilon_{aq}}{a(\tau_2 - \tau_1)} \ln \left(\frac{C_{aq}(\tau_1) - C_{aq}^{eq}}{C_{aq}(\tau_2) - C_{aq}^{eq}} \right) \quad (4-20)$$

The mass transfer coefficient, evaluated from Eq. 4-20, only characterises the transport during segmented flow in the test section and excludes any contributions in the inlet zone and in the separator.

Using the experimental results, K_{aq} is calculated and presented in Table 4-4 for the conditions studied. The aqueous phase holdup (Eq. 4-6) and the specific interfacial area (Eq. 4-9) are also given.

Table 4-4 Segmented flow mass transfer coefficient (K_{aq}), specific interfacial area (a), aqueous phase holdup (ϵ_{aq}) and their products ($K_{aq}a$, $K_{aq}a/\epsilon_{aq}$). For every case, all variables are the same as the base case, except for the stated change.

Case	$K_{aq} /$ $m\ s^{-1}$	$a /$ m^{-1}	ϵ_{aq}	$K_{aq}a /$ s^{-1}	$K_{aq}a/\epsilon_{aq} /$ s^{-1}
Base case					
($d=2\ mm$, $u_{mix}=1.06\ cm\ s^{-1}$, TBP 30%, $Q_c/Q_T=0.5$)	$2.35 \times 10^{-5} \pm 16\%$	1123	0.464	0.0264	0.0568
$u_{mix}=4.24\ cm\ s^{-1}$	$6.5 \times 10^{-5} \pm 18\%$	1224	0.450	0.079	0.18
TBP 100%	$2.18 \times 10^{-5} \pm 28\%$	1129	0.447	0.0246	0.0550
$Q_c/Q_T=0.333$	$2.43 \times 10^{-5} \pm 13\%$	1422	0.620	0.0346	0.0558
$Q_c/Q_T=0.250$	$2.46 \times 10^{-5} \pm 29\%$	1592	0.715	0.0391	0.0547

The results in Table 4-4 show that considering experimental uncertainties, there is no significant difference in the mass transfer coefficient (K_{aq}) between the base, the high TBP concentration, and both organic phase fraction cases. The mass transfer coefficient is increased significantly only for the case of high mixture velocity as the mixing is improved. The internal circulation increases significantly with mixture velocity [70], thus increasing the mass transfer coefficient.

A numerical model, first described by Tsaoulidis et al. [33] is used to study the mass transfer of U(VI) from the aqueous to the organic phase. In the model it is assumed that the effects of gravity are negligible, the liquids are Newtonian and incompressible,

and the properties (viscosities, densities, interfacial tension) are independent of the U(VI) concentrations. A single plug-slug unit is simulated with the plug in the centre, while periodic boundary conditions are applied at the ends of the unit. Cylindrical coordinates are used along with angular symmetry and only half of the 2-D unit cell is modelled. The plugs are assumed to have a cylindrical body with hemispherical caps; the plug and slug lengths are taken from the experiments. The film thickness and plug velocity are calculated from correlations given by Mac Giolla Eain et al. [69] and Abiev et al. [71], respectively. The solute diffusivities in the model are $10^{-9} \text{ m}^2 \text{ s}^{-1}$ [151], $1.03 \times 10^{-10} \text{ m}^2 \text{ s}^{-1}$ [152], and $2.56 \times 10^{-10} \text{ m}^2 \text{ s}^{-1}$ [152] for the aqueous, the 100% TBP and 30% TBP phases respectively.

The model is solved using COMSOL Multiphysics 5.4 with the 'Laminar Flow' and 'Transport of Diluted Species' physics modules. First, the Navier-Stokes and continuity equations were solved for both liquid domains (phases) in steady-state to determine the velocity and pressure profiles. Subsequently, the transient convection-diffusion equations, one for each domain, were solved to obtain the mass transfer during the movement of the plug along the channel. The initial conditions are zero concentration of solute within the slug and 0.05 mol/L within the plug. The model also assumes zero flux and non-slip boundary conditions at the channel walls. For the whole computational domain, a free triangular mesh was used, which was additionally refined along the interface and the channel wall. In all cases, the minimum and maximum element sizes along the interface were $0.02 \text{ }\mu\text{m}$ and $0.4 \text{ }\mu\text{m}$, respectively. The minimum element size along the walls is $0.1 \text{ }\mu\text{m}$ and inside each phase domain, away from the interphase, is $1.5 \text{ }\mu\text{m}$. Further refinements to the grid were not found to affect the results. Moreover, the very fine grid size used ensures the numerical diffusion is minimal. For the integration of the convection-diffusion equations, a time step of 0.05 s was used. Because of the initial condition used, very large instantaneous fluxes would occur across the interface, which could lead to initial concentration oscillations and slightly negative values in regions where the concentration is zero initially. To mitigate this problem, the interphase

discontinuity is replaced by a step function across the interface, as described by Tsaoulidis & Angeli [33]. The COMSOL modelling was done in collaboration with Dr M. Pineda, Dr D. Tsaoulidis, and Professor E. Fraga; all from The Chemical Engineering Department at UCL.

To further investigate the mass transfer and the effects of the various variables, the numerical model described above is used for the same cases shown in Table 4-4. Fig. 4-11 shows the velocity field and concentration profile of U(VI) in the aqueous phase plug and organic phase slug for the conditions of the base case at six different times. Since the simulation follows a plug, the time in the simulation corresponds to the residence time of the plug, not the mean residence time. The u_p/u_{mix} ratio, calculated using a correlation by Abiev et al. [71], ranges from 1.04 to 1.11 for the five cases in Table 4-4; this indicates the average residence time and the plug residence times are similar. At time 0, the solute is homogeneously distributed in the aqueous phase. In the first few seconds ($t \leq 10$ s), the solute in the region close to the interphase is depleted and a concentration profile, that follows the velocity profile (Fig. 4-11 a), forms. At longer times ($t > 10$ s), the solute in the region close to the interphase is mostly depleted. Mass transfer continues because there is still a driving force but the solute has to diffuse from the high concentration region in the middle of the plug to the interphase. The concentration in the aqueous phase, integrated for the whole plug, is plotted against time in Fig. 4-12 for the TBP 30% and the TBP 100% cases. The trends followed by both curves are the same as those found experimentally (Fig. 4-9). It should be noted that the residence times are not exactly the same because the experimental one is based on the mixture velocity, while the numerical one is based on the plug velocity. The difference, however, is very small as was discussed above and the residence times have not been adjusted. The experimental points show lower concentration in the aqueous phase and therefore, higher mass transfer. This is attributed to the high mass transfer that takes place at the inlet, where the two phases join initially, which is not taken into account in the model.

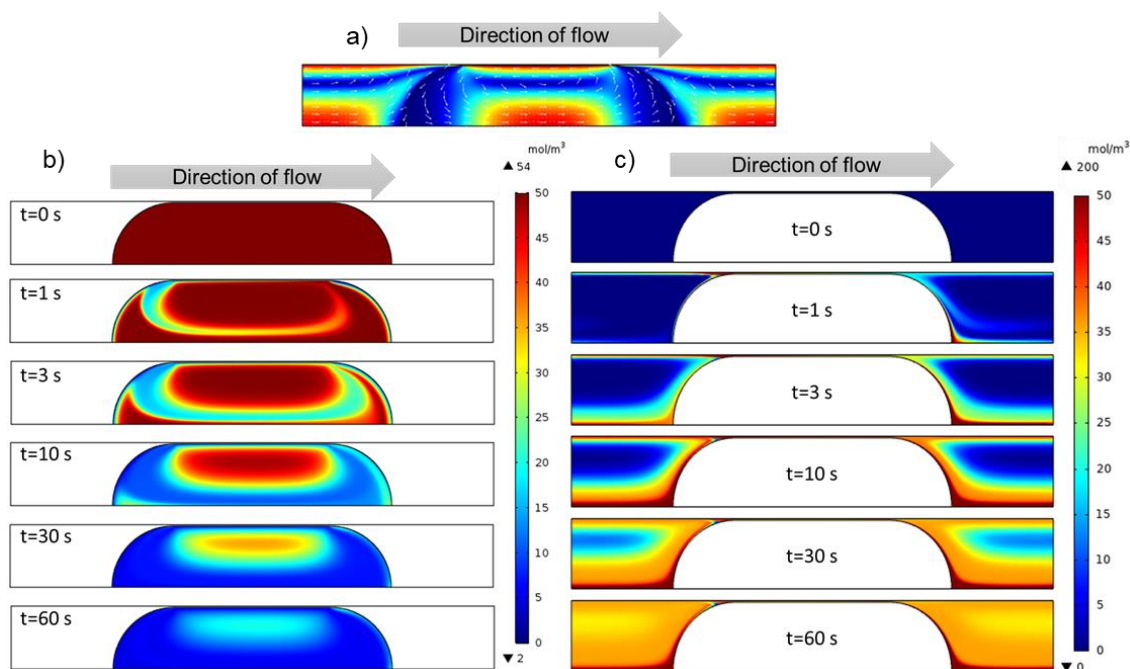


Figure 4-11 Velocity field (a) and concentration profiles of U(VI) in the plug (b) and slug (c) from 0 to 60 s for the base case ($d=2$ mm, $u_{\text{mix}}= 1.06$ cm s⁻¹, TBP 30%, $Q_c/Q_T=0.5$).

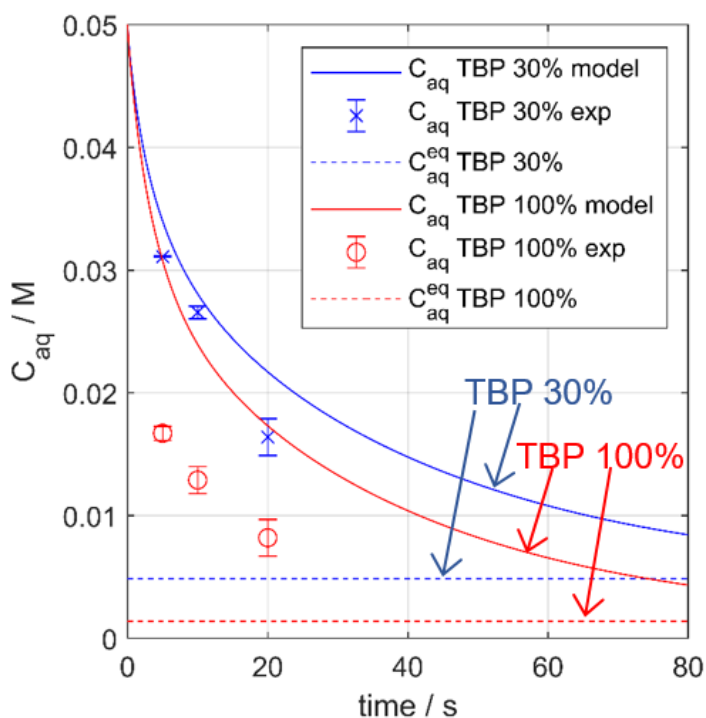


Figure 4-12 Simulated and experimental average U(VI) concentration in the aqueous phase against time for the base case (TBP 30%) and the high TBP concentration case (TBP 100%). The dashed lines represent the equilibrium concentration values ($d=2$ mm, $u_{\text{mix}}=1.06$ cm s⁻¹, $Q_c/Q_T=0.5$).

The mass transfer coefficient (K_{aq}) can be calculated from the simulations at every consecutive time step using Eq. 4-19. The results are shown in Fig. 4-13 for the base and the 100% TBP cases. As can be seen, K_{aq} decreases significantly in the beginning when there is a large concentration difference between the phases, while later ($t > 10$ s), when the uranium has been depleted from the regions close to the interphase, the change is very small. The value of K_{aq} , when it reaches a plateau, can be interpreted as a low-bound value of the mass transfer coefficient of segmented flow for those specific conditions. The experimental values of K_{aq} for the same conditions between 5 and 20 s (Eq. 4-20) are shown in Fig. 4-13.

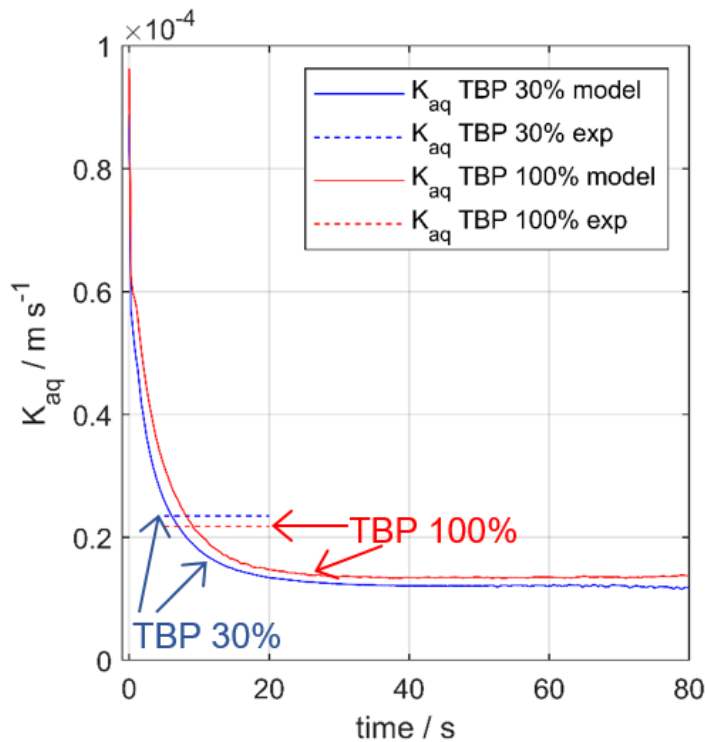


Figure 4-13 Mass transfer coefficient evolution with time for the base case (TBP 30%) and the high TBP concentration case (TBP 100%). The dashed lines represent the experimental K_{aq} values at the same conditions (Table 4-4). ($d=2$ mm, $u_{mix}=1.06$ cm s $^{-1}$, $Q_C/Q_T=0.5$).

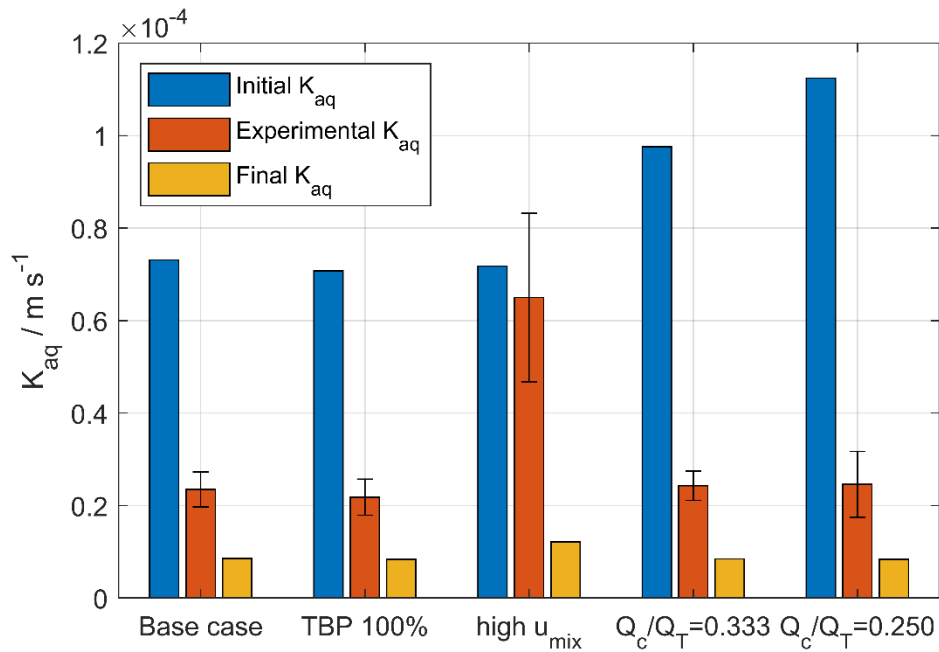


Figure 4-14 Initial, experimental, and final segmented flow mass transfer coefficients (K_{aq}). Initial K_{aq} is the mass transfer coefficient for the first time step of the simulation. Final K_{aq} is the value at which the segmented flow mass transfer coefficient approaches asymptotically.

Fig. 4-14 presents three K_{aq} values for each case studied in Table 4-4. The initial K_{aq} is the mass transfer coefficient at the first time step of the simulation ($\Delta t=0.25$ s) and is the largest K_{aq} value calculated because at the initial step the concentration difference between the phases is large and the diffusion path of the solute to the interphase is minimal. The final low K_{aq} is the value at which the mass transfer coefficient reaches a plateau. The experimental K_{aq} is the value found from the measurements calculated from Eq. 4-20 between 5 and 20 s. In all cases, the mean experimental value is between the initial and the final simulation values. The final K_{aq} values are similar in all cases except for the high u_{mix} case, which is 42% larger than the base case, because of the shorter unit length and the faster recirculation inside the plugs [70].

There is limited literature available to compare the K_{aq} values presented here for the following reasons. First, K_{aq} depends on the system (diffusivities, viscosities) and thus, it is not strictly comparable across systems. However, as long as the viscosities, densities, and their ratios are similar, the differences could potentially be accounted for. Second, K_{aq} is preferred over K_{aqa} for generality (the specific interfacial area depends on the system and in continuous flow contactors also on the inlet geometry) but few studies

determine K_{aq} because it would require measurements of the interfacial area. And third, many studies of flow contactors report the overall mass transfer coefficient, which includes the mass transfer that takes place in the inlet and in the outlet. This overestimates the mass transfer rates characteristic of segmented flow. Kashid et al. found mass transfer coefficients (K_L) of a water/iodine/kerosene extraction between 0.5×10^{-4} and $2 \times 10^{-4} \text{ m s}^{-1}$ [14] for channels with diameters from 0.5 to 1 mm, where the largest specific interfacial areas were 1970 and 780 m^{-1} , respectively [47]. Li et al. found overall mass transfer coefficients ranging from 2×10^{-3} to 10^{-2} m s^{-1} using a sulphuric acid/cyclohexanone oxime/n-hexane system in a channel with a diameter of 1 mm [86]. Sattari-Najafabidi et al. used an acid-base reaction to study the mass transfer coefficient in microchannels with an internal diameter of 0.6 mm and reported mass transfer coefficients between 0.4×10^{-5} and $1.5 \times 10^{-5} \text{ m s}^{-1}$ for specific interfacial areas up to 5500 m^{-1} [153]. The mass transfer coefficients found by Kashid et al. and Sattari-Najafabidi et al. are similar to the K_L values presented in Table 4-4 but the values found by Li et al. are significantly larger.

For packed liquid-liquid extraction columns (73 mm ID with 5/8" stainless steel Pall rings packing), Verma & Sharma report K_{aq} values between 3.76×10^{-5} and $4.55 \times 10^{-5} \text{ m s}^{-1}$ and specific interfacial areas 74 – 133 m^{-1} [154]. Rezvan et al. studied pulsed columns (disc and doughnut columns, with 76 mm ID) for a system of water/gadolinium and samarium nitrate / D2EHPA in kerosene and found K_{aq} values of 5×10^{-6} to $20 \times 10^{-6} \text{ m s}^{-1}$, for specific interfacial areas from 150 to 250 m^{-1} [155]. Doraiswamy & Sharma reported continuous phase mass transfer coefficients, specific interfacial areas, and dispersed phase holdups for several conventional liquid-liquid contactors, including spray and packed columns and mechanically agitated contactors [8]. They reported that the mass transfer coefficients range from 10^{-5} to 10^{-4} m s^{-1} for all types of contactors and the interfacial areas have values up to 1000 m^{-1} . The dispersed phase holdup depends on the contactor, and in columns, it has a maximum value of 0.1, while for mechanically agitated contactors it can reach up to 0.4.

The comparison between the K_{aq} , and a values for intensified and conventional contactors shows intensified contactors have values in similar ranges, although the a values tend to be higher. To be commercially competitive, the intensified contactors must have additional advantages over conventional ones beyond the improvements in mass transfer coefficients. For the application considered here the small-channel contactors offer the following additional advantages: 1) they can handle a wide range of densities or viscosities of the two liquid phases and enable the use of the extractant without dilution thus reducing inventories, footprint, and overall volumes; 2) the flow patterns are regular, making the process easy to model, design and control, and reducing the need for over-design; and 3) the residence times are very short, thus reducing the contactor volume needed for a particular extraction, and the radiolytic damage of the solvent.

4.5 Conclusions

The hydrodynamics and mass transfer characteristics of the uranyl extraction from an aqueous solution into an organic phase were studied in small channel contactors operating in segmented flow. The design and operational variables investigated include channel internal diameters up to 4 mm, the use of two different extractant concentrations in the organic phase, and a wide range of u_{mix} and Q_d/Q_T values; this expands the range of variables previously explored for uranium extraction in segmented flow contactors.

It was found that the plug, slug and unit (one plug and one slug) lengths depended mainly on the continuous phase volume fraction and on the capillary number based on the continuous phase, in agreement with previous works (Table 4-3). Assuming that the plug is composed of two hemispherical caps and a cylindrical body, the holdup and interfacial area can be expressed as functions of plug and unit lengths, and film thickness. Correlations are proposed to estimate the holdup and dimensionless specific interfacial area were shown to depend only on Q_d/Q_T , μ_d/μ_c , and Ca_c . (Eqs. 4-10 and 4-11). The pressure gradient for segmented flow was studied experimentally and a new model, based on the flow pattern periodicity, was proposed. The proposed dimensionless model fits the experimental results accurately over a wide range of conditions; other

available models were found to have large confidence intervals of the regression variables for the cases studied here.

The extraction efficiency and mass transfer coefficients were also obtained experimentally and compared against the predictions of a simplified numerical model. The mass transfer coefficients were mainly affected by the mixture velocity. Changes in flow rate ratio and extractant concentration affected the amount of U extracted by changing the driving force or the interfacial area available but not K_{aq} .

Segmented flow contactors have large mass transfer coefficients and interfacial areas but their principal advantages over conventional contactors are the simplified modelling of the symmetric and periodic flow pattern and the ability to operate with a variety of liquid-liquid systems with a larger range of viscosities and densities. The results here demonstrate that segmented flows in relatively large channels (up to 4 mm diameter) have good mass transfer performance and can process high flow rates (up to 11 litres per day or 8 ml min^{-1} or $10^{-7} \text{ m}^3 \text{ s}^{-1}$). To increase the throughput further, scale-out approaches need to be considered, where many channels are used in parallel. The pressure gradient model proposed here (Eqs. 4-14 to 4-16) can be used in the design of flow distributors for scale-out (see Chapters 5 and 6).

5 Model for the scale-out of small channel two-phase flow contactors

5.1 Introduction

The methodologies developed in section 3.2 are first used to demonstrate the effects of the hydraulic resistances on the flow maldistribution in double manifolds (Fig. 5-1) with a certain number of parallel channels. In addition to flow distribution, the overall pressure drop and power requirements are then estimated. The effects of increasing the number of the parallel channels in the manifold on the flow distribution and on the pressure drop and power requirements are finally investigated. This chapter considers the case where R_R is independent with respect to the flow rate. The case where R_R depends on the flow rate is discussed in Chapter 6.

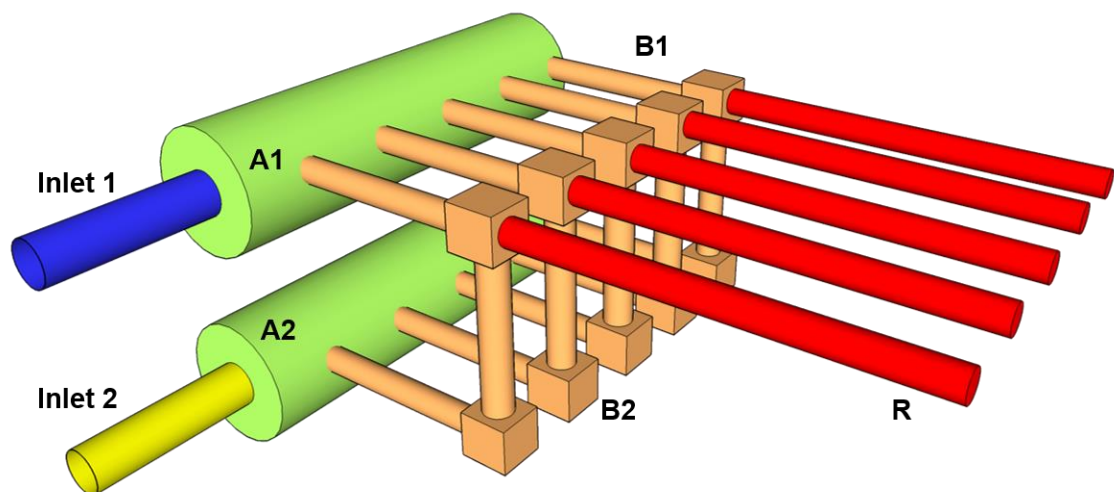


Figure 5-1 3D Schematic of a double manifold with one inlet for each fluid, distribution sections (A1, A2, green), barrier sections (B1, B2, orange), and main channels (R, red).

It is important to elucidate the applicability limits of the results presented in this chapter. Most are presented in Chapter 3, namely, the model considers that volumes are additive, the limitations of the hydraulic resistances models selected will also apply to the resistance network model, and the maldistribution descriptors are based on standard deviations and share the same properties and limitations (section 3.2.2). Additionally, the resistances are considered identical across the distributor but, in practice, there will be

differences in a built distributor. The effect of these differences, fabrication tolerances, will have a different effect if the diameter of length are different. Since the hydraulic resistance for the Hagen-Poiseuille Law (Eq. 3-14) are proportional to L^1 and d^{-4} , differences in diameter will have stronger effects compared to differences in length. The focus of this chapter in on the relationship between maldistribution and manifold design and number of channels, as such, the effects of fabrication tolerances are not explored here but have been previously addressed, for single-phase manifolds, by Amador [134].

5.2 Effect of hydraulic resistances on flow maldistribution in the double manifold

As an example of the resistance network model and the application of the flow maldistribution descriptors, a parametric study of a double manifold with 5 channels is carried out as shown in Table 5-1. The input variables are the flow rate ratio ($r=[1,5]$), and the resistance ratios ($R_A/R_R=R_B/R_R=[0.1,10]$). For all cases, $\rho > 0.05$ and only for case 6 $\rho < 0.95$ thus requiring both RCVs and PRM to characterise the maldistribution (Table 3-4).

Table 5-1 Maldistribution descriptors for r : 1 and 5, R_A/R_R : 0.1 and 10, R_B/R_R : 0.1 and 10. The double manifold modelled has 5 channels and a total flow rate of $6 \times 10^{-6} \text{ m}^3 \text{ s}^{-1}$. In case 5, channeling, where the fluid flows opposite to the designed direction, is observed.

case	r	R_A/R_R	R_B/R_R	ρ	RCV ₁	RCV ₂	PRM	$\theta / ^\circ$	a/	b/
									$10^{-6} \text{ m}^3 \text{ s}^{-1}$	$10^{-6} \text{ m}^3 \text{ s}^{-1}$
1	1	0.1	0.1	1.00	0.219	0.00	0.00	45	0.643	0.00
2	1	10	0.1	1.00	2.32	0.00	0.00	45	6.81	0.00
3	1	0.1	10	1.00	0.0419	0.00	0.00	45	0.123	0.00
4	1	10	10	1.00	1.47	0.00	0.00	45	4.32	0.00
5	5	0.1	0.1		Channeling					
6	5	10	0.1	0.853	1.78	0.588	0.451	6.3	8.71	0.576
7	5	0.1	10	1.00	0.0322	0.00	0.434	6.5	0.158	0.00
8	5	10	10	0.997	1.08	0.0672	0.163	9.5	5.31	0.0658

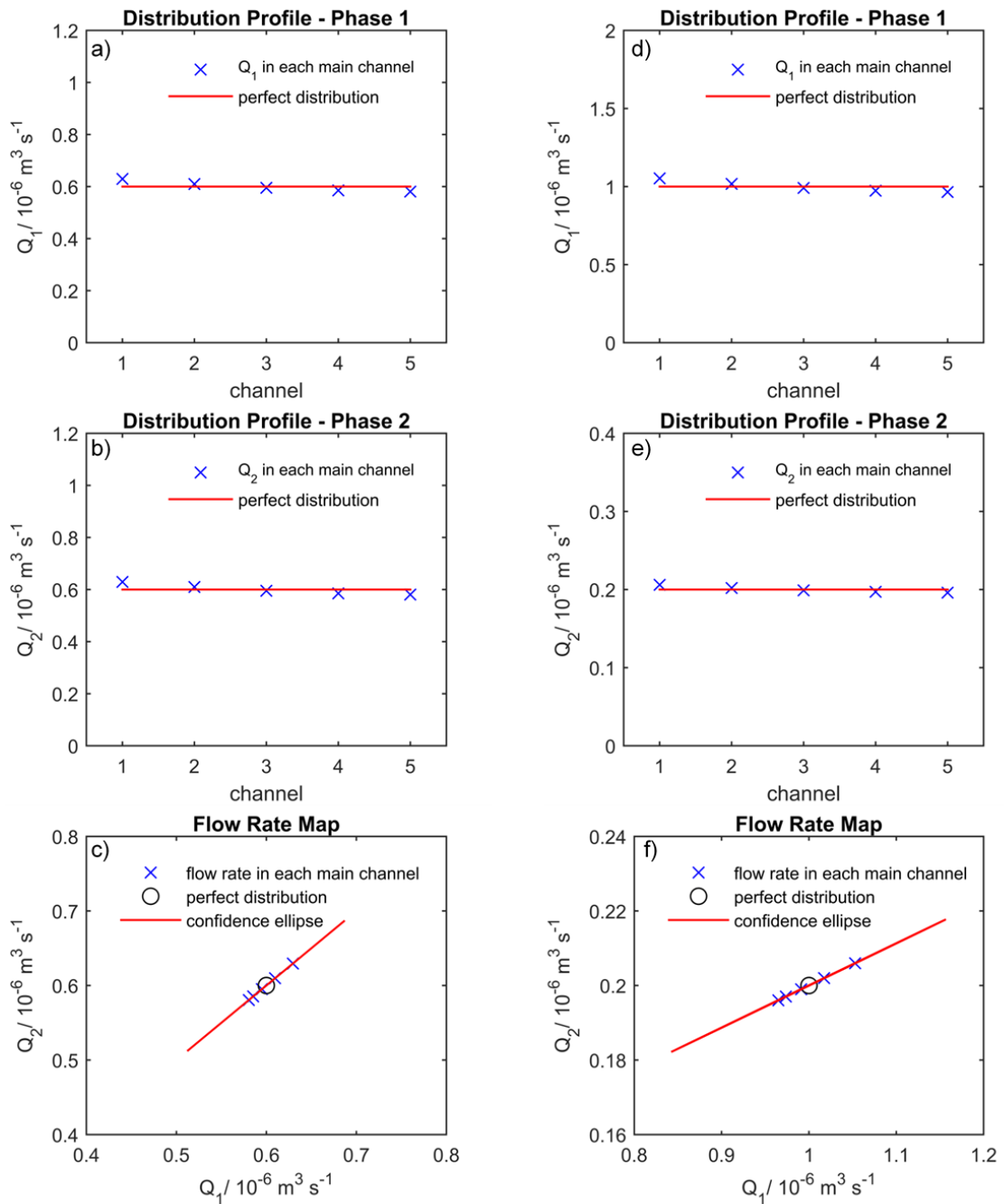


Figure 5-2 Distribution profiles and flow rate maps for cases 3 (a to c) and 7 (d to f) from Table 5-1 ($N=5$, $Q_T=6 \times 10^{-6} \text{ m}^3 \text{ s}^{-1}$). a, b, d, e) Flowrates of each phase in the channels; the perfect distribution line is calculated as $Q_{A_i,1}/N$. c, f) Flow rate maps. The circle indicates the perfect distribution case, calculated as $(Q_{A_1,1}/N, Q_{A_2,1}/N)$. The 95% confidence ellipses are also shown; the minor axis length, b , is zero in both cases and the ellipses collapse into line segments.

The cases in Table 5-1 where the flow ratio is 1, show consistent values of $\rho=1$ and $\text{PRM}=0$. In these cases, the maldistribution is completely described by RCV_1 . The lowest RCV_1 value, thus lowest maldistribution, corresponds to case 3 where $R_A/R_R=0.1$ and $R_B/R_R=10$; this case is plotted in Fig. 5-2a to c. As can be seen in Fig. 5-2a and b, the flow rate in each main channel is close to the equal distribution line. For both phases,

channels 1 and 2 have more flow rate than the average and channels 3 to 5 have slightly lower flow rates. Fig. 5-2c shows the flow rates of the two phases in each main channel in a flow rate map, together with the point of perfect distribution. In the same graph, the 95% confidence ellipse is plotted. This ellipse has its centre in the point of perfect distribution and is rotated by angle, $\theta=45^\circ$, calculated from Eq. 3-24. The major and minor axes lengths are calculated from Eqs. 3-28 and 3-29. PRM, in this case, is zero which indicates the ratio in all the channels is equal to the inlet ratio and thus the eigenvector slope ($m=\tan(\theta)$) is equal to $1/r$. Since the minor axis length is zero (from $\rho=1$ and Eqs. 3-23 and 3-29), the confidence ellipse collapses into a line segment.

Case 5 in Table 5-1, with $r=5$, and both R_A and R_B smaller than R_R presents channeling, where one of the phases flows into a channel of the opposite phase. In this case, channeling occurs because phase 1, with a larger flow rate ($r=5$), has a much larger pressure than phase two and flows into a barrier channel of phase 2. In the model, this is indicated by a negative flow rate (opposite to the positive-defined direction) in the channel where channeling has occurred. The rest of the cases with $r=5$, have $\rho>0.05$ and thus both RCVs and PRM are used to describe maldistribution. The largest maldistribution descriptors occur when $R_A/R_R=10$ and $R_B/R_R=0.1$ (case 6). Case 7 with $R_A/R_R=0.1$ and $R_B/R_R=10$ has the lowest maldistribution with the smallest RCV_1 ($\rho>0.95$ so RCV_2 is not considered). Case 7 is plotted in Fig. 5-2d to f. The distribution profiles are similar to the $r=1$ case although the ranges for each phase are different because of the different phase ratio. The flowrates in Fig. 5-2f fall in a straight line (as in Fig. 5-2c) for $r=5$ though the slope of the eigenvector ($m=0.113$) is different from the inverse of r ($1/r=0.2$). This difference represents the maldistribution of the phase ratio in each main channel, as measured by the PRM descriptor.

Case 8, with high both R_A and R_B compared to R_R has a larger RCV_1 but smaller PRM than case 7. These conflicting results show that further considerations should be taken into account when characterising maldistribution in double manifolds. For both $r=1$ and 5, RCV_1 is the smallest when $R_A/R_R=0.1$ and $R_B/R_R=10$. These ratios compare the

resistances of sections A and B with R. However, they also indirectly compare the resistances between sections A and B:

$$\frac{R_A}{R_B} = \frac{\frac{R_A}{R_R}}{\frac{R_B}{R_R}} \quad (5-1)$$

For both flow rate ratios analysed, the lowest RCV_1 values are achieved when R_A/R_B is the smallest. This suggests R_A/R_B describes RCV_1 better than the other combinations of resistance ratios. Fig. 5-3 presents logarithmic contour plots of RCV_1 and PRM in R_A/R_B - R_B/R_R planes for $N=5$ and $r=5$. For the whole range of resistance ratios plotted, ρ is larger than 0.95 and is increasingly closer to unity as R_A/R_B decreases and R_B/R_R increases in the range plotted.

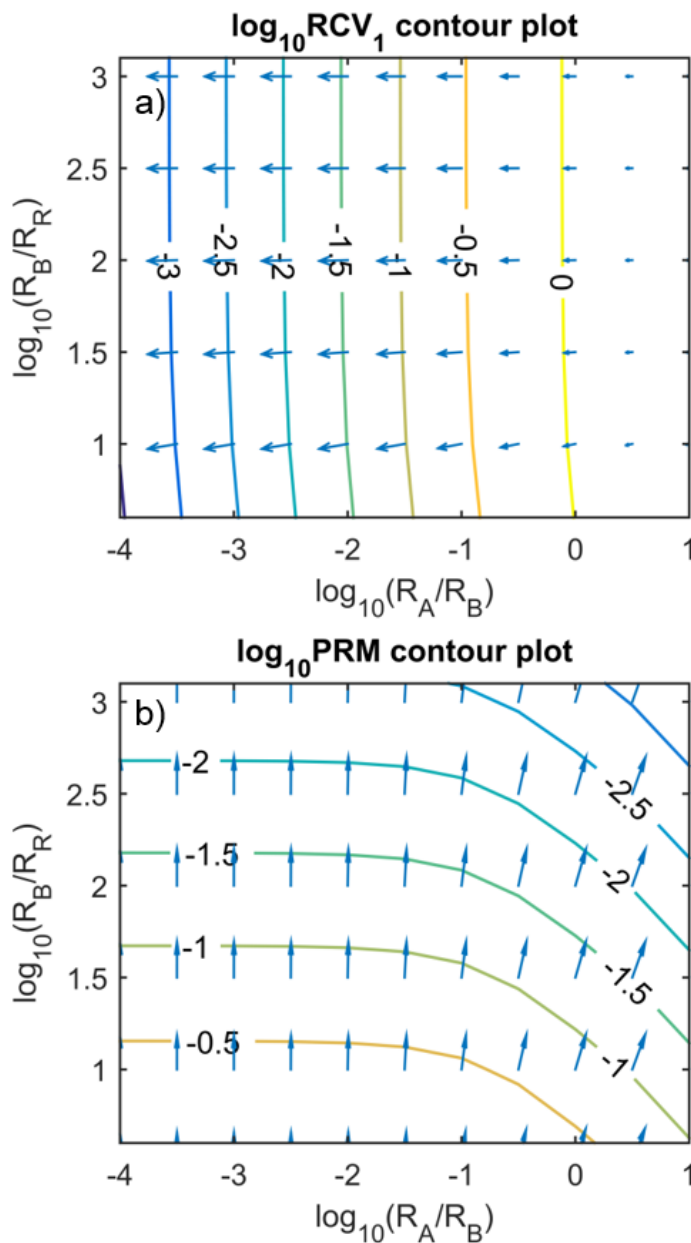


Figure 5-3 Contour plots of a) $\log_{10}RCV_1$ and b) $\log_{10}PRM$ in \log_{10} - \log_{10} planes of R_A/R_B vs. R_B/R_R . The double manifold modelled has 5 channels, $Q_{A1,1}=5 \times 10^{-6} \text{ m}^3 \text{ s}^{-1}$, $Q_{A2,1}=1 \times 10^{-6} \text{ m}^3 \text{ s}^{-1}$ ($r=5$). The arrows show the direction of greatest decrease for the maldistribution descriptors.

Results in Fig. 5-3a show RCV_1 decreases steeply as R_B increases with respect to R_A . This is shown by both the quasi-vertical contour lines and the arrows. By contrast, the ratio between R_B and R_R has a very limited influence on the behaviour of RCV_1 . Similar results were found for $r=1$. Furthermore, the model predicts channeling at $\log_{10}(R_B/R_R) < 0.5$ for the range of R_A/R_B plotted, which means that the flow distribution is severely disrupted at $R_B < 3R_R$. Fig. 5-3b presents the $\log_{10}PRM$ in the same plane as Fig. 5-3a. The results show that R_B/R_R has a stronger influence over PRM than R_A/R_B . This

is less the case as R_A/R_B increases, where the arrows and the curvature of the contour lines show that both resistance ratios affect PRM. If the arrows of greatest descent in both Fig. 5-3a and b are superimposed, they are almost perpendicular to each other. This means that the different resistance ratios affect the maldistribution descriptors practically independently. RCV_1 , which is analogous to total flow rate and residence time distribution widening, depends mostly on R_A/R_B . PRM, which is related to flow rate ratio distribution, is dependent on R_B/R_R primarily.

The current model is compared to the results of the two-phase resistance network developed by Al-Rawashdeh et al. [122,123]. These authors suggest channeling occurs when the resistivity of the barrier sections is different for each phase and the flow rates of the phases are equal [122]. This contrasts with the findings of the current model which predicts channeling only for flow rate ratios different to unity and when R_B/R_R is below a threshold value. Regarding flow maldistribution, Al-Rawashdeh's model used a single maldistribution descriptor which decreases as R_A/R_R decreases and R_B/R_R increases. In contrast, our results show maldistribution is completely characterised with at least two descriptors and these descriptors indicate that the residence time and the flow rate ratio distributions become narrower as R_A/R_B is reduced and R_B/R_R is increased.

5.3 Effect of hydraulic resistances on the pressure drop and power requirements of the double manifold

The pressure drop in the double manifold and the associated power requirements are discussed here for different channel resistance ratios. The equivalent resistance (R_{eq}) is the resistivity of a single resistor that has the same resistance as the whole network. Since a double manifold distributes two phases, this definition is modified and two equivalent resistances are defined by Eq. 5-2, one for each phase.

$$\Delta p_i = R_{eq,i} Q_i \quad (i=1, 2) \quad (5-2)$$

where Δp_i is the pressure drop of the i -th fluid and is numerically equal to the head required by the i -th pump and Q_i is the total flow rate of the i -th phase. To compute $R_{eq,i}$

for each phase, the following points are considered. First, for each phase, only the sections where that phase flows affect its R_{eq} ; this is true as long as there is no channeling. Second, and as in the previous discussion, no collection section is included in the double manifold. The equivalent resistance for each phase in double manifolds with 2 and 3 main channels can be calculated by Eqs. 5-3 and 5-4 respectively. These equations show that even for a small number of channels, the calculation of $R_{eq,i}$ is complex.

$$R_{eq,i}(N = 2) = R_{Ai} + \frac{1}{\frac{1}{(R_{Ai}+R_{Bi}+R_R)} + \frac{1}{(R_{Bi}+R_R)}} \quad (i=1, 2) \quad (5-3)$$

$$R_{eq,i}(N = 3) = R_{Ai} + \frac{1}{R_{Ai} + \frac{1}{\frac{1}{\frac{1}{(R_{Ai}+R_{Bi}+R_R)} + \frac{1}{(R_{Bi}+R_R)}}} + \frac{1}{(R_{Bi}+R_R)}} \quad (i=1, 2) \quad (5-4)$$

However, when $R_{Ai} \ll R_{Bi}$ (necessary for reducing maldistribution) the denominator in the second term of the right-hand-side depends only on $R_{Bi}+R_R$. An approximation can then be made to find the value of $R_{eq,i}$ for any number of channels, given by:

$$\frac{R_{eq,i}}{R_R} = \frac{R_{Ai}}{R_{Bi}} \frac{R_{Bi}}{R_R} + \frac{\frac{R_{Bi}}{R_R} + 1}{N} \quad (i=1, 2) \quad (5-5)$$

Eq. 5-5 shows that the dimensionless equivalent resistance increases linearly with R_B/R_R . Fig. 5-4 shows plots of $R_{eq,i}/R_R$ over R_A/R_B for different channel numbers, N , at constant R_B/R_R both from the exact solutions (Eqs. 5-3 and 5-4) and the approximation (Eq. 5-5). As can be seen, the approximation improves as R_A/R_B decreases. This figure also shows that $R_{eq,i}/R_R$ decreases as N increases.

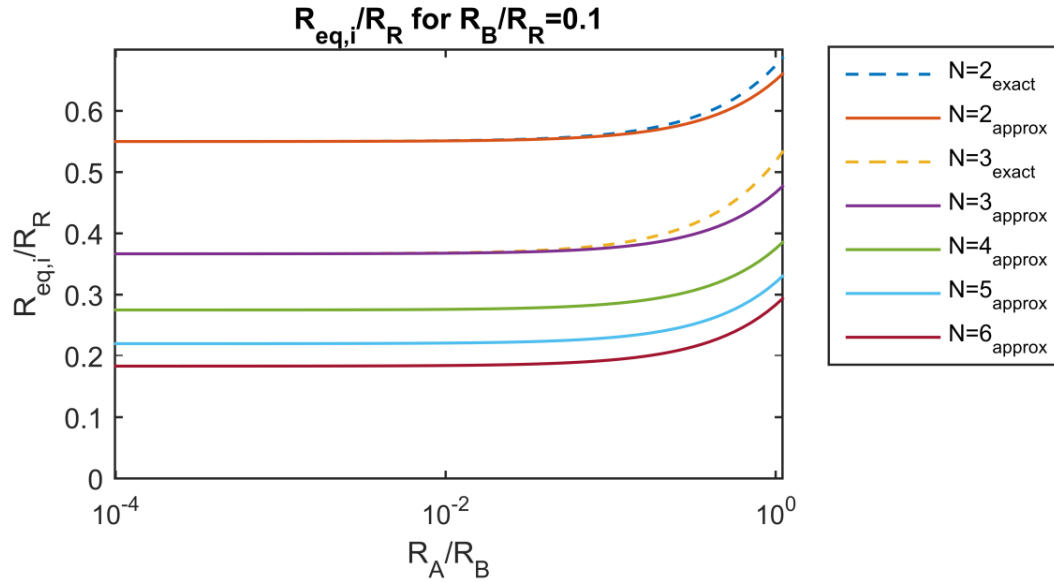


Figure 5-4 Equivalent resistances as a function of R_A/R_B and N . The dashed lines (---) show exact solutions using Eqs. 5-3 and 5-4 and the solid lines show approximations using Eq. 5-5. Calculations are for $R_B/R_R=0.1$.

The overall pressure drop for each phase can then be calculated from Eqs. 5-6 and 5-7 and the total pumping power required from Eq. 5-8. These equations are derived using Eqs. 3-15, 3-16, 5-2, and 5-5.

$$\frac{\Delta p_1}{Q_T R_R} = \frac{r}{r+1} \left(\frac{R_{A1} R_{B1}}{R_{B1} R_R} + \frac{R_{B1}+1}{N} \right) \quad (5-6)$$

$$\frac{\Delta p_2}{Q_T R_R} = \frac{1}{r+1} \left(\frac{R_{A2} R_{B2}}{R_{B2} R_R} + \frac{R_{B2}+1}{N} \right) \quad (5-7)$$

$$\frac{P_T}{Q_T^2 R_R} = \frac{\eta_1 r^2}{(1+r)^2} \left(\frac{R_{A1} R_{B1}}{R_{B1} R_R} + \frac{R_{B1}+1}{N} \right) + \frac{\eta_2}{(1+r)^2} \left(\frac{R_{A2} R_{B2}}{R_{B2} R_R} + \frac{R_{B2}+1}{N} \right) \quad (5-8)$$

where P_T is the total pumping power required, and η_i is the efficiency of the pumping system for the i -th fluid. The right-hand-side of these equations depends on the design of the double manifold. Both pressure drops and the power requirement increase linearly with R_B/R_R , while PRM (Fig. 5-3b) decreases with R_B/R_R . Pressure drop estimates, using Eqs. 5-6 and 5-7, can be used to calculate changes in the density if one of the fluids is a gas, and be used to assess the validity of the model in Section 3.2.1. A contour plot of $P_T/(Q_T^2 R_R)$ in a log-log plane of R_A/R_B - R_B/R_R is presented in Fig. 5-5, for a 5-channel manifold operating at a flow rate ratio of 5. The efficiency of both pumps is set to be 80%.

Arrows of steepest descent for the dimensionless power requirement are also included. Fig. 5-5 is plotted in the same range of resistance ratios as Fig. 5-3 for comparison. Figs. 5-3b and 5-5 have arrows pointing at opposite directions, showing that a reduction in maldistribution is directly associated with increased pressure drop and pumping power requirements. The prevalence of the R_R factors in Eqs. 5-3 to 5-8 indicates the importance of the pressure drop correlation in the main channels for the calculation of the pumping requirements. These results show quantitatively for the first time how the pumping requirements are linked to the flow maldistribution in a manifold.

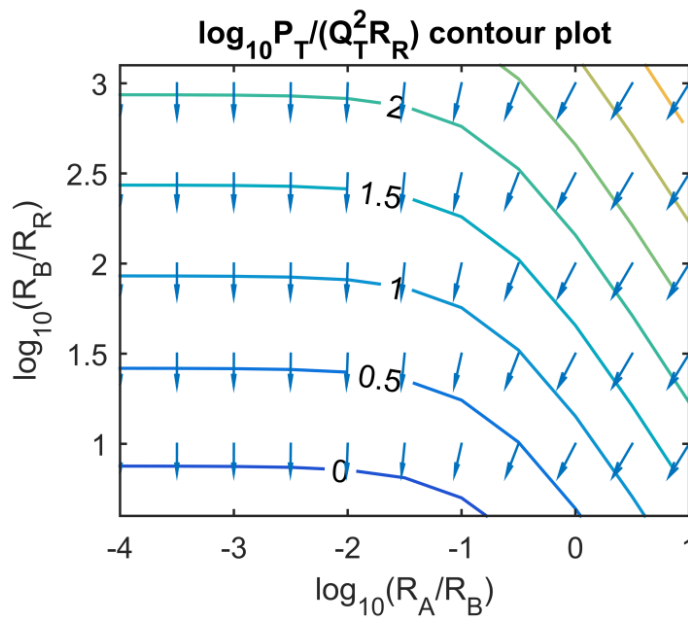


Figure 5-5 Contour plot of $\log_{10}P_T/(Q_T^2R_R)$ in a \log_{10} - \log_{10} plane of R_A/R_B vs. R_B/R_R . The double manifold modelled is symmetrical, has 5 main channels, $Q_{A1,1}=5 \times 10^{-6} \text{ m}^3\text{s}^{-1}$, $Q_{A2,1}=1 \times 10^{-6} \text{ m}^3\text{s}^{-1}$. The pumping efficiencies are 80%. The arrows show the direction of greatest decline for the dimensionless pumping power.

5.4 Effect of increasing number of channels on flow maldistribution

The purpose of double manifolds is to increase the throughputs compared to single channels. The effects of the number of main channels on flow maldistribution and the changes needed in the channel resistances to reduce or keep constant the maldistribution during scale-out are considered here. In this section $Q_{T,1ch}$ (defined in Eq. 3-15) is used instead of Q_T because it is independent of N .

Fig. 5-6 shows flow rate maps for three cases with 5, 50 and 500 channels. The same $Q_{T,1ch}$, flow rate ratio, and resistance ratios are used for all cases. As can be seen,

the distributions are highly correlated, with ρ close to unity. As the number of channels increases, maldistribution increases with respect to RCV_1 but not with respect to PRM. The increase in RCV_1 with N means that the residence time distribution, therefore, becomes wider. RCV_1 increases by a factor of 84 and 732 as the number of main channels increases from 5 to 50 and 500, respectively. In the 500 channels distributor, there is significant maldistribution with several channels having flow rates close to zero. PRM, which compares the flow rate ratios in the channels with the inlet flow rate ratio, shows the opposite trend to RCV_1 as N increases. It decreases by 18% and by 65% when N increases from 5 to 50 channels and then from 50 to 500 channels, respectively. In all cases, PRM is very small and the flow rate ratios are very similar in all channels despite the large maldistribution measured by RCV_1 .

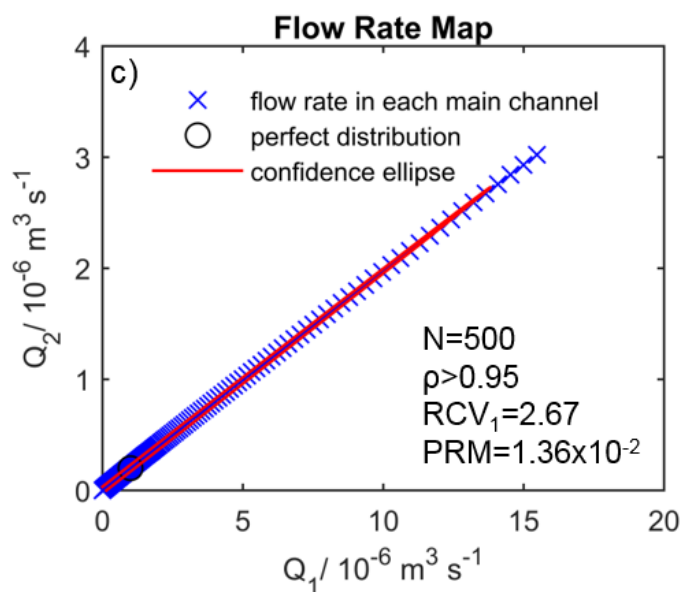
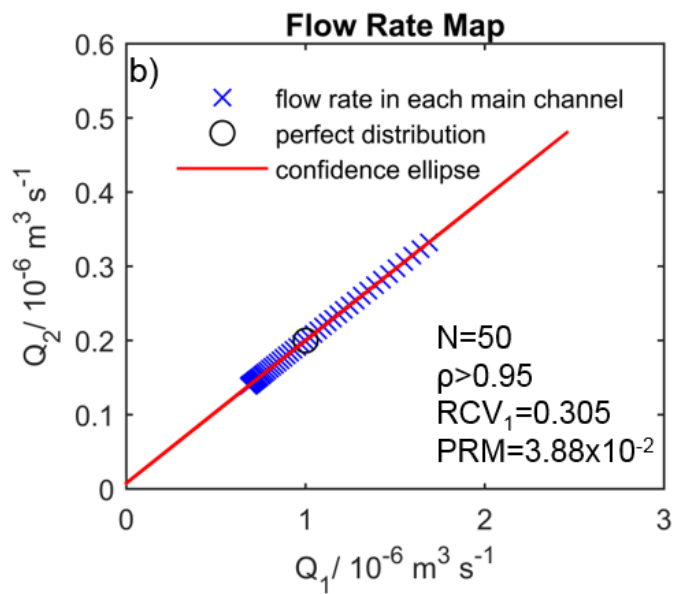
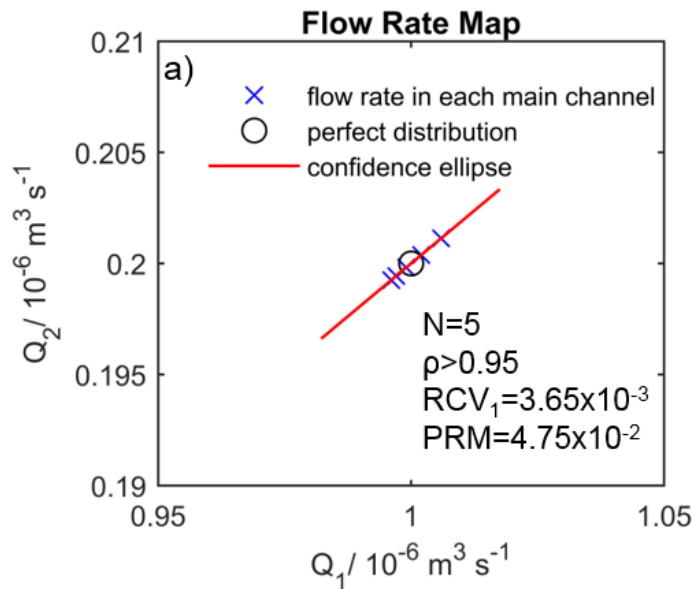


Figure 5-6 Flow rate maps for different number of main channels. For all figures, $Q_{T,1ch} = 1.2 \times 10^{-6} \text{ m}^3 \text{ s}^{-1}$, $r=5$, $R_A/R_B = 10^{-3}$, $R_B/R_R = 10^2$. In panel a) the axes do not start in the origin.

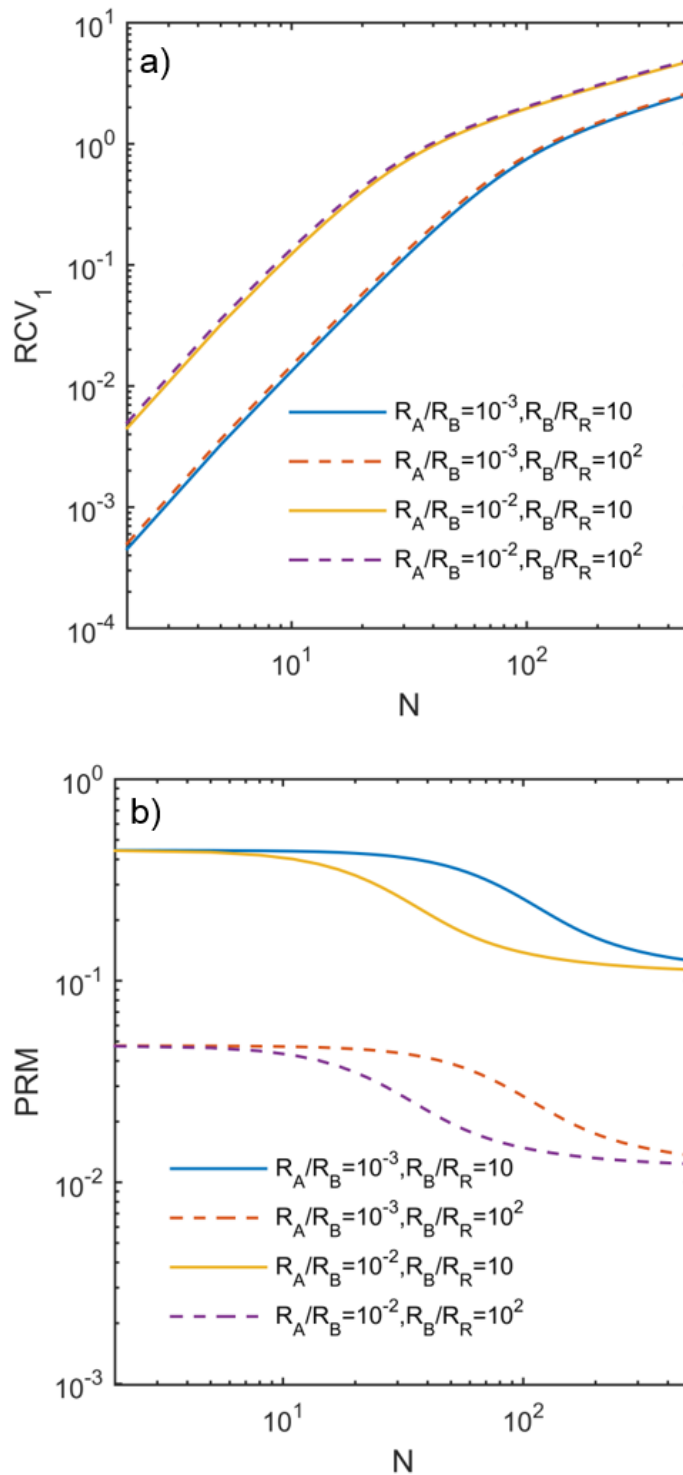


Figure 5-7 Maldistribution descriptors as functions of the number of channels for representative resistance ratios. For both panels, $Q_{T,1ch}=1.2 \times 10^{-6} \text{ m}^3\text{s}^{-1}$, $r=5$. Four combinations of resistance ratios are plotted; both types of lines (solid and dashed) have equal R_B/R_R values. For all points, ρ is larger than 0.95.

The effect of resistance ratios on flow maldistribution as the number of channels increases was also analysed. Fig. 5-7 presents the logarithmic plots of both maldistribution descriptors as functions of N for flow rate ratio equal to 5. These plots

present four cases for R_A/R_B equal to 10^{-3} or 10^{-2} and R_B/R_R equal to 10^1 or 10^2 . The results show that the trends observed for 5 channels (Fig. 5-3) also apply when N is further increased. RCV_1 depends predominantly on R_A/R_B while the effect of R_B/R_R is not significant. RCV_1 and the flow maldistribution it describes are reduced with reducing R_A/R_B values. In addition, RCV_1 increases with the number of channels; the rate of increase is high at low N values and is reduced at high N values. This trend can be explained by considering the flow rates in the main channels for $N=500$. In this case, the maldistribution is very high and some channels have flow rates very close to zero (Fig. 5-6c); as a result the increase of RCV_1 , which is statistical in nature, is not as pronounced for large channel numbers. The results for PRM in Fig. 5-7b are also in agreement with those of Fig. 5-3b. PRM depends mainly on R_B/R_R and less on R_A/R_B . PRM, and thus the distribution of flow rate ratios, are reduced when R_B/R_R is increased. PRM is constant at low values of N and reduces to a lower constant value at large values of N . This transition is also affected by the channels with zero flow rates at high N values, similar to RCV_1 described above. The value of N at which the PRM transition occurs depends on R_A/R_B .

To facilitate the use of the above observations in the design of manifolds with many parallel channels, scaling laws are suggested below, based on regression analysis. The equations will allow the design of manifolds with channel resistances that result in a given flow maldistribution or vice versa.

The variables investigated in Figs. 5-3 and 5-7 and their ranges are presented in Table 5-2. The first case examined is for inlet flow rate ratio equal to 1. The results for the whole range analysed have ρ larger than 0.95 and PRM equal to zero. Therefore, RCV_1 fully describes the maldistribution (Table 3-4). The regression coefficients are given in Eq. 5-9.

Table 5-2 Variables and their ranges used in the regressions of the maldistribution descriptors. One regression is calculated for $r=1$ and a separate regression is made for $r>1$.

Variable	Range
Number of channels, N	2 - 500
R_A/R_B	10^{-8} - 10^{-2}
R_B/R_R	10^1 - 10^7
Inlet flow rate ratio, r	1, 2 - 8

$$RCV_1 = 0.0688 N^{1.787} \left(\frac{R_A}{R_B}\right)^{0.894} \quad (R^2=0.981) \quad (5-9)$$

R_B/R_R does not appear in Eq. 5-9 because its p-value in the regression is larger than 0.05 (p-value=0.62) and it does not affect RCV_1 significantly. The exponents for N and R_A/R_B have 95% confidence intervals of $\pm 5.8\%$ and $\pm 4.6\%$, respectively. Al-Rawashdeh et al. [123] presented a similar correlation even though they measured maldistribution differently. Their correlation agrees with the results presented here, in that the exponent for N is positive and larger than one.

A second regression is performed for the same variables and the inlet flow rate ratio varying between 2 and 8 (Table 5-2). For the range of variables analysed, p is larger than 0.95. Therefore, the two descriptors, RCV_1 and PRM, contain all the statistical information needed to describe maldistribution (Table 3-4). Eqs. 5-10 and 5-11 present the coefficients for RCV_1 and PRM as functions of N, R_A/R_B , R_B/R_R , and inlet flow rate ratio.

$$RCV_1 = 0.0583 N^{1.787} \left(\frac{R_A}{R_B}\right)^{0.894} \quad (R^2=0.981) \quad (5-10)$$

$$PRM = 0.427 N^{-0.1055} \left(\frac{R_A}{R_B}\right)^{-0.0473} \left(\frac{R_B}{R_R}\right)^{-0.9954} r^{1.195} \quad (R^2=0.997) \quad (5-11)$$

Neither R_B/R_R nor the inlet flow rate ratio appear in Eq. 5-10 because their p-values are larger than 0.05 (0.48 and 0.50, respectively). The 95% confidence intervals of the N and

R_A/R_B exponents in Eq. 44 are $\pm 2.8\%$ and $\pm 2.2\%$, respectively. Since RCV_1 is independent of r , the results for one value of r apply for other flow rate ratios within the range of r considered in the regression ($2 \leq r \leq 8$). In the PRM regression, all the variables have p-values below 0.05. N , R_A/R_B , R_B/R_R , and r have 95% confidence intervals of $\pm 17\%$, $\pm 15\%$, $\pm 0.71\%$, and $\pm 5.8\%$, respectively.

With respect to RCV_1 , the regression for the cases where $r > 1$ shows very similar results to the $r=1$ case. The exponents are almost identical and the additional variable, the inlet flow rate ratio, has a very minor influence. When the flow rate ratio is larger than unity, PRM is different to zero and important for describing maldistribution. The exponent of N in Eq. 5-11 is negative and close to zero, which means that the maldistribution does not become worse as the number of channels increases. The negative exponents in the resistance ratios factors imply that PRM increases as these ratios decrease. The R_B/R_R exponent is 21 times larger than the R_A/R_B exponent; this confirms that PRM is dominated by R_B/R_R . Additionally, the exponent for R_B/R_R in Eq. 5-11 is almost -1 while, as was discussed, the pumping requirements increase linearly with R_B/R_R (Eqs. 5-5 to 5-8). This indicates that maldistribution and pumping requirements are inversely associated with each other. The flow rate ratio has the largest exponent in Eq. 5-11, which indicates effective flow distribution is harder to achieve the larger the flow rate ratio is.

The equations provide a powerful tool to assess the changes needed in the manifold design to maintain good flow distribution when the number of channels is increased. Eqs. 5-9 to 5-11 can be used to obtain scaling laws for the resistance ratios. This is done by keeping constant the maldistribution descriptor for two different numbers of channels, N_1 and N_2 . Eqs. 5-12 and 5-13 are the scaling laws for double manifolds. They calculate the changes in the resistance ratios required to maintain the flow distribution quality as the number of channels changes, for the same main channel resistance (R_R) and inlet flow rate ratio (r). The values of the exponents are given in Table 5-3 for both cases of r equal to or larger than one.

$$R_{A(N2)} = R_{A(N1)} \left(\frac{N1}{N2} \right)^X \quad (5-12)$$

$$R_{B(N2)} = R_{B(N1)} \left(\frac{N1}{N2} \right)^Y \quad (5-13)$$

Table 5-3 Values for the exponents in Eqs. 5-12 to 5-16. The choice of exponents depends on the inlet flow rate ratio, r. The uncertainties correspond to 95% confidence intervals.

Flow rate ratio	X	Y
r=1	1.998 ± 7.4%	0
r>1	1.682 ± 3.3%	0.011 ± 210%

The ratio N1/N2 in Eqs. 5-12 and 5-13 is equal to the throughput ratio of manifolds with N1 and N2 main channels. R_B does not change with the number of channels for r=1. The confidence interval for Y when r>1 is large but since the exponent is close to zero, it only has a minor effect on the R_B(N2) calculation and design. For example, when 100 times more channels (and throughput) are considered, the uncertainty on the design of R_B(N2) is around 11%.

The scaling laws proposed above are applied to the scale-out of the double manifolds modelled in Fig. 5-6. The double manifold with 5 main channels has a very low degree of maldistribution. However, when the number of channels increased by one or two orders of magnitude, the maldistribution worsened. The scale-out in Fig. 5-6 was performed by keeping the resistances constant as the number of channels increased. With the scaling laws proposed in Eqs. 5-12 and 5-13, the resistances are changed as a function of the number of channels and the improved results are shown in Fig. 5-8. The resistance ratios for the N=5 case are the same as in Fig. 5-6a, R_A/R_B=10⁻³, R_B/R_R=10². The cases with N=50 and 500, have the following resistance ratios: R_A/R_B=2.08x10⁻⁵, and 4.33x10⁻⁷; R_B/R_R=97.5, and 95.0, respectively. In all cases, the inlet flow rate ratio is 5 and Q_{T,1ch} is 1.2x10⁻⁶ m³s⁻¹. For the three cases in Fig. 5-8, ρ is larger than 0.95 and the maldistribution is described by both RCV₁ and PRM (Table 3-4).

By comparing Figs. 5-6 and 5-8 the improvements achieved with the scaling laws are evident. In the case of $N=50$, when the resistances are not scaled, RCV_1 increases 84 times from $N=5$; when the resistances are scaled, RCV_1 increases by only 12%. This is not zero because the Eqs. 5-12 and 5-13 do not fit perfectly the results of the double manifold model. Similarly, when N increases from 5 to 500 without the adjustment in resistances, the flow is severely maldistributed. In contrast, when the resistances are adjusted following Eqs. 5-12 and 5-13, RCV_1 for $N=500$ is only 4.4 times RCV_1 for $N=5$ (instead of 732 times). The results are very similar for the PRM indicator. These findings have implications on the modularity of double manifolds. Modular double manifolds designed for large throughputs will be suitable (i.e. will achieve the specified or better flow distribution) for lower throughputs while the opposite, a double manifold designed for low throughput used in high throughput applications, is not true. It should be noted that the improvements in the flow distribution are accompanied by changes in the resistances, which affect the pressure drop and power requirements; this is explored in the next section.

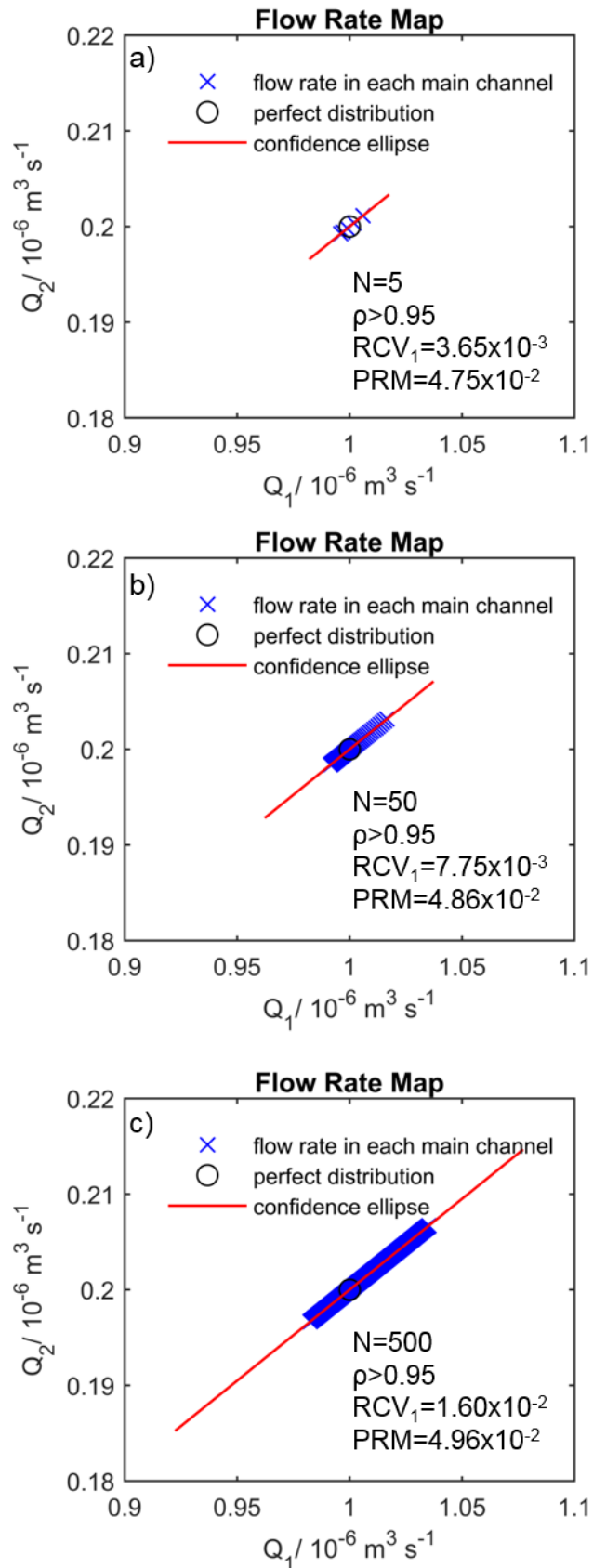


Figure 5-8 Flow rate maps of scaled-out double manifolds using the scaling laws in Eqs. 5-12 and 5-13 for $Q_{T,1ch} = 1.2 \times 10^{-6} \text{ m}^3 \text{ s}^{-1}$, $r=5$. The axes do not start in the origin. The resistance ratios are $R_A/R_B = 10^{-3}$ $R_B/R_R = 10^2$ for $N=5$, $R_A/R_B = 2.08 \times 10^{-5}$ $R_B/R_R = 97.5$ for $N=50$, and $R_A/R_B = 4.33 \times 10^{-7}$ $R_B/R_R = 95.0$ for $N=500$.

5.5 Effect of increasing number of channels on pressure drop and power requirements

The effects of increasing the number of channels on the pressure drop in the manifold and the pumping power requirements are investigated here, using the scaling laws presented in Eqs. 5-12 and 5-13. The change in pressure drop for either fluid as the number of channels increases is given by Eq. 5-14. The change in total pumping power with increasing number of channels is given by Eq. 5-15, or Eq. 5-16 for symmetrical double manifolds (with identical distributing and barrier sections for phases 1 and 2).

$$\frac{\Delta p_{i,N2}}{\Delta p_{i,N1}} = \frac{N2 \frac{R_{Ai,N1}}{R_R} \left(\frac{N1}{N2}\right)^X + \frac{R_{Bi,N1}}{R_R} \left(\frac{N1}{N2}\right)^Y + 1}{N1 \frac{R_{Ai,N1}}{R_R} + \frac{R_{Bi,N1}}{R_R} + 1} \quad (i=1, 2) \quad (5-14)$$

$$\frac{P_{T,N2}}{P_{T,N1}} = \frac{\eta_1 r^2 \left(N2 \frac{R_{A1,N1}}{R_R} \left(\frac{N1}{N2}\right)^{X-1} + \frac{R_{B1,N1}}{R_R} \left(\frac{N1}{N2}\right)^{Y-1} + 1 \right) + \eta_2 \left(N2 \frac{R_{A2,N1}}{R_R} \left(\frac{N1}{N2}\right)^{X-1} + \frac{R_{B2,N1}}{R_R} \left(\frac{N1}{N2}\right)^{Y-1} + 1 \right)}{\eta_1 r^2 \left(N1 \frac{R_{A1,N1}}{R_R} + \frac{R_{B1,N1}}{R_R} + 1 \right) + \eta_2 \left(N1 \frac{R_{A2,N1}}{R_R} + \frac{R_{B2,N1}}{R_R} + 1 \right)} \quad (5-15)$$

$$\frac{P_{T,N2}}{P_{T,N1}} = \frac{N2 \frac{R_{A,N1}}{R_R} \left(\frac{N1}{N2}\right)^{X-1} + \frac{R_{B,N1}}{R_R} \left(\frac{N1}{N2}\right)^{Y-1} + 1}{N1 \frac{R_{A,N1}}{R_R} + \frac{R_{B,N1}}{R_R} + 1} \quad (5-16)$$

The X and Y exponents are given in Table 5-3. Both the change in pressure drop and total pumping power depend on the values of N1 and N2 and not only on their ratio. The base case double manifold modelled above in Figs. 5-6 and 5-8 (N1=5, r=5, R_A/R_B=10⁻³, and R_B/R_R=10²) is used to illustrate how the pressure drop and the pumping requirements change as the number of main channels increases using the scaling laws given by Eqs. 5-12 and 5-13. As can be seen from Fig. 5-9a, the pressure drop of either phase remains almost constant with increasing number of main channels. For example for 500 main channels, the pressure drop is 0.95±10% times the pressure drop for 5 main channels. This shows that a double manifold scaled by keeping the maldistribution descriptors constant, also keeps pressure drop constant.

The power requirements, however, increase as the number of channels increases, as shown in Fig. 5-9b and the change is almost linear. The line of best fit is given by Eq. 5-17.

$$\frac{P_{T,N2}}{P_{T,N1}} = 0.2030(N2)^{0.988} \quad (R^2=0.999) \quad (5-17)$$

The 95% confidence intervals for the coefficient and exponent in Eq. 5-17 are 3.8% and 2.3% respectively. Eq. 5-17 is not a generalised scaling law because it is based on a specific case; however, it shows that despite the complexity of Eqs. 5-15 and 5-16, the pumping power scales almost linearly with the number of channels.

The almost linear increase of the pumping power with the number of channels has cost implications for the scale-out and indicates near-absence of economies of scale. Annual pumping costs depend mostly on the energy consumption (>85%) [156]; also, pumps have large scaling exponents (~0.9) on capital cost [157]. While the linearity of cost curves for the capital investment of microreactor technology had been proposed in the literature [103], the linearity of the pumping costs curve has not been shown before.

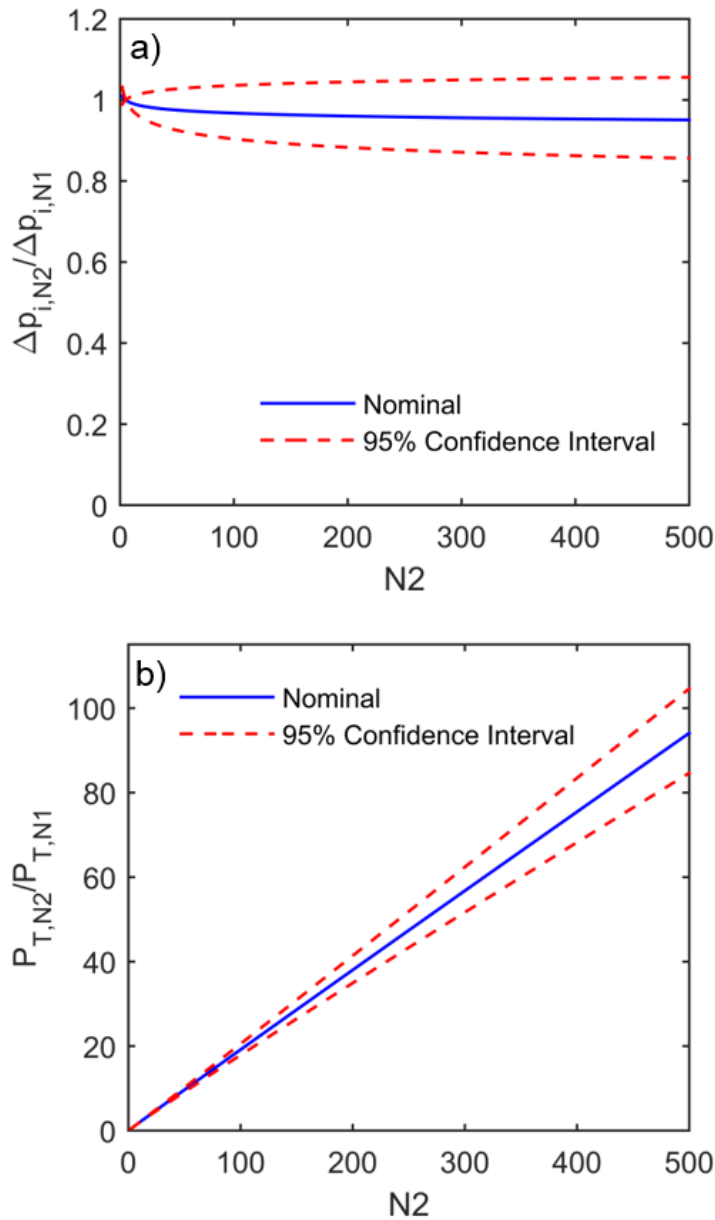


Figure 5-9 Pressure drop and pumping power requirements for scaled-out double manifolds obtained using Eqs. 5-14 and 5-16, respectively. The 95% confidence intervals lines in red dashed lines are plotted using the confidence intervals in Table 5-3. The base case has $N1=5$, $r=5$, $R_A/R_B=10^{-3}$, and $R_B/R_R=100$.

5.6 Design methodology for two-phase double manifolds

Based on the previous findings, a general methodology is proposed below for the design of double manifolds for incompressible two-phase flows or the mixing of miscible incompressible fluids. A general design methodology, including pumps and control systems selection, has been given by Zhang et al. [100].

- 1) Single-channel investigations. These studies will reveal key parameters such as optimal geometry (channel diameter and length) and flow rates for each phase

($Q_{T,1ch}$ and r) to achieve the required conversion and yield (in the case of reactors), and a function of the pressure drop with respect to the flow rate of each phase. It will be difficult to avoid maldistribution in the scale-out configurations. For this reason, it is important that the single-channel studies include a maldistribution sensitivity analysis which will show how maldistribution affects key properties, such as conversion, and what level of maldistribution parameters (i.e. RCV_1 , RCV_2 and PRM) is acceptable.

2) Design the double manifold for a required throughput. Eqs. 5-9 to 5-11 should be used to determine the hydraulic resistances of the distribution and barrier sections for values of the maldistribution parameters decided in step 1.

The coefficients of Eqs. 5-9 to 5-11 are valid if the assumptions made in Sections 3.2.1 and 3.2.2 are applicable, namely incompressible systems with a linear variation of pressure drop with flowrate. Other pressure drop equations can also be used but in this case Eq. 3-13 may have to be solved iteratively (see Section 3.2.1.1) and the coefficients in Eqs. 5-9 to 5-11 will be different.

3) Calculate the dimensions (length and diameter) of the distribution, barrier, and main channels using the resistances estimated in step 2 and the appropriate pressure drop correlation.

4) Calculate the pumping and power requirements using Eqs. 5-6 to 5-8. At this stage, the trade-off between power requirements and maldistribution parameters should be considered; if the power requirements are high, different, less stringent, maldistribution coefficients may need to be used in step 2.

5.7 Conclusions

In this chapter, the design of double manifolds (Fig. 5-1) for the scale-out of incompressible two-phase processes in small channels is studied. A statistical method, derived from principal component analysis (section 3.2.2), was developed to quantify maldistribution of both phases in two-phase flow distributors. It showed that two descriptors, RCV_1 and PRM, are relevant in most cases. The former is a measure of the total flow rate and residence time distribution in the main scale-out channels, while the latter is a measure of the distribution of the flow rate ratio in the main channels. The flow distribution was modelled using a resistance network model for incompressible flows (section 3.2.1). In the cases studied, the hydraulic resistances were considered to be independent of the flow rates and only depended on the dimensions of the channels. The methodology can also be used when the resistances depend on the flowrates, but in this case, the network model has to be solved iteratively.

Using the statistical and the resistance network methods, relationships between the design variables and maldistribution descriptors were found (Eqs. 5-9 to 5-11). It was shown that RCV_1 decreased as the ratio R_A/R_B decreased. The descriptor PRM decreased as R_B/R_R increased. Scaling laws of the hydraulic resistances for the distribution and barrier sections were also obtained which can be used to scale-out double manifolds while maintaining the same degree of maldistribution. When the scaling laws are applied, the total pressure drop of a double manifold does not change with increasing number of channels. The pumping power requirements, however, increase linearly with an increasing number of channels and throughput. The trade-off between flow maldistribution and power requirements and the implications on economies-of-scale were discussed. Based on these results, criteria for the design of double manifolds were presented.

6 Double manifold prototype and experimentation

6.1 Introduction

Following the studies on hydrodynamics and mass transfer in single small channel contactors presented in Chapter 4 and the scale-out model and methodology presented in Chapter 5, this chapter presents the development and test results of a double manifold prototype. Prototyping is a critical step in the development of novel equipment. Towler & Sinnott [157] describe how designing, assembling, and testing prototypes can help the developers (scientists and engineers) in the following tasks:

- Validate the design and identify issues that are not noticeable in models or calculations.
- Understand the manufacturing process and highlight features that may affect commercial scale manufacturing.
- Demonstrate features of a design to stakeholders and customers.
- Command further refinements needed before the final product design is selected.

Given that the number of channels is a parameter in the model presented in Section 3.2.1, the double manifold prototype can be designed to be modular with respect to the number of channels. This means the nominal throughput can vary over a wide range; this stands in stark contrast with some conventional reactor and contactor designs which are designed for a given capacity and can only operate within a small range of this value. The usefulness of capacity flexibility in one reaction or separation will depend on the variability of upstream processes and on the storage available downstream of the modular process. This change of paradigm equips the process industries with a new tool to address current and future problems.

This chapter first presents an analysis and selection of design and operation parameters for U(VI) extraction that will be used as the benchmark for the scale-out with the double manifolds. In particular, the maldistribution tolerances are selected in terms of total flow and phase ratio, considering the effect of maldistribution on extraction efficiency. Later on, the double manifold design methodology presented in Chapter 5 is

applied, using the known pressure drop behaviour (section 4.3), and its dimensions are calculated. Additional considerations for the commissioning of the prototype are considered, including entrance effects, start-up procedure, and material selection. The double manifold prototype is then tested with an inert two-phase system to assess flow distribution and with an acid-base multiphase reaction to assess the overall success of the design and commissioning techniques developed.

6.2 Design parameters and trade-offs of small-channel contactors for U(VI) extraction

Following the results in Chapter 4, an equation to determine the required length of a contactor to achieve a given extraction efficiency (Eff) is presented in Eq. 6-1.

$$\frac{L}{d} = \tau \frac{u_{mix}}{d} = \frac{\epsilon_{aq}}{(a \times d)} \frac{u_{mix}}{K_{aq}} \ln \left(\frac{1}{1-Eff} \right) = \frac{\epsilon_{aq}}{(a \times d)} \frac{Pe_{aq}}{Sh_{aq}} \ln \left(\frac{1}{1-Eff} \right) \quad (6-1)$$

where $Sh_{aq} (=K_{aq}d/D_{U|w})$ and $Pe_{aq} (=du_{mix}/D_{U|w})$ are the Sherwood and Peclet numbers defined for the aqueous (dispersed) phase. Eq. 6-1 is derived from Eq. 4-20 and the definition of the dimensionless numbers.

In order to use Eq. 6-1 for contactor design, the values of ϵ_{aq} , a , Pe_{aq} , and Sh_{aq} must be known or estimated. For the water-TBP and water-TBP 30% v/v in kerosene systems, the models in section 4.2 can be used to calculate ϵ_{aq} and a , the results in section 4.4 can be used to calculate u_{mix}/K_{aq} (or, equivalently, Pe_{aq}/Sh_{aq}). The term $\epsilon_{aq}/(a \times d)$ depends on the film thickness and the plug length (Eqs. 4-6 and 4-9). In terms of operation and design variables, it depends strongly on Q_d/Q_T , and weakly on Ca_c , μ_d/μ_c , and Re_d/Ca_c (Eqs. 4-10 and 4-11). The value of Q_d/Q_T is selected based on equilibrium reasons, rather than hydrodynamic ones. The term Pe_{aq}/Sh_{aq} , far from the inlet can be computed from the results in Table 4-4 and Fig. 4-14 for the cases tested in Chapter 4. As discussed in section 4.4.2, changes in the extractant concentration and in the flow rate ratio do not affect the K_{aq} (and thus the $u_{mix}/K_{aq}=Pe_{aq}/Sh_{aq}$) significantly. Pe_{aq} depends on the channel diameter and u_{mix} , therefore, Pe_{aq} is the main factor that can be changed to alter L/d in the right-hand side of Eq. 6-1.

The dependence of Sh_{aq} with respect to Pe_{aq} has to be further studied experimentally. As reviewed in section 2.4.1, Levich developed a model to quantify the convective flux across the interface of a moving drop [87] and determined that Sh_{aq} is proportional to $Pe_{aq}^{0.5}$ (Eq. 2-13). The experimental results in Table 4-4 ($u_{mix}=1.06$ and 4.24 cm s^{-1}), via regression analysis, indicate the best exponent for the Sh_{aq} - Pe_{aq} dependence is 0.73 with a 1- σ range between 0.48 and 0.98. According to the Final K_{aq} numerical result (Fig. 4-14), for the same conditions, the exponent should be 0.24. Therefore, the exponent proposed by Levich is approximately valid.

The logarithmic dependence of L/d on $(1-\text{Eff})$ in Eq. 6-1 means that the L/d needed to achieve 99%Eff is double that of 90%Eff; and L/d for 99.99%Eff is double that of 99%Eff. Table 6-1 shows, for the cases in Table 4-4 and two additional ones, the contactor length needed to achieve %Eff of 50% and 99%. These results show that the factor $\epsilon_{aq}/(axd)$ varies very little across the cases and thus the main factor is Pe_{aq}/Sh_{aq} . This factor ranges from 319 (for the $d=1 \text{ mm}$ case) up to 652 (for the $u_{mix}=4.24 \text{ cm s}^{-1}$ case). The length needed for 50% extraction efficiency is included in Table 6-1 because that is approximately the extraction efficiency observed after a few seconds of residence time in the channel and could be attributed to the inlet section (section 4.1.1, Figs. 4-7, 4-9, and 4-10). The Sh_{aq} for the $d=1 \text{ mm}$ and $d=4 \text{ mm}$ are estimated using the model by Levich [87].

Table 6-1 Lengths required to achieve extraction efficiencies of 50% and 99% and the corresponding factors of Eq. 6-1. The factor $\epsilon_{aq}/(a \times d)$ is calculated using imaging results (Chapter 4) and the film thickness calculated with Eq. 4-7. Sh_{aq} is calculated assuming $D_{U|w}=10^{-9} \text{ m}^2 \text{ s}^{-1}$ and the experimental K_{aq} results in Table 4-4, except for the $d=1 \text{ mm}$ and $d=4 \text{ mm}$ cases. For every case, all variables are the same as the base case, except for the stated change.

Case	$\epsilon_{aq}/(a \times d)$	$Pe_{aq} / 10^4$	Sh_{aq}	Pe_{aq}/Sh_{aq}	$L_{Eff=50\%} / \text{m}$	$L_{Eff=99\%} / \text{m}$
Base case						
($d=2 \text{ mm}$, $u_{mix}=1.06 \text{ cm s}^{-1}$, TBP 30%, $Q_o/Q_T=0.5$)	0.21	2.12	47.0	451	0.13	0.86
$u_{mix}=4.24 \text{ cm s}^{-1}$	0.18	8.48	130	652	0.17	1.1
TBP 100%	0.20	2.12	43.6	486	0.13	0.89
$Q_o/Q_T=0.333$	0.22	2.12	48.6	436	0.13	0.88
$Q_o/Q_T=0.250$	0.23	2.12	49.2	431	0.14	0.93
$d=1 \text{ mm}$	0.17	1.06	33 ⁺	319	0.038	0.25
$d=4 \text{ mm}$	0.21	4.24	66 ⁺	638	0.37	2.45

⁺ These values of Sh_{aq} are obtained using the base case and assuming Sh_{aq} is proportional to $Pe_{aq}^{0.5}$.

In Fig. 6-1, L is plotted against Eff for the base, high u_{mix} , $d=1 \text{ mm}$ and $d=4 \text{ mm}$ cases. This figure shows the fast increase of the contactor length required to achieve high extraction efficiencies. A notable case is the difference between the high u_{mix} and the $d=4 \text{ mm}$ cases; both have similar $\epsilon_{aq}/(a \times d)$ and Pe_{aq}/Sh_{aq} factors so both have similar L/d values for any given Eff . However, once L/d is multiplied by the diameter, there is a large difference in the lengths required for these two cases. The $d=4 \text{ mm}$ case requires long contactors which can be a significant expenditure in some cases, as will be discussed further below.

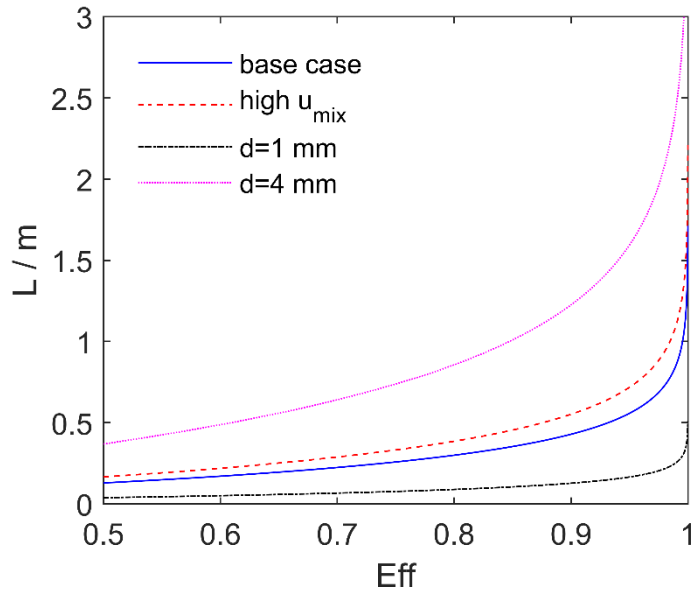


Figure 6-1 Contactor length against extraction efficiency for four of the cases in Table 6-1.

In order to design a small-channel contactor, the trade-offs between key design and operational variables must be well understood and clearly described. As discussed above, two crucial parameters are the mixture velocity and the channel diameter. Table 6-2 presents the effects that u_{mix} and d have on important variables such as the contactor length and residence time (L_{Eff} , T_{Eff}) required to achieve certain extraction efficiency, the required number of channels to achieve a certain throughput, and the pressure drop across a single contactor channel of length L_{Eff} (Δp_{Eff}). These relationships are presented as exponents of dependence where a power-law relationship is assumed and is valid for the range of conditions shown in Table 4-2. Appendix 4 includes details on how these exponents are determined.

Table 6-2 Exponents of dependence between mixture velocity and channel diameter with main channel length and residence time for a given %Eff, number of main channels for a given throughput, and pressure drop for a given %Eff.

	u_{mix}	d
Contactor length (L_{Eff})	1/2	3/2
Residence time (T_{Eff})	-1/2	3/2
Number of main channels (N)	-1	-2
Pressure drop (Δp_{Eff})	3/2	-1/2

The exponents of dependence in Table 6-2 show there are trade-offs to consider when selecting design parameters and operation set-points. In terms of mixture velocity, operating at high u_{mix} (in comparison to a base case) would require longer contactors but shorter residence time in order to achieve certain extraction efficiency. A contactor using a high u_{mix} would require fewer parallel channels but would have a higher pressure drop. In terms of channel diameter, using a larger diameter in comparison with a smaller diameter would require longer contactors with correspondingly longer residence time. In contrast, a design with a larger diameter would require fewer channels with a squared correlation, the largest exponent in Table 6-2. The pressure drop required is also smaller with contactors of larger diameters.

In terms of costs, fewer channels resulting from higher u_{mix} represent CAPEX savings, shorter residence times represent OPEX saving from solvent replacement due to radiolysis, and higher pressure drop represents higher CAPEX due to larger pumps being required and higher OPEX due to pumping energy costs. Furthermore, larger channel diameter represents higher CAPEX and OPEX due to longer channels and longer residence times, respectively. Fewer channels and lower pressure drop mean lower CAPEX and, for the pumping power expenditure, lower OPEX.

Table 6-2 clearly highlights the most important trade-offs to consider when designing multiphase small-channel contactors. The selection of the parameters will depend on a case-to-case basis considering the system and costs in hand. The most critical aspect to consider in the design of scaled-out small channel contactors is possibly the number of channels because this aspect is the least understood and developed one.

6.3 Application of the design methodology of double manifolds for mass transfer applications

This section considers the two-phase flow distributor design method presented in Chapter 5 to define the dimensions of a double manifold prototype. The final design

method is described in Fig. 6-2 in the form of a flow chart. The process can be divided into three stages, namely, input and selection, flow distribution calculations, and compliance & feasibility. In the inputs & selection stage, all the external information about the two-phase flow hydrodynamics, mass transfer and required process throughput are collated. In the flow distribution calculations stage the resistance matrix and the flow distribution are calculated, as described in section 3.2.1. Finally, the compliance and feasibility stage comprises a series of checks and, in some cases, revisions to ensure the double manifold is able to carry out the required separation.

The first step in the input and selection stage is to collect the physical properties of the fluids to be used as these properties, in particular, the viscosities are needed for the hydraulic resistance calculations. Next, the main channel nominal conditions, i.e. length, diameter, and flow rate for each phase, are selected. The acceptable tolerance of flow rate deviation for each phase from the nominal values are needed next (maldistribution tolerance, MT); these tolerances can be given in any form, including as maximum deviation of the flow rate of each phase or total flow rate and flow rate ratio deviations. Initially, the tolerances can be selected to be very tight and can be adjusted in subsequent iterations; when MTs are selected and revised, the flow pattern map should be considered in order to ensure all the main section channels will operate under the same flow pattern. The number of main section channels (N) is then selected depending on the desired throughput. As discussed in Chapter 5, a double manifold designed for a large N will provide a flow distribution inside the tolerance for distributors with a smaller number of channels; however, for a larger number of channels, the maldistribution will be higher than the tolerance. The next step is to select the dimensions, i.e. diameters and lengths, of the distribution and barrier sections channels. The initial values of these dimensions, for varying values of N, could be obtained from the values of R_A and R_B in Fig. 5-8 or other examples of effective double manifolds, like the one presented below in section 6.4.

The flow distribution calculations stage begins with the calculation of the hydraulic resistances of the A and B sections given their dimensions. Since these sections only have single-phase flows, the Hagen-Poiseuille equation (Eq. 3-14) can be used, however, it is important to verify that the Reynolds numbers in the channels are low enough to have laminar flow and, if the channels are vertically-oriented, that the effect of gravity can either be neglected or it has to be considered. Next, the steps to calculate \mathbf{Q} (Eq. 3-13) are described. These steps differ from the method described in Chapter 5 because R_R is not assumed to be independent of the flow rate. An initial estimate is obtained in two steps. First a perfect distribution is assumed (\mathbf{Q}_{ideal}) simply by dividing the flow rate for each phase and the total flow rate by N . \mathbf{Q}_{ideal} is then used to calculate $R_{R,j}$ using the selected segmented flow pressure drop model and subsequently, $R_{R,j}$ is used to calculate the flow rate vector using Eq. 3-13 and the result is called $\mathbf{Q}^\#$. This result is then used as the initial estimate in an iterative procedure where the difference is compared to a tolerance and when the difference is below the tolerance, the \mathbf{Q} calculated is the resulting flow distribution.

The final stage, compliance and feasibility, starts by checking the resulting flow distribution, given by \mathbf{Q} and its metrics (maldistribution descriptors, MD), against the maldistribution tolerance. If the distribution is not within the tolerance, the dimensions of the distribution and barrier sections should be changed. Fig. 5-3, which shows the relationship between resistances and maldistribution, can be used to guide these changes. If the total flow rate is the main issue, changes in the relative hydraulic resistances of the A and B sections will be needed; otherwise, if the main issue is the flow rate ratio, the B section should be changed without changing R_A/R_B . If the distribution is indeed within the tolerance, the next step is to calculate the power and pumping requirements, as described in section 5.3. It may be the case that the design considered achieves a good flow distribution but the pumping costs are prohibitively high; in this case, it may be necessary to relax the maldistribution tolerances in order to achieve a pragmatic and practical design. A significant amount of detail (e.g. pump and motor

costs, electricity costs) may be needed in order to know if the pumping requirements are too high but it is an important trade-off that needs to be considered. In general, this stage can be performed automatically with an optimisation routine but special attention should be put to verify that the models used (Hagen-Poiseuille and the selected two-phase pressure drop) apply for the conditions being considered.

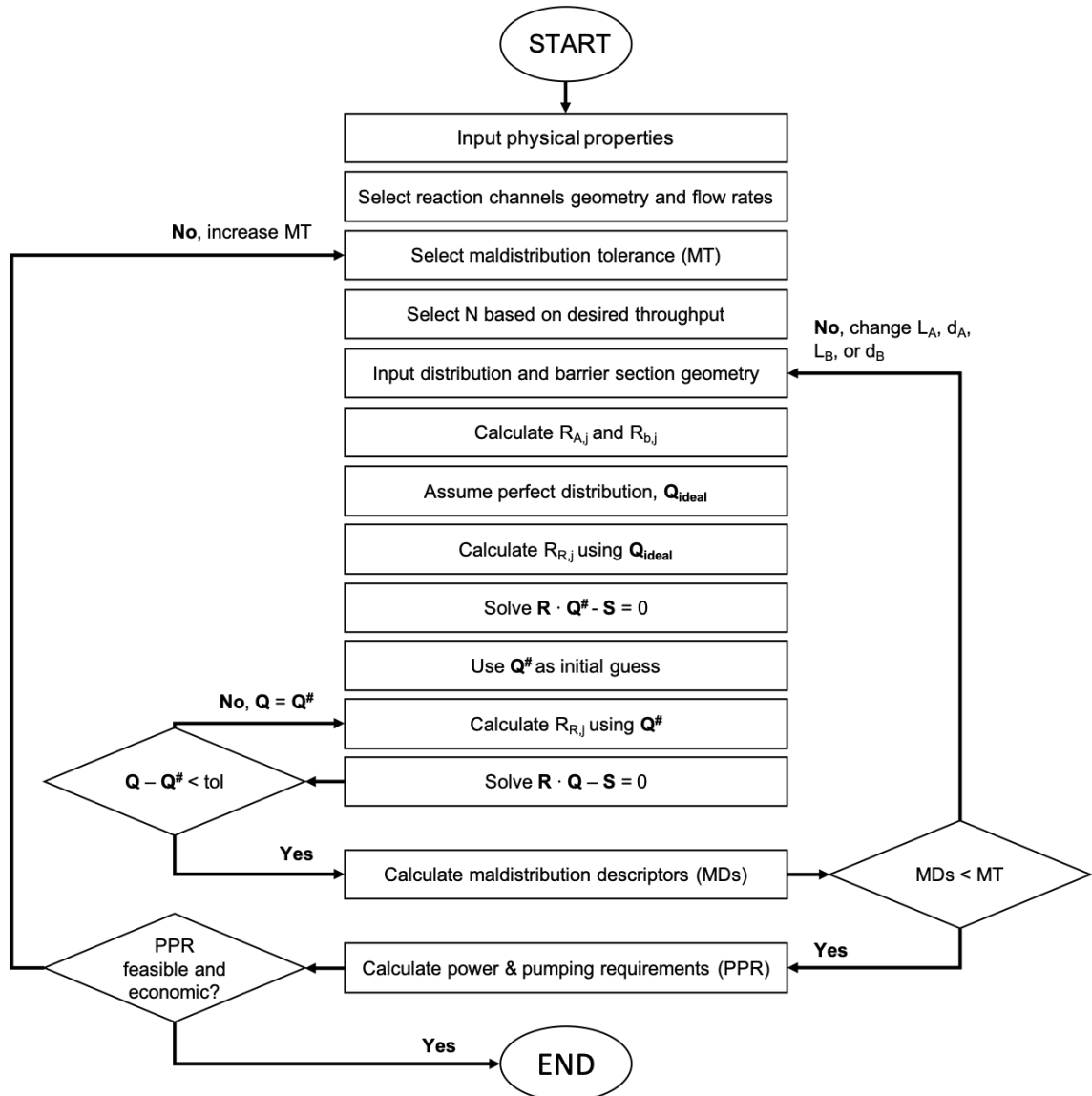


Figure 6-2 Flow chart showing the sequence of inputs, calculations, and decisions needed to design a double manifold using the resistance network model and a non-linear pressure drop model in the main section.

The method described in Fig. 6-2 is used to design a double manifold prototype. The main channels in the prototype are selected to be 2 mm internal diameter and 60 cm length, which would allow for high %Eff to be achieved in a wide range of cases. The same fluids and range of flow rates as in Chapter 4 will be considered. The plug and unit

length correlations and the pressure drop model presented in Eqs. 4-1, 4-3, 4-16 will be used. The maldistribution tolerances are taken as 1% deviation from the nominal total flow rate and flow rate ratio. The design will be based on a scale-out of 100 parallel channels. The calculations are implemented using Matlab. The design methodology is implemented using the flow chart in Fig. 6-2 and the set of requirements discussed in the previous paragraph. The fluid properties of TBP 30% and water (saturated with TBP 30%) are used because the models in Chapter 4 were obtained with these fluids. For different liquids, the pressure drop model would need to be checked. Alternatively, correlations available in the literature (e.g Kreutzer et al. [89], Jovanovic et al. [97], Mac Giolla Eain et al. [98]) can be used. The flow distribution is initially simulated with the diameter and length of the distribution section as 10 mm and 50 mm, respectively. The barrier section has a diameter of 1 mm and a length of 120 mm. These dimensions are selected to have high R_B/R_R and low R_A/R_B ratios (Fig 5-3) and tubes with these diameters are available commercially. The tolerance to find the flow rate distribution using the Matlab function 'fsolve' is set to 10^{-12} . The solution converges after 13 steps and is shown in Fig. 6-3 a. This distribution does not satisfy the specified maldistribution tolerance in terms of flow rate ratio. The next step is to change the diameter of the barrier section to 0.5 mm, which increases the R_B by a factor of 16. This diameter is selected as it is the next smaller commercially available. The distribution to this geometry is obtained again and the convergence is faster, only two steps. The distribution is shown in Fig. 6-3 b. This case satisfies both maldistribution requirements. The pumping power is interestingly reduced, even though the diameter of the barrier section is decreased while the total flow rate and the rest of the geometry remained constant. The reason for this is the fact that there are fewer reaction channels with high flow rates (deviating from the nominal one), which cause high pressure drops (and their corresponding non-linear pressure drop).

An extra step is done, increasing the diameter of the distribution section to 20 mm, in order to further improve the flow distribution. Similarly to the barrier case, this

diameter is available commercially. The solution converges after 1 step as the $Q^{\#}$ distribution is very similar to the final result, even with the tight tolerance used. As shown in Fig. 6-3 c, the distribution is much better and the pumping power requirement is unchanged. The latter effect is because the distribution section has a lower pressure drop than the barrier channels. The dimensions of the last double manifold simulation are used to commission a prototype, as described in the following section.

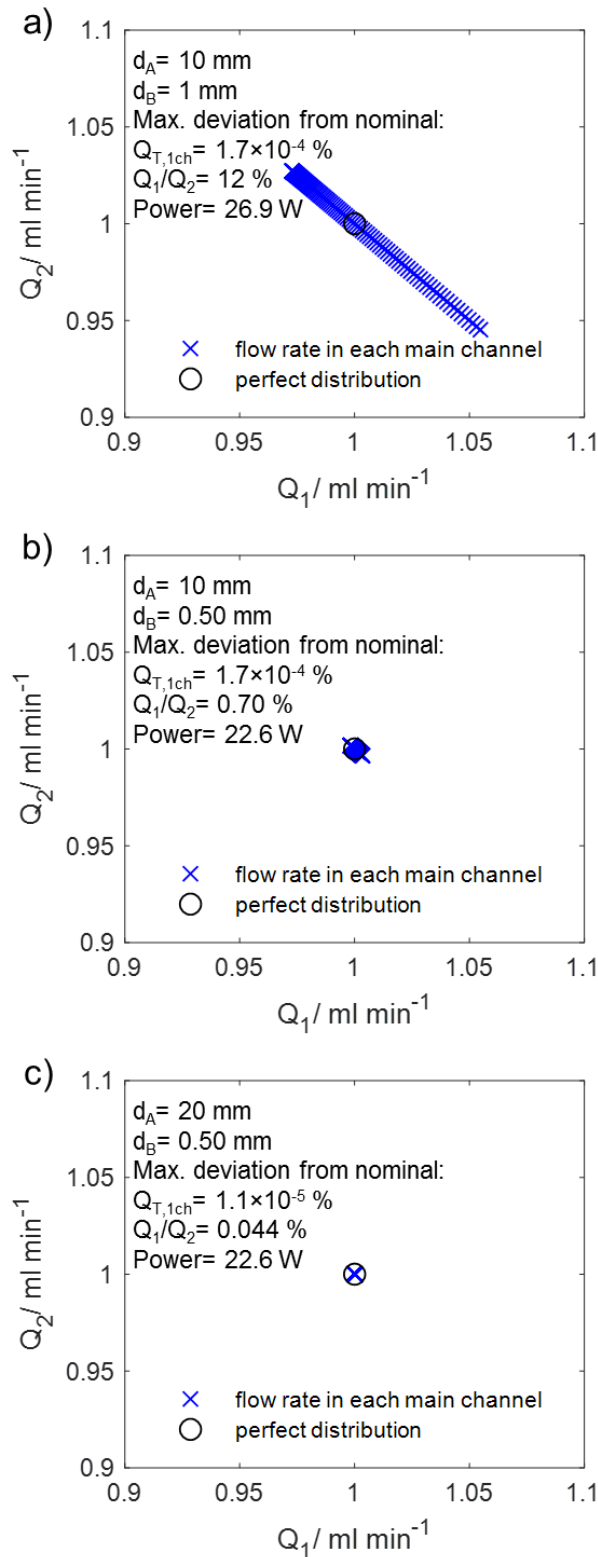


Figure 6-3 Flow distributions for double manifolds using the models in Chapter 4 and the flow chart in Fig. 6-2. Fluid 1 is the organic phase (TBP 30% v/v with kerosene) and fluid 2 is water. In all cases, the geometries are $L_R=600 \text{ mm}$, $d_R=2 \text{ mm}$, $L_A=50 \text{ mm}$, and $L_B=120 \text{ mm}$. In a), d_A and d_B are 10 and 1 mm. In b), d_A and d_B are 10 and 0.5 mm. In c), d_A and d_B are 20 and 0.5 mm.

The procedure followed to achieve the final geometry and distribution in Fig. 6-3 c is partially trial-and-error as well as using Fig. 5-3 to inform how to improve the distribution. This procedure could be performed automatically by finding an optimal double manifold geometry, however, the objective function would require additional information (e.g. costing) which is unavailable at the prototyping stage. At this stage, this procedure yields the best results with the simplest procedure.

6.4 Design and commissioning of a modular double manifold prototype

The method followed in section 6.3 gives, as a result, a set of dimensions for the double manifold. However, additional issues need to be considered for the final design and commissioning of the double manifold prototype, which are discussed here. The prototype was partly made in the High Precision Design & Fabrication Facility at the UCL Engineering Faculty. The double manifold design should also be modular and allow easy start-up.

In order for the prototype to be modular, the distribution section must be expandable. One option would be to add shut-off valves along the distribution sections to allow or shut the flow along the distribution channels. This approach can be expensive as the distribution section has a large diameter and several valves would be needed; the equipment would then have a large footprint regardless of the throughput. The approach selected here is to make the prototype modular by dividing the distribution section into 5-main channel subsections, connected with flanges. The advantage of the flanges is that there is no disruption in the internal diameter. One disadvantage is that the flanges take up some space. Since the distance between outlets in the distribution section should be constant, irrespective of the presence of flanges, the shortest distance between distribution section outlets is limited by the flange size. A schematic and photographs of the flange connections are presented in detail in Fig. 6-4 b. All the connections have threads for 1/4-28 flat bottom fittings, as shown in Fig 6-4 b ii.

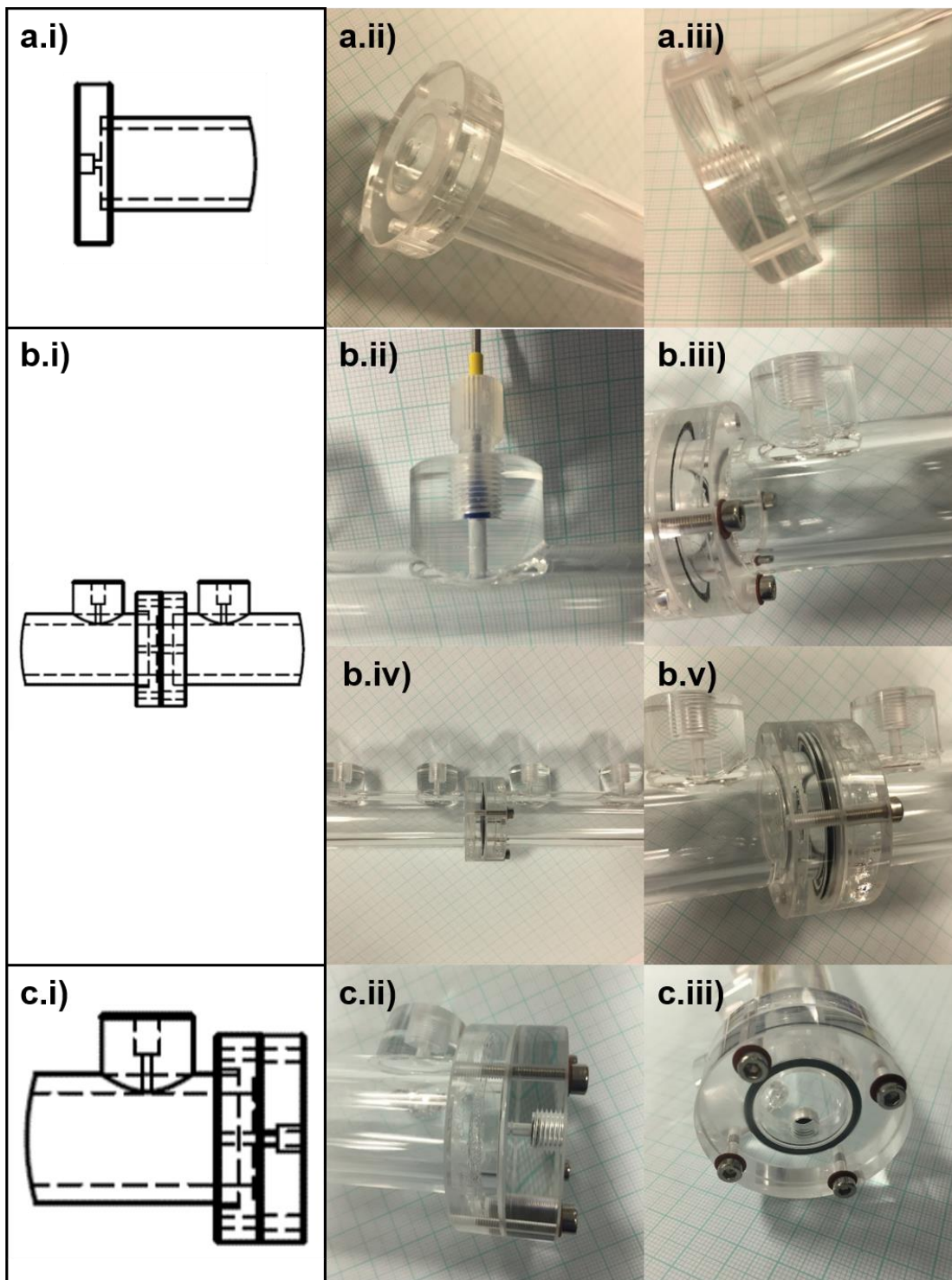


Figure 6-4 Details and features of the distribution section of the double manifold prototype. The inlet and part of the inlet section are shown in a). The flange connections used to make the prototype modular and the detail of the barrier outlets are presented in b). The end-port, opposite to the inlet, used in the fill-up procedure is presented in c)

Fill-up refers to the step after the double manifold is assembled, when each section is filled with the respective liquid displacing the air present. To avoid entrainment of one liquid into the barrier or distribution sections of the other liquid, shut-off valves are

added in the barrier sections. The pressure drop when the valve is open should be included for in the barrier section hydraulic resistance; the valve when open should preferably have approximately the same internal diameter as the barrier channels. The shut-off valves used were supplied by IDEX (part number P-782) (Fig. 6-5 b). The air displacement in the distribution sections is also a challenge. A large fraction of the air can be displaced from each distribution section through the barrier channels and then through the main channels. However, some air would remain in the distribution section. To remove the trapped air, an extra port was added at the end of the distribution sections, opposite to the inlet (Fig. 6-4 c). This port is kept open during the fill-up procedure and for the last few bubbles of air, the double manifold was physically tilted to allow the air to be displaced. To avoid tilting the manifold, the extra port could be placed facing upward; this is suggested as a feature of future design iterations. In this additional port, a pressure-relief valve could also be installed. In the design stage detailed here, such feature was not necessary as the experiments were closely observed and each test had a short duration.

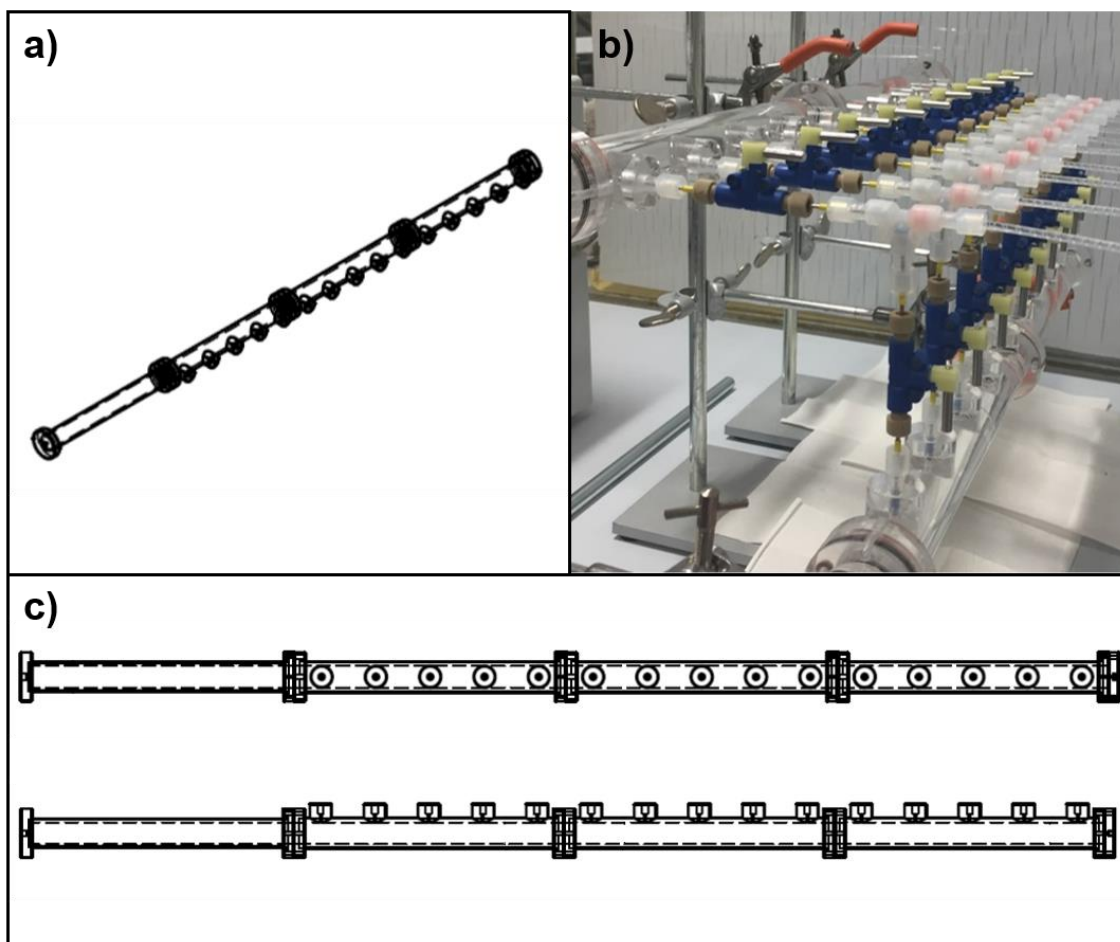


Figure 6-5 Distribution section and operating double manifold. One distribution section, including the entrance section, is presented in a). The double manifold in operation, with the shut-off valves open, is shown in b). Front view of the distribution sections are depicted in c).

The start-up procedure refers to the series of steps that must be followed from the fill-up stage up to the time when the contactor has reached steady-state. To the best of the author's knowledge, there is no mention in the available literature on how to perform the start-up procedure of multiphase, multi-channel contactors. Initially, the distribution and barrier sections are filled-up with their corresponding liquids, the valves in the barrier sections are shut-off and the pumps are off. The first step is to start the pumps and set the flow rate to $1/N$ times the required flow rate for each phase. Then, the barrier valve furthest away from the inlet is opened for one liquid and then the other liquid. This step should last until the segmented flow pattern is established in the main channel further away from the inlet. The next step is to increase the pumps flow rates by increasing the flow rates by $1/N$ of the objective flow rates. The next furthest valves are opened for each liquid and the step lasts until segmented flow is established in the

second channel as well. The procedure is repeated until all the valves are open and the main channels are operating in slug flow. This start-up procedure was developed experimentally; it was found that opening the furthest channel from the inlet was necessary to achieve segmented flow in all main channels. Other methods, such as opening the valves closest to the inlet first, were tried and were found to be ineffective.

The materials selected for each section depended on the purpose of each section. The main section channels are made of FEP, as in the experiments in Chapter 4, since they allow visual access to the flow pattern, important for the tests with the prototype. The main disadvantage is their flexibility and need of support to keep them straight; in fact, the channels retained some curvature from their packaging and some differences in the pressure drop will be due to this. This is an important characteristic that needs to be considered in further prototype iterations. For the barrier section, stainless steel is used as these tubes have high reliability in their dimensions. Furthermore, their rigidity allows for an easier assembly and more reliable pressure drop calculations than similar plastic tubes. Finally, the distribution section was made of Poly(methyl methacrylate) (PMMA) because it is transparent, rigid and a suitable material for the dimensions needed. These tubes are available at specific internal diameters and the design had to consider this. After the distribution sections were finished, as shown schematically in Fig. 6-4 a and c, they were thermally treated to remove stresses and improve their durability. The final prototype is shown assembled in Fig. 6-5 b. The final dimensions and the materials used are presented in Table 6-3. The factor L/d^4 is included for reference as this factor appears in the hydraulic resistance calculation (Eq. 3-14).

Table 6-3 Description of the materials and dimensions used for the three sections of the double manifold prototype. The final column is included because the L/d^4 factor is part of the hydraulic resistance calculation.

Section	Material	Internal diameter (d) / mm	Length (L) / mm	L/d^4 / mm^{-3}
Distribution (A)	Poly(methyl methacrylate) (PMMA)	20	50	3.1×10^{-4}
Barrier (B)	Stainless steel	0.5	120	1.9×10^3
Main (R)	FEP	2	600	3.7×10^1

An additional feature included in the double manifold prototype is an entrance section that allows a parabolic velocity profile to develop between the inlet from the pump and the first barrier outlet. The entrance length, (L_e), required to achieve the parabolic profile in laminar flows is given by [88]:

$$\frac{L_e}{d} = 0.035 \text{ Re} \quad (6-1)$$

The entrance length depends on the total flow rate of each liquid. For the prototype, the entrance section is 240 mm long and the distance from the entrance to the first barrier section is 270 mm. With the dimensions above, the largest Reynolds number the current design can accommodate is 386. Taking water at room temperature as an example, the largest flow rate this design can work with is 364 ml/min. The entrance section is depicted in Figs. 6-4 a and 6-5 a and c.

6.5 Experimental flow distribution performance of modular double manifold

The double manifold prototype, depicted in Figs. 6-4 and 6-5, was used to distribute a water and kerosene two-phase flow into 5 and 10 channels; three flow rate ratios were used in the tests while the total flow rate was kept constant. The results of the flow distribution are presented in this section while the results on mass transfer are presented in the next section. The water-kerosene fluid pair has different properties to the water-TBP 30% pair. The coefficients for the models in Chapter 4 are not known for the water-kerosene pair so the distribution cannot be predicted as in Fig. 6-3. However, the same equations were used to avoid repeating the experiments with large amounts of TBP.

The flow distribution is assessed by measuring the volume rate of each phase at each of the main channel outlets. Both these measurements take place after the start-up procedure is completed and a steady-state flow in all the channels is achieved.

In Fig. 6-6, the flow distribution of the tests are shown for 5 channels, total flow rate per channel of 2 ml min^{-1} and flow rate ratios (Q_w/Q_o) of 1, 2, and 3. The plots include the point of perfect distribution, the results of three tests under the same conditions, the confidence ellipse (plotted using the average angle (Eq. 3-24) and the axes lengths (Eqs. 3-28, 3-29)) and average maldistribution metrics (Eqs. 3-26, 3-27) for the three tests. Similar results are presented in Fig. 6-7 for tests with 10 channels and the same nominal flow rates per main channel as in Fig. 6-6.

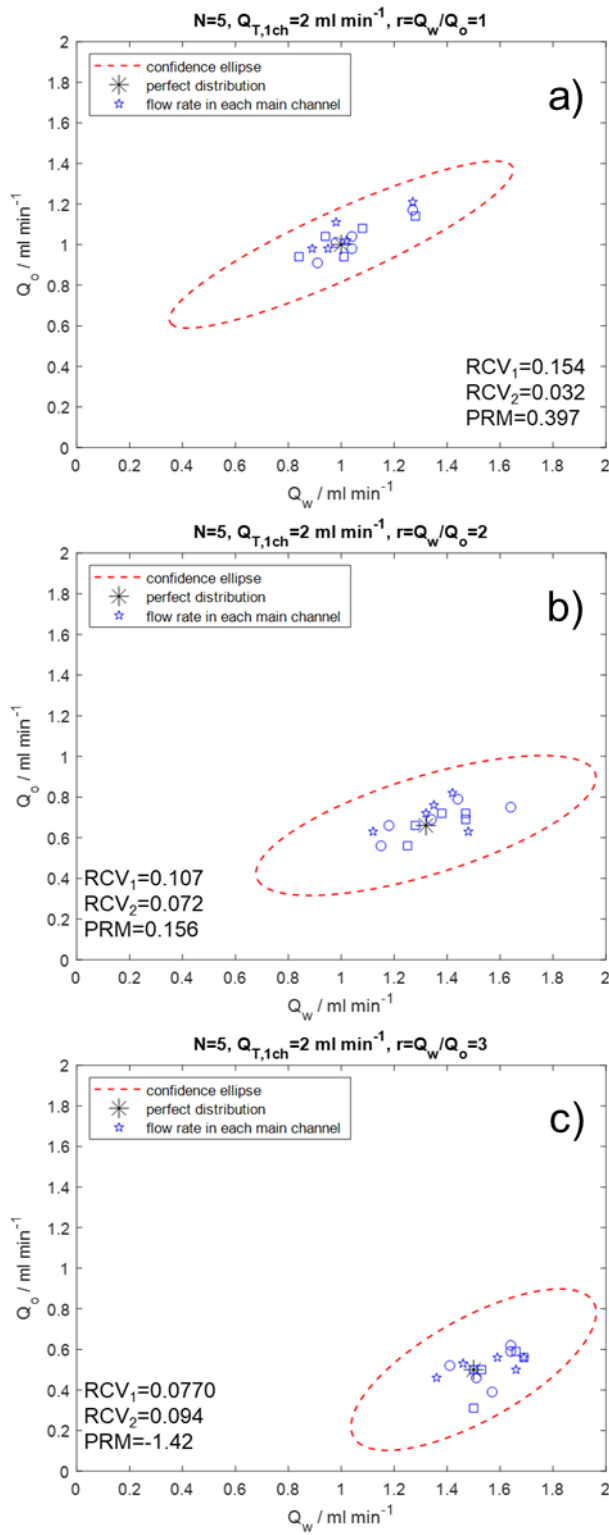


Figure 6-6 Experimental flow distribution results for double manifolds with 5 channels. The point of perfect distribution is shown in all cases and is the centre of the confidence ellipses. The square, circle and star symbols represent the measurements for each test. The maldistribution descriptors (RCV₁, RCV₂, PRM) presented are the mean values for the three tests. The ellipse angle and axes lengths are also the mean values for the three tests.

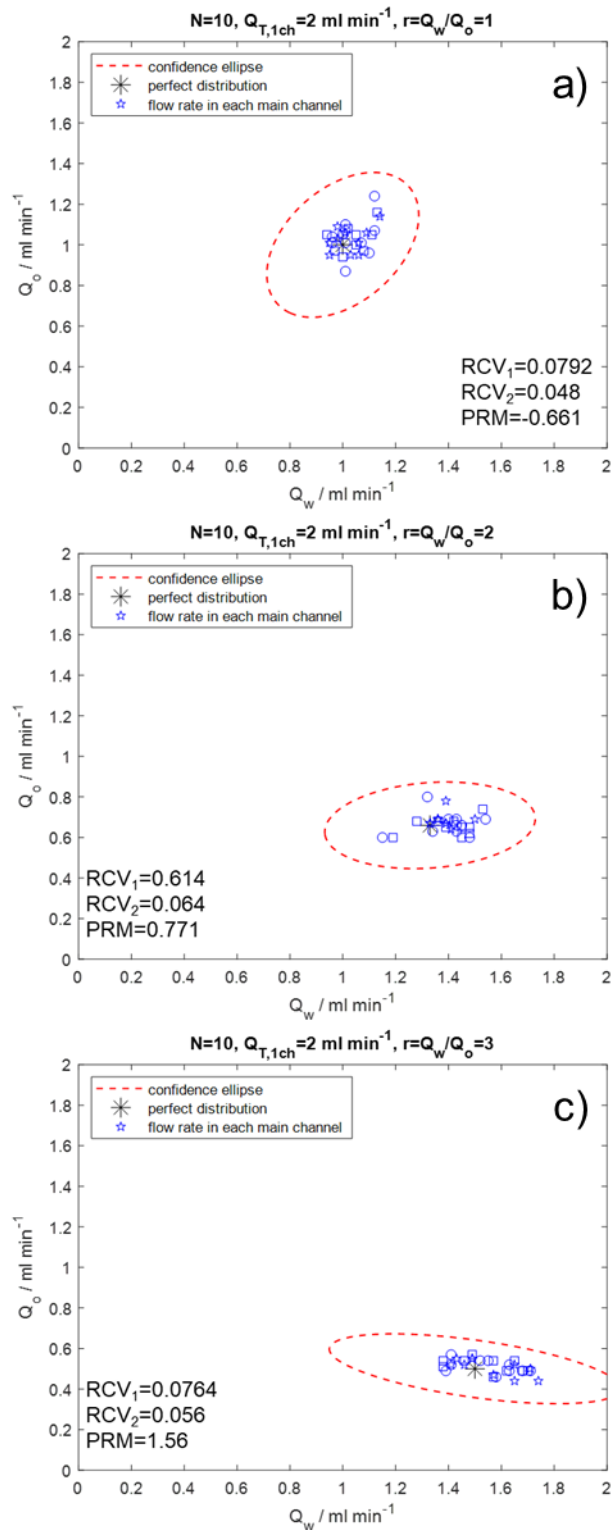


Figure 6-7 Experimental flow distribution results for double manifolds with 10 channels. The point of perfect distribution is shown in all cases and is the centre of the confidence ellipses. The square, circle and star symbols represent the measurements for each test. The maldistribution descriptors (RCV_1 , RCV_2 , PRM) presented are the mean values for the three tests. The ellipse angle and axes lengths are also the mean values for the three tests.

The three tests conducted for all cases are relatively consistent and no outliers are present (i.e. all the channels showed segmented flow). The distribution metrics are larger than the resistance ratios would predict and are not within the tolerances set in the previous section. However, it should be noted that more tests would result in slightly different confidence ellipses and maldistribution descriptors. The increase of the aqueous to organic flow rate ratio on the configuration with 5 channels is to decrease RCV_1 while RCV_2 increases; this means the ellipse becomes rounder, which is clear Fig. 6-6. This effect is not so noticeable with the 10 channels configuration. The PRM does not appear to follow a trend in either configuration. The effect of the number of channels is also not very clear. The RCV_1 , for $r=1$, decreases by a factor of 1.9 when 10 channels are used instead of 5, while for $r=3$, the RCV_1 is practically the same. The PRM is consistently closer to zero in the $N=5$ cases than the $N=10$ cases for each case. Even though the flow maldistribution is constrained around the perfect distribution points, as expected, the results in Figs. 6-6 and 6-7 indicate that the experimental flow distribution deviates from the model predictions. These deviations are to be expected because the model does not consider some flow aspects. These include the differences between the main channels (as they are slightly curved because they are made from FEP), the pressure drops not considered in the resistance network (for example in bends or expansions) and fabrication tolerances. However, all the flow rates are centred very close to the perfect distribution points and the results are consistent between tests.

These results show that the double manifold prototype can be used successfully and with a high degree of consistency to distribute two liquids into the main channels. The flow distribution is affected by the imperfections in the prototype but these results serve as a proof that this prototype and the method used to develop it can lead to a viable product without major changes.

6.6 Scaled-out reactive extraction using a modular double manifold

The test system selected to show the effectiveness of the prototype for mass transfer applications is a reactive extraction system consisting of an aqueous phase with

potassium hydroxide (KOH) and phenolphthalein (In, $pK_a^{In}=9.7$ in water [158]) as indicator, and an organic phase consisting of kerosene and acetic acid (AcOH, $pK_a^{AcOH}=4.756$ in water [158]). At the inlet, the aqueous phase has a high pH ($pH_{inlet}=12$) and is bright pink ($pH_{inlet}>pK_a^{In}$). When the two phases meet and flow in a segmented flow pattern, the acetic acid is transported from the organic phase to the aqueous phase where it dissociates ($pH_{inlet}>pK_a^{AcOH}$). The H^+ ions from the acetic acid dissociation neutralise some of the OH^- ions and the pH decreases. When the pH is at or slightly below pK_a^{In} , the aqueous phase loses its colour because the phenolphthalein is colourless in these conditions. The evolution of the colour along a channel is shown schematically in Fig. 6-8. Similar acid-base-indicator systems have been used before to study liquid-liquid mass transfer in microfluidic devices [153,159–163].

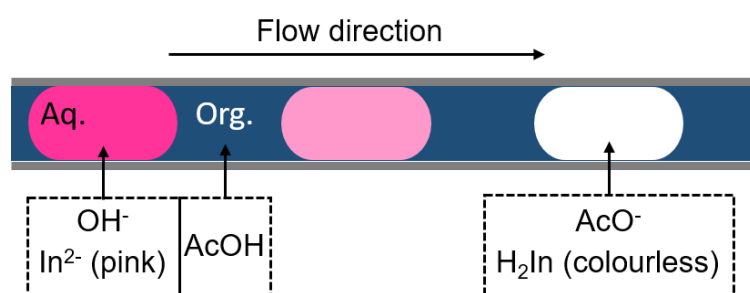


Figure 6-8 Schematic of in-flow reactive extraction of acetic acid (AcOH) in the organic (continuous) phase to the alkaline aqueous (dispersed) phase and the consequent colour change of the phenolphthalein indicator (In^{2-} to H_2In).

In the current case, the acid-base-indicator system is used to assess how the imperfect flow distribution affects the mass transfer in each channel. The differences among the parallel channels with respect to the total flow rate and the ratio of the phases determine the distribution of the positions in the main channels where the aqueous phase becomes transparent. Photographs of the double manifold prototype in operation, assembled for 10 channels, using the acid-base indicator system are presented in Fig. 6-9.

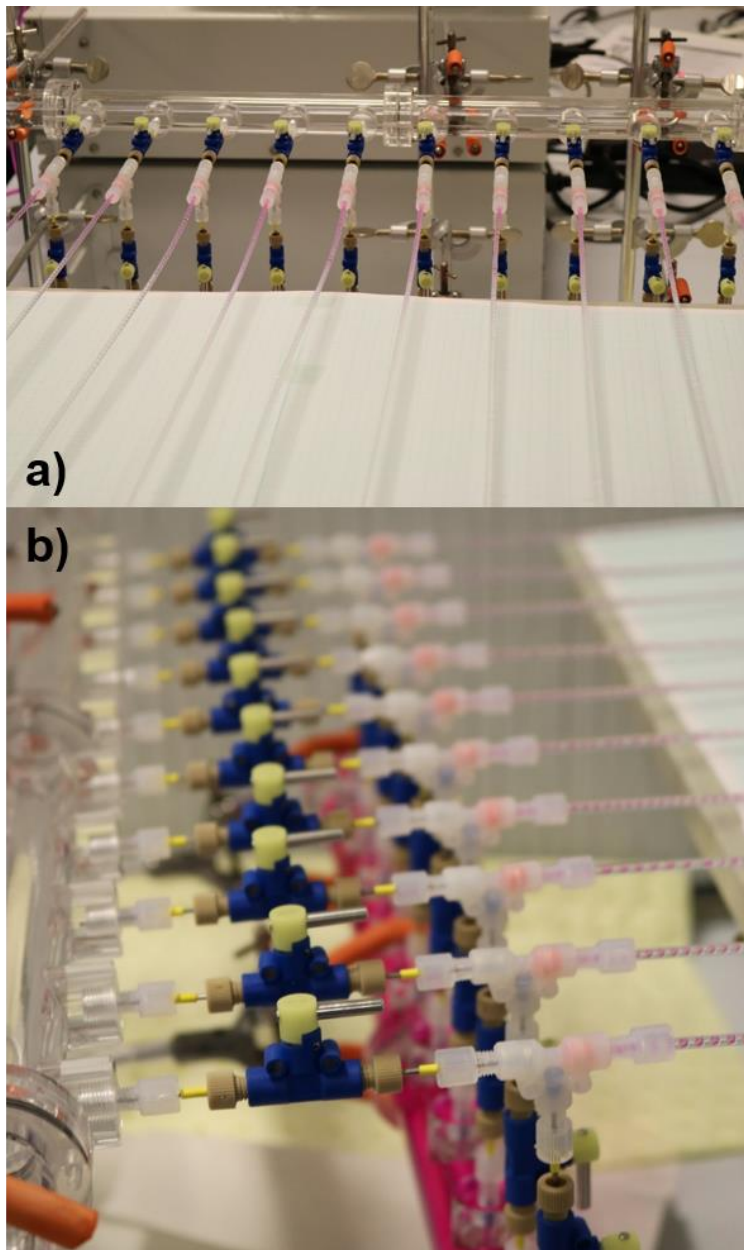


Figure 6-9 Photographs of the double manifold prototype with 10 channels operating using the acid-base-indicator system. In a) the change of colour is noticeable along the channel length. In b) the detail of the tubing-fitting connections and drop characteristics are shown.

The distribution of the positions (measured from the tee-junction) where the aqueous phase becomes transparent is used to assess the effectiveness of the double manifold prototype. The properties of both liquid phases used in this section are very similar to ones in the previous section so the flow distribution in sections 6.5 and 6.6 are expected to be comparable. Fig. 6-10 presents the results of 4 experimental conditions, each tested twice. The 4 experimental conditions correspond to two flow rates ($Q_{T,1ch}=1$ and 1.5 ml min^{-1}) and two main channel numbers (5 and 10 channels). In all cases the

inlet flow rate ratio 1. Each graph represents one test, each mark represents the length measured for each channel from the T-junction, the mean is shown as the middle bar and the standard deviation is shown with the top and bottom bars. The coefficient of variation for each test is also shown in the graphs.

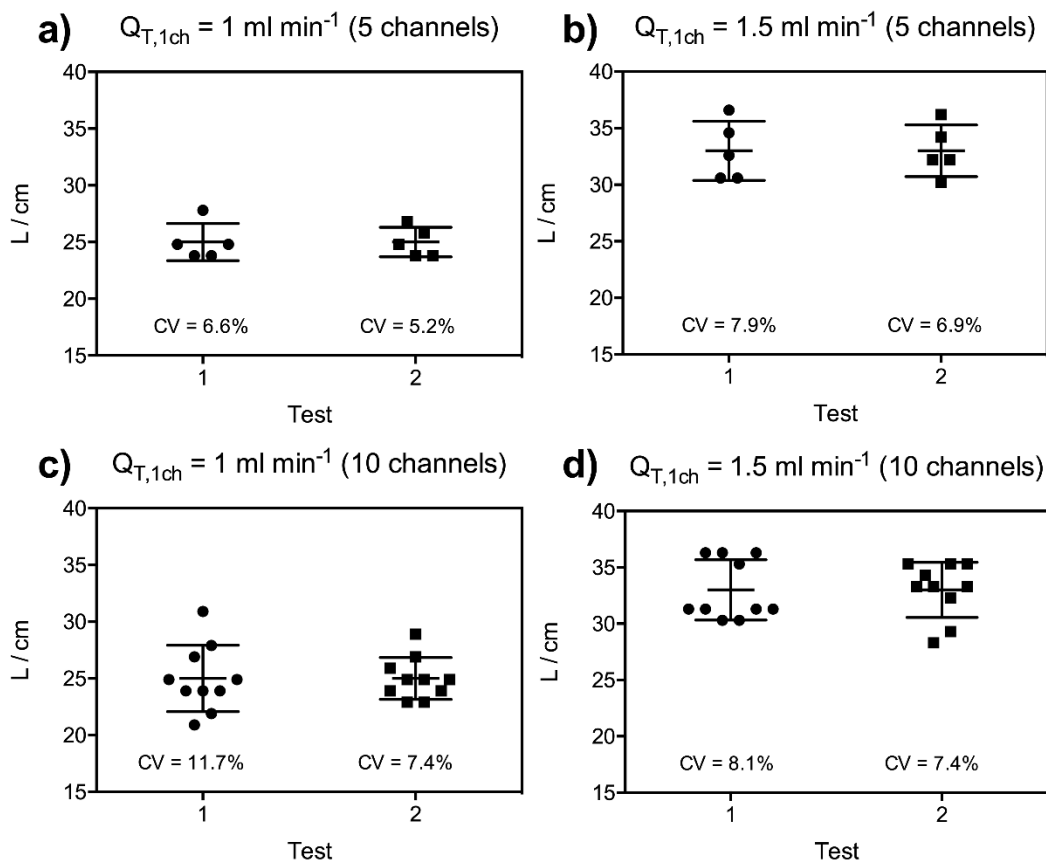


Figure 6-10 Distance from the tee-junction where the aqueous phase becomes colourless in the acid-base-indicator reactive extraction experiments. The bars represent the means and standard deviations. a) presents the case N=5, $Q_{T,1ch}=1$ ml min⁻¹. b) presents the case N=5, $Q_{T,1ch}=1.5$ ml min⁻¹. c) presents the case N=10, $Q_{T,1ch}=1$ ml min⁻¹. d) presents the case N=10, $Q_{T,1ch}=1.5$ ml min⁻¹. Note the y-axis starts at 15 cm.

The results in Fig. 6-10 show that the aqueous phase becomes colourless at similar positions in all cases tested. Increasing the total flow rate by a factor of 1.5 increases the length from the tee-junction where the aqueous phase becomes colourless by approximately a factor of 1.3. This has a close correspondence to the predicted value using the exponents of dependence (Table 6-2). The exponent of dependence for u_{mix} is 0.5 so the predicted factor would be $(1.5^{0.5})=1.22$. The variation of the distance among the channels is different for each test but there are two trends, one for each experimental

variable. In terms of flow rate, the tests with higher flow rate have a higher CV, except for test 1 in Fig. 6-10 c. This indicates there may be an effect but it is possibly weak. In terms of the number of channels, the tests with a larger number of channels have a higher CV, with no exception, which indicates the effect is possibly stronger. The higher CV for the cases with more channels is to be expected according to the double manifolds model (Eqs. 5-9 and 5-10).

As mentioned in the previous section, these results correspond to prototype tests and should only be used to partially assess quantitatively and demonstrate the capabilities of the design, rather than characteristic or nominal values for the design. Even considering this, it is necessary to determine if the results in Fig. 6-10 show that the prototype is a viable option. The challenge is that there is no clear benchmark to assess these results. One option is to compare the distribution of the lengths with the residence time distribution (RTD) of ideal reactors. The measured variances (square of the CVs) are comparable to the variance of the RTD because these contactors operate under segmented flow and the phase of interest is the dispersed phase so the behaviour is expected to be similar to that of plug flow reactors (PFRs). The variance of the RTD of single-phase CSTRs is 1 while that of single-phase PFRs is 0 [164]. The average variance (average of the square of the CVs) for the results in Fig. 6-10 is 6.2×10^{-3} . Clearly, the measured variance is very close to the RTD variance of an ideal plug flow reactor. While further studies are required, these results with up to 10 channels and low CVs show there is significant potential for this type of contactor.

The results presented here show this scale-out approach and the double manifold prototype are suitable to scale-out relatively simple solvent extraction and acid-base solvent extraction processes. Nevertheless, additional research is needed to determine if this approach and might be acceptable to other, more complex, reactive liquid-liquid processes. In processes where selectivity is important, because there may be parallel or consecutive reactions happening, the sensitivity to flow maldistribution may be amplified. These systems, however, may actually be the main candidates to be scaled-up using a

double manifold since the route towards very narrow flow distributions (and also residence time distributions) is made clear in the methodology developed here (e.g. Fig. 6-2).

6.7 Conclusions

This chapter presents the design and testing of a double manifold prototype for two-phase flows based on the findings of Chapters 3 to 5. The mass transfer results in Chapter 4 are used to determine the dimensions of the main channels and the trade-offs to consider when selecting design and operational variables. Furthermore, the design method initially developed in Chapter 5 is applied for the case of a known segmented flow pressure drop model. This results in a set of dimensions for the double manifold sections but these dimensions do not consider additional restrictions that come from building the prototype, such as using commercially available tubing, the need of an entrance length and the specification of fill-up and start-up procedures. Commissioning restrictions are discussed along with the start-up procedures and the materials and final dimensions are presented. The prototype is tested, both in terms of flow distribution and for mass transfer. These results serve as a proof-of-concept of the design method described at the end of Chapter 5.

There are two main findings from the work in this chapter. First, the resistance network model developed in Chapter 3, applied numerically and used to derive the design method in Chapter 5 is robust, as shown by the results in sections 6.5 and 6.6. This design method can be further refined, as described in Chapter 5, to include other types of resistances, such as bends, expansions, contractions, and junction effects. However, the model as used here, captures most of the effects and proved successful when used to design, commission and test a double manifold. These refinements should be considered in further prototype iterations. The second point is that the double manifold prototype presented here surpasses all the previous attempts in the literature to scale-out a two-phase system in segmented flow (reviewed in section 2.7). The scale of the tests performed here and the embedded modularity feature ensure this design can have

a significant commercial impact in a relatively short time frame. Further commercialisation remarks are included in Chapter 7.

7 Conclusions and future work

7.1 Conclusions

This chapter provides an overview of the findings in this thesis and draws conclusions on the research questions addressed in Chapters 4 to 6. The research objectives, outlined in section 1.3, are used to guide the discussion.

The first objective is to review and expand the literature on liquid-liquid small-channel flows for separations. The relevant literature is reviewed in Chapter 2 and mentions important industrial applications of liquid-liquid processes and key parameters to consider in their design and operation. In particular processes, the hydrodynamics and mass transfer in processes under the segmented flow pattern are discussed in detail. Chapter 2 ends with scale-up considerations; first, challenges regarding economies of scale are reviewed, followed by scale-up strategies, which include numbering-up; finally, previous multiphase scale-out studies are discussed. This chapter outlines relevant benchmarks both in terms of contactor performance and scale-out. Benchmarks for conventional equipment are presented in Table 2-2 and results for intensified segmented flow contactors are presented throughout sections 2.2.2 and 2.4. As for scale-out, a scale comparison with both conventional and intensified contactors is presented in section 2.7, including Table 2-4, where various cases are compiled. The multiphase scale-out with the largest number of channels reported in the literature has eight channels by Su et al. [120]. The gaps in the literature are discussed at the end of Chapter 2 and additionally in Chapters 4 to 6.

The second objective is to characterise both flow and mass transfer of the liquid-liquid segmented flow pattern in small-diameter channels. This objective was addressed in Chapter 4 along with the review presented in Chapter 2. High-speed imaging is used to measure the most important characteristics of segmented flow, namely, the plug and slug lengths. From the experiments, correlations between L_p/d and $1-L_p/L_u$ with Q_c/Q_T , μ_d/μ_c , Ca_c , and Re_c/Ca_c are developed, expressed in terms of dimensionless numbers.

The correlations were analysed and it was shown both Q_c/Q_T and Ca_c have the strongest influence on the segmented flow geometric characteristics; this was supported by a comparison of previous models available in the literature (Table 4-3). These correlations were used to propose models for the dimensionless unit length, holdup, and specific interfacial area. Furthermore, the hydrodynamic characterisation included the pressure gradient inside channels under segmented flow. Available models were shown to have limitations in terms of the variables they depend upon and the channel diameters used to obtain them. A new empirical model, based on the periodicity of the flow pattern, is obtained and shown to closely correspond to the experimental data while previous models were shown to be inaccurate for the experimental systems tested. The pressure gradient model developed here must be further tested in order to be used as a tool for the design of flow distributors for small-channel contactors. In order to characterise the mass transfer, the extraction efficiency (%Eff), the volumetric mass transfer ($K_{aq}a$), and the mass transfer (K_{aq}) coefficients were measured under several conditions (section 4.4). The extraction efficiency depends on the mixture velocity, residence time, and the concentration of extractant used. The mass transfer coefficients were determined experimentally for a range of residence time between 5 and 20 s, thus independent of inlet effects; it was found the mass transfer coefficient depends strongly on the mixture velocity but not to changes in the concentration of extractant used or flow rate ratio. The values for K_{aq} are between 2.18×10^{-5} and $6.5 \times 10^{-5} \text{ m s}^{-1}$. A CFD model implemented in Comsol Multiphysics ® was used to better understand the effects found in the mass transfer coefficients. The mass transfer close to the inlet was found to significant because most of the solute is close to the interphase at the beginning of the process. The findings were compared and contrasted with examples in the literature in similar devices and in conventional contactors. One of the most important conclusions is that the mass transfer coefficients are not especially large in small-channel contactors compared to conventional contactors, however, the large interfacial areas available in small channels provide these contactors with their characteristically large mass transfer rates that have been frequently reported in the literature. Additional advantages, in particular, the narrow

residence time distributions, may be the greatest assets of these contactors. The flow and mass transfer characterisation achieved in this thesis provides a framework of tools for contactor design as well as operation parameter selection.

Objective number three is to develop a method to design multiphase flow distributors. The motivation for this objective is shown in Table 2.4; industrially- and economically-relevant small channel contactors would need to operate in the order of hundreds or thousands of parallel channels in approximately the same conditions. This is far from being achieved in the available literature, where the few examples of multiphase scale-out contactors are under 10 channels. A robust scale-out method is still needed to scale out a large number of channels. A methodology is presented in Chapter 3 to design manifolds for two-phase flows. The methodology (section 3.2.1) is based on a resistance network model of the double manifold (Figs. 3-6, 5-1). The flow paths, mass balances, and energy balances are solved to give the flow rates in every channel of the double manifold. In addition, an advanced multivariable statistical tool (section 3.2.2), adapted from principal component analysis, is used to quantify the maldistribution in the channels. Both tools are used together in Chapter 5. In the first instance, the effect of the double manifold design for a fixed number of channels ($N=5$) is analysed. The conditions where channeling is observed are described and the effect of resistance ratios is demonstrated, for example, Fig. 5-3 is presented as a guide to improve the flow distribution in double manifolds. The pumping head and power requirements for different designs are both quantified and identified as the main trade-off when designing double manifolds. In particular, the dimensionless pumping power requirements are found to be almost inversely proportional to the phase ratio maldistribution metric. The second part of Chapter 5 presents an analysis of the effects of changing the number of channels and how to design a double manifold for as many channels as required. Scaling laws are proposed to design double manifold for a large number of channels given the design for a smaller distributor. The trade-offs with respect to pumping power are quantified also for the case where N is a variable, it is found there is an absence of economies of scale

in terms of pumping requirements. The tools developed and analysed in Chapters 3 and 5 are used to propose a design methodology for two-phase distributors and is further described in algorithmic fashion in Chapter 6 (Fig. 6-2). The results found in Chapter 5 strictly apply to the case where the hydraulic resistance is independent of the flow rate in all the sections. This is not the case in the segmented flow pattern (section 4.3) but it is necessary to understand this case in order to address more complex ones.

The fourth objective is to design and test a multiphase flow distributor prototype with a larger capacity than the examples available in the literature. The prototype development and the tests conducted using it, presented in Chapter 6, accomplish this objective. The initial step is to determine the single-channel length required to achieve a specific extraction efficiency. Table 6-1 shows how long a contactor should be to achieve different extraction efficiencies for the cases studied in Chapter 4; on the other hand, Table 6-2 generalises from this to propose exponents of dependence for different design variables depending on mixture velocity and channel diameter. These results highlight some important design trade-offs in small-channel contactor designs. The design methodology proposed in Chapter 5 is applied in Chapter 6 and a flow chart (Fig 6-2) is presented as a tool to follow the sequence of steps and decision to make along with the design. In particular, three feedback loops are identified, the first one takes into consideration the non-linearity of the pressure drop model with respect to flow rates. The second loop considers if the flow distribution quality achieved is within tolerance. The final loop then checks if the geometry selected is economical in terms of pumping requirements. The prototype is designed for a specific range of conditions (flow rates, flow rate ratios, total throughput); the design methodology can, however, be applied for other cases and situations. The procedure to select the geometries is shown, starting from a given geometry, the flow chart is followed until a geometry is found where the tolerances and requirements are met. Having tested the prototype, the fill-up and start-up procedures are described; this knowledge is out of reach from a steady-state model and as so it is crucial to report it in order to advance this technology. The prototype was

successfully used to further identify aspects of the method that can be improved in the future. Since the manufacturing of the manifold was completed in-house, there are learned lessons in the design stages, the manufacturing stages, and up to the test stages. The double manifold prototype is tested both in terms of flow distribution and in its ability to handle two-phase flows with mass transfer. These complementary results show that, even though there is space for improvement, the scale-up of the manifold is successful. The flow distribution experiments, shown in Figs 6-6 and 6-7, clearly demonstrate good flow distribution is achieved but there are deviations from the model. It is suggested these deviations are a result of factors not considered in the model, such as expansions and contractions, turns, and differences in the tubing. The experiments with an acid-base reaction use the same fluids as the flow distribution ones except for KOH, acetic acid, and phenolphthalein are added to the solutions. The result measured was the distance it takes for the solution to become colourless (starting from bright pink). The results show the flow distribution helps achieve a very narrow distribution of the length needed (Fig. 6-10). Additionally, the mass transfer results corroborate the exponent of dependence for L_{Eff} and u_{mix} , first proposed in Table 6-2. The capacity of the double manifold is modular, this has important implication to this objective. Not only do the tests with 5 and 10 channels (2 mm I.D.) presented in Chapter 6 have a larger throughput, operating in segmented flow, than any previous attempt available in the literature (reviewed in section 2.7.3), the design methodology would allow for even larger throughputs to be processed.

The final objective is to summarise and communicate the advantages, disadvantages, challenges and trade-offs of the multiphase processing technology developed in this thesis. These are presented in Table 7-1. The advantages listed are only the ones found in this work and do not necessarily include the ones previous authors may have identified for segmented flow contactors. The disadvantages stem from the fact that agitated tanks and columns are simple to build and the double manifolds are more complicated. This is an unavoidable disadvantage that needs to be considered

when a double manifold contactor and a conventional contactor are compared. The challenges listed are further described in the next section. The trade-offs listed must be considered when a double manifold is being designed.

Table 7-1 Summary of advantages, disadvantages, challenges, and trade-offs identified for multiphase processing technologies operating under segmented flow (Taylor flow) and scaled-up using double manifolds.

Advantages	<ul style="list-style-type: none"> ○ Fast mass transfer, short residence time ○ Narrow residence time distribution ○ High degree of reproducibility ○ Ability to handle relatively high-viscosity solvents ○ No density difference requirement ○ Large surface area, simple heat management and high potential for photochemical reactions ○ Potentially smaller volume and inventories required ○ Modular throughput ○ Fast process development from test to production
Disadvantages	<ul style="list-style-type: none"> ○ Many pieces in the double manifold, potentially difficult and expensive to manufacture at larger scales ○ Detailed pressure drop modelled are needed ○ Several expansions, contractions, and turns lead to potentially high pumping costs
Challenges	<ul style="list-style-type: none"> ○ Remaining scale-up uncertainty ○ Untested in a large range of conditions ○ More research needed around the mixing zone ○ Flow separators based on membranes is still expensive ○ Fill-up and start-up procedures requiring 2xN shut-off valves – expensive ○ Demonstrate scalability to large scales ○ Demonstrate the effect and suitability of diverse main channel materials
Trade-offs	<ul style="list-style-type: none"> ○ Pressure drop and flow distribution ○ Detailed pressure drop model and cost of obtaining them for new systems

7.2 Future Work

This section outlines the steps to follow in the development of intensified small-channel contactors based on the results presented in this dissertation. The steps are divided according to the range of scales explored in this thesis, described in Fig. 1-3. The future work outlined here addresses topics worth investigating in the whole spectrum of R&D, some are more suitable for fundamental academic research while others are geared towards facilitating commercial impact.

-Transport phenomena: Fluid dynamics & Mass transfer.

There is significant research so far at the transport phenomena and fluid dynamics scales, as demonstrated in Chapters 2 and 4. The further research and development steps that can be taken at this scale should be informed by the challenges at the larger scales in order to realise more readily the commercial potential of this technology. Three key areas to work forward at this scale are; the characterisation of the mixing junction, in particular the mass transfer and pressure drop; the validation of the pressure drop model presented in section 4.3 with other systems and in different conditions; the study of a diverse range of geometries, systems, and operating conditions.

A significant fraction of the mass transfer takes place very close to the mixing junction. The %Eff results, in section 4.4.1, show that, in most cases, more than 40% of the possible extraction takes place in the first 5 seconds of residence time. The mass transfer coefficient close to the mixing zone, calculated using the numerical model described in section 4.4.2, can be up to one order of magnitude larger than the mass transfer coefficient far from the mixing zone (Figs. 4-13 and 4-14). This finding should be used to inform design decisions to optimise the contactor in order to further reduce the mean residence time required for a certain %Eff. The results in Chapter 4 are restricted to tee-junctions with the same diameter as the main channel; these channels do not have to scale together and this is an area that can be studied further to find optimal designs.

Other mixing configurations and morphologies could be considered and compared with tee-junctions regarding their potential in practical contactors. The pressure drop at the mixing junction also needs to be evaluated and included in the resistance network model developed in Chapters 5 and 6. None of these research directions are completely novel and research is already available, however, what is missing is a demonstration of the available results and models to larger channel sizes and commercially-relevant systems.

The pressure drop model, presented in Chapter 4, is based on the observation that the segmented flow pattern is regular and the pressure gradient inside the channel can be modelled as a periodic function. The model is dimensionless and depends on variables that can be measured accurately. Figs. 4-4 and 4-5 show this model is also precise and accurate for the conditions tested, which include a wide range of channel diameters, flow velocities, and flow rate ratios (Table 4-2). However, the model has only been validated with one inlet configuration, two liquid pairs, and three channel internal diameters. The pressure gradient under segmented flow pattern for more fluid pairs with a large range of dimensionless numbers (Re , Ca , $\mu_c/\mu_d\dots$), more channels sizes, and more inlet configurations should be obtained to further validate the model. Furthermore, the coefficients in Eq. 4-15 are empirical (obtained with via regression analysis of experimental data). If this model is to be used in other systems, a first-principles model should be developed to explain the good agreement of this model with the experimental data. The exclusive use of easily accessible measurements, namely, plug and unit lengths as well as fluids properties, should be continued.

As mentioned above, there is abundant research at this scale; one interesting step forward would be to create or adapt tools to facilitate the development of multiphase processing technologies. Two tools, one experimental and one computational are described here. The experimental tool, whose value and need is made clear in Chapters 3 and 4, is a plug-and-play, modular optical sensor kit that could precisely and accurately measure plug and slug lengths as well as plug frequency (and thus plug velocity). Such a tool would be a low-cost replacement to the high-speed camera used in this work. The

'plug-and-play' aspect is a requirement if it is to be used with different channels. The modularity means several sensors should be placed in parallel channels to have simultaneous measurements of many channels, this would be useful to test further prototypes as in Chapter 6. In some cases, this tool would be used in parallel to a high-speed camera to ensure reliability and reproducibility. The use of this fast and low-cost tool would also allow for more data points to be obtained and therefore be able to test and develop more reliable models of the segmented flow pattern. There are examples of such optical sensors to make measurements in segmented flow processes (e.g. [165,166]) but they have not considered their application in scale-out. The numerical tool that can be proposed from the work at the mass-transfer scale is to develop a library of plug-slug geometries in Comsol Multiphysics ® and simulate the mass transfer in a model similar to the one used in section 4.4.2. These results could be used to reverse engineer mixing junctions and operating conditions in order to achieve optimal mass transfer conditions. These results could be further implemented in a computational-assisted-design tool that could find the optimal design and operating parameters for specific multiphase processes. These tools would enable the study of a wider spectrum of conditions as testing becomes simpler and less costly. Surely, new opportunities will be found as more systems, with different behaviours and properties are studied.

-Scale-out: Flow rate & ratio maldistribution.

Steps forward at the scale where flow distribution happens, which ranges from fluid dynamics scales and up to process equipment scales, are more fundamental than the previous scale because less research has been conducted. While the configuration of the double manifold (Fig. 5-1.) has several advantages, it would be important to carry out resistance network models and similar analyses to the ones conducted in Chapter 5 to other configurations. Another important step forward at this scale is to review the assumptions made in the development of the models (section 3.2) and study the effect of fabrication tolerances and flow disruptions. Finally, while the trade-off between flow maldistribution and pumping power was clearly established in Chapter 5, a case study

with real manufacturing, maldistribution, and pumping costs is needed to further clarify their relationship.

The double manifold configuration used throughout Chapters 3, 5, and 6 is only one of many possibilities. Studying other configurations, such as having the feed of each phase opposite to each other, or in the middle, or having the distribution section as a bifurcation manifold, could reveal the advantages and disadvantages of each configuration. The advantage of having developed maldistribution metrics (section 3.2.2) that are independent of the distribution section and correlate straightforwardly to process performance metrics will allow for fast screening of the manifold configurations described above.

The assumptions used to develop the models and analyse their results capture the key aspects of the flow distribution problem. However, moving forward will require for the resistance network model to consider the effects of inlets, mixing, expansions, contractions, bends, fabrication tolerances and even time-dependent effects such as pulsing from the pumps and channel blockages. The pumping power calculations also include a simplified model (section 5.3). More refined models would be needed in future studies. Chapter 5 considers only linear pressure gradients (with respect to flow rate) but sections 3.2.1.1 and 6.3 presents an iterative solution that can solve for more complex pressure gradient models. These iterative methods should continue to be used, and if possible refined, in any future modelling work. Advances in these directions will increase the confidence in these design tools and will facilitate the expansion of this technology to different systems (including gas-liquid, solid-gas-liquid, solid-liquid-liquid) and a wider range of processes (absorptions, reactions, reactive extractions, flow chemistry including photochemistry).

Finally, one important step forward at this scale is to do a techno-economic analysis of a case study where the trade-off between maldistribution and pumping requirements is quantified (Chapter 5). This would require to select a specific application in order to quantify the costs of having residence time and flow rate ratio differences

among parallel channels in the main section of a double manifold. The costs of manufacturing, especially after considering fabrication tolerances, must be included in this study. The findings of such a case study would inform design decisions for double manifold prototypes.

-Prototype: Design, build, improve novel reactor.

This scale includes processing equipment, including manufacturing, and instrumentation. This scale is where the least information is available. There are three directions to move forward and each one of these involves a wide range of activities. The first direction is to implement the recommendations to improve the prototype, outlined in Chapter 6. The second one is to follow-up from the aforementioned scales and to improve the design as well as develop a tool to obtain optimal designs. Third; considering the scale-out needed requires hundreds and even thousands of channels; design, test, and improve a prototype that can handle these numbers of channels.

Proposing recommendations for the prototype, after going through the design, manufacturing, and testing processes (Chapter 6) is the main reason the prototype was developed in the first place. These recommendations will guide the future work for this prototype to make it more effective, more practical and, especially, safer. The recommendations include: Adding a pressure relief valve and an air outlet (for fill-up) facing upwards. Implement a method to make sure all the main channels are the same (to minimise pressure differences among main channels). Where back-pressure is used, appropriately select the materials and test the prototype. Implement automatic valves for ease of fill-up and start-up.

The design methodology for double manifold contactors, developed in Chapters 5 and 6, was proven successful with the flow distribution and mass transfer results in Chapter 6. However, the design obtained and used to manufacture the prototype tested is not necessarily optimal in many ways. For example, the footprint of the contactor was not considered among the variables while the pumping requirements were only justified

as feasible but not optimised. In order to improve the double manifold design, the optimal main channel design and operating conditions for mass transfer should be implemented. These decisions will be informed by the other future work outlined above in this section. Furthermore, an optimisation tool could be developed and used to propose optimal double manifold designs and operating parameters.

The ultimate goal of this research is to be able to have the advantages of intensified small-channel contactors be applied to large, commercial-scales and compared against conventional contactor technologies. As reviewed in Chapter 2, this means the scale-out required is above 100 channels to have comparable throughput with commercially-available contactors. The double manifold configuration used in this thesis expanded to hundreds or thousands of channels would need to be extremely long and inconvenient even though feasible considering that the results in Chapter 5 refer to manifolds of up to 500 channels. For this reason, a multi-level double manifold would be the best solution at those throughput scales. Schematics for multi-level double manifolds are presented in Figs. 7-1 and 7-2. The dimensions used in these schematics follow the ones used in the prototype (Chapter 6) and may not be accurate for a final multi-level double manifold design. A multi-level double manifold consists of several double manifolds stacked vertically and feeds on a single source for each fluid. This configuration could be modelled with an appropriate resistance network and, in general, similar work as the one presented in Chapters 5 and 6. There is significant work to do before an optimally designed multi-level double manifold is tested but it will most definitively be possible after following the steps described in this section.

-Select commercial applications, protect IP.

The technology shown in this thesis may have significant commercial potential, especially if the steps above are followed. To take the technology forward its commercial potential needs to be shown by selecting a profitable commercial application to demonstrate it; this would entail protecting the intellectual property (IP) of the invention involved.

While the advantages of scale-out multiphase contactors are clear, in order to replace current technologies there should be a substantial profit margin. Case studies must be identified to carry out a comparative analysis. Since the most important advantages are related to the increased safety and improved quality control of the processes while the important remaining challenges are around the scalability to very large throughputs, three important process industries to look at are nuclear reprocessing, fine chemicals and pharmaceuticals for the large potential impact in comparison to conventional processing. The nascent field of urban mining, extracting useful materials (i.e. critical raw materials) from urban waste, could also be considered as it could be a significant source of resources in the present century [167,168] and is in line with the SDGs presented in Fig. 1-1.

Protecting the IP developed in this thesis and after the aforementioned future work is completed is of paramount importance. This requires collaboration with the technology transfer office at UCL (UCLB). The patent applications should be made as soon as possible, preferably before or simultaneously as the commercial potential is demonstrated. The commercial opportunities should be grasped as this is a certain way to ensure the findings in this thesis have impact within the process industries.

This section outlines a very wide range of possible steps forward that can be taken and originate, at least partially, from the results presented in this thesis. As described in the Impact Statement (pp. 7), the work presented here has significant commercial potential and the steps presented here provide a clear path to follow in order to materialise it.

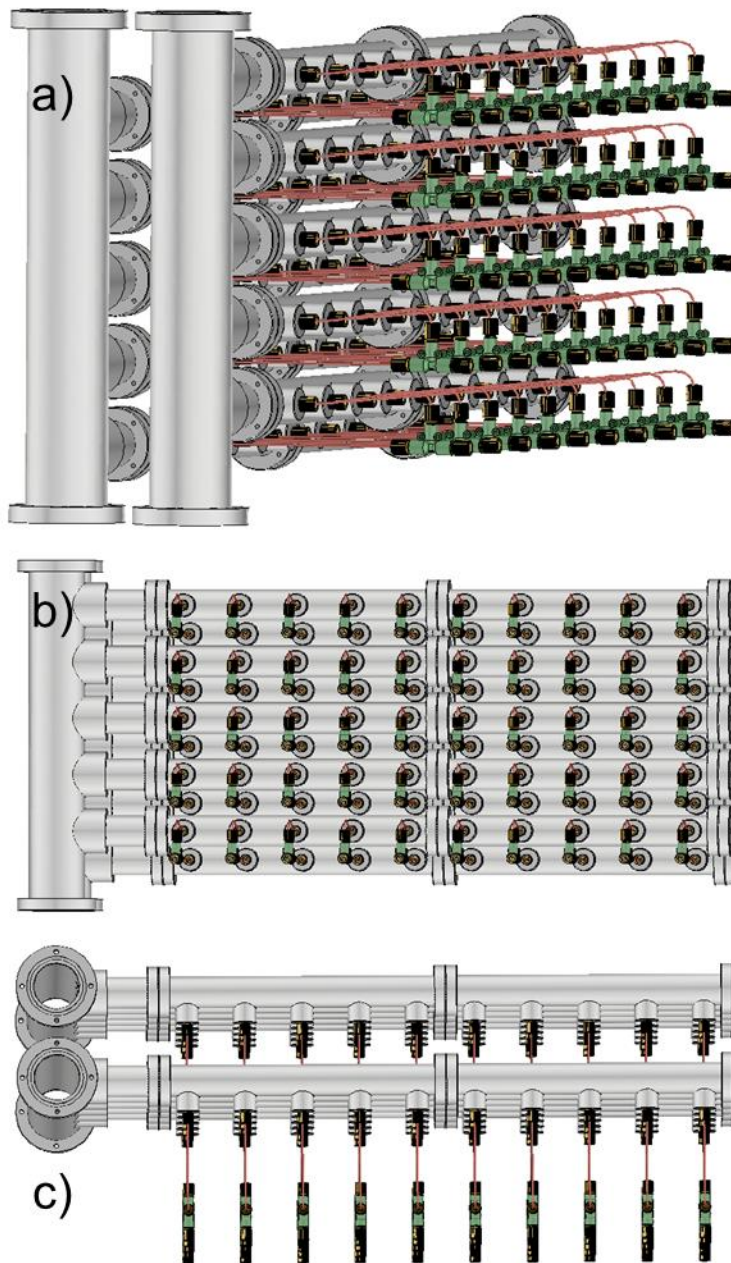


Figure 7-1 Multi-level double manifold schematic with 50 main channels. This design can potentially increase the throughput with a minimal footprint. The path followed by each phase consists of one vertical feed section, an inlet section to allow a parabolic velocity profile to develop, a distribution section, a barrier section, a mixing junction, and the main channels. The a), b), and c) panels correspond to side, front, and top views, respectively.

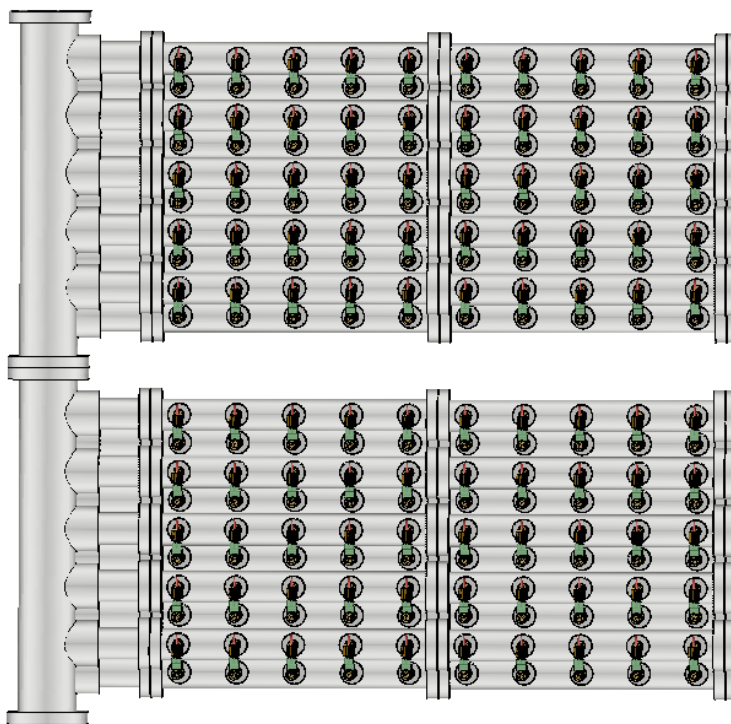


Figure 7-2 Front view of a multi-level double manifold schematic with 100 main channels. Such a multi-level double manifold, depending on main channel diameter and flow velocity (Table 2-4), could process similar throughputs as conventional contactors with the advantages of segmented-flow contactors.

References

- [1] United Nations Department of Global Communications, Sustainable Development Goals, (2015). <https://sustainabledevelopment.un.org/sdgs> (accessed April 14, 2019).
- [2] R.H. Perry, D.W. Green, Perry's Chemical Engineers' Handbook, 2008. <https://doi.org/10.1036/0071511334>.
- [3] A. Górak, A. Stankiewicz, Intensified Reaction and Separation Systems, *Annu. Rev. Chem. Biomol. Eng.* 2 (2011) 431–451. <https://doi.org/10.1146/annurev-chembioeng-061010-114159>.
- [4] K.F. Jensen, Flow chemistry-Microreaction technology comes of age, *AIChE J.* 63 (2017) 858–869. <https://doi.org/10.1002/aic.15642>.
- [5] K.L. Nash, G.J. Lumetta, eds., *Advanced separation techniques for nuclear fuel reprocessing and radioactive waste management*, Woodhead Publishing, 2011.
- [6] M. Benedict, T.H. Pigford, H.W. Levi, *Nuclear Chemical Engineering*, McGraw-Hill, 1981.
- [7] E. Alper, ed., *Mass Transfer with Chemical Reaction in Multiphase Systems, Volume 1: Two-Phase Systems*, Martinus Nijhoff Publishers & NATO Scientific Affairs Division, 1983.
- [8] L.K. Doraiswamy, M.M. Sharma, *Heterogeneous reactions: analysis, examples, and reactor design*, John Wiley & Sons, New York, 1984.
- [9] D.M. (editor) Ruthven, *Wiley: Kirk-Othmer Separation Technology, 2 Volume Set, 2nd Edition* - Wiley, (2008). <http://www.wiley.com/WileyCDA/WileyTitle/productCd-0470127414.html> (accessed January 5, 2016).
- [10] T.C. Lo, M.H.I. Baird, C. Hanson, *Handbook of solvent extraction*, Wiley, 1983.

- [11] M. Ahmad, M. Ajab Khan, M. Zafar, S. Sultana, Practical Handbook on Biodiesel Production and Properties, 2013.
- [12] K. Piradashvili, E.M. Alexandrino, F.R. Wurm, K. Landfester, Reactions and Polymerizations at the Liquid–Liquid Interface, *Chem. Rev.* 116 (2016) 2141–2169. <https://doi.org/10.1021/acs.chemrev.5b00567>.
- [13] H.H. Bieber, R. Ker, Engineering Design Considerations for an Extraction Plant, in: *Handb. Solvent Extr.*, 1982: pp. 901–917.
- [14] M.N. Kashid, Y.M. Harshe, D.W. Agar, Liquid-liquid slug flow in a capillary: An alternative to suspended drop or film contactors, *Ind. Eng. Chem. Res.* 46 (2007) 8420–8430. <https://doi.org/10.1021/ie070077x>.
- [15] T. Kletz, *Process Plants: A Handbook for Inherently Safer Design*, Taylor & Francis, 1998.
- [16] H.A. Stone, A.D. Stroock, A. Ajdari, Engineering Flows in Small Devices, *Annu. Rev. Fluid Mech.* 36 (2004) 381–411. <https://doi.org/10.1146/annurev.fluid.36.050802.122124>.
- [17] C.Y. Yin, A.N. Nikoloski, M. Wang, Microfluidic solvent extraction of platinum and palladium from a chloride leach solution using Alamine 336, *Miner. Eng.* 45 (2013) 18–21. <https://doi.org/10.1016/j.mineng.2013.01.013>.
- [18] F.H. Kriel, G. Holzner, R.A. Grant, S. Woollam, J. Ralston, C. Priest, Microfluidic solvent extraction, stripping, and phase disengagement for high-value platinum chloride solutions, *Chem. Eng. Sci.* 138 (2015) 827–833. <https://doi.org/10.1016/j.ces.2015.08.055>.
- [19] F.H. Kriel, C. Binder, C. Priest, A Multi-Stream Microchip for Process Intensification of Liquid-Liquid Extraction, *Chem. Eng. Technol.* 40 (2017) 1184–1189. <https://doi.org/10.1002/ceat.201600728>.
- [20] Q. Li, P. Angeli, Intensified Eu(III) extraction using ionic liquids in small channels,

- Chem. Eng. Sci. 143 (2016) 276–286. <https://doi.org/10.1016/j.ces.2016.01.004>.
- [21] S. Yin, J. Pei, J. Peng, L. Zhang, C. Srinivasakannan, Study on mass transfer behavior of extracting La(III) with EHEHPA (P507) using rectangular cross-section microchannel, *Hydrometallurgy*. 175 (2018) 64–69. <https://doi.org/10.1016/j.hydromet.2017.10.027>.
- [22] K.S. Pedersen, J. Imbrogno, J. Fonslet, M. Lusardi, K.F. Jensen, F. Zhuravlev, Liquid-liquid extraction in flow of the radioisotope titanium-45 for positron emission tomography applications, *React. Chem. Eng.* 3 (2018) 898–904. <https://doi.org/10.1039/c8re00175h>.
- [23] K. Wang, G. Luo, Microflow extraction: A review of recent development, *Chem. Eng. Sci.* 169 (2017) 18–33. <https://doi.org/10.1016/j.ces.2016.10.025>.
- [24] N. Sen, M. Darekar, K.K. Singh, S. Mukhopadhyay, K.T. Shenoy, S.K. Ghosh, Solvent Extraction and Stripping Studies in Microchannels with TBP Nitric Acid System, *Solvent Extr. Ion Exch.* 32 (2014) 281–300. <https://doi.org/10.1080/07366299.2013.850290>.
- [25] M. Darekar, K.K. Singh, S. Mukhopadhyay, K.T. Shenoy, S.K. Ghosh, Solvent extraction in microbore tubes with UNPS–TBP in dodecane system, *Sep. Purif. Technol.* 128 (2014) 96–105. <https://doi.org/http://dx.doi.org/10.1016/j.seppur.2014.03.002>.
- [26] M. Darekar, K.K. Singh, S. Mukhopadhyay, K.T. Shenoy, Single-stage micro-scale extraction: Studies with single microbore tubes and scale-up, *Sep. Purif. Technol.* 158 (2016) 160–170. <https://doi.org/10.1016/j.seppur.2015.11.041>.
- [27] M. Darekar, K.K. Singh, P. Sapkale, A.K. Goswami, S. Mukhopadhyay, K.T. Shenoy, On microfluidic solvent extraction of uranium, *Chem. Eng. Process. - Process Intensif.* 132 (2018) 65–74. <https://doi.org/10.1016/j.cep.2018.08.007>.
- [28] C. Mariet, A. Vansteene, M. Losno, J. Pellé, J.P. Jasmin, A. Bruchet, G. Hellé,

Microfluidics devices applied to radionuclides separation in acidic media for the nuclear fuel cycle, *Micro Nano Eng.* 3 (2019) 7–14. <https://doi.org/10.1016/j.mne.2019.02.006>.

- [29] D. Tsaoulidis, E.G. Ortega, P. Angeli, Intensified extraction of uranium(VI) in impinging-jets contactors, *Chem. Eng. J.* 342 (2018) 251–259. <https://doi.org/10.1016/j.cej.2018.02.049>.
- [30] H. Hotokezaka, M. Tokeshi, M. Harada, T. Kitamori, Y. Ikeda, Development of the innovative nuclide separation system for high-level radioactive waste using microchannel chip-extraction behavior of metal ions from aqueous phase to organic phase in microchannel, *Prog. Nucl. Energy.* 47 (2005) 439–447. <https://doi.org/10.1016/j.pnueene.2005.05.045>.
- [31] D. Tsaoulidis, V. Dore, P. Angeli, N. V. Plechkova, K.R. Seddon, Extraction of dioxouranium(VI) in small channels using ionic liquids, *Chem. Eng. Res. Des.* 91 (2013) 681–687. <https://doi.org/10.1016/j.cherd.2013.01.008>.
- [32] D. Tsaoulidis, V. Dore, P. Angeli, N. V. Plechkova, K.R. Seddon, Dioxouranium(VI) extraction in microchannels using ionic liquids, *Chem. Eng. J.* 227 (2013) 151–157. <https://doi.org/10.1016/j.cej.2012.08.064>.
- [33] D. Tsaoulidis, P. Angeli, Effect of channel size on mass transfer during liquid – liquid plug flow in small scale extractors, *Chem. Eng. J.* 262 (2015) 785–793. <https://doi.org/10.1016/j.cej.2014.10.012>.
- [34] D. Tsaoulidis, P. Angeli, Effect of channel size on liquid-liquid plug flow in small channels, *AIChE J.* 62 (2016) 315–324. <https://doi.org/10.1002/aic.15026>.
- [35] G. Hellé, S. Roberston, S. Cavadias, C. Mariet, G. Cote, Toward numerical prototyping of labs-on-chip: modeling for liquid–liquid microfluidic devices for radionuclide extraction, *Microfluid. Nanofluidics.* 19 (2015) 1245–1257. <https://doi.org/10.1007/s10404-015-1643-8>.

- [36] G. Hellé, C. Mariet, G. Cote, Liquid–liquid microflow patterns and mass transfer of radionuclides in the systems Eu (III)/HNO₃/DMDBTDMA and U (VI)/HCl/Aliquat® 336, *Microfluid. Nanofluidics*. (2014) 1113–1128. <https://doi.org/10.1007/s10404-014-1403-1>.
- [37] I. Vural Gürsel, S.K. Kurt, J. Aalders, Q. Wang, T. Noël, K.D.P. Nigam, N. Kockmann, V. Hessel, Utilization of milli-scale coiled flow inverter in combination with phase separator for continuous flow liquid–liquid extraction processes, *Chem. Eng. J.* 283 (2016) 855–868. <https://doi.org/10.1016/j.cej.2015.08.028>.
- [38] K.G. Biswas, G. Das, S. Ray, J.K. Basu, Mass transfer characteristics of liquid–liquid flow in small diameter conduits, *Chem. Eng. Sci.* 122 (2015) 652–661. <https://doi.org/10.1016/j.ces.2014.07.029>.
- [39] A. Woitalka, S. Kuhn, K.F. Jensen, Scalability of mass transfer in liquid–liquid flow, *Chem. Eng. Sci.* 116 (2014) 1–8. <https://doi.org/10.1016/j.ces.2014.04.036>.
- [40] M. Lämmermann, W. Schwieger, H. Freund, Experimental investigation of gas–liquid distribution in periodic open cellular structures as potential catalyst supports, *Catal. Today*. 273 (2016) 161–171. <https://doi.org/10.1016/j.cattod.2016.02.049>.
- [41] A. Potdar, L.C.J. Thomassen, S. Kuhn, Structured Porous Millireactors for Liquid–Liquid Chemical Reactions, *Chemie-Ingenieur-Technik*. 91 (2019) 592–601. <https://doi.org/10.1002/cite.201800128>.
- [42] C. Hutter, C. Allemann, S. Kuhn, P. Rudolf von Rohr, Scalar transport in a milli-scale metal foam reactor, *Chem. Eng. Sci.* 65 (2010) 3169–3178. <https://doi.org/10.1016/j.ces.2010.02.002>.
- [43] J.J. John, S. Kuhn, L. Braeken, T. Van Gerven, Ultrasound assisted liquid–liquid extraction in microchannels-A direct contact method, *Chem. Eng. Process. Process Intensif.* 102 (2016) 37–46. <https://doi.org/10.1016/j.cep.2016.01.003>.
- [44] J.J. John, S. Kuhn, L. Braeken, T. Van Gerven, Ultrasound assisted liquid–liquid

- extraction with a novel interval-contact reactor, *Chem. Eng. Process. Process Intensif.* 113 (2017) 35–41. <https://doi.org/10.1016/j.cep.2016.09.008>.
- [45] L. Arsenjuk, F. Kaske, J. Franzke, D.W. Agar, Experimental investigation of wall film renewal in liquid–liquid slug flow, *Int. J. Multiph. Flow.* 85 (2016) 177–185. <https://doi.org/10.1016/j.ijmultiphaseflow.2016.06.009>.
- [46] J. Koch, G. Shivelor, Design Principles for Liquid-Liquid Extraction, *CEP Mag.* (2015). <http://www.aiche.org/resources/publications/cep/2015/november> (accessed January 6, 2016).
- [47] D. Bascone, P. Angeli, E.S. Fraga, A modelling approach for the comparison between intensified extraction in small channels and conventional solvent extraction technologies, *Chem. Eng. Sci.* 203 (2019) 201–211. <https://doi.org/10.1016/j.ces.2019.03.074>.
- [48] R.D. Chambers, M. a. Fox, D. Holling, T. Nakano, T. Okazoe, G. Sandford, Versatile Gas/Liquid Microreactors for Industry, *Chem. Eng. Technol.* 28 (2005) 344–352. <https://doi.org/10.1002/ceat.200407123>.
- [49] M. Al-Rawashdeh, F. Yu, T.A.A. Nijhuis, E.V. V. Rebrov, V. Hessel, J.C.C. Schouten, Numbered-up gas–liquid micro/milli channels reactor with modular flow distributor, *Chem. Eng. J.* 207–208 (2012) 645–655. <https://doi.org/10.1016/j.cej.2012.07.028>.
- [50] K.P. Cole, J.M. Groh, M.D. Johnson, C.L. Burcham, B.M. Campbell, W.D. Diserod, M.R. Heller, J.R. Howell, N.J. Kallman, T.M. Koenig, S.A. May, R.D. Miller, D. Mitchell, D.P. Myers, S.S. Myers, J.L. Phillips, C.S. Polster, T.D. White, J. Cashman, D. Hurley, R. Moylan, P. Sheehan, R.D. Spencer, K. Desmond, P. Desmond, O. Gowran, Kilogram-scale prexasertib monolactate monohydrate synthesis under continuous-flow CGMP conditions, *Science* (80-.). 356 (2017) 1144–1150. <https://doi.org/10.1126/science.aan0745>.

- [51] J. Harmsen, Process intensification in the petrochemicals industry: Drivers and hurdles for commercial implementation, *Chem. Eng. Process. Process Intensif.* 49 (2010) 70–73. <https://doi.org/10.1016/j.cep.2009.11.009>.
- [52] A. Holbach, N. Kockmann, Counter-current arrangement of microfluidic liquid-liquid droplet flow contactors, *Green Process. Synth.* 2 (2013) 157–167. <https://doi.org/10.1515/gps-2013-0006>.
- [53] E.C. Sindermann, A. Holbach, A. de Haan, N. Kockmann, Single stage and countercurrent extraction of 5-hydroxymethylfurfural from aqueous phase systems, *Chem. Eng. J.* 283 (2016) 251–259. <https://doi.org/10.1016/j.cej.2015.07.029>.
- [54] T. Vandermeersch, L. Gevers, W. De Malsche, A robust multistage meso flow reactor for liquid-liquid extraction separating Co/Ni with cyanex 272, *Sep. Purif. Technol.* 168 (2016) 32–38. <https://doi.org/10.1016/j.seppur.2016.05.014>.
- [55] N. Weeranoppanant, A. Adamo, G. Sapparaiuly, E. Rose, C. Fleury, B. Schenkel, K.F. Jensen, Design of Multistage Counter-Current Liquid–Liquid Extraction for Small-Scale Applications, *Ind. Eng. Chem. Res.* 56 (2017) 4095–4103. <https://doi.org/10.1021/acs.iecr.7b00434>.
- [56] N. Shao, A. Gavriilidis, P. Angeli, Flow regimes for adiabatic gas-liquid flow in microchannels, *Chem. Eng. Sci.* 64 (2009) 2749–2761. <https://doi.org/10.1016/j.ces.2009.01.067>.
- [57] E. V. Rebrov, Two-phase flow regimes in microchannels, *Theor. Found. Chem. Eng.* 44 (2010) 355–367. <https://doi.org/10.1134/s0040579510040019>.
- [58] M. Sattari-Najafabadi, M. Nasr Esfahany, Z. Wu, B. Sunden, Mass transfer between phases in microchannels: A review, *Chem. Eng. Process. - Process Intensif.* 127 (2018) 213–237. <https://doi.org/10.1016/j.cep.2018.03.012>.
- [59] D. Tsaoulidis, V. Dore, P. Angeli, N. V. Plechkova, K.R. Seddon, Flow patterns

and pressure drop of ionic liquid-water two-phase flows in microchannels, *Int. J. Multiph. Flow.* 54 (2013) 1–10. <https://doi.org/10.1016/j.ijmultiphaseflow.2013.02.002>.

- [60] M.N. Kashid, D.W. Agar, Hydrodynamics of liquid-liquid slug flow capillary microreactor: Flow regimes, slug size and pressure drop, *Chem. Eng. J.* 131 (2007) 1–13. <https://doi.org/10.1016/j.cej.2006.11.020>.
- [61] J. Jovanović, E. V. Rebrov, T.A. (Xander) Nijhuis, V. Hessel, J.C. Schouten, Phase-Transfer Catalysis in Segmented Flow in a Microchannel: Fluidic Control of Selectivity and Productivity, *Ind. Eng. Chem. Res.* 49 (2010) 2681–2687. <https://doi.org/10.1021/ie9017918>.
- [62] Y. Zhao, G. Chen, Q. Yuan, Liquid-liquid two-phase flow patterns in a rectangular microchannel, *AIChE J.* 52 (2006) 4052–4060. <https://doi.org/10.1002/aic.11029>.
- [63] J. Jovanović, E. V. Rebrov, T.A. (Xander) Nijhuis, M.T. Kreutzer, V. Hessel, J.C. Schouten, Liquid–Liquid Flow in a Capillary Microreactor: Hydrodynamic Flow Patterns and Extraction Performance, *Ind. Eng. Chem. Res.* 51 (2012) 1015–1026. <https://doi.org/10.1021/ie200715m>.
- [64] Z. Cao, Z. Wu, B. Sundén, Dimensionless analysis on liquid-liquid flow patterns and scaling law on slug hydrodynamics in cross-junction microchannels, *Chem. Eng. J.* 344 (2018) 604–615. <https://doi.org/10.1016/j.cej.2018.03.119>.
- [65] P. Garstecki, M.J. Fuerstman, H.A. Stone, G.M. Whitesides, Formation of droplets and bubbles in a microfluidic T-junction—scaling and mechanism of break-up, *Lab Chip.* 6 (2006) 437. <https://doi.org/10.1039/b510841a>.
- [66] T. Fu, Y. Wu, Y. Ma, H.Z. Li, Droplet formation and breakup dynamics in microfluidic flow-focusing devices: From dripping to jetting, *Chem. Eng. Sci.* 84 (2012) 207–217. <https://doi.org/10.1016/j.ces.2012.08.039>.
- [67] T.A. Prileszky, B.A. Ogunnaike, E.M. Furst, Statistics of droplet sizes generated

- by a microfluidic device, *AIChE J.* 62 (2016) 2923–2928.
<https://doi.org/10.1002/aic.15246>.
- [68] Q. Li, P. Angeli, Experimental and numerical hydrodynamic studies of ionic liquid-aqueous plug flow in small channels, *Chem. Eng. J.* 328 (2017) 717–736.
<https://doi.org/10.1016/j.cej.2017.07.037>.
- [69] M. Mac Giolla Eain, V. Egan, J. Punch, Film thickness measurements in liquid-liquid slug flow regimes, *Int. J. Heat Fluid Flow.* 44 (2013) 515–523.
<https://doi.org/10.1016/j.ijheatfluidflow.2013.08.009>.
- [70] V. Dore, D. Tsaoulidis, P. Angeli, Mixing patterns in water plugs during water/ionic liquid segmented flow in microchannels, *Chem. Eng. Sci.* 80 (2012) 334–341.
<https://doi.org/10.1016/j.ces.2012.06.030>.
- [71] R. Abiev, S. Svetlov, S. Haase, Hydrodynamics and Mass Transfer of Gas-Liquid and Liquid-Liquid Taylor Flow in Microchannels, *Chem. Eng. Technol.* 40 (2017) 1985–1998. <https://doi.org/10.1002/ceat.201700041>.
- [72] S. Haase, Characterisation of gas-liquid two-phase flow in minichannels with co-flowing fluid injection inside the channel, part II: gas bubble and liquid slug lengths, film thickness, and void fraction within Taylor flow, *Int. J. Multiph. Flow.* 88 (2017) 251–269. <https://doi.org/10.1016/j.ijmultiphaseflow.2016.09.002>.
- [73] A. Matsuoka, K. Noishiki, K. Mae, Experimental study of the contribution of liquid film for liquid-liquid Taylor flow mass transfer in microchannel, *Chem. Eng. Sci.* 155 (2016) 306–313. <https://doi.org/10.1016/j.ces.2016.08.021>.
- [74] M.N. Kashid, I. Gerlach, S. Goetz, J. Franzke, J.F. Acker, F. Platte, D.W. Agar, S. Turek, Internal circulation within the liquid slugs of a liquid-liquid slug-flow capillary microreactor, *Ind. Eng. Chem. Res.* 44 (2005) 5003–5010.
<https://doi.org/10.1021/ie0490536>.
- [75] R. Gupta, S.S.Y. Leung, R. Manica, D.F. Fletcher, B.S. Haynes, Hydrodynamics

of liquid-liquid Taylor flow in microchannels, *Chem. Eng. Sci.* 92 (2013) 180–189.
<https://doi.org/10.1016/j.ces.2013.01.013>.

- [76] T.C. Thulasidas, M.A. Abraham, R.L. Cerro, Flow patterns in liquid slugs during bubble-train flow inside capillaries, *Chem. Eng. Sci.* 52 (1997) 2947–2962.
[https://doi.org/10.1016/S0009-2509\(97\)00114-0](https://doi.org/10.1016/S0009-2509(97)00114-0).
- [77] T. Abadie, C. Xuereb, D. Legendre, J. Aubin, Mixing and recirculation characteristics of gas-liquid Taylor flow in microreactors, *Chem. Eng. Res. Des.* 91 (2013) 2225–2234. <https://doi.org/10.1016/j.cherd.2013.03.003>.
- [78] D. Tsaoulidis, *Studies of intensified small - scale processes for liquid - liquid separations in spent nuclear fuel reprocessing* Dimitrios Tsaoulidis, 2014.
- [79] N. Di Miceli Raimondi, L. Prat, C. Gourdon, J. Tasselli, Experiments of mass transfer with liquid-liquid slug flow in square microchannels, *Chem. Eng. Sci.* 105 (2014) 169–178. <https://doi.org/10.1016/j.ces.2013.11.009>.
- [80] N. Di Miceli Raimondi, L. Prat, C. Gourdon, P. Cognet, Direct numerical simulations of mass transfer in square microchannels for liquid–liquid slug flow, *Chem. Eng. Sci.* 63 (2008) 5522–5530. <https://doi.org/10.1016/j.ces.2008.07.025>.
- [81] Q. Zhang, H. Liu, S. Zhao, C. Yao, G. Chen, Hydrodynamics and mass transfer characteristics of liquid–liquid slug flow in microchannels: The effects of temperature, fluid properties and channel size, *Chem. Eng. J.* 358 (2019) 794–805. <https://doi.org/10.1016/j.cej.2018.10.056>.
- [82] J. Yue, L. Luo, Y. Gonthier, G. Chen, Q. Yuan, An experimental study of air–water Taylor flow and mass transfer inside square microchannels, *Chem. Eng. Sci.* 64 (2009) 3697–3708. <https://doi.org/10.1016/j.ces.2009.05.026>.
- [83] R.E. Treybal, *Mass-transfer operations*, 3rd ed., McGraw-Hill, 1981.
- [84] B. Hanson, *Process engineering and design for spent nuclear fuel reprocessing and recycling plants*, in: *Reprocess. Recycl. Spent Nucl. Fuel*, Elsevier, 2015: pp.

125–151. <https://doi.org/10.1016/B978-1-78242-212-9.00006-X>.

- [85] S. Ramji, A. Rakesh, S. Pushpavanam, Modelling mass transfer in liquid-liquid slug flow in a microchannel, *Chem. Eng. J.* 364 (2019) 280–291. <https://doi.org/10.1016/j.cej.2019.01.075>.
- [86] L. Li, J. Zhang, C. Du, G. Luo, Determination of the Liquid/Liquid Mass Transfer Coefficient for Each Phase in Microchannels, *Ind. Eng. Chem. Res.* 57 (2018) 9028–9036. <https://doi.org/10.1021/acs.iecr.8b01976>.
- [87] V.G. Levich, *Physicochemical Hydrodynamics*, 2nd ed., Prentice-Hall, 1962.
- [88] R.B. Bird, W.E. Stewart, E.N. Lightfoot, *Transport Phenomena*, 2nd ed., John Wiley & Sons, New York, 2002.
- [89] M.T. Kreutzer, F. Kapteijn, J.A. Moulijn, C.R. Kleijn, J.J. Heiszwolf, Inertial and interfacial effects on pressure drop of Taylor flow in capillaries, *AIChE J.* 51 (2005) 2428–2440. <https://doi.org/10.1002/aic.10495>.
- [90] S.M. Ghiaasiaan, Pressure Drop in Two-Phase Flow, in: *Two-Phase Flow, Boil. Condens.*, Cambridge University Press, Cambridge, 2018: pp. 207–227. <https://doi.org/10.1017/CBO9780511619410.011>.
- [91] R.W. Lockhart, R.C. Martinelli, Proposed correlation of data for isothermal two-phase, two-component flow in pipes, *Chem. Eng. Progr.* 45 (1949) 39–48.
- [92] K.A. Triplett, S.M. Ghiaasiaan, S.I. Abdel-Khalik, A. LeMouel, B.N. McCord, Gas–liquid two-phase flow in microchannels Part ii: void fraction and pressure drop, *Int. J. Multiph. Flow.* 25 (1999) 395–410. [https://doi.org/10.1016/S0301-9322\(98\)00055-X](https://doi.org/10.1016/S0301-9322(98)00055-X).
- [93] W. Zhang, T. Hibiki, K. Mishima, Correlations of two-phase frictional pressure drop and void fraction in mini-channel, *Int. J. Heat Mass Transf.* 53 (2010) 453–465. <https://doi.org/10.1016/j.ijheatmasstransfer.2009.09.011>.

- [94] F.P. Bretherton, The motion of long bubbles in tubes, *J. Fluid Mech.* 10 (1961) 166. <https://doi.org/10.1017/S0022112061000160>.
- [95] E. Walsh, Y. Muzychka, P. Walsh, V. Egan, J. Punch, Pressure drop in two phase slug/bubble flows in mini scale capillaries, *Int. J. Multiph. Flow.* 35 (2009) 879–884. <https://doi.org/10.1016/j.ijmultiphaseflow.2009.06.007>.
- [96] M.J.F. Warnier, M.H.J.M. De Croon, E. V. Rebrov, J.C. Schouten, Pressure drop of gas-liquid Taylor flow in round micro-capillaries for low to intermediate Reynolds numbers, *Microfluid. Nanofluidics.* 8 (2010) 33–45. <https://doi.org/10.1007/s10404-009-0448-z>.
- [97] J. Jovanović, W. Zhou, E. V. Rebrov, T.A. Nijhuis, V. Hessel, J.C. Schouten, Liquid-liquid slug flow: Hydrodynamics and pressure drop, *Chem. Eng. Sci.* 66 (2011) 42–54. <https://doi.org/10.1016/j.ces.2010.09.040>.
- [98] M. Mac Giolla Eain, V. Egan, J. Howard, P. Walsh, E. Walsh, J. Punch, Review and extension of pressure drop models applied to Taylor flow regimes, *Int. J. Multiph. Flow.* 68 (2015) 1–9. <https://doi.org/10.1016/j.ijmultiphaseflow.2014.09.006>.
- [99] S.V. Luis, E. Garcia-Verdugo, *Chemical Reactions and Processes under Flow Conditions*, Royal Society of Chemistry, Cambridge, 2009. <https://doi.org/10.1039/9781847559739>.
- [100] J. Zhang, K. Wang, A.R. Teixeira, K.F. Jensen, G. Luo, Design and Scaling Up of Microchemical Systems: A Review, *Annu. Rev. Chem. Biomol. Eng.* 8 (2017) 285–305. <https://doi.org/10.1146/annurev-chembioeng-060816-101443>.
- [101] D. Brennan, *Process Industry Economics*, The Institution of Chemical Engineers, 1998.
- [102] J. Harmsen, *Process Economics and Environmental Impacts of Process Intensification in the Petrochemicals, Fine Chemicals and Pharmaceuticals*

- Industries, in: *Process Intensif. Green Chem.*, 2013: pp. 369–378.
<https://doi.org/10.1002/9781118498521.ch14>.
- [103] J.B. Powell, Application of multiphase reaction engineering and process intensification to the challenges of sustainable future energy and chemicals, *Chem. Eng. Sci.* 157 (2016) 15–25. <https://doi.org/10.1016/j.ces.2016.09.007>.
- [104] F. Kaske, S. Dick, S.A. Pajoochi, D.W. Agar, The influence of operating conditions on the mass transfer performance of a micro capillary contactor with liquid–liquid slug flow, *Chem. Eng. Process. Process Intensif.* 108 (2016) 10–16. <https://doi.org/10.1016/j.cep.2016.06.010>.
- [105] C. Amador, A. Gavriilidis, P. Angeli, Flow distribution in different microreactor scale-out geometries and the effect of manufacturing tolerances and channel blockage, *Chem. Eng. J.* 101 (2004) 379–390. <https://doi.org/10.1016/j.cej.2003.11.031>.
- [106] J.M. Commenge, L. Falk, J.P. Corriou, M. Matlosz, Optimal Design for Flow Uniformity in Microchannel Reactors, *AIChE J.* 48 (2002) 345–358. <https://doi.org/10.1002/aic.690480218>.
- [107] J. Wang, Theory of flow distribution in manifolds, *Chem. Eng. J.* 168 (2011) 1331–1345. <https://doi.org/10.1016/j.cej.2011.02.050>.
- [108] K.W. Oh, K. Lee, B. Ahn, E.P. Furlani, Design of pressure-driven microfluidic networks using electric circuit analogy, *Lab Chip.* 12 (2012) 515–545. <https://doi.org/10.1039/C2LC20799K>.
- [109] O. Tonomura, S. Nagahara, M. Kano, S. Hasebe, Fluid Distribution and Blockage Diagnosis in Parallel Microchannel Configurations, in: *10th Int. Conf. Microreact. Technol.*, 2008.
- [110] L. Wang, X. Kong, Y. Qi, Optimal Design for Split-and-Recombine-Type Flow Distributors of Microreactors Based on Blockage Detection, *Chinese J. Chem.*

Eng. 24 (2016) 4–10. <https://doi.org/10.1016/j.cjche.2016.04.021>.

- [111] E. V. Rebrov, I.Z. Ismagilov, R.P. Ekatpure, M.H.J.M. De Croon, J.C. Schouten, Header design for flow equalization in microstructured reactors, *AIChE J.* 53 (2007) 28–38. <https://doi.org/10.1002/aic.11043>.
- [112] T. Shimanouchi, Y. Kataoka, T. Tanifuji, Y. Kimura, S. Fujioka, K. Terasaka, Chemical conversion and liquid-liquid extraction of 5-hydroxymethylfurfural from fructose by slug flow microreactor, *AIChE J.* 62 (2016) 2135–2143. <https://doi.org/10.1002/aic.15201>.
- [113] M. Saber, J.M. Commenge, L. Falk, Microreactor numbering-up in multi-scale networks for industrial-scale applications: Impact of flow maldistribution on the reactor performances, *Chem. Eng. Sci.* 65 (2010) 372–379. <https://doi.org/10.1016/j.ces.2009.06.010>.
- [114] E. V. Rebrov, J.C. Schouten, M.H.J.M. de Croon, Single-phase fluid flow distribution and heat transfer in microstructured reactors, *Chem. Eng. Sci.* 66 (2011) 1374–1393. <https://doi.org/10.1016/j.ces.2010.05.044>.
- [115] G. Agrawal, N.S. Kaisare, S. Pushpavanam, K. Ramanathan, Modeling the effect of flow mal-distribution on the performance of a catalytic converter, *Chem. Eng. Sci.* 71 (2012) 310–320. <https://doi.org/10.1016/j.ces.2011.12.041>.
- [116] M. Schubert, S. Kost, R. Lange, T. Salmi, S. Haase, U. Hampel, Maldistribution susceptibility of monolith reactors: Case study of glucose hydrogenation performance, *AIChE J.* 62 (2016) 4346–4364. <https://doi.org/10.1002/aic.15334>.
- [117] D.A. Hoang, C. Haringa, L.M. Portela, M.T. Kreutzer, C.R. Kleijn, V. Van Steijn, Design and characterization of bubble-splitting distributor for scaled-out multiphase microreactors, *Chem. Eng. J.* 236 (2014) 545–554. <https://doi.org/10.1016/j.cej.2013.08.066>.
- [118] D.A. Hoang, Breakup of confined droplets in microfluidics, TU Delft, 2013.

- [119] D. Chugh, S. Roy, J. Shao, M.H. Al-Dahhan, Experimental Investigation of Gas-Liquid Flow in Monolith Channels Using Monofiber Optical Probes, *AIChE J.* 63 (2017) 327–336. <https://doi.org/10.1002/aic>.
- [120] Y. Su, K. Kuijpers, V. Hessel, T. Noël, A convenient numbering-up strategy for the scale-up of gas–liquid photoredox catalysis in flow, *React. Chem. Eng.* 1 (2016) 73–81. <https://doi.org/10.1039/C5RE00021A>.
- [121] M.N. Kashid, a. Gupta, a. Renken, L. Kiwi-Minsker, Numbering-up and mass transfer studies of liquid–liquid two-phase microstructured reactors, *Chem. Eng. J.* 158 (2010) 233–240. <https://doi.org/10.1016/j.cej.2010.01.020>.
- [122] M. Al-Rawashdeh, L.J.M. Fluitsma, T.A. Nijhuis, E.V. Rebrov, V. Hessel, J.C. Schouten, Design criteria for a barrier-based gas–liquid flow distributor for parallel microchannels, *Chem. Eng. J.* 181–182 (2012) 549–556. <https://doi.org/10.1016/j.cej.2011.11.086>.
- [123] M. Al-Rawashdeh, X. Nijhuis, E. V. Rebrov, V. Hessel, J.C. Schouten, Design methodology for barrier-based two phase flow distributor, *AIChE J.* 58 (2012) 3482–3493. <https://doi.org/10.1002/aic.13750>.
- [124] M. Darekar, K.K. Singh, J.M. Joshi, S. Mukhopadhyay, K.T. Shenoy, Single-stage microscale solvent extraction in parallel microbore tubes using a monoblock distributor with integrated microfluidic junctions, *Sep. Sci. Technol.* 52 (2017) 2213–2223. <https://doi.org/10.1080/01496395.2017.1279181>.
- [125] S.V.N.V.N. Ayyappa, M. Balamurugan, S. Kumar, U. Kamachi Mudali, Mass transfer and hydrodynamic studies in a 50mm diameter centrifugal extractor, *Chem. Eng. Process. Process Intensif.* 105 (2016) 30–37. <https://doi.org/10.1016/j.cep.2016.04.005>.
- [126] H.J.A. Vermijs, H. Kramers, Liquid-liquid extraction in a “rotating disc contactor,” *Chem. Eng. Sci.* 3 (1954) 55–64. [https://doi.org/10.1016/0009-2509\(54\)85014-7](https://doi.org/10.1016/0009-2509(54)85014-7).

- [127] Z. Likidis, K. Schügerl, Recovery of penicillin by reactive extraction in centrifugal extractors, *Biotechnol. Bioeng.* 30 (1987) 1032–1040. <https://doi.org/10.1002/bit.260300906>.
- [128] PubChem Database, Compound Summary Dodecane, (n.d.). <https://pubchem.ncbi.nlm.nih.gov/compound/Dodecane>.
- [129] P. Schatzberg, Solubilities of Water in Several Normal Alkanes from C7 to C16, *J. Phys. Chem.* 67 (1963) 776–779. <https://doi.org/10.1021/j100798a014>.
- [130] Q. Tian, H. Liu, Densities and viscosities of binary mixtures of tributyl phosphate with hexane and dodecane from (298.15 to 328.15) K, *J. Chem. Eng. Data.* 52 (2007) 892–897. <https://doi.org/10.1021/je060491o>.
- [131] S. Nave, C. Mandin, L. Martinet, L. Berthon, F. Testard, C. Madic, T. Zemb, Supramolecular organisation of tri-n-butyl phosphate in organic diluent on approaching third phase transition, *Phys. Chem. Chem. Phys.* 6 (2004) 799. <https://doi.org/10.1039/b311702b>.
- [132] A. Adamo, P.L. Heider, N. Weeranoppanant, K.F. Jensen, Membrane-Based, Liquid–Liquid Separator with Integrated Pressure Control, *Ind. Eng. Chem. Res.* 52 (2013) 10802–10808. <https://doi.org/10.1021/ie401180t>.
- [133] A. Nagaki, K. Hirose, O. Tonomura, S. Taniguchi, T. Taga, S. Hasebe, N. Ishizuka, J.I. Yoshida, Design of a Numbering-up System of Monolithic Microreactors and Its Application to Synthesis of a Key Intermediate of Valsartan, *Org. Process Res. Dev.* 20 (2016) 687–691. <https://doi.org/10.1021/acs.oprd.5b00414>.
- [134] C. Amador Zamarreño, Principles of two-phase flow microreactors and their scale-out, University College London, 2006.
- [135] P. Angeli, a Gavriilidis, Hydrodynamics of Taylor flow in small channels: a review, *Proc. Inst. Mech. Eng. Part C J. Mech. Eng. Sci.* 222 (2008) 737–751. <https://doi.org/10.1243/09544062JMES776>.

- [136] D.N. Tsinoglou, G.C. Koltsakis, D.K. Missirlis, K.J. Yakinthos, Transient modelling of flow distribution in automotive catalytic converters, *Appl. Math. Model.* 28 (2004) 775–794. <https://doi.org/10.1016/j.apm.2003.12.006>.
- [137] H. Liu, P. Li, J. Van Lew, D. Juarez-Robles, Experimental study of the flow distribution uniformity in flow distributors having novel flow channel bifurcation structures, *Exp. Therm. Fluid Sci.* 37 (2012) 142–153. <https://doi.org/10.1016/j.expthermflusci.2011.10.015>.
- [138] J. Wang, H. Wang, Discrete method for design of flow distribution in manifolds, *Appl. Therm. Eng.* 89 (2015) 927–945. <https://doi.org/10.1016/j.applthermaleng.2015.06.069>.
- [139] M. Mohammadi, G.N. Jovanovic, K. V. Sharp, Numerical study of flow uniformity and pressure characteristics within a microchannel array with triangular manifolds, *Comput. Chem. Eng.* 52 (2013) 134–144. <https://doi.org/10.1016/j.compchemeng.2012.12.010>.
- [140] C. Pistoresi, Y. Fan, L. Luo, Numerical study on the improvement of flow distribution uniformity among parallel mini-channels, *Chem. Eng. Process. Process Intensif.* 95 (2015) 63–71. <https://doi.org/10.1016/j.cep.2015.05.014>.
- [141] E.R. Delsman, A. Pierik, M.H.J.M. De Croon, G.J. Kramer, J.C. Schouten, Microchannel Plate Geometry Optimization for Even Flow Distribution at High Flow Rates, *Chem. Eng. Res. Des.* 82 (2004) 267–273. <https://doi.org/10.1205/026387604772992864>.
- [142] C. Anbumeenakshi, M.R. Thansekhar, Experimental investigation of header shape and inlet configuration on flow maldistribution in microchannel, *Exp. Therm. Fluid Sci.* 75 (2016) 156–161. <https://doi.org/10.1016/j.expthermflusci.2016.02.004>.
- [143] C.C. Wang, K.S. Yang, J.S. Tsai, I.Y. Chen, Characteristics of flow distribution in

compact parallel flow heat exchangers, part I: Typical inlet header, *Appl. Therm. Eng.* 31 (2011) 3226–3234.
<https://doi.org/10.1016/j.applthermaleng.2011.06.004>.

- [144] M. Mendorf, H. Nachtrodt, A. Mescher, A. Ghaini, D.W. Agar, Design and control techniques for the numbering-up of capillary microreactors with uniform multiphase flow distribution, *Ind. Eng. Chem. Res.* 49 (2010) 10908–10916.
<https://doi.org/10.1021/ie100473d>.
- [145] A. Marchitto, F. Devia, M. Fossa, G. Guglielmini, C. Schenone, Experiments on two-phase flow distribution inside parallel channels of compact heat exchangers, *Int. J. Multiph. Flow.* 34 (2008) 128–144.
<https://doi.org/10.1016/j.ijmultiphaseflow.2007.08.005>.
- [146] P. Yuan, G.B. Jiang, Y.L. He, X.L. Yi, W.Q. Tao, Experimental study on the performance of a novel structure for two-phase flow distribution in parallel vertical channels, *Int. J. Multiph. Flow.* 53 (2013) 65–74.
<https://doi.org/10.1016/j.ijmultiphaseflow.2012.05.006>.
- [147] T.F. Cox, *An Introduction to Multivariate Data Analysis*, 1st ed., Hodder Education, London, 2005.
- [148] NIST, NIST/SEMATECH e-Handbook of Statistical Methods, 2003.
<http://www.itl.nist.gov/div898/handbook/eda/section3/eda3674.htm> (accessed January 29, 2018).
- [149] S.F. Ellermeyer, D.G. Robinson, Integrals of Periodic Functions, *Math. Mag.* 74 (2001) 393. <https://doi.org/10.2307/2691036>.
- [150] K. Miyabayashi, O. Tonomura, S. Hasebe, Estimation of gas and liquid slug lengths for T-shaped microreactors, *Chem. Eng. J.* 262 (2015) 1137–1143.
<https://doi.org/10.1016/j.cej.2014.10.075>.
- [151] S. Kerisit, C. Liu, Molecular simulation of the diffusion of uranyl carbonate species

- in aqueous solution, *Geochim. Cosmochim. Acta.* 74 (2010) 4937–4952.
<https://doi.org/10.1016/j.gca.2010.06.007>.
- [152] V. Friehmelt, A. He, Z. Yang, G. Marx, The diffusion coefficients and viscosities of the $\text{UO}_2(\text{NO}_3)_2 \cdot 2\text{TBP}$ complex in organic solvents, *Inorganica Chim. Acta.* 111 (1986) 89–93. [https://doi.org/10.1016/S0020-1693\(00\)82223-9](https://doi.org/10.1016/S0020-1693(00)82223-9).
- [153] M. Sattari-najafabadi, M.N. Nasr Esfahany, M.N. Esfahany, M.N. Nasr Esfahany, Intensification of liquid-liquid mass transfer in a circular microchannel in the presence of sodium dodecyl sulfate, *Chem. Eng. Process. Process Intensif.* 117 (2017) 9–17. <https://doi.org/10.1016/j.cep.2017.03.011>.
- [154] R.P. Verma, M.M. Sharma, Mass transfer in packed liquid-liquid extraction columns, *Chem. Eng. Sci.* 30 (1975) 279–292. [https://doi.org/10.1016/0009-2509\(75\)80078-9](https://doi.org/10.1016/0009-2509(75)80078-9).
- [155] R. Torkaman, M. Torab-Mostaedi, J. Safdari, M.A. Moosavian, M. Asadollahzadeh, Mass transfer coefficients in pulsed column for separation of samarium and gadolinium, *Iran. J. Chem. Chem. Eng.* 36 (2017) 145–158.
- [156] J.D. Kumana, M.R. Suarez, Analyzing the Performance of Pump Networks Part 2: Improving Pump Efficiency, *CEP AIChE.* (2018).
<https://www.aiche.org/resources/publications/cep/2018/february/analyzing-performance-pump-networks-part-2-improving-pump-efficiency>.
- [157] G. Towler, R. Sinnott, *Chemical Engineering Design - Principles, Practice and Economics of Plant and Process Design* (2nd Edition), 2nd ed., 2013.
<https://app.knovel.com/web/toc.v/cid:kpCEDPPEP4>.
- [158] J.R. Rumble, ed., *CRC Handbook of Chemistry and Physics*, (Internet Version 2019), 100th Edit, CRC Press/Taylor & Francis, Boca Raton, FL, 2019.
- [159] R.H. Liu, M.A. Stremler, K.V. Sharp, M.G. Olsen, J.G. Santiago, R.J. Adrian, H. Aref, D.J. Beebe, Passive mixing in a three-dimensional serpentine microchannel,

- J. Microelectromechanical Syst. 9 (2000) 190–197.
<https://doi.org/10.1109/84.846699>.
- [160] D.S. Kim, I.H. Lee, T.H. Kwon, D.-W. Cho, A barrier embedded Kenics micromixer, J. Micromechanics Microengineering. 14 (2004) 1294–1301.
<https://doi.org/10.1088/0960-1317/14/10/002>.
- [161] J. Cha, J. Kim, S.K. Ryu, J. Park, Y. Jeong, S. Park, S. Park, H.C. Kim, K. Chun, A highly efficient 3D micromixer using soft PDMS bonding, J. Micromechanics Microengineering. 16 (2006) 1778–1782. <https://doi.org/10.1088/0960-1317/16/9/004>.
- [162] S.W. Lee, D.S. Kim, S.S. Lee, T.H. Kwon, A split and recombination micromixer fabricated in a PDMS three-dimensional structure, J. Micromechanics Microengineering. 16 (2006) 1067–1072. <https://doi.org/10.1088/0960-1317/16/5/027>.
- [163] M.N. Kashid, Experimental and Modelling Studies on Liquid-Liquid Slug Flow Capillary Microreactors, Universitat Dortmund, 2007.
- [164] E.B. Nauman, Residence time theory, Ind. Eng. Chem. Res. 47 (2008) 3752–3766. <https://doi.org/10.1021/ie071635a>.
- [165] N.T. Nguyen, S. Lassemono, F.A. Chollet, Optical detection for droplet size control in microfluidic droplet-based analysis systems, Sensors Actuators, B Chem. 117 (2006) 431–436. <https://doi.org/10.1016/j.snb.2005.12.010>.
- [166] G. Glotz, C.O. Kappe, Design and construction of an open source-based photometer and its applications in flow chemistry, React. Chem. Eng. 3 (2018) 478–486. <https://doi.org/10.1039/c8re00070k>.
- [167] E. Van Eygen, S. De Meester, H.P. Tran, J. Dewulf, Resource savings by urban mining: The case of desktop and laptop computers in Belgium, Resour. Conserv. Recycl. 107 (2016) 53–64. <https://doi.org/10.1016/j.resconrec.2015.10.032>.

[168] E.U. European Union, Study on the review of the list of critical raw materials, Eur. Comissmion. (2017) 93. <https://doi.org/10.2873/876644>.

Appendix

1. Pressure drop model derivation

As described in section 4.3, the average pressure gradient in a tube of length L with fully developed segmented flow with unit length L_u , can be modelled according to Eq. 4-12; assuming the pressure gradient is a periodic function, as shown by Li & Angeli in Fig. A-1 [8].

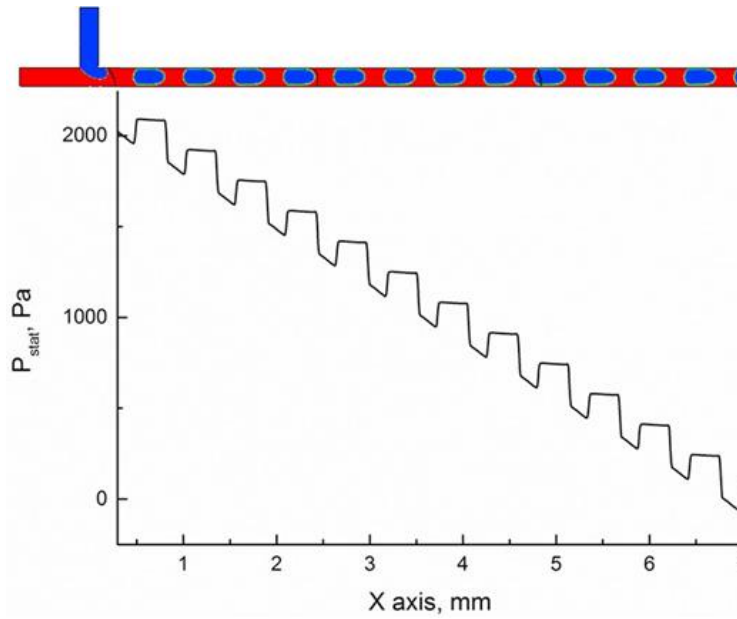


Figure A-1 Profile of the pressure at the wall for a segmented flow pattern. Sourced from “Experimental and numerical hydrodynamic studies of ionic liquid-aqueous plug flow in small channels” By Li Q. & Angeli P. [8].

The integrand in Eq. 4-12 can be simplified by assuming it is composed of independent and constant contributions from the plug and slug fractions of the plug-slug unit. Eq. A1 defines the domain for each contribution; the continuous contribution runs for the length of the slug while the dispersed contribution does so for the length of the plug. The substitution of Eq. A-1 in the integrand of Eq. 4-12 results in Eq. A-2.

$$\left(\frac{\Delta p}{L}\right) = \begin{cases} \left(\frac{\Delta p}{L}\right)_c & 0 \leq x \leq L_s \\ \left(\frac{\Delta p}{L}\right)_d & L_s < x \leq L_u \end{cases} \quad (\text{A-1})$$

$$\int_0^{L_u} \left(\frac{\Delta p}{L}\right) dx = \left(\frac{\Delta p}{L}\right)_c \int_0^{L_s} dx + \left(\frac{\Delta p}{L}\right)_d \int_{L_s}^{L_u} dx = \left(\frac{\Delta p}{L}\right)_c L_s + \left(\frac{\Delta p}{L}\right)_d L_p \quad (\text{A-2})$$

Substituting Eq. A-2 in Eq. 4-12 yields Eq. A-3. As described in section 4.3, the continuous contribution to the pressure gradient is modelled as being equal to the Hagen- Poiseuille flow pressure gradient (Eq. A-4).

$$\left(\frac{\Delta p}{L}\right)_{\text{overall}} = \left(\frac{\Delta p}{L}\right)_c \frac{L_s}{L_u} + \left(\frac{\Delta p}{L}\right)_d \frac{L_p}{L_u} = \left(\frac{\Delta p}{L}\right)_c \left(1 - \frac{L_p}{L_u}\right) + \left(\frac{\Delta p}{L}\right)_d \frac{L_p}{L_u} \quad (\text{A-3})$$

$$\left(\frac{\Delta p}{L}\right)_c = \frac{32\mu_c u_{\text{mix}}}{d^2} \quad (\text{A-4})$$

Finally, substituting Eq. A-4 in Eq. A-3 yields Eq. 4-13. Using the definitions for friction factors and Reynolds numbers in section 4.3, Eq. 4-14 follows directly.

2. Derivation of holdup and specific interfacial area models

The holdup and specific interfacial area models (section 4.2) are derived here starting from the assumption of straight plugs with hemispherical caps. The area and volume of a plug in this model are given in Eqs. A-5 and A-6.

$$A_p = A_{\text{cylinder}} + 2 A_{\text{hemisphere}} = \pi d_p L_p \quad (\text{A-5})$$

$$V_p = V_{\text{cylinder}} + 2 V_{\text{hemisphere}} = \frac{\pi}{12} d_p^2 (3L_p - d_p) \quad (\text{A-6})$$

The definition of the holdup is presented in Eq. A-7. V_d is the total volume of the dispersed phase in the contactor and N_p is the total number of plugs in the contactor. Considering the number of plugs is equal to the number of units and equal to L/L_u , Eq. A-8 is derived. In the limit where $\delta \rightarrow 0$, $d_p = d$, and thus Eq. 4-5 is obtained.

$$\varepsilon = \frac{V_d}{V_T} = \frac{V_p N_p}{V_T} \quad (\text{A-7})$$

$$\varepsilon \frac{L_u}{d} = \frac{d_p^2}{d^2} \left(\frac{L_p}{d} - \frac{d_p}{3d} \right) \quad (\text{A-8})$$

Similarly, the definition of specific interfacial area is presented in Eq. A-9. A_d is the total interfacial area inside the contactor. The same argument of $N_p = L/L_u$ is used and Eq. A-10 is obtained. In the limit where $\delta \rightarrow 0$, $d_p = d$, and thus Eq. 4-8 is obtained.

$$a = \frac{A_d}{V_T} = \frac{A_p N_p}{V_T} \quad (\text{A-9})$$

$$a \times d = 4 \frac{d_p}{d} \frac{L_p}{L_u} \quad (\text{A-10})$$

3. Matlab code for the calculation of the R matrix

The Matlab code developed to calculate the R matrix for any value of N (Eq. 3-13), described in section 3.2.1, is included below.

```

%last terms of the first lines of the R matrix
C_R=zeros(N-1,N);
for i=1:N;
    for j=1:N-1;
        if i<j;
            C_R(j,i)= -RC(N-j+1)/RR(j);
        end
        if i==j;
            C_R(j,i)= -1-RC(N-j+1)/RR(j);
        end
        if j==i-1;
            C_R(j,i)= RR(j+1)/RR(j);
        end
    end
end

%first terms of the first lines of R matrix
AB1_R=zeros(N-1,N);
for i=1:N;
    for j=1:N-1;
        if i==j;
            AB1_R(j,i)=-RB1(j)/RR(j);
        end
        if i==j+1;
            AB1_R(j,i)=(RB1(j+1)+RA1(j+1))/RR(j);
        end
        if i>j+1;
            AB1_R(j,i)=RA1(j+1)/RR(j);
        end
    end
end

%first terms of the first lines of R matrix
AB2_R=zeros(N-1,N);
for i=1:N;
    for j=1:N-1;
        if i==j;
            AB2_R(j,i)=-RB2(j)/RR(j);
        end
        if i==j+1;
            AB2_R(j,i)=(RB2(j+1)+RA2(j+1))/RR(j);
        end
        if i>j+1;
            AB2_R(j,i)=RA2(j+1)/RR(j);
        end
    end
end

R=ones(3*N);
R(1:(N-1),:)= [AB1_R, zeros(N-1,N), C_R];
R(N:2*N-2,:)= [zeros(N-1,N), AB2_R, C_R];
R((2*N)-1:3*N-2,:)= [eye(N), eye(N), -eye(N)];
R(3*N-1:3*N,:)= [ones(1,N), zeros(1,2*N); zeros(1,N), ones(1,N), zeros(1,N)];

```

4. Exponents of dependence for L_{Eff} , τ_{Eff} , N , and Δp_{Eff}

The derivation of the exponents of dependence, presented in Table 6-2, are presented here. A power-law dependence for L_{Eff} , τ_{Eff} , N , and Δp_{Eff} with respect to both u_{mix} and d is assumed.

The corresponding exponents for L_{Eff} and τ_{Eff} are obtained using Eq. 6-1, 2-13, and 4-6 to 4-11. As mentioned in section 6.2, the factor $\varepsilon_{\text{aq}}/(a \times d)$ depends weakly (i.e. the exponent of dependence is close to zero) on Ca_c and Re_c/Ca_c and therefore it depends weakly on d and u_{mix} . Therefore, following Eq. 2-13, L_{Eff}/d is proportional to $(u_{\text{mix}} \times d)^{0.5}$, shown in Eq. A-11, where C is a constant independent of d , u_{mix} , and $D_{U|w}$. By multiplying L_{Eff}/d by d , the exponents of $1/2$ for u_{mix} and $3/2$ for d are found.

$$\frac{L}{d} = \frac{\varepsilon_{\text{aq}}}{(a \times d)} \frac{(u_{\text{mix}} d)^{0.5}}{D_{U|w}^{0.5} C} \ln \left(\frac{1}{1 - \text{Eff}} \right) \quad (\text{A-11})$$

The residence time needed to achieve a given extraction efficiency (τ_{Eff}) is proportional to L_{Eff} and inversely proportional to u_{mix} (Eq. A-12). Therefore, the same exponent for d is valid for τ_{Eff} as is for L_{Eff} and the exponent for u_{mix} is the same as for L_{Eff} minus one.

$$\tau_{\text{Eff}} = \frac{L_{\text{Eff}}}{u_{\text{mix}}} \quad (\text{A-12})$$

The exponents of dependence for N are the result of finding how N changes for a given throughput (Eq. A-13). N is inversely proportional to u_{mix} and to d^2 .

$$N = \frac{4Q_T}{\pi u_{\text{mix}} d^2} \quad (\text{A-13})$$

As detailed in section 4.3, the pressure gradient in segmented flow pattern is proportional to u_{mix} and d^{-2} . It follows from Eq. A-14 and the exponents for L_{Eff} that the pressure drop in a contactor long enough to achieve a given extraction efficiency (Δp_{Eff}) is proportional to $d^{-1/2}$ and $u_{\text{mix}}^{3/2}$.

$$\Delta p_{\text{Eff}} = \left(\frac{\Delta p}{L} \right) L_{\text{Eff}} \quad (\text{A-14})$$

